U.PORTO

FEUP FACULDADE DE ENGENHARIA
UNIVERSIDADE DO PORTO

Structural reduced scale models based on similitude theory

Cristiano José Pereira Coutinho

2017

Structural reduced scale models based on similitude theory

Cristiano José Pereira Coutinho

Thesis submitted to the Faculty of Engineering of the University of Porto - FEUP

in partial fulfillment of the requirements for the degree of

Doctor in Mechanical Engineering

Advisor: José Fernando Dias Rodrigues, Ph.D.
Associate Professor at FEUP

Co-Advisor: António José Caetano Baptista, Ph.D.
Project Manager and Senior Researcher at INEGI

Department of Mechanical Engineering (DEMec)

Doctoral Program in Mechanical Engineering (PRODEM)

Faculty of Engineering of the University of Porto (FEUP)

Porto, 2017

Aos meus pais e irmã,
À Sara.

"*And when you get to the point, where all you want to do is be successful as bad as you want to breathe, then you'll be successful. That's how bad you got to want it!*

Most of you say you want to be successful, but you don't want it bad. You just kind of want it.

You don't want it badder than you want to party. You don't want it as much as you want to be cool. Most of you don't want success as much as you want to sleep."

Eric D. Thomas, Ph.D.
(Motivational speaker)

Acknowledgements

Few people would be willing to coordinate a thesis on this topic. Therefore, first of all I would like to express my gratitude to Dr. Prof. José Dias Rodrigues and to Dr. Eng. António José Caetano Baptista; both provided valuable help and so I am truly grateful for the significant time and effort taken while coordinating and reviewing my thesis research.

Accepting the responsibility of be my main coordinator, Dr. Prof. José Dias Rodrigues allowed us to apply in 2012 for the national *FCT Call for PhD Studentships*, and, as a consequence, he gave me the opportunity to attend the doctoral program in 2013. As my coordinator, he provided me with all the scientific support he could, as well as with import advices in crucial moments.

Similarly, I would like to acknowledge the countless motivational, personal and technical support provided by Dr. Eng. António Caetano Baptista as my co-coordinator at the Institute of Science and Innovation in Mechanical and Industrial Engineering (INEGI).

I also acknowledge the institutional support received from INEGI, particularly from Eng. João Paulo Pereira, the director of my host department. The necessary conditions for my research activities and additional financial support, when proven necessary, were never denied.

Regarding the experimental activities, I would like to thank the valuable help given by: Eng. Santiago Villa, Eng. Luís Moreira and José Bouças in the manufacturing process of the experimental setups; Eng. Andreia Durães, Eng. Miguel Figueiredo and Rui Silva, who provided means to perform the experimental testing in theirs labs; Dr. Eng. Pedro Moreira and Eng. Nuno Viriato in the instrumentation and data acquisition during tests.

I would also like to thank other occasional help from various co-workers, of whom I emphasize those minor but countless helps provided by former colleague Eng. Tiago Guimarães as well as his always contagious good mood that I will hardly forget.

This thesis is dedicated to my parents (José Passos Coutinho and Deolinda Pereira Forte) and sister (Cristina Pereira Coutinho), and to Sara as well.

Financial Support

I gratefully acknowledge the financial support provided by the Portuguese funding institution *FCT - Fundação para a Ciência e a Tecnologia*, under grant SFRH/BD/87538/2012, funded by *Programa Operacional Potencial Humano/Fundo Social Europeu* (POPH/FSE).

I also acknowledged the Project NORTE-01-0145-FEDER-000022 - SciTech - Science and Technology for Competitive and Sustainable Industries, cofinanced by *Programa Operacional Regional do Norte* (NORTE2020), through *Fundo Europeu de Desenvolvimento Regional* (FEDER).

Abstract

Similitude theory is a branch of engineering science concerned with establishing the necessary and sufficient conditions of similarity among phenomena and has been applied to different fields such as structural engineering, vibration and impact problems. Reduced scale model testing is still nowadays a valuable design tool, helping engineers to accurately predict the behavior of oversized prototypes through scaling laws applied to the obtained experimental results.

In the fist part of this thesis, the fundamental and theoretical basis on the similitude theory are provided and selected state-of-the-art approaches are briefly compared in their scope, advantages and disadvantages.

Then the developments in the methodologies used to create reduced scale models as a design tool are reviewed, including those based in the use of: dimensional analysis, differential equations and energetic methods. Besides, given their importance, some major areas of research are reviewed apart: impacted structures, rapid prototyping of scale models and size effects.

In the second part, new approaches to the structural similitude are presented. One of them is an improved approach, based on the concept of applying the similitude theory to the governing equations of plates, minimizing simplifications, whose potential advantages are investigated. The analysis of commercial honeycomb panels is chosen as an interesting case study to evaluate the scaled model testing performance and demonstrate the application of the derived scaling relationships.

Additionally, an original Modular Approach is presented. The objective is to improve how the similitude theory is applied to governing equations, overcoming both its primary and secondary identified weaknesses. Stiffened plates with flat bar or T-stiffeners are selected to demonstrate the use of the Modular Approach and the accuracy of the scaled model testing, through numerical simulations and an extensive experimental program.

In the third part, the Modular Approach is extended in order to establish thermal-structural similitude. The coupled thermal-structural simulation of structural welding in specimens of different scales is presented in order to evaluate the accuracy of the scaled modeling, as well as the limitations in establishing similitude for conductive-convective-radiative systems.

Finally, the constitutive similitude of welded joints is addressed. Taking into account that material constitutive similarity is one of the requisites to achieve similitude of structural behavior, the focus of this research is in establishing similarity conditions regarding relevant welding parameters, such that the constitutive similitude is improved as much as possible, even if the thermal similitude has to be distorted.

Keywords

- Similitude theory;
- Structural similitude;
- Generalized scaling relationships;
- Anisotropic plates;
- Honeycomb structures;
- Modular Approach;
- Beam;
- Stiffened plates;
- Static analysis;
- Dynamic analysis;
- Frequency response
- Thermal-structural similitude;
- Constitutive similitude;
- Structural welding;

Resumo

A teoria da similitude é um ramo da ciência da engenharia dedicado a estabelecer as condições necessárias e suficientes para a semelhança entre fenómenos e tem sido aplicada em diferentes campos tais como engenharia estrutural, problemas de vibração e impacto. A análise de modelos à escala reduzida é ainda hoje uma valiosa ferramenta de projeto, ajudando os engenheiros a prever com precisão o comportamento de protótipos de grandes dimensões através de leis de escala aplicadas aos resultados experimentais obtidos.

Na primeira parte desta tese, as bases fundamentais e teóricas da teoria da similitude são fornecidas e algumas das abordagens mais avançadas são brevemente comparadas no seu campo de aplicação, vantagens e desvantagens.

Em seguida, os desenvolvimentos nas metodologias utilizadas para criar modelos de escala reduzida como uma ferramenta de projeto são revistos, incluindo aqueles baseados no uso de: análise dimensional, equações diferenciais e métodos energéticos. Além disso, dada a sua importância, algumas áreas principais de pesquisa são analisadas separadamente: estruturas sujeitas a impacto, prototipagem rápida de modelos à escala e efeitos de tamanho.

Na segunda parte são apresentadas novas abordagens à similitude estrutural. Uma delas é uma abordagem melhorada, baseada no conceito de aplicar a teoria da similitude às equações diferenciais de movimento de placas, minimizando as simplificações, cujas potenciais vantagens são investigadas. A análise de painéis comerciais de favo de mel é escolhida como um caso de estudo interessante para avaliar o desempenho do teste de modelos à escala, bem como para demonstrar a aplicação das relações de escala derivadas.

Adicionalmente, é apresentada uma Abordagem Modular original. O objetivo é melhorar a forma como a teoria da similitude é aplicada às equações diferenciais de movimento, superando tanto as suas deficiências primárias como as secundárias. Placas reforçadas com barras planas ou reforços em T são selecionadas para demonstrar o uso da Abordagem Modular e a exatidão do teste de modelos à escala, através de simulações numéricas e de um extenso programa experimental.

Na terceira parte, a Abordagem Modular é extendida por forma a permitir estabelecer similitude termo-estrutural. A simulação acoplada termo-estrutural da soldadura estrutural em provetes de diferentes escalas é apresentada com o objetivo de avaliar a precisão da modelação à escala, bem como as limitações sentidas no estabelecimento de similitude para sistemas condutivos-convectivos-radiativos.

Por fim, a similitude constitutiva de juntas soldadas é abordada. Tendo em vista que a similitude constitutiva é um dos requisitos para se obter similitude do comportamento estrutural, o foco desta pesquisa está em estabelecer condições de similaridade relacionadas com parâmetros relevantes de soldadura, de tal forma que a similitude constitutiva seja melhorada tanto quanto possível, ainda que a similitude térmica tenha que ser distorcida.

Palavras chave

- Teoria da similitude;
- Similitude estrutural;
- Relações de escala generalizadas;
- Placas anisotrópicas;
- Estruturas de favo de mel;
- Abordagem Modular;
- Viga;
- Placas reforçadas;
- Análise estática;
- Análise dinâmica;
- Resposta em frequência
- Similitude termo-estrutural;
- Similitude constitutiva;
- Soldadura estrutural;

Contents

List of Figures

List of Tables

Nomenclature

(x, y, z)	Cartesian coordinate system
t	time
T	temperature
α	receptance
Y	mobility
A	accelerance
ω	frequency
f_i	i^{th} natural frequency of vibration

Constitutive behavior

σ_i	normal stress
τ_{ij}	engineering shear stress
$\sigma_{ij}\,(=\tau_{ij})$	tensorial shear stress
E_i	Young modulus
ν_{ij}	Poisson coefficient
$\rho_0^{(k)}$	k^{th} ply mass density
ρ_0	mass density
G_{ij}	shear modulus
Q_{ij}	ply stiffnesse
$\overline{Q}_{ij}^{(k)}$	k^{th} ply reduced stiffness
$\overline{Q}_{ij}$	laminate reduced stiffness
ϵ_i	normal strain
γ_{ij}	engineering shear strain
$\epsilon_{ij}\,(=\gamma_{ij}/2)$	tensorial shear strain
A_{ij}	laminate extensional stiffness
D_{ij}	laminate bending stiffness
B_{ij}	laminate bending-extensional stiffness
ϵ^{el}	elastic strain
ϵ^{pl}	plastic strain
ϵ^{th}	thermal strain

Displacement field and loading variables

u, v, w	displacements in the x, y, z directions
u_0, v_0, w_0	displacements along the neutral axis or plane
$\theta_x, \theta_y, \theta_z$	rotations around the x, y, z axes
f_x, f_y, f_z	body forces

Subscripts and Superscripts

$_p$	(large scale) prototype
$_m$	scaled model
$_{plate}$	plate substructure
$_{beam}$	beam substructure

Plate substructures

a, b, h	plate dimensions along the x, y, z directions
q_x, q_y, q_z	sum of external forces per unit area
m_x, m_y, m_z	sum of external moments per unit area
N_x, N_y, N_{xy}	in-plane force resultants per unit length
$\breve{N}_x, \breve{N}_y, \breve{N}_{xy}$	in-plane edge loadings per unit length
Q_x, Q_y	transverse force resultants per unit length in the z direction, along the x, y axis
M_x, M_y, M_{xy}	moment resultants per unit length

Beam substructures

b, h	beam cross-sectional dimensions along the y, z directions
q_x, q_y, q_z	sum of external forces per unit length
m_x, m_y, m_z	sum of external moments per unit length
N_x	normal force resultant (in the x direction)
Q_y, Q_z	transverse force resultants in the y, z directions, along the x axis
M_x, M_y, M_z	moment resultants in the x, y, z directions

Scaling factors (example for external forces)

$\lambda_{q_x}, \lambda_{q_y}, \lambda_{q_z}$	scaling factors for the external forces q_x, q_y, q_z
λ_q	scaling factor for external forces, in the context of complete similitude ($\lambda_q = \lambda_{q_x} = \lambda_{q_y} = \lambda_{q_z}$)

Heat transfer

ρ	mass density
c_p	specific heat capacity
k	temperature-dependent thermal conductivity
α	temperature-dependent thermal expansion coefficient
h	convective heat transfer coefficient
ε	surface emissivity
$\vec{q}$	conduction heat flux
$\dot{q}_g$	volumetric rate of thermal energy generation
$\dot{q}_c$	convective heat flux
$\dot{q}_r$	radiative heat flux
T_s	surface temperature
T_∞	fluid temperature
T_{sur}	temperature of a much larger, isothermal surrounding surface
σ	Stefan Boltzmann constant
∇	spacial gradient operator

Structural welding

(ξ, y, z)	mobile Cartesian coordinate system with origin at the heat source point
R	distance to heat source point
r	radial distance to weld center line
d	base material thickness
d_c	critical base material thickness
T_0	initial temperature
T_p	peak temperature
T_f	melting temperature
$\dot{Q}$	net power
H	heat input
U	welding voltage
I	welding current
v	average linear torch velocity
η	thermal efficiency
$s1, s2$	characteristic bead dimensions
$S1, S2$	characteristic weld dimensions
n	number of beads
R_{T_i}	cooling rate at temperature T_i
$t_{8/5}$	cooling time from 800°C to 500°C

Acronyms

CFD	Computational Fluids Dynamics
CHT	Conductive Heat Transfer
DF	Displacement Field
DOF	Degree of Freedom
EDA	Energy Distribution Approach
EM	Equations of Motion
ESM	Empirical Similarity Method
FDM	Fused Deposition Method
FE	Finite Element
FEM	Finite Element Method
FMR	Force and Moment Resultants
FRF	Frequency Response Function
GMA	Gas Metal Arc
GMAW	Gas Metal Arc Welding
HAZ	Heat Affected Zone
LAC	Local Amplitude Criterion
MS	Medium Scaled model
MSS	Material and Stacking Sequence
P	Prototype
RCvHT	Radiative/Convective Heat Transfer
RP	Rapid Prototyping

SDR	Strain - Displacement Relations
SLA	Stereolithography
SS	Small Scaled model
SSR	Stress - Strain Relations
STAGE	Similitude Theory applied to Governing Equations (of the system)
TSM	Traditional Similarity Method

Part I.

From the Introduction to the State of the Art

1. Introduction

1.1. Background

1.1.1. The model analysis as a simulation technique

Before production of a new product, the associated design stage is often subjected to many investigations through theoretical analysis and experimental verification. If a new system is complex enough such that no mathematical model can be formulated to predict its behavior, even making assumptions, then extensive experimental evaluation may be necessary until the system gains the necessary reliability and desired performance (Simitses and Rezaeepazhand, 1992). For large and oversized systems, creating the actual working conditions for testing the prototype most of the time is impossible. Even when a prototype test is possible, it is expensive, time consuming, and difficult to control (Jha, 2004; Simitses and Rezaeepazhand, 1992).

In those situations, as shown in figure 1.1, alternatively to the direct observation on the prototype, as well as, to the simulation techniques using mathematical models, it is possible to simulate the prototype with a (similar) scaled model (Simitses and Rezaeepazhand, 1992; Young, 1971). This technique allows to study very complex problems with relative simplicity and, in many cases, with fewer assumptions that those required with others techniques. One of the potential disadvantages of scaled models is that some expenses associated with experimental testing must be incurred (Young, 1971).

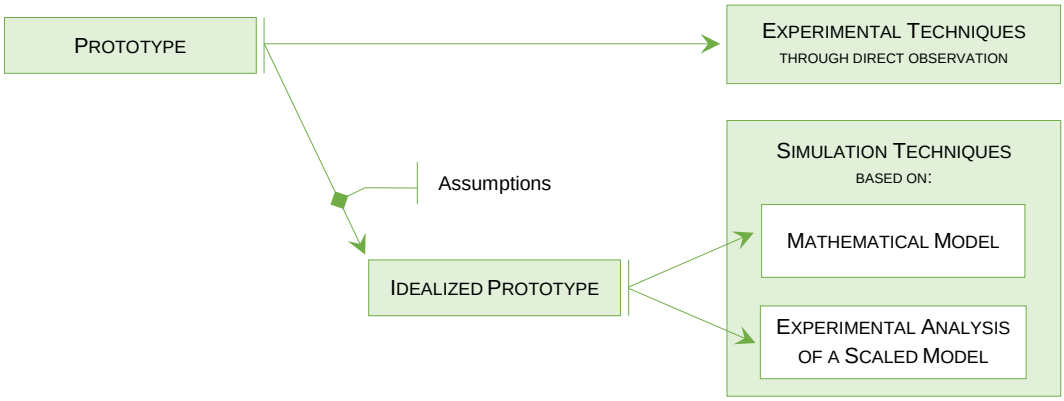

Figure 1.1.: Flowchart for problem analysis through experimental or simulation techniques.

The relatively recent emergence and routine use of extremely powerful digital computer hardware and software has had a major impact on design capabilities and procedures (Chambers, 2009). Even so, testing of subscale models is still nowadays arguably considered, by the aeronautical engineers, as *"one of the more viable and valuable design tools since the advent of flight"* (Chambers, 2009).

1.1.2. Fields of application

Similitude theory is a branch of engineering science concerned with establishing the necessary and sufficient conditions of similarity among phenomena. It has been applied to different fields such as structural engineering, vibration and impact problems, helping engineers and scientists to accurately predict the behavior of the prototype, through scaling laws applied to the experimental results of a scale model related to the prototype by similarity conditions (Ramu et al., 2013; Simitses and Rezaeepazhand, 1992; Szucs, 1980), as outlined in figure 1.2.

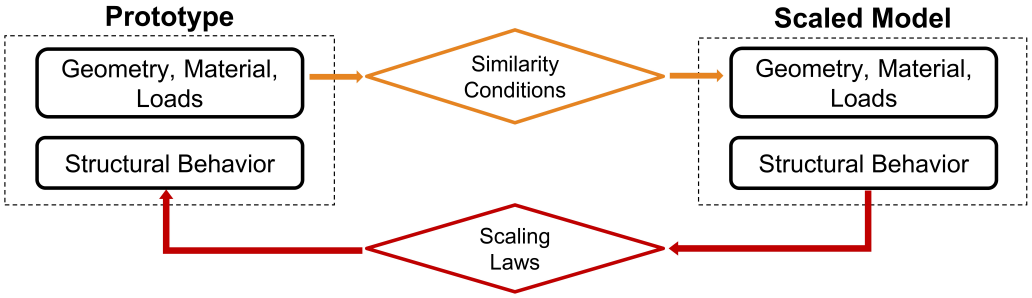

Figure 1.2.: Conceptual diagram for the prediction of the structural behavior of an oversized prototype, based on the experimental results of a scaled model.

The shipping, civil and automobile industries are some examples were the engineers rely heavily on expensive experimental tests in order to verify the component and system analytical predictions, as well as the performance requirements of the design, before going into production (Simitses et al., 2000). Some specific fields where scale models technology has been used include (Jackson, 1990):

- Dynamic modeling of civil engineering structures such as platforms, buildings, dams and bridges;
- Impact analysis of vehicles for safety and crashworthiness;
- Simulation of structural response to blast loads.

This also applies to the aerospace industry where aircraft and spacecraft comprise a class of structures that require an even higher level of reliability, performance and safety. Indeed, most of the initially published studies were motivated by the increased use of reinforced composite materials in aerospace structures (Simitses et al., 2000).

1.2. Motivation

From the evolution of the number of documents regarding reduced scale modeling (in figure 1.3), a large number of publications is observed between the early 60's and the mid 70's, and then only after the late 80's.

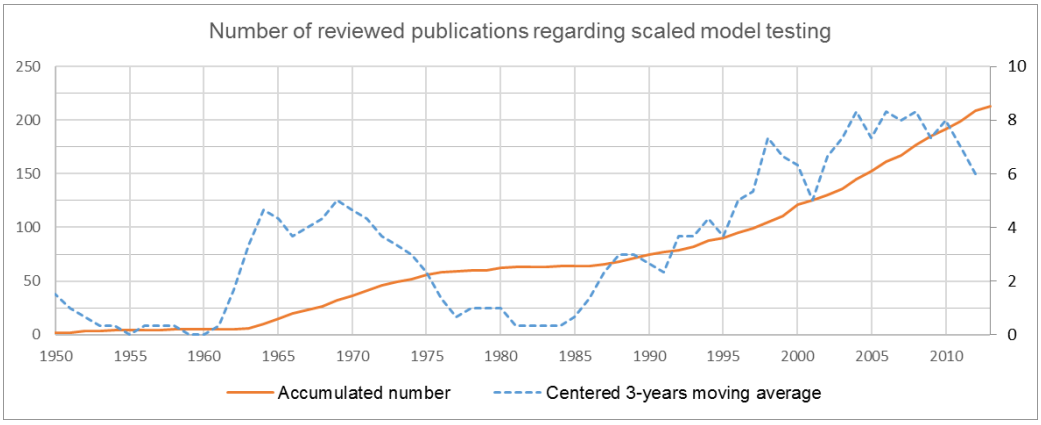

Figure 1.3.: Number of reviewed publications regarding scaled model testing: cumulative value and centered 3-year moving average.

One may argue that the rise and growth of the world wide web, after the mid 90's, enabled scientific research to be published more rapidly than ever before and made available on-line for a large audience. However, according to Sinatra et al. (2015) the fact is that the number of papers published each year (both in physics and general science) has been increasing exponentially for the past 110 years.

Still, this information is compatible with figure 1.3 if one considers that:

- The research in the 60's and early 70's was driven confidentially by the aerospace industry, clearly motivated by the *space race*;
- Despite the currently modest value, after 1985 the cumulative number of publications in figure 1.3 has been rising exponentially.

This demonstrates that although the use of scientific models based on dimensional analysis was firstly proposed by Rayleigh (1915) a century ago, the value and virtues of the reduced scale model testing got attention of the general scientific community only in the last three decades.

The reported aerospace case studies has reached a level of complexity much higher than those presented in most of the current (unconfidential) scientific publications.

Therefore the motivation for further research, including that in this thesis, comes from the desire of developing an intuitive methodology, able to take advantage of the known potential of the experimental scaled model testing. Such methodologies would contribute to the intuitive design of functional demonstrator of new concepts in industrial context, and as a consequence, they would make economically viable the experimental testing of complex or disruptive structures.

1.2.1. Value and virtues of the scaled model testing

As already highlighted, the high cost and potentially dangerous test conditions associated with some applications make scaled model testing an ideal alternative to performing

experiments on prototypes (Jackson, 1990). Its use for simulation of complex engineering problems has been found to be particularly valuable in three respects (Baker et al., 1991; Jha, 2004):

- To obtain experimental data for quantitative evaluation of a particular theoretical analysis;
- To explore the fundamental behavior involved in a little-understood phenomenon;
- To obtain quantitative data for use in prototype design problems, particularly when mathematical theory is overly complex or even nonexistent.

According to Baker et al. (1991), between others, the applications of similarity methods has the additional virtues:

- To generate a functional relationship empirically to solve a general problem;
- To evaluate limitations for an expensive system already in existence;
- To obtain results when no other method of analysis is possible.

1.2.2. Iconic examples

In order to demonstrate the potential of model testing, some examples are given below where the use of scale models helped to overcome some of the greatest engineering challenges. Unfortunately for such highly complex case studies the details of the applied methodology in the creation and use of scaled models are often not available.

1.2.2.1. X-48 Blended Wing Body aircraft

The X-48 aircraft concept, created in 1997, and currently under development by Boeing and NASA, is an experimental unmaned aerial vehicle for investigation into the characteristics of blended wing body (BWB) aircraft, a type of flying wing (Chambers, 2009). Norman Princen, Boeing's chief engineer for the project said:

> "Earlier wind-tunnel testing and the upcoming flight testing are focused on learning more about the BWB's low speed flight-control characteristics, especially during takeoffs and landings. Knowing how accurately our models predict these characteristics is an important step in the further development of this concept." (Petrescu and Petrescu, 2012)

Gary Cosentino, lead flight operations engineer (in NASA Dryden Flight Research Center) had already said:

> "Often, during X-48 flight test, we have seen behaviors in flight not predicted by analysis nor wind tunnel data, and just as often, the behavior of the aircraft in flight is better than our predictions." (Cosentino, 2010)

Several news and videos were published on the flight tests made with 8.5% scale models of the X-48B and X-48C configurations, respectively, after 2007 and 2012[1]. The configuration X-48B, referred by Norman Princen, has undergone almost 15 years of research, and even

(a)

(b)

Figure 1.4.: The remotely operated scale model of the X-48C Blended Wing Body aircraft[3] lifting off Rogers Dry Lake at Edwards Air Force Base, on its first test flight (August 7, 2012)[1]. (Photos by: NASA / Carla Thomas)

so, after his tunnel and flight model testing, modifications were implemented in the X-48C configuration (see figure 1.4) with the intention to explore the potential for reducing noise[2].

[1] www.nasa.gov/centers/dryden/news/FactSheets/FS-090-DFRC.html#.U3Is1lfLKVo (Last accessed: 02-11-2016)

[2] www.nasa.gov/centers/dryden/status_reports/X-48C.html#.U3IJLFfLKVo (Last accessed: 02-11-2016)

[3] www.nasa.gov/centers/dryden/news/NewsReleases/2012/12-16.html (Last accessed: 02-11-2016)

1.2.2.2. Aurora Borealis icebreaker

Aurora Borealis, with construction scheduled after 2012, was designed to be a unique vessel: a combination of a heavy icebreaker, a scientific drilling ship and a multi-purpose research platform that can operate year-round in all polar waters.

To date, research icebreakers of comparable size and capacity for year-round autonomous operations in all polar waters are neither available for commercial nor for scientific operations worldwide.

A dynamic positioning system capable for maneuvering in ice is mandatory for this task - an absolute novelty in the shipping industry. Extensive model tests (see figure 1.5) in the ice tanks of the Hamburg Ship Model Basin (HSVA) and Aker Arctic Research Center (AARC) have proven that Aurora Borealis is indeed able to dynamically position in ice cover with thickness of two meters and more[4] (Lembke-Jene et al., 2011).

Figure 1.5.: Scaled model testing of the Aurora Borealis icebreaker[4]. (Photo by: AWI / Jan Meier)

[4] www.awi.de/en/news/press_releases/detail/item/technical_design_of_the_new_european_research_icebreaker_aurora_borealis_finished/?cHash=e4189f5ec1 (Last accessed: 07-05-2014)

1.2.2.3. Akashi-Kaikyo bridge

Located in Akashi Strait, with a total and central span lengths of 3911m and 1991m respectively, Akashi-Kaikyo Bridge is the longest span bridge in the world. The Bridge was designed to resist both strong wind (280km/h) and tidal current (4.0m/s), as well as, great earthquakes such as the Kobe earthquake, which occurred in 1995 during the construction and that increased the span lengths about a meter .

Given these conditions, several analysis were made. Even a 1/100-scale model of the bridge was constructed and thoroughly tested, as shown in figure 1.6, with the purpose of develop a structure stable enough to resist the wind loadings (Yim).

(a)

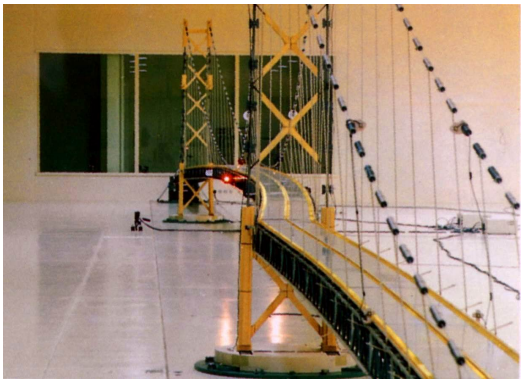

(b)

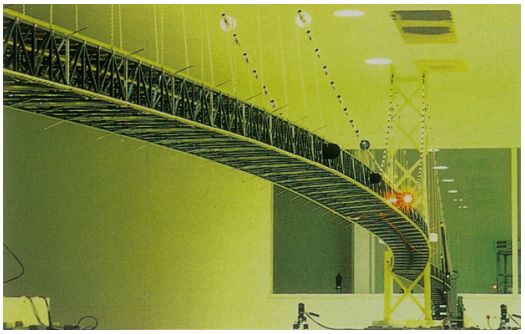

(c)

Figure 1.6.: 1/100-scale model of the Akashi-Kaikyo bridge (figure a), undergoing wind loads (figures b and c)[5]. (Photos by *unknown author*)

[5] `www.lmc.ep.usp.br/people/hlinde/estruturas/akashi.htm` (Last accessed: 02-11-2016)
`www.jb-honshi.co.jp/english/bridgeworld/bridge.html` (Last accessed: 02-11-2016)

1.2.2.4. The Burj Khalifa tower

Located in the United Arab Emirates, the Burj Khalifa reaches 828 meters in height and therefore is the world's tallest building and free standing tower[6].

Scale models of this skyscraper were subjected to over 40 wind tunnel tests to examine the effects the wind would have on the tower and its occupants[7], including:

- Initial tests to verify the wind climate of Dubai;
- Large structural analysis models and facade pressure tests;
- Micro-climate analysis of the effects at terraces and around the tower base;
- Temporary conditions during the construction stage were tested with the tower cranes on the tower to ensure safety at all times.

In this case, besides other modifications, the nuanced understanding of wind loads given to structural engineers by the tunnel testing led to a dramatic design change: the entire building was rotated 120° to reduce wind loading (Feblowitz, 2010).

- An unusual detailed description of the application of scale models:

Rowan Williams Davis Irwin Inc. (RWDI), one of the world's leading wind engineering consulting firm, has handled the testing for numerous projects around the world that, besides the Burj Khalifa, include the Hong Kong International Commerce Center, the Freedom Tower on the World Trade Center Site, the Tacoma Narrows Bridge and Taipei 101 (Feblowitz, 2010).

The National Research Council Institute for Aerospace Research (NRC-IAR) is another company involved in this project. According to Dr. Guy Larose, senior research officer and wind engineer[6]:

> "When a project requires tests that exceed RWDI's own capabilities, Dr. Irwin partners with NRC", that "has the only Canadian facility capable of performing (9m by 9m) wind tunnel tests at high Reynolds numbers on large-scale models."

For its own tests, RWDI had built a model of the entire tower at a scale of 1:500 (see figure 1.7a), and performed the tests at a relatively low Reynolds number. For the NRC tests, RWDI provided a 1/50-scale model of the top third of the tower (see figure 1.7b) made of balsa wood and aircraft plywood, with all the external detail carefully crafted[6].

Usually, prior to construction, complete architectural drawings of the building are given by the structural engineers to wind-engineering experts at RWDI (Feblowitz, 2010). The company simulates and analyzes many of the environmental effects on superstructures using a variety of tools, including wind tunnel testing, and computational fluid dynamics (CFD) using Fluent and a custom-designed program called VirtualWind. Certain studies, like the wind tunnel pressure test, requires a physical scale model of the proposed building to be constructed, along with the surrounding terrain and cityscape[9], such as in figure 1.8.

With its electronic taps (eTAPS) add-on for SolidWorks the outputs for a series of recommended design wind pressures are added to the electronic model. Then, the study models

[6] `www.nrc-cnrc.gc.ca/eng/achievements/highlights/2008/wind_buildings_bridges.html` (Last accessed: 02-11-2016)

[7] `www.burjkhalifa.ae/en/TheTower/Design.aspx#Wind%20Tunnel%20Testing` (Last accessed: 09-05-2014)

[8] `www.rwdi.com/#!wind-engineering/c20jt` (Last accessed: 09-05-2014)

[9] `www.cadalyst.com/aec/3d-model-automation-not-just-blowing-wind-3697#sthash.DSR1v0An.dpuf` (Last accessed: 02-11-2016)

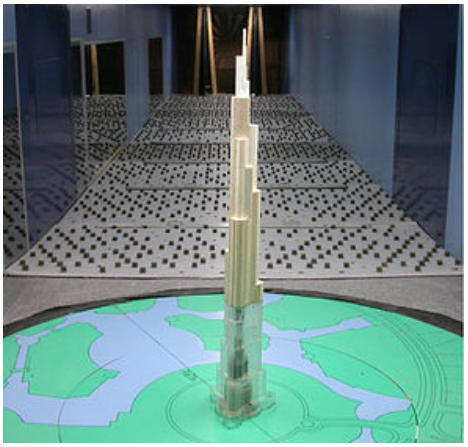

(a) 1/500-scale model

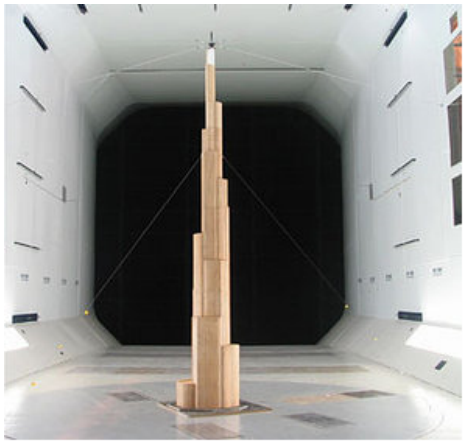

(b) Partial 1/50-scale model

Figure 1.7.: Burj Khalifa structural model tested at two scales[8]. (Photos by *unknown author*)

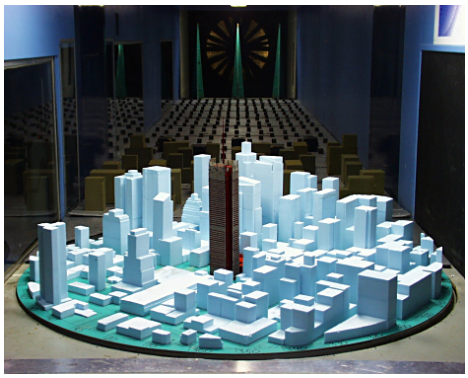

Figure 1.8.: A detailed model of a building ready for the wind tunnel test. The building's surroundings are handcrafted using rigid foam[9]. (Photo by *unknown author*)

are constructed using rapid prototyping technology (RP) or stereolithography (SLA) from 3D Systems, automating the installation of pressure taps, since the model parts can come out of the SLA machine incorporating pressure tubes and holes perfectly spaced for testing. The 1/500-scale model of the Burj Khalifa, for example, contains 1140 separate pressure taps for collecting wind data[9].

All of the measured data is then fed into computer models in order to perform additional analysis (Feblowitz, 2010).

1.2.2.5. Pioneering applications of scaled models in Portugal

Edgar Cardoso (1930-2000) is consensually recognized as a brilliant bridge designer and an enthusiastic pioneer of experimental scale model testing of bridges (Cruz, 2016). Developing new structural concepts and innovative construction techniques, he was the designer of some outstanding audacious elegant bridges in several continents. Some of that designs redefined new world records and deserved a worldwide diffusion and recognition (Cruz, 2016).

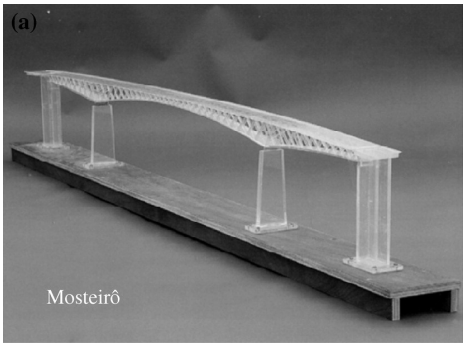

(a) Mosteiró bridge

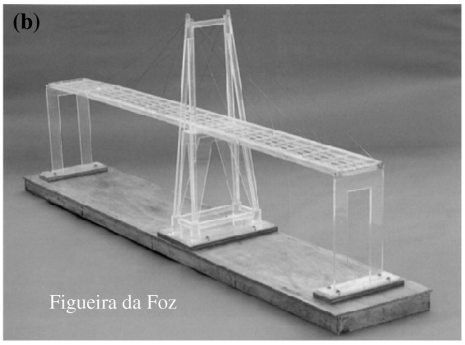

(b) Figueira da Foz bridge

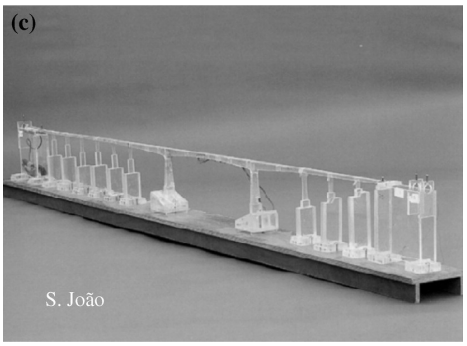

(c) S. João bridge

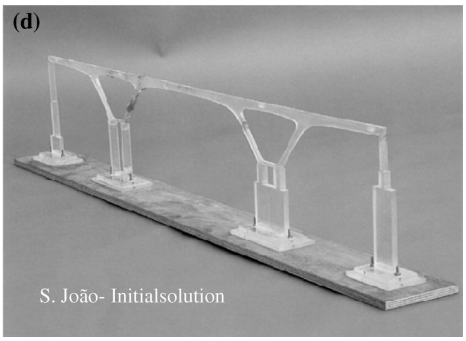

(d) S. João bridge - initial solution

(e) 1/200-scale model for the complete Arrabida bridge

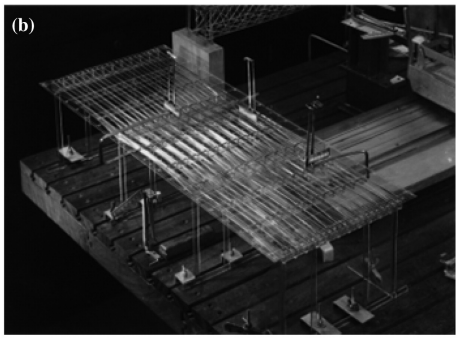

(f) 1/100-scale model for the deck of the Arrabida bridge

Figure 1.9.: Reduced scaled models regarding bridges designed by Eng. Edgar Cardoso (Cruz, 2016). (Photos by *unknown author*)

According to Cruz (2016) Edgar Cardoso's intuition has been progressively enhanced and purified with the experience he accumulated with hundreds of small-scale models such as those in figure 1.9 and with the structural behavior observation. The preference of Edgar Cardoso for experimental methods is highlighted in the following statement made when

planning the Arrábida Bridge:

> "I would frankly like to state that, although I always seek an analytical resolution for everything, it was only once experimental conformation was obtained that I proceed to the algebraic calculation of the various issues. Only after the experimental analysis based on the tests on the reduced scale models did I formulate the various hypothesis that led to an analytical resolution of the various problem. We sometimes work backwards only to comply with what is classically established, why not confess it?"

Concluding, Edgar Cardoso provided us with a large number of examples of experimental reduced scale modeling applied to the bridge design. However, scarce documentation exist regarding the knowledge required for the design and application of the scale models.

1.3. Objectives

Similitude theory is a branch of the engineering science concerned with establishing the necessary and sufficient conditions of similarity among phenomena, and has been applied to different fields such as structural engineering, vibration and impact problems.

The present research was initiated in order to explore how to correctly infer the behavior of a full scale structure from the analysis of a reduced scale functional prototype, by using the structural similarity conditions and scaling laws, which in this thesis are named by the more general term: scaling relationships.

Based on the acquired extensive knowledge about the fundamentals of structural scaling, other of initial objectives is the improvement of the state-of-the-art approaches and/or the development of new methodologies capable to mitigate currently identified limitations.

The developed knowledge is intended to be acquired not only from literary sources and theoretical/numerical studies, but also from the results and experience gained through experimental testing. As the analysis of scale models for simple structures such as plates, beams and shells have already been addressed, the aim for the current research is the experimental testing of stiffened plates whose more complex geometry is obtained assembling simpler structural elements.

Structural similitude is frequently addressed in the literature; constitutive similitude between the prototype and its scaled models is widely recognized as one of the required similarity conditions.

The welding processes widely used for manufacturing of large scale structures may affect the material constitutive behavior in heat affected zone, as well as the global structural response due to the residual deformations and/or stresses. Although such effect is frequently neglected on structural design, it may affect the accuracy of predictions based on the experimental analysis of scaled models.

In this context, the study of constitutive similarity, as a requirement for structural similarity, has become one of the main objectives of the presented research. Its relevance in numerous practical applications justifies the effort invested in the final part of this work.

The potential and advantages of the scale models for industry as a design tool are undeniable, but the best sources of information and knowledge to create them may not be readily available. Therefore, one of the initials tasks is covering the lack of a literature review, providing as much as possible a complete perspective of the scientific contributions to the use of scaled models based on similitude theory, ever since its establishment as a branch of the engineering science.

1.4. Thesis layout

In part I, after this introduction, chapter 2 provides the preliminary and fundamental theoretical basis required to those reading this document or interested in addressing research in the field. Then, chapter 3 presents the literature review of developments in the methodologies used to create reduced scale models as a design tool, including those based on the use of dimensional analysis, differential equations and energetic methods. Besides, given their importance, some major areas of research were reviewed apart.

Part II presents an improved methodology and a new approach to structural similitude. The potential advantages in applying the similitude theory to the governing equations of plates, minimizing the simplifications is investigated in chapter 4. Generalized scaling relationships are provided for static, dynamic and stability analysis from which it is possible to derive, not only the scaling laws for the previously studied plates, but also for any anisotropic (monolithic, sandwich or laminated) plate. In addition, the finite element analysis of commercial honeycomb panels was the chosen case study to demonstrate and evaluate the scaled model testing performance.

Although more structured and straightforward, the applied methodology to derive the generalized scaling laws is neither simple nor intuitive. Chapter 5 presents an original Modular Approach which preserves the advantages of generalized scaling laws and overcomes their limitations. Besides, one of the major achievement is that the similitude theory can be applied to complex structures through differential equations of its simple substructures, even if the governing equations for the whole structure are not available. The static analysis of a plate with flat stiffeners in different scales is selected to demonstrate the use of the Modular Approach and the accuracy of the scaled model testing.

Additionally, in Chapter 6 the scaled experimental testing of a plate with T-stiffeners is documented. The structural similarity conditions derived by the Modular Approach for the stiffened plate are investigated. The structural response of full-scale and reduced-scale structures is predicted by means of the finite element models and measured experimentally. Then, the accuracy of experimental scaled model testing is compared with that of the numerical simulation.

Part III addresses both the thermal-structural and the constitutive similitude. In chapter 7 the Modular Approach is extended in order to allow the thermal-structural scaling relationships to be derived for complex structures. The thermal-structural FE-models of a large and small scale weld butt joint are used to demonstrate the validity and accuracy of the derived relationships.

Finally, in chapter 8 the structural welding is demonstrated as one research area where, regarding the development of scaled models for structural simulation, it is more important to achieve constitutive similarity of the welded joints, rather than thermal-structural similitude between the welding process of the prototype and its scaled model.

2. Similitude theory

Abstract

The fundamental and theoretical basis on the similitude theory are provided. Besides, the Dimensional Analysis is introduced as an independent method, which is combined with the Buckingham's pi-theorem in the Traditional Similarity Method (TSM). This and two other state-of-the-art approaches are briefly compared with regard to their scope of application, advantages and disadvantages.

2.1. Introduction

The current chapter provides the preliminary and fundamental theoretical basis required to those reading this document or interested in addressing research in the field.

The similitude theory is presented in the first part along with the main concepts and definitions. Then, the Dimensional Analysis is equally introduced as an independent method which combined with the Buckingham's pi-theorem yields mutually independent and dimensionless terms that have long been used to establish similitude among phenomena. A complete perspective of the contributions to the use of scaled models is given in chapter 3. Therefore, the last part of the current chapter is devoted to provide and facilitate the basic comparison and understanding of selected main approaches used in those contributions.

Szucs (1980) on the topic of similitude theory, Baker et al. (1991) on the methods to establish the similarity conditions, and Sonin (2001) particularly on the use of Dimensional Analysis published some manuals that are a reference in those topics, and therefore they were often cited.

2.2. Basic concepts and definitions

Baker et al. (1991) present the definition of *model* and *prototype*, frequently used throughout this work, given by Murphy[1]:

> "A model is a device which is so related to a physical system that observations on the model may be used to predict accurately the performance of a physical system in the desire respect."

> "The physical system for which the predictions are to be made is called the prototype."

Unless otherwise stated, the word *model* refers therefore to a physical device as defined previously, and should not be confused with any other type of models employed in engineering, such as the mathematical models (Baker et al., 1991).

Scaling is another commonly used word, defined by Baker et al. (1991) as being synonymous with *modeling* or *scale modeling*, and implying a change in one or more physical parameters between a model and a prototype.

The last definitions to be introduced are some frequent types of model:

[1] Murphy, G. (1950). Similitude in engineering. New York, Ronald Press.

- *Replica model* (Baker et al., 1991):

  "A physical model of a prototype which is geometrically similar in all respects to the prototype and employs identically the same materials at similar locations."

- *Distorted model* (Liang and Reinhorn, 2011):

  "The model is a reproduction of the prototype, but two or more different scales are used."

- *Dissimilar material model* (Baker et al., 1991):

  "A model which is geometrically similar to a prototype but made of different material. The material must, however, have properties which can be correlated with those in the prototype."

- *Dissimilar model* (Liang and Reinhorn, 2011):

  "No physical resemblance between model and prototype."

  also known as an *analog system*, and referred by Young (1971) as a tool to solve the prototype's mathematical model.

2.3. Similitude: The concept and theory

Similitude theory is a branch of science concerned with establishing the necessary and sufficient conditions of similarity among phenomena; Kline[2] called it *the systems's theory of experimentation*. These criteria of similitude will assist the study of new systems, allowing to use the results from previous studies, as well as from systems that can be more easily studied than the original. Here, similitude in systems means similarity of behavior in some specific aspects; therefore, knowing how the state of a given system responds to a certain stimulus, it is intend to predict the response of all the similar systems to similar range of stimuli (Simitses and Rezaeepazhand, 1992; Szucs, 1980).

In mathematical terms, according to Baker et al. (1991), the *general definition of similarity* was presented by Langhaar[3] as follows:

> "The function f' is similar to the function f, provided the ratio f'/f is a constant, when the functions are evaluated for homologous times. The constant $\lambda = f'/f$ is called the scale factor for the function f."

Latter, Szucs (1980) stated that as long as a system can be characterized in terms of a mathematical model:

> "The sufficient and necessary condition of similitude between two systems is that the mathematical model of one be related by bi-unique transformation to that of the other."

It means that, given the characteristics vectors of the prototype X_p and model X_m, containing all the parameters and variables of the systems, then a transformation matrix $[\Lambda]$ can be found, such that (Simitses and Rezaeepazhand, 1992; Szucs, 1980):

$$\{X_p\} = [\Lambda]\{X_m\} \qquad or \qquad \{X_m\} = [\Lambda]^{-1}\{X_p\} \tag{2.1}$$

[2] Kline, S. J. (1965). Similitude and approximation theory. New York, Springer-Verlag.
[3] Langhaar, H. L. (1951). Dimensionless analysis and theory of models. New York, John Wiley & Sons.

Finally, it may be appropriate to emphasize some topic on the Szucs (1980) viewpoint of the similitude concept:

- It makes no sense to speak of similitude in general, this is, the characteristics under which two objects are similar must also be stated;
- The decision of what parameters and variables are relevant and which may be disregarded (for the problem in hand), will always depend on the nature of the problem to be solved.
- The statements of similitude theory are founded on a rigorous mathematical basis, and therefore, if sometimes the conditions of similitude are not easily realized, that is due to the complexity of the problem rather than to deficiencies of the method.

Types of similarity

Depending on the behavior characteristics that one wants to scale, different types of similarity can be defined.

Considering a model (subscript m) and a prototype (subscript p) in which homologous (this is, corresponding, but not necessarily equal) points and times are related by the constants:

$$\lambda_x = \frac{x_m}{x_p}, \quad \lambda_y = \frac{y_m}{y_p}, \quad \lambda_z = \frac{z_m}{z_p}, \quad \lambda_t = \frac{t_m}{t_p} \tag{2.2}$$

then, the two systems are said to be *geometrically similar* if,

$$\lambda_x = \lambda_y = \lambda_z = \lambda_L \tag{2.3}$$

where λ_L is the scale factor for a generic length quantity (Baker et al., 1991; Pankhurst, 1964). This is, a model is said to be geometrically similar to its prototype if the dimensions have been scaled by the same factor. In the extreme, geometric similarity requires that all geometric dimensions of a system be scaled to produce an exact replica model, which however is in most cases impractical or impossible to achieve (Jackson, 1990).

Frequently the geometric similarity is still assumed, by some authors, to be a somehow necessary condition to achieve the similitude among systems. Szucs (1980) made a very clear distinction between geometric similarity and similitude, stating that:

> "Geometric similarity is not even a necessary condition of similitude, let alone a sufficient one: indeed it is often an obstacle to similitude!"

A geometrically similar plaster model and the electric analog model of a mechanical process are the given examples, respectively, of how geometric similitude is neither sufficient nor necessary for structural similitude (Szucs, 1980).

Indeed, for most people the geometric similarity may be very misleading. If proportional enlargement or reduction did not affect a given structure, then the behavior of the full-sized device would always be easily studied with a replica model. Szucs (1980) cites the example of Galilei that very early (in 1638) counter proved this illusion with two scaled bones[4], as well as other examples found in nature.

[4] *"the greater of which is only thrice longer than the smaller, but sufficiently thickened to carry a larger animal as safely as the smaller bone carries the smaller animal. Clearly, the bone thus enlarged looks impossibly heavy; clearly, if one is to preserve the proportions of the original human limbs on the enlarged body, one must use a different bone substance, one of greater strength, or a body substance of less weight. Otherwise the enlarged body would be broken by its own weight." (Galilei, 1638)* (Szucs, 1980)

Other types of structural similarity can be defined, with the respective scaling factors. For the sake of brevity, just the concepts are presented below, but additional considerations can be found in several manuals.

- *Kinematic similarity*: similarity of the motion. According to Baker et al. (1991) or Jackson (1990), the Langhaar's definition of kinematic similarity[3] is as follows:

  > "The motions of two systems are similar, if homologous particles lie at homologous points at homologous times."

- *Dynamic similarity*: similarity of the homologous net forces experienced by homologous parts of the systems. If the model and prototype are kinematically similar and if the mass distribution are similar, then dynamic similarity exists (Baker et al., 1991), being easily inferred from Newton's second law (Jackson, 1990).

- *Constitutive similarity*: similarity in the stress-strain curve or constitutive properties of materials. This means that a model can be fabricated from homologous materials at homologous locations in corresponding structures, provided that the nondimensional stress-strain curves of materials are similar (Baker et al., 1991).

Despite what has just been presented, and to demonstrate the apparent contradiction between authors on some topics, it is cited the Spring Edition (1986) of the Kline book[2] widely recognized as a reference on the similitude theory:

> "Two systems will exhibit similar behavior if geometric, kinematic, and dynamic similarity are all guaranteed; furthermore these conditions will be fulfilled if the two systems are made geometrically similar and if the ratios of all the pertinent forces are made the same in the two problems."

Indeed, Szucs and Kline made consistent statements if well understood. In other words, they stated that to achieve the structural similitude is not necessary to respect the geometric similarity; but being possible to achieve that condition, it will not be sufficient and additional similarity conditions may have to be respected to obtain the desired structural similitude.

2.4. Dimensional Analysis

The dimensional analysis requires all system variables to be listed, in order to apply the Buckingham's pi-theorem. This way, the number of parameters is reduced by obtaining a functional relationship between product groups of variables, such that these terms are mutually independent and dimensionless (Harris and Sabnis, 1999; Jha, 2004; Simitses and Rezaeepazhand, 1992).

2.4.1. Basic concepts and definitions

The concepts presented below are an overview of the definitions given by Sonin (2001): one of the most recent and complete manuals, inspired by many other authors in the areas of dimensional analysis and similarity.

Base quantities The *base quantities* form a complete set of basic building blocks for an open-ended system of derived quantities that may be introduced as necessary. The base and derived quantities together provide a rational basis for describing and analyzing the physical world in quantitative terms (Sonin, 2001).

Unit and numerical value A base quantity can be expressed as a multiple of standard sample of its own kind, that is, it can be measured in terms of a *unit*, that may be chosen arbitrarily. If $\boldsymbol{a}$ is a unit chosen for quantities of type $\boldsymbol{A}$, the process of measurement yields a *numerical value* A, this is: $\mathbf{A} = A\mathbf{a}$ (Sonin, 2001).

As by convention all base quantities of the same kind are always measured in terms of the same unit, the ratio of the numerical values of any two quantities of the same kind is independent of base unit size (Sonin, 2001).

Derived quantities, dimensions and dimensionless quantities A *derived quantity* of the first kind is a product of various powers of numerical values of base quantities. The *dimension* of any physical quantity, whether base or derived, is a formula that defines how numerical value of the quantity changes when the base unit sizes are changed[5]. Therefore, a derived quantity is *dimensionless* if its numerical value remains invariant when the base units are changed (Sonin, 2001).

Physical equations and dimensional homogeneity A mathematical equation that correctly describes a physical relationship between a numerical value Q_0 and a set $Q_1, Q_2, ..., Q_n$ of other physical quantities:

$$Q_0 = f(Q_1, Q_2, ..., Q_n) \tag{2.4}$$

must be *dimensionally homogeneous*, and will therefore remain valid when base units sizes are changed arbitrarily, this is, Q_0 and f will change by the same factor (Sonin, 2001).

2.4.2. The steps of dimensional analysis and the pi-theorem

Although the dimensional analysis process is widely explained and exemplified in several publications, in this section the main steps are introduced. Sonin published a book (Sonin, 2001) which is one of the best manuals to get a deeper insight of the following method:

1. Identify a complete set of n independent quantities $Q_1 ... Q_n$ that determine the value of Q_0:

   $$Q_0 = f(Q_1, Q_2, ..., Q_n) \tag{2.5}$$

   The set is *complete* if no other quantity can affect the value of Q_0, and *independent* if the value of each member can be adjusted arbitrarily without affecting the value of any other member (Sonin, 2001).

2. List the dimensions of the variables. To this end, a type of system of units must be previously selected, such as the Length-Mass-Time that leads to dimensions of the form:

   $$[Q_i] = L^{l_i} M^{m_i} t^{\tau_i} \tag{2.6}$$

   Then, from the complete set of physically independent variables pick a *complete, dimensionally independent subset* $Q_1 ... Q_k$, and express the dimension of each the remaining variables in terms of the dimensions of the subset variables:

   $$[Q_i] = [Q_1^{N_{i1}} \, Q_2^{N_{i2}} \, ... \, Q_k^{N_{ik}}] \qquad i \in \{0, k+1, k+2, ..., n\}$$

[5] Note that in common parlance the terms unit and dimension are often used synonymously, but such usage is undesirable in a treatise where fundamental understanding is paramount. In a sense, the concept of dimension were introduced to avoid talking of "units" for quantities that may have no physical representation, but whose numerical values nevertheless depend on the choice of base quantities.

Note that, although the subset $Q_1 ... Q_k$ may be picked by trial and error, the number of independent quantities k is unique for the set $Q_1 ... Q_n$, never exceeding the number of base dimensions in the last one.

The exponents N_{ik} can be found either by inspections or using any formal algebraic method.

3. The pi-terms are written, with the exponents N_{ik} determined previously, as follows:

$$\pi_i = \frac{Q_{k+i}}{Q_1^{N_{(k+i)1}} \, Q_2^{N_{(k+i)2}} \, ... \, Q_k^{N_{(k+i)k}}} \qquad i \in \{0, k+1, k+2, ..., n\}$$

4. The equation 2.5 can be alternatively written as:

$$\pi_0 = f(Q_1, Q_2, ..., Q_k, \pi_1, \pi_2, ..., \pi_{n-k})$$

However, from the principle that any physically meaningful equation must be dimensionally homogeneous, one can conclude that $Q_1, Q_2, ..., Q_k$ must in fact be absent from the previous equation.

Thus, it was achieved the final result of dimensional analysis:

$$\pi_0 = \psi(\pi_1, \pi_2, ..., \pi_{n-k}) \tag{2.7}$$

which expresses the *Buckingham's pi-theorem*. Many of the authors publishing in the area of dimensional analysis, such as Bridgman (1922), Charlton (1954), Simitses and Rezaeepazhand (1992), Sonin (2001) or Jha (2004), describing for slightly different words this theorem originally stated by Buckingham (1914) as follows:

> "Any equation:
>
> $$f(Q_1, Q_2, ..., Q_n) = 0 \tag{2.8}$$
>
> which describes completely a relation subsisting among a number of physical quantities, of an equal or smaller number of different kinds, is reducible to the form:
>
> $$\psi(\pi_1, \pi_2, ..., \pi_i) = 0 \tag{2.9}$$
>
> in which the $\pi's$ are all the independent dimensionless products of the form $Q_1^{a_1} \, Q_2^{a_2} \, ... \, Q_n^{a_n}$ that can be made. If k is the number of fundamental units required in an absolute system for measuring the n quantities, the number of dimensionless products is:
>
> $$i = n - k \quad "$$

2.4.3. Alternative methods of dimensional analysis

The pi-theorem requires the existence of a complete set of dimensionless quantities, that however is not unique. As just seen, although following well defined steps, the constructions of the most adequate set of pi-terms is made by trial-and-error, considering for example possible limitations in future experimental tests.

Several methods were developed with the purpose of obtaining easier and more suited procedure. According to Jackson (1990), Simitses and Rezaeepazhand (1992), Barr presented a survey of several methods for dimensional analysis: the Rayleigh method, and various modi-

fications such as the Buckingham method, the Echelon Matrix method, the Basic Stepwise method, and the Proportionalities method.

Baker et al. (1991) also presented an alternative procedure for obtaining pi-terms, which indeed was the procedure used by Jackson (1990). Another procedure, proposed by Thomas Szirtes (of the SPAR Aerospace), were described and exemplified by Rao (1996).

Matrix approach

The method presented by Baker et al. (1991), as other methods, construct a dimensional matrix (see table 2.1), where each column represents a variable, and each row represents a fundamental dimension. Thus, the elements in a given column are the powers to which each dimension is raised, for the variable represented by that column.

	Q_0	Q_1	Q_2	...	Q_n
M	m_0	m_1	m_2	...	m_n
L	l_0	l_1	l_2	...	l_n
t	τ_0	τ_1	τ_2	...	τ_n

Table 2.1.: Generic example of a dimensional matrix for a problem with n relevant quantities, using a MLt unit system.

Performing a row reduction on the matrix, it can be modified to the reduced row echelon form (Gauss-Jordan elimination), this is, a matrix where all the leading coefficients are 1 with 0 elsewhere in the column of that coefficient (see table 2.2). Note that, the quantities associated with each of the columns of the dimensional matrix may depend on the columns changes made during the row reduction.

	Q_j	Q_k	Q_l	Q_m	...	Q_r
M	1	0	0	c_{1m}	...	c_{1r}
L	0	1	0	c_{2m}	...	c_{2r}
T	0	0	1	c_{3m}	...	c_{3r}

Table 2.2.: Possible reduced row echelon form of the dimensional matrix from table 2.1.

This allows to find the rank of the matrix, which is the size of the obtained identity submatrix, or in practical terms, the number of fundamental units k referred in the pi-theorem.

Additionally, one can easily obtain the equations (as many as the rank of the dimensional matrix) relating the powers a_i of each quantity dimension $[Q_i]$ present in the equation of dimensional homogeneity:

$$M^0L^0T^0 = [Q_0]^{a_0}[Q_1]^{a_1}[Q_2]^{a_2}...[Q_n]^{a_n} \tag{2.10}$$

For the given generic example, the equations would be the following:

$$\begin{aligned} a_j &= -(c_{1m}a_m + ... + c_{1r}a_r) \\ a_k &= -(c_{2m}a_m + ... + c_{2r}a_r) \\ a_l &= -(c_{3m}a_m + ... + c_{3r}a_r) \end{aligned} \tag{2.11}$$

After substitution in the equation of dimensional homogeneity, and collecting terms with the same exponents, yields $n - k$ pi-terms (Baker et al., 1991).

2.5. Introduction to the state-of-the-art approaches

A complete perspective of the contributions to the use of scaled models based on similitude theory is presented in chapter 3. As depicted in figure 2.1, this supplementary section is intended to facilitate the basic comparison and understanding of three of the main approaches:

- Traditional Similarity Method (TSM);
- Empirical Similarity Method (ESM);
- Similitude theory applied to governing equations of the system (STAGE).

which were used in those contributions to derive the similarity conditions between the prototype and its scaled model.

	Type of Approach to Obtain Scaling Relationships:		
	Experimental		Analytic / Numerical
Initial approaches:	Empirical Similarity Method (ESM)	Traditional Similarity Method (TSM)	Similitude Theory applied to Governing Equations (STAGE)
Main scope of applications:	Rapid prototyping of models.	Systems with unknown behavior.	Any system with available governing equations.
Advantage:	The transformation matrix is derived empirically.	Simple although requiring great effort and skill.	System's behavior is explicitly related with its parameters and variables.
Disadvantage:	Extra effort manufacturing and testing additional specimen pair.	Most adequate set of pi-terms is made by trial and error and may have little physical meaning.	Requires mathematical formulation of the physics of the problem.
Advanced approaches for distorted models:	Advanced ESM	TSM + Model Variation	STAGE + Sensitivity Analysis
Main limitations:	Requires additional experimental testing, both in small and large scale.	May require additional scaled models and experimental analysis.	Mainly restricted to linear static and frequency analysis.

Figure 2.1.: Overview of the state-of-the-art approaches to obtain scaling relationships. The main scope, advantages and disadvantages of each approach are covered, as well as the main limitations using distorted models.

Globally speaking, if all similarity conditions are satisfied, the two systems are completely similar (Simitses and Rezaeepazhand, 1992). However, due to limitations on conducting the experiment, often complete similarity is difficult to achieve or even undesirable. When at least one of the similarity conditions cannot be satisfied, partial similarity is achieved. In this case the model which has some relaxation in similarity conditions is called distorted model, whose behavior is different from that observed when complete similarity exist (Rezaeepazhand and Simitses, 1993; Rezaeepazhand et al., 1995, 1996a,b; Rezaeepazhand and Wisnom, 2009; Simitses and Rezaeepazhand, 1992, 1993a,b).

2.5.1. Traditional Similarity Method

2.5.1.1. Description

By using dimensional analysis, an incomplete form of the characteristic equation can be formulated in terms of $n-k$ nondimensional products of the n variables and parameters of the system:

$$\pi_0 = \psi(\pi_1, \pi_2, ..., \pi_{n-k}) \tag{2.12}$$

where k is the number of fundamental units.

If the pi-terms of the functional equation (2.12) are the same for two systems, this is, for the prototype (p) and its scaled model (m):

$$\pi_i^{(p)} = \pi_i^{(m)} \qquad i \in \{1, 2, ..., n-k\} \tag{2.13}$$

then, $\psi^{(p)} = \psi^{(m)}$ even if the functional equation is not completely known, and hence:

$$\pi_0^{(p)} = \pi_0^{(m)} \tag{2.14}$$

These equalities of pi-terms determine the conditions for which the two systems are similar; they are called the *similarity conditions* or *scaling laws* (Simitses and Rezaeepazhand, 1992).

Depending on how the equation of dimensional homogeneity was set up and solved, the individual dimensionless terms may have little physical meaning. This is identified by Baker et al. (1991) as the only real weakness of developing model laws via the pi-theorem.

2.5.1.2. Limitations using distorted models

For a distorted model, inequality of some pi-terms causes a change in scale factors of those terms. Pi-terms which include these scale factors will also change. In this case, the number of unknown scale factors is greater than the number of similarity equations and additional relationships between variables are needed. Dimensional analysis cannot provide these relationships. These additional relationships between variables can be established by the governing equations of the system, such as equations of equilibrium and compatibility, kinematic relations, material behavior equations and boundary conditions. If these equations are not available, by conducting a series of experiments the effect of distortions on each term can be found while the other terms are kept constant. A sufficient amount of data should be determined from model tests so that these relationships can be understood clearly (Simitses and Rezaeepazhand, 1992).

2.5.1.3. Improved approach: Method of model variation

One of the oldest documents referring the model variation as a method to assess the influence of the distorted variables is a contractor report prepared by Wissmann (1968) (available since 2009). The use of one particular model configuration as the starting point, employing variations to define the model law in the vicinity of this model was also found by Wissmann in a conference paper from 1963, edited by Baker (ASME, 1963). In other words, the method derives the model law from the experimental (and theoretical) knowledge of a function and its derivations at one particular point (Wissmann, 1968).

Employing dimensional analysis, Wissmann assumed that it is possible to scale the model for the variables π_1, π_2, ..., π_s; but not for π_{s+1}, π_{s+2}, ..., π_{n-k}. Therefore with the increments in the distorted *pi*-terms defined as:

$$\Delta\pi_q = \pi_q^{(p)} - \pi_q^{(m)} \qquad (q = s+1, s+2, ..., n-k)$$

the prototype functional equation can be express as:

$$\pi_0^{(p)} = \psi \left[\pi_1^{(m)}, \pi_2^{(m)}, ..., \pi_s^{(m)}, \left(\pi^{(m)} + \Delta\pi\right)_{s+1}, \left(\pi^{(m)} + \Delta\pi\right)_{s+2}, ..., \left(\pi^{(m)} + \Delta\pi\right)_{n-k} \right] \tag{2.15}$$

The prototype's behavior can therefore be predicted through the following Taylor expansion:

$$\pi_0^{(p)} = \pi_0^{(m)} + \sum_{q=s+1}^{n-k} \frac{\partial \pi_0^{(m)}}{\partial \pi_q^{(m)}} \Delta\pi_q + \frac{1}{2} \sum_{p=s+1}^{n-k} \sum_{q=s+1}^{n-k} \frac{\partial^2 \pi_0^{(m)}}{\partial \pi_p^{(m)} \partial \pi_q^{(m)}} \Delta\pi_p \Delta\pi_q + \ldots \tag{2.16}$$

where each derivative must be found through at least one additional experiment or theoretical relation (Wissmann, 1968).

2.5.2. Empirical Similarity Method

2.5.2.1. Description

The Empirical Similarity Method (ESM) was proposed to overcome some of the inherent difficulties and inaccuracies in other methods caused by model distortions. In this context, model distortions refers to discrepancies between the actual scale models and those required between a system and its scaled model (for example by the TSM). Two examples are the distinct material behavior induced by the rapid prototyping of scaled models or the geometric (shape) distortions (Cho and Wood, 1997; Cho et al.; Dutson and Wood, 2002).

As depicted in figure 2.2, besides the prototype and its scaled model, the method requires a geometrically simple specimen pair: one fabricated from a rapid prototyping process and another from the actual production process (Cho et al., 1998). The changes (between scales) in material properties, size and loading conditions are captured in the scale transformation matrix ($[S]$ or $[S']$), while changes (for the same scale) in geometric shape can be captured in the form transformation matrix ($[F]$ or $[F']$), such that:

$$\begin{aligned} \left\{x^{(p)}\right\} = [S'] \left\{x^{(m)}\right\} &= [S'] [F] \left\{x^{(ms)}\right\} \\ = [F'] \left\{x^{(ps)}\right\} &= [F'] [S] \left\{x^{(ms)}\right\} \end{aligned} \tag{2.17}$$

Size here refers to parametric scaling of the overall length dimensions.

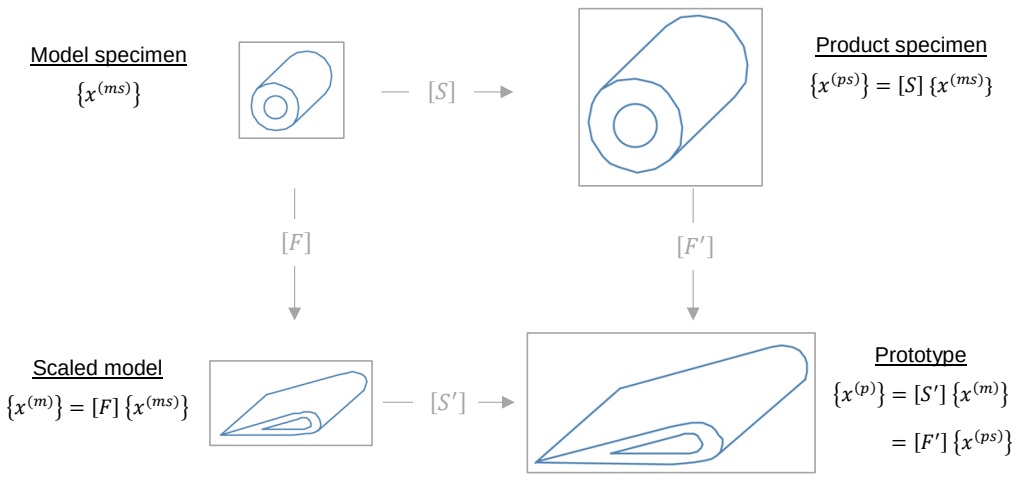

Figure 2.2.: Conceptual diagram of the Empirical Similarity Method. (Adapted from (Dutson et al., 2003))

The ESM is based on the assumption that the variations captured by the transformation

matrix $[F]$ in the state vector are independent from those captured by the transformation matrix $[S]$:

$$\begin{aligned}[F'] &= [F] \\ [S'] &= [S]\end{aligned} \tag{2.18}$$

This assumption allows to firstly derive the scale transformation matrix $[S]$ from a geometrically simple specimen pair and then apply it to systems with distinct geometric features (Cho et al., 1998). So, the relation between the behaviors of the model and prototype (in equations (2.17)) can be written as follows:

$$\left\{x^{(p)}\right\} = [S]\left\{x^{(m)}\right\} \tag{2.19}$$

One of the advantages of the method is that even if the material properties of the product or model systems are not available, the prototype's behavior can be predicted. The major disadvantage is the required effort manufacturing and testing the additional simple specimen pair (Dutson and Wood, 2002).

2.5.2.2. Limitations using distorted models

Although the ESM has the ability to capture model distortions in the scale transformation matrix $[S]$, other type of distortions called specimen distortions still invalidate the assumptions of the ESM expressed by equations (2.18), introducing errors in the predictions (Dutson and Wood, 2002).

Specimen distortions in this context are referred as inconsistencies between the scaling of the system pair ($[S']$) and that of the specimen pair ($[S]$), such that $S \neq S'$. It can also be any inconsistency regarding the scaling between the models ($[F]$) and between the prototypes ($[F']$), causing $F \neq F'$ (Dutson and Wood, 2002).

2.5.2.3. Improved approach: Advanced ESM

The goal of the Advanced ESM is to capture the change in the scale transformation matrix $[S]$ as the form parameters change, or alternatively, to capture the change in the form transformation matrix $[F]$ as the scale parameters change (Dutson and Wood, 2002). At least an additional intermediate specimen pair is required.

In general, n intermediate specimen pairs allow for the construction of an n^{th} order Newton's Divided Difference Interpolating Polynomial (which is an Lagrange polynomial that incorporates divided differences $f[x_0]$, $f[x_0, x_1]$, ..., $f[x_0, x_1, ..., x_n]$):

$$\begin{aligned}P_n(x) = f[x_0] + f[x_0, x_1](x - x_0) + \\ + f[x_0, x_1, x_2](x - x_0)(x - x_1) + ... + \\ + f[x_0, x_1, ..., x_n](x - x_0)...(x - x_{n-1})\end{aligned} \tag{2.20}$$

If a change in a form parameter u_i is being discretized, the second order polynomial prediction of $[S]$ is given by:

$$\begin{aligned}[S] = [S]_0 + \frac{[S]_1 - [S]_0}{u_{i_1} - u_{i_0}}(u_i - u_{i_0}) + \\ + \frac{\left(\frac{[S]_2 - [S]_1}{u_{i_2} - u_{i_1}} - \frac{[S]_1 - [S]_0}{u_{i_1} - u_{i_0}}\right)}{u_{i_2} - u_{i_0}}(u_i - u_{i_0})(u_i - u_{i_1})\end{aligned} \tag{2.21}$$

2.5.3. Similitude Theory applied to Governing Equations

2.5.3.1. Description

An intuitive approach was initially proposed by Kline (1965), applying the Similitude Theory to Governing Equations, which with proper boundary and initial conditions, explicitly define the response of the system as function of its independent variable and parameters (Simitses and Rezaeepazhand, 1992). For simplicity, in this manuscript it is referred by the acronym "STAGE".

The method can either be applied directly to the differential equations or indirectly to their solution. The first option is the most advantageous approach, and its application was introduced and exemplified by (Simitses and Rezaeepazhand, 1992) in a technical report. It allows to define $n+r$ relations among the scaling factors for the m variables and parameters of the system. As r of those $n+r$ relations are redundant, its number can be reduced selecting any sub-set of n non-redundant scaling relationships (i.e., scaling laws and similarity conditions).

So, if the two systems are completely similar, $m-n$ scale factors can be chosen freely and the values of the other scale factors are found by using n scaling relationships (Simitses and Rezaeepazhand, 1992, 1993b).

According to Baker et al. (1991) the primary weakness of this approach is that one must know enough about the physics of the problem to be able to write down a complete set of governing equations. This is not at all a restriction on the TSM, which only requires a list of the physical parameters, as well as, their basic dimensions. Even so, not having to solve the governing equations to develop a scaled model is an advantage.

Procedure for application of STAGE directly to equations

In the first stepwise procedure proposed by Baker et al. (1991) a hypothesis for specific model laws were firstly advanced by assuming interrelations between the scale factors of all the parameters. Only then, these assumptions were tested verifying if the equation of the prototype, written with model scaled variables[6], remained identical to the equation of the model.

This is however an unnecessary trial-and-error procedure, that can be simplified inverting the steps as described in a report by Simitses and Rezaeepazhand (1992). The similarity conditions between model and prototype are then more easily determined through the following steps:

- For each variable x_i define a scale factor as follows:

$$\lambda_{x_i} = \frac{x_{im}}{x_{ip}} \tag{2.22}$$

- Into the differential equation of the prototype, substitute the variables x_{ip} by the model scaled variable x_{im}/λ_{xi};
- Require the result of the previous substitution to be the differential equation of the model. This will happen if the coefficients, obtained by grouping the scale factors in each term of the equation, are all equal.
- Repeat a similar process for the boundary conditions.

[6] By model scaled variables one should consider each of the model variables multiplied by the respective scale factor.

Szucs (1980) had already presented this method in his book, additionally showing that dimensionless terms can be obtained from the derived similarity conditions.

2.5.3.2. Limitations using distorted models

Due to relaxations on the similarity conditions and their effect on model behavior, the accuracy of prototype's predictions becomes dependent of the selected sub-set of n non-redundant scaling relationships.

In the literature, in order to select the scaling laws which have the most accurate prediction, usually all of the model parameters except one are chosen to respect the similarity conditions. Then, the effect of this relaxation in the accuracy of the design scaling laws for a wide range of this parameter is investigated. For example, for laminated structures, scaled down models with different stacking sequence, material properties, number of plies, and geometric parameters are considered. (Rezaeepazhand and Simitses, 1993, 1997; Rezaeepazhand et al., 1995, 1996a,b; Rezaeepazhand and Wisnom, 2009; Simitses and Rezaeepazhand, 1993a,b).

Therefore, the main limitation in the use of the partial similitude, as just described, is that the error introduced in the predictions due to the relaxation of a given similarity condition is not quantified. Using a case study with known solution, the scaling laws which have the most accurate prediction are established. However, in a structure with different geometry or structurally more complex, the effect of each parameter is likely to change, modifying the accuracy of the design scaling laws. Even so, in these cases, as no known solution is available, the previously selected similarity conditions are re-used assuming that they are still the most accurate.

3. Literature review

Abstract

Similitude theory is a branch of engineering science concerned with establishing the necessary and sufficient conditions of similarity among phenomena, and has been applied to different fields such as structural engineering, vibration and impact problems. Testing of sub-scale models is still nowadays a valuable design tool, helping engineers to accurately predict the behavior of oversized prototypes through scaling laws applied to the obtained experimental results.

In this chapter it has been reviewed the developments in the methodologies used to create reduced scale models as a design tool, including those based in the use of: dimensional analysis, differential equations and energetic methods. Besides, given their importance, some major areas of research were reviewed apart: impacted structures, rapid prototyping of scale models and size effects. At last, some topics on which additional efforts can be undertaken are highlighted.

3.1. Introduction

This chapter aims to cover the lack of a review providing as much as possible a complete perspective of the scientific contributions to the use of scaled models based on similitude theory, ever since its establishment as a branch of the engineering science. The potential and advantages of the scale models for industry as a design tool are undeniable, but the best sources of information and knowledge to create them may not be readily available.

On the other hand, although the scientific publications usually include a brief and specific analysis of the state of the art covering the most relevant and recent researches on a specific topic, sometimes relevant contributions already presented few decades before were missed. Highly focused on the structural similitude of laminated plates and shells, Simitses et al. (2000) presented the only known review. Since then, several research works were published including some innovative approaches such as the use of the governing total energy equation (section 3.3.2.2), the use of energetic methods (section 3.3.4), the sequential similitude method (section 3.4.1) or even the empirical similarity methods (section 3.4.2.2).

In a recent monograph, Chambers (2009) claims that NASA has been leading contributions to the technology of model testing for over 80 years, since its predecessor: the NACA. Virtually every technical discipline studied by NACA and NASA for application to aerospace vehicles has used unique and specialized models, including the fields of aerodynamics, structures and materials, propulsion, and flight controls. Indeed, as claimed by Chambers, many of the improvements to the state of the art were presented in reports prepared under contract or in publications resulting from granted research programs, most of them totally and other partially supported by NASA. After the update to the NASA Technical Reports Server on 2013, more than fifty new reports related to scale models, structural similitude and/or scale design studies were detected, most of them confidentially produced between the sixties and the nineties. These reported case studies reached a level of complexity much higher than those presented in most of the current (unconfidential) scientific publications.

Compiling all of the available information, the following review intends therefore to give a complete and clear perspective of how the knowledge evolved in both the scientific and industrial realities.

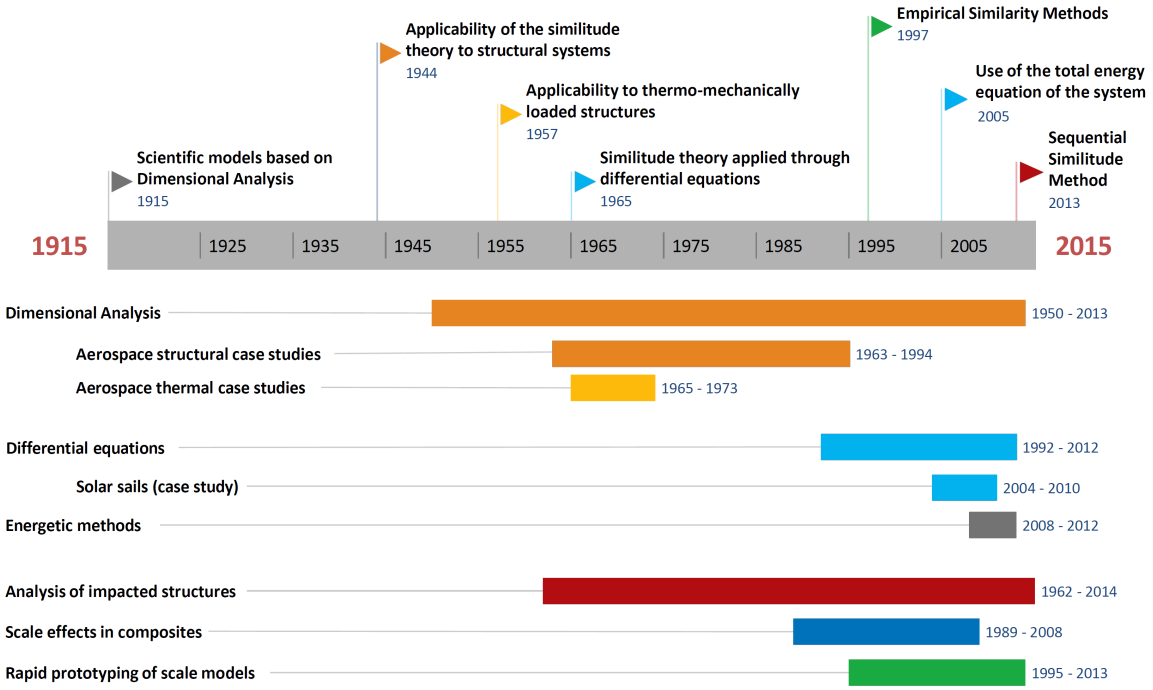

Figure 3.1.: Time overview of the main innovations, methodologies and case studies on the use of scale models.

3.2. Historical review

The work presented by Rayleigh (1915) is consensually recognized as the first presentation of the use of scientific models, based on dimensional analysis. However, it would take almost thirty years until Goodier and Thomson (1944) had firstly discussed the applicability of the theory of similitude to structural systems (Simitses et al., 2000). That technical note, prepared for NACA with restricted access, include a test program that would latter be omitted in a more succinct publication by Goodier (1950). Both documents presented the same systematic procedure for establishing similarity conditions employing dimensional analysis. For such a preliminary document, it is impressive how deep is the insight given into the analysis of large deflections, buckling, plastic behavior, and materials with nonlinear stress-strain characteristics, as well as into simpler structural problems.

In the following years, a set of published books dealt with similitude and modeling principles, and most of them with dimensional analysis. Simitses et al. (2000) in their review cited the following: Langhaar (1951), Charlton (1954), Pankhurst (1964) and Gukhman (1965). Furthermore, the authors emphasize three other books from:

- Kline (1965) for giving a perspective on the method to establish the similarity conditions, based on both dimensional analysis and the direct use of governing equations;
- Szucs (1980) for being particularly thorough on the topic of similitude theory, with emphasis on the direct use of the equations of the system;
- Singer et al. (1997) as the most recent, and for including a chapter about modeling with emphasis on dimensional analysis concepts.

The books published by Baker et al. (1991) and Sonin (2001) are good alternatives to those published, respectively, by Kline (1965) and Singer et al. (1997).

Although some alternative approaches to establish the similarity conditions has meanwhile been proposed and successfully applied, the use of dimensional analysis keep motivating, as no other, some authors to publish new manuals (or chapters) such as the following: Harris and Sabnis (1999), Szirtes (2007), Tan (2011). However, even the most recent manuals are mainly written with an academic purpose, and usually the referred case studies or examples are relatively simple.

Some of the remaining references of this review are presented in section 3.3, according to the approach applied to derive the similarity conditions:

- Use of dimensional analysis;
- Use of differential equations;
- Combined application of methodologies;
- Use of energetic methods.

The other references are reviewed apart in section 3.4, inside some of the major current areas of research and regardless of the methodologies applied.

3.3. Current methods to apply the similitude theory

3.3.1. Use of dimensional analysis

The derivation of the scaling laws by dimensional analysis requires all system variables to be listed in, in order to apply the Buckingham's pi-theorem. This way, the number of parameters is reduced by obtaining a functional relationship between product groups of variables, such that these terms are mutually independent and dimensionless (Harris and Sabnis, 1999; Jha, 2004; Simitses and Rezaeepazhand, 1992).

Concepts such as dimensions and units seems so logical that they are now taken completely for granted. It is difficult to realize that the present state of physical description did not always exist (Harris and Sabnis, 1999). At the same time, much confusion between similarity and dimensional analysis had existed for over more than a century (Jha, 2004), with several authors devoting their investigations to these topics.

A historico-critical review of dimensional analysis was presented by Macagno in 1971, and has been widely cited since then. Such a deep review of the dimensional analysis is out of purpose of this work; a brief insight of the developed work over more than two centuries is allowed here, with more detailed information available, for example, in the reviews of Baker et al. (1991) or Jha's master thesis (Jha, 2004), that closely followed the Macagno's review.

The genesis of modern theory of dimensional analysis dates back to the concept of geometric similitude firstly used by Galileo, with the meaning of quantities, units and dimensional homogeneity discussed by Euler just in 1765. Lagrange and Laplace formulated the principles of dimensional analysis, based on Euler's work, and latter Fourier in 1822 established the foundations of dimensional analysis, being one of the first to recognize the existence of dimensionless groups. Much work had been carried out by Carvalho, Vashy and Riabouchinsky before Buckingham developed the pi-theorem in 1914 (Jha, 2004). Indeed, some authors argue that the pi-theorem should more appropriately be attributed to Vashy that in 1892 published a paper with a formulation very close to that of the pi-theorem (Baker et al., 1991). This theorem forms the basis for investigating physical relationships within the framework of similarity (Jha, 2004) and were discussed and revised by Bridgman, Brickhoff, Langhaar, Van Driest, and Brand (Simitses and Rezaeepazhand, 1992).

Further explanation and examples of the dimensional analysis process is available from several publications, such as the book by Sonin (2001) that provides a deep insight of the method.

3.3.1.1. Structural similitude

A state of the art on structural dynamics modal testing, up to 1968, is included in a contract report presented by Wissmann (1968). The author documented the existence of recent investigations on some interesting means of combining dimensional analysis with a partial insight into a given problem. The result of the new approaches is a distorted model in which only the relevant unknown parameters need to be scaled (Wissmann, 1968).

Wissmann proceeded with his review stating that the advent of aeroelastic flutter models in the 1940's showed that complete dynamical similarity (replica models), used until then, was impractical for the aircraft industry, and would anyway lead to erroneous results because of model imperfections. Although full scale testing had been used widely, the sheer size of the modern (to date) launch vehicles, such as the Saturn I, recaptured the interest in the use of both replica and distorted models (Wissmann, 1968).

Indeed, from a historical perspective of the structural dynamics testing research, presented by Horta and Kvaternik (2000), covering the time period since the early sixties until the year 2000, it is easily realized how important the model design became. From the several studies that allowed a deeper understanding of the many unique dynamic characteristics of spacecrafts, as well as the resolution of anomalies, the following can be selected and grouped as follow:

- Early spacecraft scaled model testing
  - The Nimbus spacecraft (distorted) 1/5- and (simplified) 1/2-scale models (Carden and Herr, 1964);
  - The lunar lander 1/6-scale model (dynamically similar) (Blanchard, 1968; Herr and Leonard, 1967);
  - The dynamically scaled 3/8-model of an early version of the Viking spacecraft lander (McGehee and Stubbs, 1973).
- Launch vehicle scaled model testing
  - The Saturn I 1/5-scale replica model (Catherine, 1965; Mixson and Catherine, 1964a,b);
  - The Titan III 1/5-replica model, in both the A (Thompson, 1967), B (Peele and Thompson, 1968) and C-configuration (Morosow and Jaszlics, 1966);
  - The Saturn V 1/10-model (partly approximated) (Leadbetter, 1970; Leadbetter et al., 1967; Peele et al., 1970; Pinson and Leonard, 1969);
  - The distorted 1/40 scale Saturn V model (Adelman and Steeves, 1968; Catherine, 1968; Grimes et al., 1970; Steeves and Catherine, 1968);
  - The 1/15 scale shuttle dynamic model (Fralich et al., 1972; Leadbetter and Kiefling, 1971; Leonard and Morgan, 1970; Thornton, 1971);
  - The shuttle 1/8 scale dynamic model (Bernstein et al., 1974; Blanchard et al., 1977; Grumman Aerospace Corporation, 1972; Leadbetter et al., 1976; Levy et al., 1974; Mason et al., 1974a,b; Pinson, 1975; Zalesak, 1975).
- Under the Dynamics Scale Model Technology program (McGowan et al., 1991):

- Generic multi-body dynamic model for the space station (Belvin and Edighoffer, 1986b);
- The early space station 1/10-scale generic model (McGowan et al., 1990);
- Early space station 1/5:1/10-hybrid-scale dynamic model (Javeed et al., 1993);
- Hoop column antenna (Belvin and Edighoffer, 1986a; Schroeder et al., 1989);
- Other related studies: Shih et al. (1987), Letchworth et al. (1988) and Hsu et al. (1989) discussed the possibility of scaled model testing of space station geometries, especially for vibration analysis. Most of the studies have used complete similarity between model and prototype (Simitses et al., 2000). Additionally it can be referred the existence of a preliminary design, analysis and costing of a dynamic scale model of the NASA Space Station (Gronet et al., 1987), as well as, the conceptual design and analysis of a dynamic scale model of the Space Station Freedom (Davis et al., 1994).

Additionally, one can cite an investigation about the use of scale models to determine vehicle characteristics (Jaszlics and Park, 1969; Penning, 1969) and a technical paper about the similitude requirements and scaling relationship that apply to wind-tunnel and free-flight model airplane testing (Wolowicz et al., 1979). Although more focused on aerodynamic studies, the latter derives the similitude requirements from the functional dependence of the force and moments on the geometry, kinematics, and (aero) dynamics of a aircraft.

Besides the specialized dynamics modal testing applied by the aerospace industry, other laboratory techniques were proposed for the experimental analysis of structures under dynamic loads, including the shaking-table testing in the 1940s and the pseudo-dynamic testing in the early 1980s. Although developed primarily for seismic testing of structures, according to Williams and Blakeborough (2001) there is considerable potential for their application to other load types in the fields of civil and mechanical engineering.

Once again, limited capacity of the available equipment and economic reasons often motivated the use of scaled models based on the similitude theory (Kumar et al., 1997). Assuming that the model and prototype are made of the same material, as the scaling relationships obtained according to the principles of dimensional analysis do not yield a unique set of scale factors, the researchers have applied and compared mainly the following three distinct procedures: the mass-based, time-based and acceleration-based procedure, where the scale factor for density, time and acceleration, are respectively chosen to be unitary. A more detailed comparison is presented by Kim et al. (2004); Kumar et al. (1997).

Regarding applications on the mechanical structural engineering field the following researches are known. Kumar et al. (1997); Usami and Kumar (1996) studied the inelastic seismic response steel bridge piers of hollow box section using the pseudo-dynamic testing. Usami and Kumar (1996) tested the 1/8-scale model through the mass-based approach, while Kumar et al. (1997) presented a comparison of the results obtained through both the mass- and time-based approach. Later, Chung et al. (1999) conducted the shake table testing of a three-storey metallic structure, base isolated by laminated rubber bearings, through a 1/4-scale model designed according to the acceleration-based approach. The research was intended to evaluate the inelastic behavior of the base isolation system, validate the substructuring pseudo-dynamic testing of the same model, and to develop an analytical for earthquake response. More recently, Kim et al. (2004) compared the results of the pseudo-dynamic testing of manufactured wide flange cantilever steel columns, obtained according to the mass-, time- and acceleration-based approaches.

Some authors often highlight the lack of confidence predicting the prototype's behavior for nonlinear dynamic response. In the review by Williams and Blakeborough (2001), keeping

the same Cauchy and Froude numbers in the model equal to those of the prototype is stated as the necessary condition to achieve dynamic similitude. However, as the Cauchy number takes into account the elastic restoring forces, the similitude laws are generally derived in the elastic range, which according to Kim et al. (2004) may justify the discrepancies obtained predicting inelastic behaviors.

For the sake of clarity, some conclusions from other researches regarding aerospace applications, based on the use of governing equations, are here introduced in advance. Davis et al. (1994); Gronet et al. (1987) stated that replica modeling is required to capture in the model much of the dynamic nonlinear behavior of the prototype. Such approach yield the same scaling factors as the mass-based approach, helping to understand why the other are inappropriate to scale inelastic behaviors. One of the main drawbacks of the replica modeling technique is that the gravitational acceleration is required to be scaled during the model testing. The aerospace industry has developed and applied some methods to simulate reduced gravitational force for prototype studies on Earth (Stubbs, 1971), while on the known applications regarding shaking table and pseudo-dynamic testing the inability to scale the gravitational acceleration is usually either neglected or ignored.

In any of the previously referred approaches, the model and prototype are assumed as manufactured from the same materials. If significant scale effects are not avoided the material similarity is disrespected and therefore discrepancies should be expected. Kim et al. (2004) proposed a modified approach to compensate stiffness distortions caused by variations on steel properties, structure fabrication or even test setup. The scale factor for stiffness is replaced by the measured elastic stiffness ratio of prototype to scaled model, and the remaining scale factors are changed accordingly. In the absence of stiffness distortions, the proposed scaling laws are the same as in the acceleration-based approach . Kim et al. (2009) also presented a modified version of the acceleration-based approach to face the technical difficulties in reproducing the non-linear material properties of concrete for small scales, however a detailed review of the reduced scale modeling applied to concrete structures is out of the scope of this work.

Besides the investigations on impacted structures, very few works using exclusively the dimensional analysis were presented recently. Even so, Ramu et al. (2013) used this approach to establish the structural similitude for elastic models made from different materials. The scaling laws were then applied to the static deflection obtained numerically for the metallic roof slab of a nuclear reactor and experimentally from a 1/12-scale model made of bonded Perspex® (plastic) sheets.

3.3.1.2. Thermal similitude

The establishment of thermal similitude can be considered either as an independent or as a complementary task in the deduction of the structural similitude for a specific case study. Also in this technical discipline, NACA and NASA led for decades the contributions to the technology of model testing. O'Sullivan (1957) prepared a report where the simultaneous effects of transient aerodynamic heating and external loads on aircraft structures is studied with the purpose of determining through scaled model testing the ability of a structure to withstand flight to supersonic speeds.

A similar study was prepared by Katzoff (1963) about scaling criteria for the design and testing of thermal models, focused on spacecraft structures, followed by the experiments of Harrison and Jones (1965) on simple structures, as well as, a set of similarity ratios given in a tabular form by Watkins (1966). Later, Marshall et al. (1969) present a report covering the work performed during an analytical and experimental study of the possible limitations existent in utilizing small-scale models for determination of spacecraft thermal behavior,

including some sections about the problems of selecting (different) materials for a thermal model.

Until then, the transient behavior of thermal models has been greatly neglected; Maples and Scogin (1970) prepared a report covering an investigation with the primary objective of developing a practical method for thermal modeling of a conduction-radiation design, under transient conditions.

The available information from NASA ends with two reports (Marshall and Foster, 1973; Shannon, 1972) describing the development and demonstration of practical thermal scale modeling techniques applicable to radiation - conduction - convection systems with particular emphasis on the cabin atmosphere/cabin wall thermal interface, resulting therefore on a practical tool for manned spacecraft applications as the Skylab and Space Shuttle Orbiter.

In a recent study, published by Sabour and Bhat (2010), the research of the scale modeling approach in thermal testing of aircraft components were resumed. According to the authors, the idea of thermal scaling has been validated experimentally. It is therefore a possible solution at the design stage, when it is not possible to carry out experimental validation of the design analysis on prototype structures.

One of the covered concepts is the combined use of thermal similitude with the *Thermal Acceleration Method*, useful when high-temperature strength data are needed for conditions for which there is no experimental information. This is particularly true for long-time creep and stress-rupture data, where it is quite possible that the creep strength to give 1% deformation in 100000 hours (11.4 years) is required, although the alloy has been in existence for only 2 years (Sabour and Bhat, 2010).

Furthermore, Sabour and Bhat claim to be pioneers using a dissimilar material (thermal) model, since, unfortunately, the latest report from NASA that the authors seem to know is that published by Katzoff (1963).

3.3.2. Differential equations

Kline (1965) and Baker et al. (1991) soon presented the concept of applying the similitude theory through the differential equations instead of the dimensional analysis. In 1991, Baker et al. cited Kline as being the only known author already using this concept as the primary method.

In the nineties several papers were published often without properly referencing those original authors. Although the following analysis focus only on the published papers and reports since then, the original authors of these concepts have just been clearly assigned.

3.3.2.1. Similitude theory applied to the solution of the differential equations

The proceedings of an workshop held at NASA Langley Research Center (Jackson, 1994) are one of the "first" documents were the similitude theory was applied to known (assumed) analytical solutions. The document presents a wide discussion on the scaling effects in: (1) structures, (2) material properties, failure and damage detection, and (3) impact response.

Using the referred approach Simitses, Starnes and Rezaeepazhand have published several papers that deal with the design of scaled-down models and the use of the test data of these models to predict the behavior of large prototypes. The behavior includes displacements, stresses, buckling loads and natural frequencies of laminated beam-plates, plates and shells (Simitses et al., 2000).

Regarding the analysis of plates, the structural similitude was derived for the following study cases:

- The buckling caused by axial compression (Simitses, 2001; Simitses and Rezaeepazhand, 1993a,b) or shear load (Simitses and Rezaeepazhand, 1993a) of simply supported symmetric laminated cross ply plates, as well as the shear buckling of symmetric, angle ply laminated plates (Rezaeepazhand and Simitses, 1993);
- The free vibration of simply supported, symmetric, angle (Rezaeepazhand et al., 1995) and cross (Rezaeepazhand et al., 1995; Simitses, 2001) ply laminates;
- The flutter speed of angle-ply (Rezaeepazhand and Yazdi, 2011) and cross-ply (Yazdi and Rezaeepazhand, 2011a) laminates subjected to an air flow.

On the other hand, regarding the analysis of cylindrical shells the following topics were studied:

- The buckling of simply supported, symmetric cross-ply laminated cylinders caused by axial compression (Rezaeepazhand et al., 1996b) or external pressure (Simitses et al., 1997);
- The free vibration of symmetric cross-ply laminated cylinders (Rezaeepazhand et al., 1996a) and (isotropic) orthogonally stiffened cylindrical shells (Torkamani et al., 2008, 2009).

The structural similitude was also established for the free vibration of shells with double curvature (Rezaeepazhand and Simitses, 1997), as well as, for a laminated cylindrical tube under tensile, torsion and bending loads, and under external and internal pressure (Chouchaoui and Ochoa, 1999; Chouchaoui et al., 1999).

It is interesting to note that the approach used by Torkamani and his collaborators (Torkamani et al., 2008, 2009) is slightly different from the other. The authors additionally re-wrote the characteristic equation in therms of dimensionless parameters and only then applied the similitude theory.

3.3.2.2. Similitude theory applied directly to the differential equations

The use of the previous method is dependent on the availability of an exact or approximate analytical solution of the governing equations, valid for the geometry, boundary conditions and loading of the structure being scaled. Applying the similitude theory directly to the governing equations that limitation can be overcome.

One of the "first" documents to present a study to explore this method of similitude analysis is a technical report prepared by Simitses and Rezaeepazhand (1992). Despite the advantages of this new method, his application remained restricted mainly to the following case studies:

- The cylindrical bending of (simply supported) laminated beam-plates subjected to transverse loads (Simitses, 2001; Simitses and Rezaeepazhand, 1992, 1993b);
- The buckling of:
  - symmetric, cross-ply laminated plates caused by biaxial (Ungbhakorn, 2001) and shear (Ungbhakorn, 2001) loading;
  - symmetric, angle-ply laminated plates caused by biaxial loading (Singhatanadgid and Ungbhakorn, 2002a);
  - anti-symmetrically, cross-ply and angle-ply laminated plates subjected to biaxial loading (Ungbhakorn and Singhatanadgid, 2003c);

  - polar orthotropic annulus plates under internal and external compressive or torsional shear loads (Singhatanadgid and Ungbhakorn, 2005);
  - axially compressed sandwich column without and with geometric imperfections (Frostig and Simitses, 2004);
  - unidirectional delaminated beam-plates (Rezaeepazhand and Wisnom, 2009);

- The free vibration of anti-symmetrically laminated cross and angle-ply plates (Singhatanadgid and Ungbhakorn, 2002b);

- The effect of delamination damage on flutter pressure of angle-ply laminated composite plates (Yazdi and Rezaeepazhand, 2011b), as well as, cross-ply and quasi-isotropic laminated plates (Yazdi and Rezaeepazhand, 2012).

The free and forced vibration characteristics of isotropic plates were also numerically predicted by Wu (2003, 2005), while Singhatanadgid and Na Songkhla presented an experimental validation of the similarity requirements for the natural frequencies of thin isotropic plates (Na Songkhla and Singhatanadgid, 2005; Singhatanadgid and Na Songkhla, 2008).

Fewer studies on the structural similitude of shells were made; only the buckling and free vibration of symmetric (Ungbhakorn and Singhatanadgid, 2003b) and anti-symmetric (Ungbhakorn and Wattanasakulpong, 2007) cross-ply, as well as, anti-symmetric angle-ply (Ungbhakorn and Singhatanadgid, 2003a) laminated cylindrical shells were investigated by Ungbhakorn and his collaborators.

A more complex case study was presented by Hilburger et al. (2001). The response of a built-up, multi-cell noncircular composite structure subjected to combined internal pressure and mechanical loads was studied analytically. The scaling laws derived from governing equations for shear deformable plates (based on first-order shear-deformable plate theory) are used for predicting the structural response of a prototype representative of a portion of a blended wing body transport aircraft.

Similitude theory applied to the equations in dimensionless form

This methodology may be applied with a slightly difference: the governing equations are taken into dimensionless form, and only then the similarity conditions are derived.

Canfield et al. (2004) presented similarity criteria, for scaling solar sail systems, written as dimensionless terms, while Canfield et al. (2010) presented almost the same investigation, but with the similarity criteria written in terms of scale factors (although not explicitly defined), and some numerical predictions of 20, 30 and 40-m solar sail from the results of a 10-m prototype. The experimental testing and demonstration of a 1/4-symmetry deployable system with 10 m in size (Gaspar et al., 2006; Murphy et al., 2004), as well as, of a 20-m full system (Gaspar et al., 2005; Laue et al., 2005) are documented as activities supporting the system and analytical development that will ensure scalable design and accurate predictions for larger ground systems, a flight demonstration system (40-m scale), and mission systems of up to 200 m on a side (Murphy et al., 2004).

Similitude theory applied to the governing total energy equation

Kasivitamnuay and Singhatanadgid (2005) proposed a slightly different method based on the fact that the governing differential equation of several structures can be derived by the variational methods of the governing energy equation. The concept of the method is that a total potential energy of a similar scaled model has to be proportional to that of full size structure and satisfy the principle of conservation of energy.

According to the authors, this method provides clear scaling results of a full-sized structure, since the whole members are scaled simultaneously rather than scaled separately. Besides, the energy equation includes not only the domain of the structure and the applied loads but also the boundary conditions. Therefore no complementary methodology, such as the dimensional analysis, is required to derive the implicit scaling factors for the supporting conditions, because they are obtained directly.

Concluding, both methods have the same order of generality, leading to the same scaling factors. The use of the energy equation simply has the advantages of being more straightforward and efficient, directly giving the scaling factors for the structural behavior even when the structure is constructed from several members (Kasivitamnuay and Singhatanadgid, 2005; Ungbhakorn and Singhatanadgid, 2009).

The methodology was successfully applied to the static deflection and free vibration of isotropic thin plates by Kasivitamnuay and Singhatanadgid (2005) and latter to the vibration response of generally laminated doubly curved shallow shells by Ungbhakorn and Singhatanadgid (2009).

3.3.3. Combined application of methodologies

The approaches presented here are somehow a set of methodologies which, although having something in common with the previous, include some innovative aspects such as the use of the Finite Element Method (FEM) to create the structural model, as well as the use of modal analysis to obtain a one degree of freedom generalized governing equation.

Vassalos (1999) presented some valuable information to the appropriate use of scale models in the design of marine structures. The concept of physical similarity, the dimensional analysis and the use of governing equations are referred by the authors as the main approaches used to plan model experiments.

Wu et al. (2002) applied the modal analysis to the matrix equations of motion, given by the FEM. From the obtained equation, governing i^{th} mode of vibration of the system, the authors listed the relevant variables and parameters for the problem being analyzed. Then, the dimensional analysis was applied to derive the similarity conditions. A gantry crane structure was given as a demonstrator of the methodology.

A slightly different approach uses the similitude theory applied directly to the same equation governing the i^{th} mode of vibration of the system. Additionally, and as a complementary tool, the dimensional analysis is used to derive the scale factors for all the relevant variables neither appearing in the governing equation nor being related to the other variables by any equation. Using this approach, Wu predicted the (free and forced) vibration characteristics of an elastically supported isotropic plate subjected to circular moving loads (Wu, 2006), as well as, the lateral vibration characteristics of a rotor-bearing prototype, for free and forced vibration (Wu, 2007).

Another method based on FEM and frequency response function (FRF) analysis was proposed by Gang et al. (2010).

3.3.4. Use of energetic methods

In the last years a new approach known as the Energy Distribution Approach (EDA) is being developed. The similitude is defined by using relationships among mode shapes, natural frequencies, and damping loss factors (Mace, 2003). Specifically, EDA has already been used by De Rosa and Franco in order to predict the original and scaled responses of coupled plate-plate and beam-plate systems (De Rosa and Franco, 2008, 2010).

Two other works were published by De Rosa and his collaborators based on the usage of the EDA. De Rosa et al. (2011) presented some preliminary analyses for simple plate and plate assemblies, using analytical models. Further steps such as the adoption of FEM and experimental measurements were indicated as a means to proceed with better recreations of realistic assemblies. In other work, De Rosa et al. (2012) presented the similitude for acoustic-elastic linear systems where these were defined by both analytical and finite element approaches. The results showed that the proposed approach can open interesting possibilities for applications. The need for further work is clearly established, particularly with the introduction of more complex and realistic structures such as beams, stiffened plates and shells.

3.4. Major areas of research

The following publications are reviewed apart and grouped as belonging to some of the most current and relevant areas of research. So, more than one methodology may be referred in each of the next sections. For example, the dimensional analysis remained the primary method in the most of the publications concerning impacted structures, and very few innovations were made; on the other hand, to reduce the limitations in the use of prototyped models new approaches were specifically proposed to that end.

3.4.1. Impacted structures

Concerning the use of models to study the structural behavior of shells subjected to static, dynamic and impulse loads, Simitses et al. (2000) refer the following studies:

- "An analysis of the similitude requirements for scale model determination of the buckling of a thin shell structure of arbitrary shape and thickness under impulsive pressure loading" presented by Ezra (1962) applying dimensional analysis;
- An investigation based on dimensional analysis for an orthotropic cylinders subjected to combined loading published by Morgan (1964);
- Using the Love's equations of motion for thin shells, Soedel (1971) derived approximate similitude relationships to examine free as well as forced vibrations. By means of partial similitude, the author introduced the shell thickness as a parameter independent of the scaled surface geometry.

In order to properly understand the scaling rules governing impact, some experimental studies were performed.

Morton (1988) used dimensional analysis to derive scaling laws for impact-loaded carbon-fiber composite beams, while Qian et al. (1971) considered the governing equations of the system to obtain scaling laws for impact-loaded composite plates. Both experimental investigations have been developed to characterize the size effect in material behavior for inelastic analysis (Simitses et al., 2000).

According to Ferguson (1995), Wen and Jones (1993) presented an experimental investigation into the geometrically similar scaling laws for circular plates impacted at low velocity (5 m/s). The scaling effects that low velocity impact has on both strain rate sensitive and insensitive materials are examined using the pi-terms derived by Jones (1989). Additionally, Atkins (1988) supplemented the research on low velocity impact by providing the scaling laws for bodies undergoing simultaneous plastic flow and crack propagation, whose deformations can be adequately described by rigid-plastic fracture mechanics. On the other hand,

Anderson et al. (1992) computationally and later Ferguson (1995) experimentally studied the hypervelocity impact (2 km/s) with the purpose of quantifying the effects of strain rate on replica-model experiments of penetration and perforation. Both investigations used dimensional analysis.

Other recent investigations were presented with focus on the strain-rate effects on the use of different materials (for the model and prototype) and on the use of distorted models for impacted structures:

- Oshiro and Alves (2004) proposed a technique to solve the problems caused by strain-rate effects on impacted structures, recurring to an alternative dimensionless basis, associated to a mathematical model which allows the calculation of a correction factor for the impact velocity.

  A double plate structure under axial impact load and a clamped beam under transverse blast load were scaled and numerically analyzed (Oshiro and Alves, 2004). For being extremely sensitive to strain rate material effects, the elastic-visco-plastic shells under axial impact of a mass were used as a more complex case study for the proposed technique (Oshiro and Alves, 2007);

- Alves and Oshiro applied the technique presented by the same authors (Oshiro and Alves, 2004), to simple structures subjected to axial and transverse impact loads, when the prototype and the model are made of different materials (Alves and Oshiro, 2006a), and correcting the impact mass instead of the impact velocity (Alves and Oshiro, 2006b);

- Oshiro and Alves (2009) modified the technique previously presented in their publication (Oshiro and Alves, 2004) using a different constitutive law to relate the dynamic flow stress to the strain rate. Again, the same simple case studies were used.

  Mazzariol et al. (2010) adapted this modified technique, changing the impact mass instead of the impact velocity. T cross-section beams, clamped in both ends and struck at mid-span by a mass were studied experimentally (and numerically) to predict the behavior of a model 20 times larger (studied numerically).

  Oshiro et al. tested experimentally the same prototype, as well as a model 4 times larger, using the modified approach (from Oshiro and Alves (2009)) with the impact velocity changed;

- Oshiro and Alves (2012) in order to take, when necessary, the distorted geometry of the model into account, introduced a new correction factor for the impact velocity in the methodology previously presented by them (Oshiro and Alves, 2009);

- Mazzariol and Alves (2013) present a similarity approach that takes into account the differences in material quasi-static properties by changing the impact mass factor, while the increase in dynamic stress due to strain-rate was considered by changing impact velocity factor. The dimensionless numbers obtained (with the Norton-Hoff model) by Oshiro and Alves (2009) were firstly rearranged, and then the Cowper-Symonds equation were used as viscoelastic formulation, to write the dynamic stress. The response of aluminum circular tubes axially impacted were compared experimentally with the response of 1/2-scale aluminum models, as well as, with 1/2- and 3/4-scale models made of mild steel.

  The same authors applied this approach to numerically analyze the structural response of circular plates impacted by a steel sphere (Mazzariol and Alves, 2014). An

aluminum prototype is predicted with the response of a 1/1-scale steel model, as well as 1/10-scale aluminum and steel models. The performance of the approach is compared with other available on the literature (MLT basis (Baker et al., 1991), Calladine Sugestion, VSG basis (Oshiro and Alves, 2009)).

A more complex case study was presented, by Calle and Alves, in a review of studies about ship collision, where the experimental use of scaled-models is one of the main topics. As referred by the authors, scaled models are important to the naval engineering due to the ship size, and therefore due to the expensive experimental tests. Although widely used in hydrodynamic ship aspects, the models are not commonly used to study the structural behavior. The following works were cited:

- Blok and Dekker (1979) tested a 1/45-scale tanker model being displaced laterally to collide against a static protected jetty to measure the added mass due to the hydrodynamic effect (Calle and Alves);
- Hagiwara et al. (1983) analyzed experimentally the ship collision event using 1/10-scale models made of thin steels plates. The objective was to estimate the energy involved in low-energy ship collisions. However, some aspects such as the non-similarity in material failure or the simplifications made to the model invalidated the experiments (Calle and Alves);
- Lehmann and Peschmann (2002) developed a large-scale ship collision experiment in a 1/3 scale by adapting two inland waterway vessels (Calle and Alves);
- Tabri et al. (2008) built scaled ship models to simulate a ship collision event. The tanker models made of wood were constructed in a 1/35 scale (Calle and Alves).

Another research program using scale models was conducted at NASA Langley Research Center to develop and demonstrate an innovative and cost-effective crashworthy fuselage concept for light aircraft (Jackson et al., 2003). During the first two years the fuselage concept was designed and evaluated through fabrication and testing of a 1/5-scale model (Jackson and Fasanella, 1999). During the third-year, a full-scale prototype was fabricated by "scaling-up" the geometry and constitutive properties of the 1/5-scale model (Fasanella and Jackson, 2002; Jackson et al.).

Recently, Shokrieh and Askari (2013) presented a study on the prediction of the critical buckling load of impacted composite laminates, where the concept of a *sequential similitude method* is introduced.

The methodology consists in two sequential steps: firstly the similitude method is developed for impact loading to produce similar damage areas in all plates, and then, similarity is developed between plates under buckling loading, without considering the effect of initial damages on buckling equations. Therefore, the similarity conditions can be derived for structures subjected to sequentially loading situations, provided that each loading event is simulated independently (Shokrieh and Askari, 2013).

Other complementary researches related with the similitude analysis applied to structural impact problems were found, including those: cited by Oshiro and Alves (2012) and published by: Atkins (1999); Li and Jones (2000); Me-Bar (1997); Neuberger et al. (2007); Schleyer et al. (2004); Zhao (1998); cited by Mazzariol and Alves (2013) and published by: Christoforou and Yigit (2009); Jiang et al. (2006b); Yulong et al. (2008); as well as those found during this research, published by: Ambur et al. (2005); Bazant (1993); Carrillo and

Cantwell (2008); Christoforou and Yigit (1998); Emori (1973); Jiang et al. (2006a); Jones et al. (2007); Snyman (2010); Sutherland and Guedes Soares (2007); Viot et al. (2008); Yigit and Christoforou (2007).

3.4.2. Rapid prototyping of scale models

For the contemporary industries focused in continuously improving the product development process, the reliable functional testing with rapid prototypes is a promising tool able to link the design and manufacturing processes. Some technical issues affecting the prediction accuracy have historically prevented effective functional testing while the Traditional Similarity Method (TSM) prevailed. Based on dimensional analysis, the TSM is sensitive to distortions such as differences between the model and prototype materials. Therefore, to overcome such limitations the Empirical Similarity Method (ESM), as well as, other variations of the method were proposed. The ESM empirically derives a mathematical transformation between prototype and product behavior from the experimental testing of a geometrically simple specimen pair (Cho and Wood, 1997; Cho et al.; Dutson and Wood, 2002).

3.4.2.1. Traditional Similarity Method

Accordingly to Cho et al. (1998), very little literature about the rapid prototyping (RP) of scale models existed at the late nineties: a research presented by Dornfeld (1994) and other presented by Steinchen et al. (1995). Most of that studies, based on dimensional analysis, just experimentally examined the test results without providing a way to improve test results (Cho et al., 1998). Although equally limited, Mahn and Bayly (1999) presented an interesting analysis of the practical issues in the prediction of model properties of aluminum prototypes using impacted SLA models. The adverse effects of mass loading, anisotropy, damping and non-linearities in the material were all considered (Mahn and Bayly, 1999).

Since then, more studies concerning the rapid prototyping methods were published, most of them related with the wind tunnel testing. The models were obtained with fused deposition method (FDM) using ABS plastic or PEEK, stereolithography, selective laser sintering and laminated object manufacturing (using plastic reinforced with glass or paper) (Springer, 1998), as well as, FDM with polycarbonate (Nadooshan et al., 2007). Chuk and Thomson (1998) compared a total of ten rapid prototyping techniques in their ability to make wind tunnel models in a timely and cost effective manner.

Several authors concluded that rapid prototyping technologies are applicable for models which do not undergo significant loads. The parts obtained with RP using plastic materials or even metal powders do not provide enough structural integrity for testing, and therefore numerically controlled machining was still best for any component enduring significant loads (Chuk and Thomson, 1998; Nadooshan et al., 2007; Springer, 1998).

With the purpose of improving the structural integrity of RP models, reducing the manufacturing period and cost, Dang-guo et al. (2013, 2011) introduced a preliminary design and manufacturing technique for hybrid high-speed wind-tunnel models with an internal metal frame (produced by simple and conventional processing methods) and an outer resin (fabricated by stereolithography).

Fujino et al. (2003) had already applied a similar method to experimentally analyze the flutter characteristics of an over-the-wing engine mount configuration. The 1/4-scale model tested in a low speed wind tunnel, as well as the 1/6 and 1/20-scale models, tested in a transonic wind tunnel test, employed spar-strip construction. Once again, an aluminum spar provided the required stiffness distribution in bending and torsion while the required

mass and inertial properties were provided by lead or tungsten weights in each strip. Finally, the strips made of rapid prototyping provided the wing shape, with the gaps between the strips aerodynamically sealed with sponge rubber.

A different kind of case study was presented by Ziemian et al. (2010). The authors investigated the correlation between the dynamic behavior of a full-scale steel prototype and a small-scale plastic model fabricated using FDM, simulated in a shake-table.

3.4.2.2. Empirical Similarity Methods

None of the previous researches had proposed any kind of change or innovation in the establishment of the structural similitude between the models and the prototypes. They tried to overcome the limitations of rapid prototyping, testing different RP techniques and materials, but kept the similitude methodology unchanged.

On the other hand, Cho and his collaborators presented and continuously developed a novel empirical similitude method for the functional test with rapid prototypes: the Empirical Similarity Method (ESM)(Cho and Wood, 1997; Cho et al., 1998).

Their focus was initially placed on the material issues, especially the non-similar characteristics of the rapid prototyping and production materials, the distinct level of isotropy and homogeneity, or even the restrictions on loading conditions (Cho and Wood, 1997). These authors claim that their method is more suitable to solve distorted similarity problems. With that purpose, the involvement of a geometrically simple specimen pair is proposed: one fabricated from a rapid prototyping process and another from the actual production process. The state transformation is derived from these specimens, and it is assumed that it can be also applied to systems with distinct geometric features (Cho et al., 1998). The methodology were validated through:

- Numerical prediction of the stress of an aluminum slotted rod at the potential failure point, using a nylon slotted rod and two specimens (Cho et al.);
- Numerical (Cho et al.) and experimental (Cho et al., 1998) prediction of the transient temperature of an aluminum mold at relevant points, using nylon molds (fabricated by SLS) and two specimens;
- Numerical prediction of the principal strains of the aluminum rod at seven randomly selected point of interest, using a nylon rod, and two specimens (Cho et al., 1998).

Latter, Cho et al. (1999) would propose the construction of error measures to utilize with confidence the results obtained testing functional scale models. A numerical example of the error estimation procedure is given through the problem of predicting the steady-state temperature of a turbine blade (Cho et al., 1999).

Finally an Advanced ESM was also presented to increase the applicability of the ESM (Dutson et al., 2003; Dutson and Wood, 2002). Simultaneously, a Lumped ESM (Cho et al., 2005; Dutson and Wood, 2002) was applied, as suggested in a previous work (Cho et al., 1999), to correlate distorted systems composed of more than one part. The presented examples in these investigations include the prediction of: the deflection of a cantilever beam with five holes under a concentrated load at the tip. (Dutson et al., 2003; Dutson and Wood, 2002); the required shooting force of an archery bow (Cho et al., 2005); the steady-state temperature of a CPU cooled by polymer heat sinks fabricated with rapid prototyping technology (SLS) (Cho et al., 2005; Dutson and Wood, 2002).

Lastly, it is pointed the need for an overall approach for functional testing with rapid prototyping, allowing to choose between the available methods (Dimensional analysis, ESM, Advanced ESM, ...) (Dutson et al., 2003).

More recently, Zhu et al. (2011) presented a novel method to design and fabricate aeroelastic wing models, for wind tunnel tests, using stereolithography. According to similarity laws, the structurally similar model was designed through a sequential design procedure of dimensional scaling, stiffness optimization and mass optimization.

3.4.3. Size effects

Although the concepts of *scaling effects* and *size effects* can be easily misinterpreted, the distinction is rarely presented. Following the definitions presented by Simitses et al. (2000), scaling effects mean the effects of changing the geometric dimensions of a structure on its response to external causes, such as forces. On the other hand, the *size effects* are more closely related to changes on behavior characteristics of materials, such as strength and stiffness, which indirectly also affects the structural behavior.

Indeed, test data obtained in the laboratory on small coupon-type specimens are routinely assumed to be valid for full scale structures with no regard for possible distortions due to size or scale. This assumption is made even though a size effect in failure behavior of metallic structures has been well documented (Jackson, 1990).

In their review Simitses et al. (2000) cited the proceedings of a workshop held at NASA Langley Research Center (Jackson, 1994) as one of the main sources of recent studies on size effects. The workshop presented a wide discussion on the scaling effects in: (1) structures, (2) material properties, failure and damage detection, and (3) impact response. Several authors concluded that the size effect on stiffness is almost nonexistent, but there was no consensus in relation to the size effect on strength (Simitses et al., 2000).

Other researches were carried out by Jackson and Fasanella (1989), Kellas and Morton (1992), Hamada and Ramakrishna (1995), Nettles et al. (1999), Tarfaoui et al. (2007), and McKown et al. (2008). This information should be analyzed in detail especially if one wants to scale the prototype behavior beyond its linear elastic threshold.

3.4.4. Other researches and publications

Given the incremental invention of the so-called Motorized Momentum Exchange Tether, proposed by Cartmell in 1998, for space vehicle propulsion, a program of terrestrial scale-model experimentation was funded by ESA during 1999-2001 with the intention to prove certain practicalities of this motorized concept (Cartmell et al., 2003). Thus, a suitably scaled model was designed and built on the basis of an extended application of the Buckingham pi-theorem, and appropriate dynamic scaling criteria were obtained for both rigid body spin-up and flexural vibration within the system (Cartmell et al., 2003).

Other research program was created at NASA with the purpose of updating the current buckling design guidelines (published in the late 1960's and early 1970's). The SBKF project has the goal of developing new analysis-based shell buckling design factors (knockdown factors) able to take full advantage of the modern materials, precision manufacturing processes and new structural concepts (Hilburger et al., 2012). Although, accessing relevant information concerning the scaling procedure was not possible, it is widely documented the buckling experimental testing of different orthogrid-stiffened metallic cylindrical-shells: two 8-ft-diameter models and a 27.5-ft-diameter prototype (Hilburger et al., 2012). Ensuring that the scaling assumptions are correct is assumed as one of the main concerns, in order to have confidence in the future scale-up of the subscale test data.

3.5. Concluding remarks

The main purpose of this review is to help engineers and scientists in the field of reduced scale models, providing them the set of relevant references required for their research. As a secondary purpose some topics on which additional efforts can be undertaken are highlighted.

A detailed analysis of the state of the art revealed a significant number of publications based mainly on the dimensional analysis or alternatively on the use of differential equations. The dimensional analysis applied to structural systems were firstly discussed by Goodier and Thomson (1944). Although even the most recent books and manuals had been published mainly with an academic purpose, containing simple examples of dimensional analysis, the published aerospace industry case studies demonstrated the applicability for complex structures. However, the correct use of dimensional analysis, although very simple, requires great effort and skill. When selecting the complete and independent set of quantities affecting the structural behavior, not even the smallest detail can be overlooked, while irrelevant quantities should be avoided as much as possible. Besides, the obtained pi-terms are not unique; although following well defined steps the construction of the most adequate set of pi-terms is made by trial-and-error.

On the other hand, a more intuitive approach was initially proposed by Kline in 1965, applying the similitude theory through the governing equations that explicitly define the response of the system as a function of its independent variables. The two main approaches developed since then were the use of the solution for the differential equations and the direct use of those equations. Although the last avoids the need to solve the equation explicitly, one still needs to know enough about the physics of the problem to be able to write down a complete set of governing equations. This primary weakness may explain why this method was rarely applied in the literature to structures more complex than plates and shells, since the governing equations were not available.

Other methodology recently proposed by De Rosa and his collaborators has been developed since 2008 for the analysis of the dynamic response of structural and acousto-elastic assemblies. It is defined by invoking the energy distribution approach which allows the exact representation of all the fundamental parameters in terms of modal coordinates. Despite its complexity and specific applicability, this is one of the main suggestions to solve the absent of governing equations for complex structures.

Indeed, with the increasing computational resources, other approaches proposed by some authors, such as the similitude theory used along with the finite element method to create the structural model, are by far the more tempting line of research to establish the similitude for complex structures.

Other areas of research, where very interesting and inspiring work has been done, continuously improving existing methods, include the rapid prototyping of models and the analysis of impacted structures.

3.6. Recommended research

An overview of the previously researched fields regarding structural similitude of plates and shells, derived through the governing equations, is presented in table 3.1.

Unmarked cells represent topics not covered by any of the analyzed references in this review, and so, possibly requiring additional research.

Note that in the previously reviewed papers where the similitude theory was applied directly to the governing equations of plates or shells, the methodology suffers from a secondary weakness: as simplifications are applied to the governing equations (for example considering

Table 3.1.: Overview of previously researched fields in structural similitude of plates and shells. If the similitude theory was applied to the solution of the governing differential equations, directly to those equations or through both methods, then each research field is marked, respectively, as ✓□, □✓or ✓✓.

		Plates		Shells	
		Isotropic	Laminated	Cylindrical	Double Curvature
Static	Cylindrical bending	□□	□✓	□□	□□
	Torsion, bending and pressure	□□	□□	✓□	□□
Buckling	Axial compression	□□	✓✓	✓✓	□□
	Shear load	□□	✓✓	□□	□□
	External pressure	□□	□□	✓□	□□
Vibration	Free	□✓	✓□	✓✓	✓□
	Forced	□✓	□□	□□	□□
	Flutter speed	□□	✓□	□□	□□
Flutter pressure		□✓	□✓	□□	□□

that the laminate coupling stiffness terms B_{ij} are zero) the generality is lost and the whole process will have to be repeated for a structure which does not respect the assumptions.

Alternatively, the investigation of the potential advantages in applying the similitude theory to the governing equations of plates or shells, minimizing the simplifications is suggested and addressed in the second part of the thesis by chapter 4. An improved approach is intended to be created for static, dynamic and stability analysis, deriving the similarity conditions and scaling laws from a generalized set of scaling relationships, without having to apply the similitude theory to the governing equations with specific simplifications related to the plate being studied.

Part II.

New approaches to Structural Similitude

4. Generalized scaling relationships for anisotropic plates

Abstract

The main purpose of this chapter is the investigation of potential advantages in applying the similitude theory to the governing equations of plates, minimizing simplifications. It is demonstrated that through this approach, the obtained generalized scaling relationships allow to derive, not only the scaling laws for the previously studied plates, but also for any anisotropic (monolithic, sandwich or laminated) plate.

In addition, the analysis of commercial honeycomb panels was chosen as an interesting case study to evaluate the scaled model testing performance. Both its advantages and the disadvantages are presented, with the results accuracy compared to that obtained through detailed and simplified finite element models currently used in this specific research area. Besides, it was identified one of the possible causes for inconsistencies unexpectedly found in previously published researches regarding commercial honeycomb cores.

4.1. Introduction

4.1.1. Research background

A complete perspective of the contributions to the use of scaled models based on similitude theory has been presented in previous chapter. Kline (1965) and Baker et al. (1991) soon presented the concept of applying the similitude theory through the differential equations instead of the dimensional analysis. In 1991, Baker et al. cited Kline as still being the only known author already using this concept as the primary method.

The method can either be applied directly to the differential equations or indirectly to their solution. The first option is the most advantageous approach, and its application was introduced and exemplified by Simitses and Rezaeepazhand (1992) in a technical report. The similarity of structural behavior between plates was studied using that approach in the following case studies:

- The cylindrical bending of (simply supported) laminated beam-plates subjected to transverse loads (Simitses, 2001; Simitses and Rezaeepazhand, 1992, 1993b);
- The buckling of: symmetric, cross-ply laminated plates caused by biaxial (Ungbhakorn, 2001) and shear (Ungbhakorn, 2001) loading; symmetric, angle-ply laminated plates caused by biaxial loading (Singhatanadgid and Ungbhakorn, 2002a); anti-symmetrically, cross-ply and angle-ply laminated plates subjected to biaxial loading (Ungbhakorn and Singhatanadgid, 2003c);
- The free vibration of anti-symmetrically laminated cross and angle-ply plates (Singhatanadgid and Ungbhakorn, 2002b).

The free and forced vibration characteristics of isotropic plates were also numerically predicted by Wu (2003, 2005), while Singhatanadgid and Na Songkhla presented an experimental validation of the similarity requirements for the natural frequencies of thin isotropic plates (Na Songkhla and Singhatanadgid, 2005; Singhatanadgid and Na Songkhla, 2008).

In those researches, the considered equations are written in terms of the displacements and stiffnesses. In order to reduce the complexity of the process through which the scaling relationships are derived, simplifications are applied to the governing equations, for example considering that the laminate coupling stiffness terms B_{ij} are zero. As a consequence, the generality is lost and the whole process will have to be repeated for a plate which does not respect the considered assumptions. This is identified as one of the weaknesses of the methodology, that despite its virtues is still based on a very limiting procedure.

4.1.2. Objectives

The main purpose of the research in this chapter is to investigate the potential advantages in applying the similitude theory to the governing equations, minimizing the simplifications. The obtained generalized scaling relationships are expected to allow quick derivation not only of the scaling laws for the previously studied plates, but also for any anisotropic (monolithic, sandwich or laminated) plate.

Ungbhakorn and Singhatanadgid (2009) were the only known authors deriving the generalized scaling laws specifically for vibrating doubly curved shallow shells. They used the total energy of the system instead of the governing equations. Already after the development of the research in this chapter, Yu and Li (2016) published generalized similitude requirements and scaling laws of orthogonally stiffened cylindrical panels and shells for buckling and free vibration, also using the total energy of the system instead of the governing equations.

4.2. Derivation of the similarity conditions

Considering a standard (x, y, z) coordinate system, as in figure 4.1, with u, v, w denoting the displacements in the respective axis, the equations of motion for a generally laminated anisotropic thin plate under transverse loading q_z can be written as follows (Ashton and Whitney, 1970):

$$\frac{\partial N_x}{\partial x} + \frac{\partial N_{xy}}{\partial y} = \rho\, \ddot{u}_0 \tag{4.1a}$$

$$\frac{\partial N_{xy}}{\partial x} + \frac{\partial N_y}{\partial y} = \rho\, \ddot{v}_0 \tag{4.1b}$$

$$\frac{\partial^2 M_x}{\partial x^2} + 2\frac{\partial^2 M_{xy}}{\partial x \partial y} + \frac{\partial^2 M_y}{\partial y^2} + N_x \frac{\partial^2 w}{\partial x^2} + 2N_{xy}\frac{\partial^2 w}{\partial x \partial y} + N_y \frac{\partial^2 w}{\partial y^2} + q_z = \rho\, \ddot{w} \tag{4.1c}$$

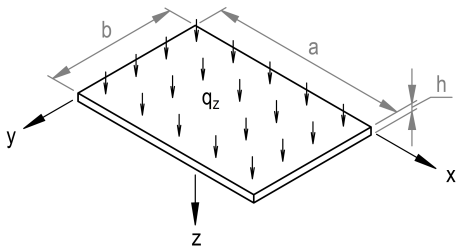

Figure 4.1.: Plate under transverse loading.

with the force and moment resultants defined as:

$$\begin{Bmatrix} N_x \\ N_y \\ N_{xy} \end{Bmatrix} = \begin{bmatrix} A_{11} & A_{12} & A_{16} \\ & A_{22} & A_{26} \\ \text{sym} & & A_{66} \end{bmatrix} \begin{Bmatrix} \epsilon_x^0 \\ \epsilon_y^0 \\ \gamma_{xy}^0 \end{Bmatrix} + \begin{bmatrix} B_{11} & B_{12} & B_{16} \\ & B_{22} & B_{26} \\ \text{sym} & & B_{66} \end{bmatrix} \begin{Bmatrix} \kappa_x \\ \kappa_y \\ \kappa_{xy} \end{Bmatrix} \tag{4.2a}$$

$$\begin{Bmatrix} M_x \\ M_y \\ M_{xy} \end{Bmatrix} = \begin{bmatrix} B_{11} & B_{12} & B_{16} \\ & B_{22} & B_{26} \\ \text{sym} & & B_{66} \end{bmatrix} \begin{Bmatrix} \epsilon_x^0 \\ \epsilon_y^0 \\ \gamma_{xy}^0 \end{Bmatrix} + \begin{bmatrix} D_{11} & D_{12} & D_{16} \\ & D_{22} & D_{26} \\ \text{sym} & & D_{66} \end{bmatrix} \begin{Bmatrix} \kappa_x \\ \kappa_y \\ \kappa_{xy} \end{Bmatrix} \tag{4.2b}$$

where the extensional (A_{ij}), bending (D_{ij}) and bending-extensional coupling (B_{ij}) laminate stiffnesses are given by:

$$(A_{ij}, B_{ij}, D_{ij}) = \int_{-h/2}^{h/2} \overline{Q}_{ij}^{(k)} \left(1, z, z^2\right) dz \tag{4.2c}$$

In previous equation, $\overline{Q}_{ij}^{(k)}$ are the k^{th} ply reduced stiffnesses. The mass density per unit length ρ in equations (4.1) is given by:

$$\rho = \int_{-h/2}^{h/2} \rho_0^{(k)} dz$$

where $\rho_0^{(k)}$ is the k^{th} ply mass density.

Considering small strains but moderate rotations, the strain components (Reddy, 2004) are the following:

$$\epsilon_x^0 = \frac{\partial u_0}{\partial x} + \frac{1}{2}\left(\frac{\partial w}{\partial x}\right)^2 \tag{4.3a}$$

$$\epsilon_y^0 = \frac{\partial v_0}{\partial y} + \frac{1}{2}\left(\frac{\partial w}{\partial y}\right)^2 \tag{4.3b}$$

$$\gamma_{xy}^0 = \frac{\partial u_0}{\partial y} + \frac{\partial v_0}{\partial x} + \frac{\partial w}{\partial x}\frac{\partial w}{\partial y} \tag{4.3c}$$

$$\kappa_x = -\frac{\partial^2 w}{\partial x^2} \tag{4.3d}$$

$$\kappa_y = -\frac{\partial^2 w}{\partial y^2} \tag{4.3e}$$

$$\kappa_{xy} = -2\frac{\partial^2 w}{\partial x \partial y} \tag{4.3f}$$

The selected governing equations are based on the following necessary assumptions:

1. The plate has an arbitrary number of layers perfectly bounded together;
2. The plate materials are continuous everywhere;
3. The plate is thin and in an approximated state of plane stress ($\sigma_z = \sigma_{yz} = \sigma_{zx} = 0$), so the transverse shear strains ϵ_{xz} and ϵ_{yz} are negligible;
4. Tangential displacements u and v are linear functions of z coordinate;
5. The transverse normal strain ϵ_z is negligible;

and optional restrictions (Ashton and Whitney, 1970; Chia, 1980; Reddy, 2004):

1. Each layer is orthotropic (three planes of material symmetry), with arbitrary elastic properties and orientation, and obeys the generalized Hooke's law;
2. Small strains but moderate rotations (special case of geometric non-linearity);
3. The plate has constant thickness;
4. Rotary inertia terms are negligible;
5. There are no body forces;
6. The two boundary planes are free from shear stresses, and the plate is only subjected to transverse normal stress q_z.

By applying the similitude theory to those equations, as demonstrated in appendix A.1, the following similarity conditions are obtained:

$$\frac{\lambda_{N_x}}{\lambda_x} = \frac{\lambda_{N_{xy}}}{\lambda_y} = \lambda_\rho \lambda_{\ddot{u}_0} \tag{4.4a}$$

$$\frac{\lambda_{N_{xy}}}{\lambda_x} = \frac{\lambda_{N_y}}{\lambda_y} = \lambda_\rho \lambda_{\ddot{v}_0} \tag{4.4b}$$

$$\frac{\lambda_{M_x}}{\lambda_x^2} = \frac{\lambda_{M_{xy}}}{\lambda_x \lambda_y} = \frac{\lambda_{M_y}}{\lambda_y^2} = \lambda_{N_x}\frac{\lambda_w}{\lambda_x^2} = \lambda_{N_{xy}}\frac{\lambda_w}{\lambda_x\lambda_y} = \lambda_{N_y}\frac{\lambda_w}{\lambda_y^2} = \lambda_{q_z} = \lambda_\rho \lambda_{\ddot{w}} \tag{4.4c}$$

which in turn yield the following scaling laws for bending analysis:

$$\lambda_{N_x} = \lambda_{N_{xy}}\frac{\lambda_x}{\lambda_y} \tag{4.5a}$$

$$\lambda_{N_y} = \lambda_{N_{xy}}\frac{\lambda_y}{\lambda_x} \tag{4.5b}$$

$$\lambda_{M_x} = \lambda_{M_{xy}}\frac{\lambda_x}{\lambda_y} \tag{4.5c}$$

$$\lambda_{M_y} = \lambda_{M_{xy}}\frac{\lambda_y}{\lambda_x} \tag{4.5d}$$

$$\lambda_w = \frac{\lambda_{M_i}}{\lambda_{N_i}} \qquad i = x, y, xy \tag{4.5e}$$

$$\lambda_{q_z} = \frac{\lambda_{M_x}}{\lambda_x^2} \tag{4.5f}$$

and three more scaling laws for vibration analysis:

$$\lambda_{\ddot{u}_0} = \frac{\lambda_{N_x}}{\lambda_\rho \lambda_x} \tag{4.6a}$$

$$\lambda_{\ddot{v}_0} = \frac{\lambda_{N_{xy}}}{\lambda_\rho \lambda_x} \tag{4.6b}$$

$$\lambda_{\ddot{w}} = \frac{\lambda_{q_z}}{\lambda_\rho} \tag{4.6c}$$

For the sake of simplicity, in the following similarity conditions, derived by application of the similitude theory to the constitutive equations (4.2), the variables $\left(\epsilon_x^0, \epsilon_y^0, \gamma_{xy}^0, \kappa_x, \kappa_y, \kappa_{xy}\right)$ will be referred as $(\hat{\epsilon_1}, \hat{\epsilon_2}, \hat{\epsilon_6}, \hat{\kappa_1}, \hat{\kappa_2}, \hat{\kappa_6})$.

$$\lambda_{N_x} = \lambda_{A_{11}} \lambda_{\hat{\epsilon_1}} \tag{4.7a}$$
$$\lambda_{N_y} = \lambda_{A_{12}} \lambda_{\hat{\epsilon_1}} \tag{4.7b}$$
$$\lambda_{N_{xy}} = \lambda_{A_{66}} \lambda_{\hat{\epsilon_6}} \tag{4.7c}$$

$$\lambda_{M_x} = \lambda_{D_{11}} \lambda_{\hat{\kappa_1}} \tag{4.7d}$$
$$\lambda_{M_y} = \lambda_{D_{12}} \lambda_{\hat{\kappa_1}} \tag{4.7e}$$
$$\lambda_{M_{xy}} = \lambda_{D_{66}} \lambda_{\hat{\kappa_6}} \tag{4.7f}$$

There are many other possibilities for the second member of equations (4.7). The equations (4.8) to (4.13) represent these possibilities, and can be seen as additional similarity conditions depending on the material properties and stacking sequence. For example, for symmetric laminated plates all the membrane-bending coupling terms (B_{ij}) will be assumed to be zero, and so the similarity conditions (4.8), (4.9), (4.12) and (4.13) should not be considered.

$$\lambda_{A_{11}} \lambda_{\hat{\epsilon_1}} = \lambda_{B_{11}} \lambda_{\hat{\kappa_1}} \tag{4.8a}$$
$$\lambda_{A_{12}} \lambda_{\hat{\epsilon_1}} = \lambda_{B_{12}} \lambda_{\hat{\kappa_1}} \tag{4.8b}$$
$$\lambda_{A_{66}} \lambda_{\hat{\epsilon_6}} = \lambda_{B_{66}} \lambda_{\hat{\kappa_6}} \tag{4.8c}$$

$$\lambda_{D_{11}} \lambda_{\hat{\kappa_1}} = \lambda_{B_{11}} \lambda_{\hat{\epsilon_1}} \tag{4.9a}$$
$$\lambda_{D_{12}} \lambda_{\hat{\kappa_1}} = \lambda_{B_{12}} \lambda_{\hat{\epsilon_1}} \tag{4.9b}$$
$$\lambda_{D_{66}} \lambda_{\hat{\kappa_6}} = \lambda_{B_{66}} \lambda_{\hat{\epsilon_6}} \tag{4.9c}$$

$$\lambda_{A_{11}} \lambda_{\hat{\epsilon_1}} = \lambda_{A_{1j}} \lambda_{\hat{\epsilon_j}} \qquad j = 2, 6 \tag{4.10a}$$
$$\lambda_{A_{12}} \lambda_{\hat{\epsilon_1}} = \lambda_{A_{2j}} \lambda_{\hat{\epsilon_j}} \qquad j = 2, 6 \tag{4.10b}$$
$$\lambda_{A_{66}} \lambda_{\hat{\epsilon_6}} = \lambda_{A_{j6}} \lambda_{\hat{\epsilon_j}} \qquad j = 1, 2 \tag{4.10c}$$

$$\lambda_{D_{11}} \lambda_{\hat{\kappa_1}} = \lambda_{D_{1j}} \lambda_{\hat{\kappa_j}} \qquad j = 2, 6 \tag{4.11a}$$
$$\lambda_{D_{12}} \lambda_{\hat{\kappa_1}} = \lambda_{D_{2j}} \lambda_{\hat{\kappa_j}} \qquad j = 2, 6 \tag{4.11b}$$
$$\lambda_{D_{66}} \lambda_{\hat{\kappa_6}} = \lambda_{D_{j6}} \lambda_{\hat{\kappa_j}} \qquad j = 1, 2 \tag{4.11c}$$

$$\lambda_{B_{11}} \lambda_{\hat{\epsilon_1}} = \lambda_{B_{1j}} \lambda_{\hat{\epsilon_j}} \qquad j = 2, 6 \tag{4.12a}$$
$$\lambda_{B_{12}} \lambda_{\hat{\epsilon_1}} = \lambda_{B_{2j}} \lambda_{\hat{\epsilon_j}} \qquad j = 2, 6 \tag{4.12b}$$
$$\lambda_{B_{66}} \lambda_{\hat{\epsilon_6}} = \lambda_{B_{j6}} \lambda_{\hat{\epsilon_j}} \qquad j = 1, 2 \tag{4.12c}$$

$$\lambda_{B_{11}}\lambda_{\hat{\kappa_1}} = \lambda_{B_{1j}}\lambda_{\hat{\kappa_j}} \qquad j = 2,6 \tag{4.13a}$$
$$\lambda_{B_{12}}\lambda_{\hat{\kappa_1}} = \lambda_{B_{2j}}\lambda_{\hat{\kappa_j}} \qquad j = 2,6 \tag{4.13b}$$
$$\lambda_{B_{66}}\lambda_{\hat{\kappa_6}} = \lambda_{B_{j6}}\lambda_{\hat{\kappa_j}} \qquad j = 1,2 \tag{4.13c}$$

Finally, applying the similitude theory to equations (4.3), from the linear strain components, the following scaling laws for strains, curvatures and in-plane displacements can be derived:

$$\lambda_{\epsilon_x^0} = \frac{\lambda_{u_0}}{\lambda_x} \tag{4.14a}$$
$$\lambda_{\epsilon_y^0} = \frac{\lambda_{v_0}}{\lambda_y} \tag{4.14b}$$
$$\lambda_{\gamma_{xy}^0} = \frac{\lambda_{u_0}}{\lambda_y} \tag{4.14c}$$

$$\lambda_{\kappa_x} = \frac{\lambda_w}{\lambda_x^2} \tag{4.14d}$$
$$\lambda_{\kappa_y} = \frac{\lambda_w}{\lambda_y^2} \tag{4.14e}$$
$$\lambda_{\kappa_{xy}} = \frac{\lambda_w}{\lambda_x\lambda_y} \tag{4.14f}$$

$$\lambda_{u_0} = \frac{\lambda_y}{\lambda_x}\lambda_{v_0} \tag{4.15}$$

and additionally from the nonlinear strain components $\frac{1}{2}\left(\frac{\partial w}{\partial x}\right)^2$, $\frac{1}{2}\left(\frac{\partial w}{\partial y}\right)^2$ and $\frac{\partial w}{\partial x}\frac{\partial w}{\partial y}$, one can derive three more similarity conditions:

$$\frac{\lambda_{u_0}}{\lambda_x} = \frac{\lambda_w^2}{\lambda_x^2}$$
$$\frac{\lambda_{v_0}}{\lambda_y} = \frac{\lambda_w^2}{\lambda_y^2}$$
$$\lambda_{u_0} = \frac{\lambda_w^2}{\lambda_x}$$

which through condition (4.15) are simplified to the following:

$$\lambda_w^2 = \lambda_{u_0}\lambda_x \tag{4.16}$$

4.2.1. Static (bending) analysis

Substituting the derived scaling laws of force and moment resultants (4.7), and the scaling laws of strains and curvatures (4.14) in the equations (4.5) and (4.6), the following scaling

laws for bending analysis are obtained:

$$\lambda_{A_{11}} = \lambda_{A_{66}} \frac{\lambda_x^2}{\lambda_y^2} \tag{4.17a}$$

$$\lambda_{A_{12}} = \lambda_{A_{66}} \tag{4.17b}$$

$$\lambda_{D_{11}} = \lambda_{D_{66}} \frac{\lambda_x^2}{\lambda_y^2} \tag{4.17c}$$

$$\lambda_{D_{12}} = \lambda_{D_{66}} \tag{4.17d}$$

$$\lambda_{u_0} = \frac{\lambda_{D_{11}}}{\lambda_{A_{11}}} \frac{1}{\lambda_x} \tag{4.17e}$$

$$\lambda_{v_0} = \frac{\lambda_{D_{12}}}{\lambda_{A_{12}}} \frac{1}{\lambda_y} \tag{4.17f}$$

$$\lambda_{u_0} = \frac{\lambda_{D_{66}}}{\lambda_{A_{66}}} \frac{1}{\lambda_x} \tag{4.17g}$$

$$\lambda_{q_z} = \lambda_{D_{11}} \frac{\lambda_w}{\lambda_x^4} \tag{4.17h}$$

The remaining similarity conditions can be derived from equation sets (4.8) to (4.13). From equations (4.8):

$$\frac{\lambda_{A_{11}}}{\lambda_{B_{11}}} = \frac{\lambda_w}{\lambda_{u_0} \lambda_x} \tag{4.18a}$$

$$\frac{\lambda_{A_{12}}}{\lambda_{B_{12}}} = \frac{\lambda_w}{\lambda_{u_0} \lambda_x} \tag{4.18b}$$

$$\frac{\lambda_{A_{66}}}{\lambda_{B_{66}}} = \frac{\lambda_w}{\lambda_{u_0} \lambda_x} \tag{4.18c}$$

From equations (4.9):

$$\frac{\lambda_{D_{11}}}{\lambda_{B_{11}}} = \frac{\lambda_{u_0} \lambda_x}{\lambda_w} \tag{4.19a}$$

$$\frac{\lambda_{D_{12}}}{\lambda_{B_{12}}} = \frac{\lambda_{u_0} \lambda_x}{\lambda_w} \tag{4.19b}$$

$$\frac{\lambda_{D_{66}}}{\lambda_{B_{66}}} = \frac{\lambda_{u_0} \lambda_x}{\lambda_w} \tag{4.19c}$$

From equations (4.10)

$$\frac{\lambda_{A_{11}}}{\lambda_{A_{12}}} = \frac{\lambda_{v_0}}{\lambda_{u_0}} \frac{\lambda_x}{\lambda_y} \tag{4.20a}$$

$$\frac{\lambda_{A_{11}}}{\lambda_{A_{16}}} = \frac{\lambda_x}{\lambda_y} \tag{4.20b}$$

$$\frac{\lambda_{A_{12}}}{\lambda_{A_{22}}} = \frac{\lambda_{v_0}}{\lambda_{u_0}} \frac{\lambda_x}{\lambda_y} \tag{4.21a}$$

$$\frac{\lambda_{A_{12}}}{\lambda_{A_{26}}} = \frac{\lambda_x}{\lambda_y} \tag{4.21b}$$

$$\frac{\lambda_{A_{16}}}{\lambda_{A_{66}}} = \frac{\lambda_x}{\lambda_y} \tag{4.22a}$$

$$\frac{\lambda_{A_{26}}}{\lambda_{A_{66}}} = \frac{\lambda_{u_0}}{\lambda_{v_0}} \tag{4.22b}$$

From equations (4.11)

$$\frac{\lambda_{D_{11}}}{\lambda_{D_{12}}} = \frac{\lambda_x^2}{\lambda_y^2} \tag{4.23a}$$

$$\frac{\lambda_{D_{11}}}{\lambda_{D_{16}}} = \frac{\lambda_x}{\lambda_y} \tag{4.23b}$$

$$\frac{\lambda_{D_{12}}}{\lambda_{D_{22}}} = \frac{\lambda_x^2}{\lambda_y^2} \tag{4.24a}$$

$$\frac{\lambda_{D_{12}}}{\lambda_{D_{26}}} = \frac{\lambda_x}{\lambda_y} \tag{4.24b}$$

$$\frac{\lambda_{D_{16}}}{\lambda_{D_{66}}} = \frac{\lambda_x}{\lambda_y} \tag{4.25a}$$

$$\frac{\lambda_{D_{26}}}{\lambda_{D_{66}}} = \frac{\lambda_y}{\lambda_x} \tag{4.25b}$$

From equations (4.12)

$$\frac{\lambda_{B_{11}}}{\lambda_{B_{12}}} = \frac{\lambda_x^2}{\lambda_y^2} \tag{4.26a}$$

$$\frac{\lambda_{B_{11}}}{\lambda_{B_{16}}} = \frac{\lambda_x}{\lambda_y} \tag{4.26b}$$

$$\frac{\lambda_{B_{12}}}{\lambda_{B_{22}}} = \frac{\lambda_x^2}{\lambda_y^2} \tag{4.27a}$$

$$\frac{\lambda_{B_{12}}}{\lambda_{B_{26}}} = \frac{\lambda_x}{\lambda_y} \tag{4.27b}$$

$$\frac{\lambda_{B_{16}}}{\lambda_{B_{66}}} = \frac{\lambda_x}{\lambda_y} \tag{4.28a}$$

$$\frac{\lambda_{B_{26}}}{\lambda_{B_{66}}} = \frac{\lambda_y}{\lambda_x} \tag{4.28b}$$

From equations (4.13) it is obtained the same conditions as from (4.12) if:

$$\lambda_{u_0} = \frac{\lambda_y}{\lambda_x}\lambda_{v_0} \tag{4.29}$$

which is the same one as equation (4.15) derived from the similarity conditions for strains.

4.2.2. Vibration analysis

Once again, using the derived scaling laws of force and moment resultants (4.7), as well as the scaling laws of strains and curvatures (4.14), to substitute in the equations (4.6), the following scaling laws are additionally obtained for vibration analysis:

$$\lambda_{\ddot{v}_0} = \frac{\lambda_y}{\lambda_x}\lambda_{\ddot{u}_0} \tag{4.30a}$$

$$\lambda_{\ddot{u}_0} = \frac{\lambda_{A_{11}}}{\lambda_\rho}\frac{\lambda_{u_0}}{\lambda_x^2} \tag{4.30b}$$

$$\lambda_{\ddot{w}} = \frac{\lambda_{q_z}}{\lambda_\rho} \tag{4.30c}$$

4.2.3. Implicit scaling factors

In addition to the explicit scaling factors appearing in the scaling laws derived from governing equations, some implicit scaling factors, relating for example to the supporting (boundary) conditions or excitation mechanisms, might need to be suitably defined. Wu (2003), the first known author to present this distinction, used the dimensional analysis theory to determine the implicit scaling factors.

4.2.3.1. Stretching and stability analysis

For arbitrary in-plane edge loadings ($\breve{N}_x, \breve{N}_y, \breve{N}_{xy}$) stretching or compressing the plate, up to three additional similarity conditions can be established considering the boundary conditions:

$$\breve{N}_x = N_x \qquad \Longrightarrow \lambda_{\breve{N}_x} = \lambda_{N_x} \tag{4.31a}$$

$$\breve{N}_y = N_y \qquad \Longrightarrow \lambda_{\breve{N}_y} = \lambda_{N_y} \tag{4.31b}$$

$$\breve{N}_{xy} = N_{xy} \qquad \Longrightarrow \lambda_{\breve{N}_{xy}} = \lambda_{N_{xy}} \tag{4.31c}$$

Replacing the similarity conditions (4.7a) to (4.7c), (4.14a) and (4.14c), the following scaling laws are obtained:

$$\boxed{\lambda_{\breve{N}_x} = \lambda_{A_{11}}\frac{\lambda_{u_0}}{\lambda_x}} \tag{4.32a}$$

$$\boxed{\lambda_{\breve{N}_y} = \lambda_{A_{12}}\frac{\lambda_{u_0}}{\lambda_x}} \tag{4.32b}$$

$$\boxed{\lambda_{\breve{N}_{xy}} = \lambda_{A_{66}}\frac{\lambda_{u_0}}{\lambda_y}} \tag{4.32c}$$

The scaling factors can alternatively be derived in terms of bending stiffnesses replacing

(4.7d) to (4.7f), (4.14d) and (4.14f) in equations (4.5e):

$$\boxed{\lambda_{\breve{N}_x} = \lambda_{D_{11}} \frac{1}{\lambda_x^2}} \tag{4.33a}$$

$$\boxed{\lambda_{\breve{N}_y} = \lambda_{D_{12}} \frac{1}{\lambda_x^2}} \tag{4.33b}$$

$$\boxed{\lambda_{\breve{N}_{xy}} = \lambda_{D_{66}} \frac{1}{\lambda_y \lambda_x}} \tag{4.33c}$$

It should be noted that these scaling factors are valid to establish structural similitude between models subjected either to stretching (positive) or compressive (negative) loads. Besides, given that the non-linear equations (4.1) govern both the primary (stable) and secondary (unstable) paths, within the scope of moderate rotations (Brush and Almroth, 1975), this scaling factors are also valid for stability analyses, this is, the prediction of critical buckling loads.

4.2.3.2. Frequency response analysis

Consisting of a set of Frequency Response Functions (FRFs), the Frequency Response Model describes the structure's response to a standard excitation, from which the response for any particular case can be constructed. The standard excitation is usually a sinusoidal force applied at each point on the structure individually and at every frequency within a specified range. Depending on the response parameter, the FRFs can be defined in several forms, including the following:

$$\begin{aligned}
\text{Receptance:} \quad & \alpha(j\omega) = \frac{\text{displacement}}{\text{force}} \quad \left[\frac{\text{m}}{\text{N}}\right] \\
\text{Mobility:} \quad & Y(j\omega) = \frac{\text{velocity}}{\text{force}} \quad \left[\frac{\text{m}}{\text{sN}}\right] \\
\text{Accelerance:} \quad & A(j\omega) = \frac{\text{acceleration}}{\text{force}} \quad \left[\frac{\text{m}}{\text{s}^2\text{N}}\right]
\end{aligned}$$

where $j = \sqrt{-1}$ is the complex operator and ω is the frequency of the response (Ewins, 2000).

Either analyzing the dimensions of each FRF form or the variables in the previous ratios used to define them, it is possible to derive the following scaling laws:

$$\lambda_\alpha = \frac{\lambda_w}{\lambda_{q_z}} \tag{4.34a}$$

$$\lambda_Y = \frac{\lambda_{\dot{w}}}{\lambda_{q_z}} = \frac{\lambda_w}{\lambda_t \lambda_{q_z}} \tag{4.34b}$$

$$\lambda_A = \frac{\lambda_{\ddot{w}}}{\lambda_{q_z}} = \frac{\lambda_w}{\lambda_t^2 \lambda_{q_z}} \tag{4.34c}$$

Similarly, considering the frequency as the number of cycles per unit time:

$$\lambda_\omega = \lambda_t^{-1} \tag{4.35}$$

4.2.4. Complete similitude

The set of scaling relationships governing the structural similitude of any anisotropic laminated plate respecting the assumptions and restrictions stated in page 4.2, in static, vibration and/or buckling behavior should be a subset of independent equations chosen between the following: (4.15), (4.16), (4.17) to (4.28) and (4.30) plus any relevant implicit scaling factor.

Unless some of the selected set of similarity conditions cannot be satisfied, complete similitude will be achieved. In that case, the set of equations can be simplified as shown below.

In most of the complete similitude analyses presented in the literature, this simplification is based on the assumption of some kind of similitude, sometimes wrongly classified as geometric similitude. This assumption ranges from the simplest $\lambda_x = \lambda_y$ to the most restrictive condition $\lambda_x = \lambda_y = \lambda_z = \lambda_u = \lambda_v = \lambda_w$, which indeed implies more than geometric similitude.

In the following deduction of complete similitude, only the in-plane geometric similitude $\lambda_x = \lambda_y$ will be assumed. All the other conditions are derived from this assumption and from the previously derived similarity conditions.

4.2.4.1. Static (bending) analysis

Given the assumption:

$$\boxed{\lambda_x = \lambda_y} \tag{4.36}$$

the equation (4.15) yields:

$$\boxed{\lambda_{u_0} = \lambda_{v_0}} \tag{4.37}$$

Then, the equations (4.17a) and (4.17b) yield:

$$\lambda_{A_{11}} = \lambda_{A_{12}} = \lambda_{A_{66}} = \lambda_A \tag{4.38}$$

and the equations (4.17c) and (4.17d) imply that:

$$\lambda_{D_{11}} = \lambda_{D_{12}} = \lambda_{D_{66}} = \lambda_D \tag{4.39}$$

Having all these similarity conditions in mind, the remaining scaling laws (4.18) to (4.28), derived from the constitutive equations, can be reduced to:

$$\boxed{\lambda_{A_{ij}} = \lambda_A} \tag{4.40a}$$

$$\boxed{\lambda_{B_{ij}} = \lambda_B} \tag{4.40b}$$

$$\boxed{\lambda_{D_{ij}} = \lambda_D} \tag{4.40c}$$

$$\boxed{\lambda_w = \frac{\lambda_A}{\lambda_B}\lambda_{u_0}\lambda_x} \tag{4.40d}$$

$$\boxed{\lambda_w = \frac{\lambda_B}{\lambda_D}\lambda_{u_0}\lambda_x} \tag{4.40e}$$

In the same way the remaining scaling laws derived from the equations of motion (4.17e)

to (4.17g) and (4.17h) yield respectively:

$$\boxed{\lambda_{u_0} = \frac{\lambda_D}{\lambda_A \lambda_x}} \tag{4.41}$$

$$\boxed{\lambda_w = \lambda_{q_z} \frac{\lambda_x^4}{\lambda_D}} \tag{4.42}$$

Note that from equations (4.40d) and (4.40e) it can be derived:

$$\frac{\lambda_D}{\lambda_A} = \frac{\lambda_{u_0}^2 \lambda_x^2}{\lambda_w^2}$$

which, considering the equation (4.41), leads to the same similarity condition as equation (4.16), obtained from nonlinear strains:

$$\boxed{\lambda_w^2 = \lambda_{u_0} \lambda_x} \tag{4.43}$$

4.2.4.2. Vibration analysis

Additionally, considering the definition of the linear accelerations, the similarity conditions (4.30) for vibration analysis of anisotropic laminated plates are rewritten as:

$$\lambda_{u_0} = \frac{\lambda_x}{\lambda_y} \lambda_{v_0} \tag{4.44a}$$

$$\boxed{\lambda_t^2 = \frac{\lambda_x^2}{\lambda_A} \lambda_\rho} \tag{4.44b}$$

$$\boxed{\lambda_t^2 = \frac{\lambda_w}{\lambda_{q_z}} \lambda_\rho} \tag{4.44c}$$

Moreover, from equations (4.44b) and (4.44c) the condition:

$$\frac{\lambda_x^2 \lambda_{q_z}}{\lambda_A \lambda_w} = 1$$

can be derived. On the other hand, from equations (4.41) and (4.42) it follows that:

$$\frac{\lambda_x^2 \lambda_{q_z}}{\lambda_A \lambda_w} = \frac{\lambda_{u_0}}{\lambda_x} \qquad \Longrightarrow \qquad \lambda_{u_0} = \lambda_x \tag{4.45}$$

which in turn implies:

$$\boxed{\lambda_x = \lambda_y = \lambda_{u_0} = \lambda_{v_0}} \tag{4.46}$$

Equations (4.17e) to (4.17g) used to obtain the equation (4.41), and then the equations (4.43), (4.45) and (4.46), are derived from the set of equations (4.5e). This set of equations is associated with the inclusion of in-plane forces in the equation of motion (4.1c). Although these terms have been considered, frequently the effect of in-plane forces on bending is neglected. Assuming that large in-plane forces are not applied externally to the plate, it is possible to show that the in-plane forces generated by coupling are not large enough to invalidate linear theory (Ashton and Whitney, 1970).

Figure 4.2 provide an overview of the equation's flow in the derivation of scaling relation-

ships of anisotropic plates presented so far in section 4.2.

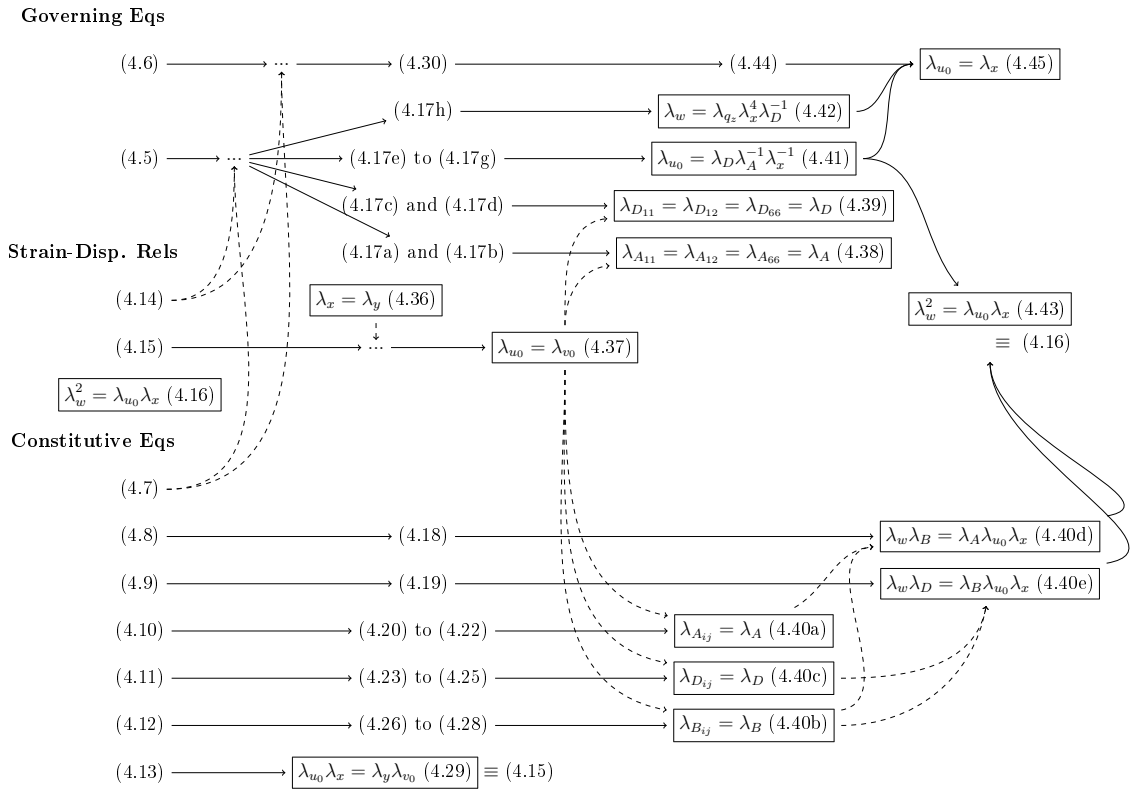

Figure 4.2.: Equation's flow diagram in the derivation of scaling relationships of plates, based on the use of governing equation.

4.2.4.3. Further simplification of scaling laws

The previous boxed equations represent an intermediate state of the scaling laws for complete similitude. However some of these equations can be further simplified if one considers the mathematical expressions for stretching, bending and coupling stiffnesses. From equation (4.2c) the terms A_{ij}, B_{ij}, D_{ij} can be rewritten as follows:

$$A_{ij} = \sum_{k=1}^{N} \overline{Q}_{ij}^{(k)}(z_k - z_{k-1}) \quad = h \cdot f_{A_{ij}} \tag{4.47a}$$

$$B_{ij} = \frac{1}{2}\sum_{k=1}^{N} \overline{Q}_{ij}^{(k)}(z_k^2 - z_{k-1}^2) = h^2 \cdot f_{B_{ij}} \tag{4.47b}$$

$$D_{ij} = \frac{1}{3}\sum_{k=1}^{N} \overline{Q}_{ij}^{(k)}(z_k^3 - z_{k-1}^3) = h^3 \cdot f_{D_{ij}} \tag{4.47c}$$

where $f_{A_{ij}}$, $f_{B_{ij}}$ and $f_{D_{ij}}$ are functions of the material properties (by means of the stiffnesses Q_{ij}), stacking sequence $[\theta_1, ..., \theta_N]$ and total number of plies N.

For partial similitude the scaling factors have to be computed numerically as follows:

$$\lambda_{A_{ij}} = \lambda_h \cdot \lambda_{f_{A_{ij}}}$$
$$\lambda_{B_{ij}} = \lambda_h^2 \cdot \lambda_{f_{B_{ij}}}$$
$$\lambda_{D_{ij}} = \lambda_h^3 \cdot \lambda_{f_{D_{ij}}}$$

On the other hand, for complete similitude, expanding the summation for A_{ij}, with $z_k = c_k h$:

$$A_{ij} = h\left(\overline{Q}_{ij}^{(1)}(c_1 - c_0) + \overline{Q}_{ij}^{(2)}(c_2 - c_1) + \overline{Q}_{ij}^{(3)}(c_3 - c_2) + ... + \overline{Q}_{ij}^{(N)}(c_N - c_{N-1})\right)$$

and taking the coefficients c_k as constants, from the similitude theory it is obtained the following similarity condition:

$$\lambda_{A_{ij}} = \lambda_h \lambda_{\overline{Q}_{ij}^{(1)}} = \lambda_h \lambda_{\overline{Q}_{ij}^{(2)}} = ... = \lambda_h \lambda_{\overline{Q}_{ij}^{(N)}}$$

From these conditions it is first of all concluded that for complete similitude the model and prototype necessarily must have the same number of plies (N). Additionally, all the transformed stiffnesses $\overline{Q}_{ij}^{(k)}$ must have the same scaling factor $\lambda_{\overline{Q}^{(k)}}$ which in practice is equivalent to impose that the model and prototype are made of the same material and stacking sequence.

This conclusion was firstly presented by Simitses and Rezaeepazhand (1993b) with a slightly different demonstration, using the first equality of equations (4.47) and additionally the relation $\lambda_{A_{11}}\lambda_{D_{11}} = \lambda_{B_{11}}^2$, which is a particular case of equation $\lambda_A \lambda_D = \lambda_B^2$ derivable from equations (4.40d) and (4.40e).

Moreover, it can be concluded that with the same material properties and stacking sequence, the scaling factor for the reduced stiffness $\lambda_{\overline{Q}^{(k)}}$ is unitary. This conclusion was also presented by Simitses and Rezaeepazhand (1992) in a technical report.

So, for complete similitude of static analyses:

$$(4.40a) \implies \lambda_{A_{ij}} = \lambda_A = \lambda_h \tag{4.48a}$$
$$(4.40b) \implies \lambda_{B_{ij}} = \lambda_B = \lambda_h^2 \tag{4.48b}$$
$$(4.40c) \implies \lambda_{D_{ij}} = \lambda_D = \lambda_h^3 \tag{4.48c}$$
$$(4.40d) \implies \lambda_w = \frac{\lambda_{u_0}\lambda_x}{\lambda_h} \tag{4.48d}$$
$$(4.42) \implies \lambda_{q_z} = \frac{\lambda_w \lambda_h^3}{\lambda_x^4} \tag{4.48e}$$

If equation (4.43) applies, then equation (4.48d) yields:

$$(4.43) \implies \lambda_h = \lambda_w$$

If the materials in both structures have the same mass density ρ_0 in homologous parts,

then $\lambda_\rho = \lambda_h$, simplifying the similitude criteria for vibration analysis as follows:

$$(4.44b) \implies \lambda_t = \lambda_x \tag{4.49a}$$

$$(4.44c) \implies \lambda_{q_z}\lambda_t^2 = \lambda_w\lambda_h \xrightarrow{+(4.48e)} \lambda_h = \lambda_x \tag{4.49b}$$

$$(4.46) \implies \lambda_x = \lambda_y = \lambda_{u_0} = \lambda_{v_0} \tag{4.49c}$$

4.3. Validation with scaling laws from the literature

4.3.1. Cylindrical bending of laminated beam-plates

Simitses and Rezaeepazhand (1992, 1993b) developed similarity conditions for orthotropic laminated beam-plates subjected to transverse line loads, assuming that the displacements functions are independent of y, and so that $u_0 = u_0(x)$, $v = 0$, $w = w(x)$. Applying the similitude theory to the governing equations and boundary conditions for cylindrical bending the authors obtained the following similarity conditions for transverse deflections:

$$\lambda_{A_{11}}\lambda_{D_{11}} = \lambda_{B_{11}}^2 \tag{4.50a}$$

$$\lambda_w\lambda_{D_{11}} = \lambda_x^4\lambda_{q_z} \tag{4.50b}$$

$$\lambda_{A_{11}}\lambda_{u_0}\lambda_x = \lambda_w\lambda_{B_{11}} \tag{4.50c}$$

$$\lambda_{B_{11}}\lambda_{u_0}\lambda_x = \lambda_w\lambda_{D_{11}} \tag{4.50d}$$

The same similarity conditions were presented by Simitses (2001) in a more recent work. One of the equations (4.50a) to (4.50c) is redundant. So, besides the equation (4.50a), just two of them are necessary to establish complete similarity of static deflection between the scale model and the prototype (Simitses and Rezaeepazhand, 1992, 1993b).

Additionally, Simitses and Rezaeepazhand (1992, 1993b) also presented the following similarity conditions for the normal stress $\sigma_{xx}^{(k)}$:

$$\lambda_{\sigma_x^{(k)}} = \lambda_{\overline{Q}_{11}^{(k)}}\frac{\lambda_{u_0}}{\lambda_x} \tag{4.51a}$$

$$\lambda_{\sigma_x^{(k)}} = \lambda_{\overline{Q}_{11}^{(k)}}\frac{\lambda_w^2}{\lambda_x^2} \tag{4.51b}$$

$$\lambda_{\sigma_x^{(k)}} = \lambda_{\overline{Q}_{11}^{(k)}}\lambda_z\frac{\lambda_w}{\lambda_x^2} \tag{4.51c}$$

4.3.1.1. Analyzed case studies

The accuracy of the behavioral similarity condition (4.50b) was evaluated analytically (Simitses and Rezaeepazhand, 1992, 1993b), trying to predict the maximum deflection of a E-Glass/Epoxy plate $(0/90/0/...)_{96}$ from the theoretical data of a model $(0/90/0/...)_{16}$, with the same material properties. The authors concluded that the derived scaling law can be used with high level of accuracy.

Also for partial similitude, they concluded that (4.51c) predicts very well the normal stress σ_{xx}. On the order hand, the condition (4.51b) cannot predict the behavior of the prototype accurately, whereas the equation (4.51a) is not a suitable similarity condition, since its predicted data does not match the theoretical results (Simitses and Rezaeepazhand, 1992, 1993b).

The same verification was taken experimentally (Simitses and Rezaeepazhand, 1992) using the data of cylindrical bending tests of 10 orthotropic plates, provided to the authors as private communication by Professors Shive Chaturverdi and Robert Sierakowski. The plates are made of E-Glass and Kevlar/Epoxy with different number of layers and stacking sequences.

4.3.1.2. Validation of the methodology from section 4.2

Analyzing the applicability of the similarity conditions and scaling laws derived in section 4.2.4 it is verified that:

- The simplifications assumed for cylindrical bending lead to undefined scaling factors for the variables y and v_0. For this reason the similarity conditions (4.36) and (4.37) do not have to be verified;
- The equations (4.40a) to (4.40c) are available just for the stiffnesses terms with $(ij) = (11)$, because all the others do not appear in the governing equations for cylindrical bending;
- Neglecting the effect of in-plane forces on bending, equations (4.41) and (4.43) are not used;
- Equations (4.40d), (4.40e) and (4.42) are the same as (4.50b) to (4.50d).

It is thus apparent that even for a problem with so much simplifications, if its governing equations can be derived from the equations of motion of a general laminated anisotropic plate (4.1), then the respective conditions for complete similitude will be a subset of the similarity conditions derived in section 4.2.4.

4.3.2. Vibration characteristics of the elastically restrained isotropic flat plates

Wu (2003) predicted the vibrations characteristics of a full-size system, such as natural frequencies, mode shapes and the transverse deflections, by means of the corresponding scale models and the associated scaling factors. The author used the equation of motion for an undamped uniform rectangular plate, subjected to a concentrated force with magnitude $f(t) = q_z(x, y, t) \times ab$ applied at the point (x_f, y_f):

$$\frac{Eh^3}{12(1-\nu^2)}\left(\frac{\partial^4 w}{\partial x^4} + 2\frac{\partial^4 w}{\partial x^2 \partial y^2} + \frac{\partial^4 w}{\partial y^4}\right) + \rho h \frac{\partial^2 w}{\partial t^2} = \frac{f(t)}{ab} \cdot \delta(x - x_f) \cdot \delta(y - y_f) \tag{4.52}$$

Based on similitude theory, Wu (2003) presented the following similarity conditions for the dynamic similitude between a full-size and a scale model made of the same material:

$$\lambda_h^3 \frac{\lambda_w}{\lambda_x^4} = \lambda_h^3 \frac{\lambda_w}{\lambda_x^2 \lambda_y^2} = \lambda_h^3 \frac{\lambda_w}{\lambda_y^4} = \frac{\lambda_h \lambda_w}{\lambda_t^2} = \frac{\lambda_f}{\lambda_a \lambda_b} \tag{4.53}$$

These conditions are equivalent to the following set of scaling laws:

$$\lambda_x = \lambda_y \tag{4.54}$$

$$\lambda_t = \frac{\lambda_x^2}{\lambda_h} \tag{4.55}$$

$$\frac{\lambda_f}{\lambda_a \lambda_b} = \lambda_{q_z} = \lambda_h^3 \frac{\lambda_w}{\lambda_x^4} \tag{4.56}$$

Additionally Wu used the dimensional analysis theory to obtain the following implicit scaling factors:

- Natural frequency (ω) or excitation frequency (Ω):

$$\lambda_\omega = \lambda_\Omega = \frac{1}{\lambda_t} \tag{4.57}$$

- Translational spring (k_l):

$$\lambda_{k_l} = \frac{\lambda_f}{\lambda_w} \tag{4.58}$$

- Rotational spring (k_r):

$$\lambda_{k_r} = \lambda_f \lambda_w \tag{4.59}$$

- Moving-load speed (V):

$$\lambda_V = \lambda_w \lambda_t \tag{4.60}$$

- Damping ratio (ξ):

$$\lambda_\xi = 1 \tag{4.61}$$

4.3.2.1. Analyzed case studies

In the case studies presented by Wu (2003) the complete similitude between models was always respected. The author selected the transverse deflection scaling factor λ_w as the fundamental scaling parameter and from dimensional analysis obtained one of the many possible solutions for the scaling factors:

$$\lambda_i = \lambda_w^{-1} \qquad (i = \omega, \Omega) \tag{4.62a}$$

$$\lambda_i = 1 \qquad (i = V, \xi) \tag{4.62b}$$

$$\lambda_i = \lambda_w \qquad (i = b, l, h, w, x, y, t, k_l) \tag{4.62c}$$

$$\lambda_f = \lambda_w^2 \tag{4.62d}$$

$$\lambda_{k_r} = \lambda_w^3 \tag{4.62e}$$

By numerical methods[1] Wu concluded that both the free and forced vibration characteristics of full size system can be precisely predicted with the scale model and the associated scaling laws. The referred system is composed by a flat isotropic plate elastically restrained by translational and rotational springs along two opposite sides. The free vibration, and

[1] Finite element method and Jacobi method for free vibration analysis, plus the mode-superposition method incorporated with the Duhamel integration to obtain the forced vibration responses.

the forced vibration caused by a stationary harmonic load or a moving constant point load or both were studied. For the last loading case an elastic foundation was included.

4.3.2.2. Validation of the methodology from section 4.2

The plate formulation used by Wu does not take into account the effects of shear deformation and rotary inertia. Additionally in-plane loadings are not considered, and it is assumed the plate has small deformation.

So, having this in mind it is possible to demonstrate that from the boxed scaling laws derived in section 4.2.4 just the equations (4.36), (4.40c), (4.42) and (4.44c) have to be verified[2]. Equation (4.40c) is implicit from the definition of isotropic material, and the other three for complete similitude are equivalent to (4.48c), (4.48e) and (4.49b), which in turn are exactly the same system as (4.54).

4.3.3. Buckling of laminated plates subjected to biaxial or shear loading

Although Simitses and Rezaeepazhand already knew the advantages of applying the similitude theory to the governing differential equations directly, they never used that method in their published investigations (Rezaeepazhand and Simitses, 1993; Simitses and Rezaeepazhand, 1993a,b) to predict the buckling loads. Instead, they used the solution for those equations.

Anyway, later a few authors demonstrated the merits of the similitude theory applied directly to the governing differential equations of buckling. Ungbhakorn (2001) studied symmetric cross-ply laminated plates subjected to biaxial or shear loads. Singhatanadgid and Ungbhakorn (2002a) additionally studied angle-ply laminated plates, but just for biaxial loads.

In all these papers the authors concluded that the complete similitude is achieved when the prototype and model have:

- Complete geometric similarity:

$$\lambda_x = \lambda_y \tag{4.64}$$

- The same load ratio, for biaxial loads:

$$\left(\frac{\breve{N}_y}{\breve{N}_x}\right)_p = \left(\frac{\breve{N}_y}{\breve{N}_x}\right)_m \tag{4.65}$$

  which in turn implies: $\lambda_{\breve{N}_x} = \lambda_{\breve{N}_y}$

- The same scaling factor for all the non-zero laminate flexural stiffnesses

$$\lambda_D = \lambda_{D_{ij}} \ , \qquad \forall\, D_{ij} \neq 0 \tag{4.66}$$

[2]This can be done reducing the equations 4.1 to:

$$\frac{\partial^2 M_x}{\partial x^2} + 2\frac{\partial^2 M_{xy}}{\partial x \partial y} + \frac{\partial^2 M_y}{\partial y^2} + q_z = \rho \frac{\partial^2 w}{\partial t^2} \tag{4.63}$$

and considering just the similarity conditions derived from the latter equation, and all the other directly related to this one, without forgetting the assumption of small rotations.

Alternatively, given that the approach developed in section 4.2 is relatively robust to a large range of simplifications, it is possible to just neglect all the final (boxed) similarity conditions including undetermined scaling factors, which in this case are: λ_{u_0}, λ_{v_0}, as well as all the $\lambda_{A_{ij}}$ and $\lambda_{B_{ij}}$.

Besides, Ungbhakorn and Singhatanadgid (2003c) claim to had applied for the first time the similitude theory to the governing equations of anti-symmetrically laminated plates. The authors assumed a more restrictive condition than (4.64):

$$\lambda_x = \lambda_y = \lambda_u = \lambda_v = \lambda_w \tag{4.67}$$

and concluded that besides equations (4.65) and (4.66), for complete similitude between the prototype and its model, it is required that:

$$\lambda_{A_{ij}} = \lambda_A \ , \qquad \forall\ A_{ij} \neq 0 \tag{4.68}$$

$$\lambda_{B_{ij}} = \lambda_B \ , \qquad \forall\ B_{ij} \neq 0 \tag{4.69}$$

$$\lambda_A \lambda_b^2 = \lambda_B \lambda_b = \lambda_D \tag{4.70}$$

In all the referred works (Singhatanadgid and Ungbhakorn, 2002a; Ungbhakorn, 2001; Ungbhakorn and Singhatanadgid, 2003c) scaling laws equivalent to the equations (4.33a), (4.33b) and/or (4.33c), derived in section 4.2.3.1 for biaxial and shear loads, were obtained.

4.3.3.1. Analyzed case studies

Ungbhakorn (2001) applied the scaling laws only to isotropic plates, under complete similitude and under distortion on Young's modulus. In both situations, the predicted buckling loads show exact agreement between predicted and theoretical results.

Singhatanadgid and Ungbhakorn (2002a) examined the scaling law (4.33a) by appliyng it to the buckling problem of cross-ply laminated plates studied by Tuttle et al. (1999). Although both predicted and experimental buckling loads were available, the authors used just the predicted values. The case studies can be grouped as follows:

1. **Complete similitude**: Prototype with the same stacking sequence and thickness as the model ($[0/90]_{2s}$ and $[\pm 45]_{2s}$), but five times larger;
2. Plates with the same size but different ply thickness and stacking sequence. A $[0/90]_{2s}$ laminated plate was the selected model to predict the following prototypes buckling behavior:
   a) **Ply level scaling**: $[0_2/90_2]_{2s}$
   b) **Sublaminate-level scaling**: $[0/90]_{4s}$
3. **Sublaminate-level scaling**: Plates with the same size and stacking sequence $[\pm 45]_{ns}$ but with different ply thickness. $[\pm 45]_{4s}$ and $[\pm 45]_{7s}$ were the models selected for two different analyses. In each one, the remaining plates with $n \in [2, 7]$ were considered as prototypes.
4. **Distortion in material properties**: $[0/90]_{2s}$ graphite/epoxy prototype modeled from E-glass/epoxy laminates with the same stacking sequences and five times smaller.

For the items 1 and 2a the buckling loads of all prototypes determined from the scaling law agree exactly with the numeric result from theory.

For the remaining items the condition $\lambda_D = \lambda_{D_{ij}}\ ,\forall\ D_{ij} \neq 0$, is not respected and therefore complete similitude is not achieved. For that reason the study 2b had relative difference between results up to 13%.

For the 3^{rd} item the discrepancies between results are less than 6%. Having in mind that in both studied cases the terms $\lambda_{D_{11}}, \lambda_{D_{12}}, \lambda_{D_{22}}, \lambda_{D_{66}}$ are equal, but different from

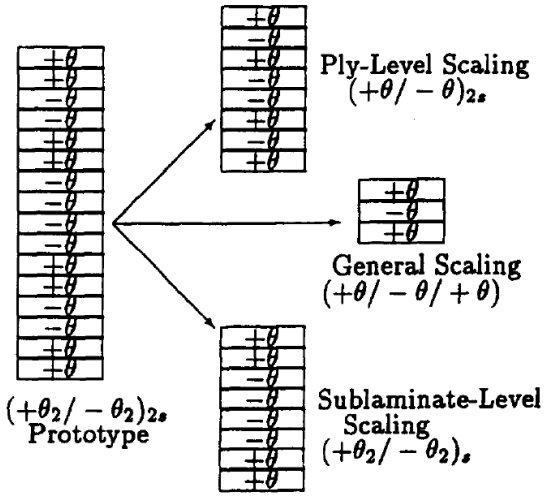

Figure 4.3.: Different possibilities for distortion of the number of plies (Rezaeepazhand and Simitses, 1997).

$\lambda_{D_{16}} = \lambda_{D_{26}}$, the authors concluded that as the number of plies exceeds eight, the effect of twisting coupling stiffness, D_{16} and D_{26}, dies out rapidly and the approximate similitude calculation can consider only the remaining terms as λ_D, leading almost to the absent of discrepancy in the results.

Finally for the last item, the discrepancies are in the range of 13.5% to 27.2%, as a consequence of the high difference in the $\lambda_{D_{ij}}$ scaling factors.

Ungbhakorn and Singhatanadgid (2003c) tested the scaling laws using closed-form solutions to obtain the buckling loads. The main conclusions of the authors are the following:

- For all cases of complete similitude, the predicted buckling loads of the prototypes give exact agreement with their theoretical results;
- Models with distortion in number of plies show good agreement when the number of plies is equal or greater than 8;
- By using distorted models in lamina material properties, the results also show it is possible to predict the buckling load of laminated prototypes provided the differences in $\lambda_{D_{ij}}$ are kept to a minimum;
- As a consequence of the non-uniformity of stiffness scaling factors, the distortion of stacking sequences does not show good agreement between theoretical and predicted values.

4.4. Analysis of honeycomb panels

4.4.1. Introduction

In the last decade sandwich panels have been widely implemented as structural elements due to their characteristic light weight and high performance. Wings, floor, ceiling, fuselage or cargo compartment paneling in modern aircrafts (Lister, 2014), helicopters (Sadowski and Bęc, 2011), aerospace vehicles or satellites (Boudjemai et al., 2012), boats or building

constructions are examples of applications where weight saving is critical (Burlayenko and Sadowski, 2009).

When designing such complex structures, the use of analytical methods become very tedious if not impossible. The computational methods, such as the Finite Element Method (FEM), may be an alternative to accurately simulate highly complicated problems, given that the problem size and detail are kept below critical values; otherwise, either impractical computational time or unfordable processing capacity will be demanded. Besides, FEM models require a detailed study before the model is sent to the solver (Boudjemai et al., 2012).

In the present case study, it will be considered the aluminum honeycomb panel from figure 4.4, manufactured with the 0.625"-thick Hexcel-3/8-5052-0.004 commercial core and 5/32"-thick 5052 aluminum face sheets. The core is limited to 10 by 10 cells in order to keep the computational cost at moderate levels.

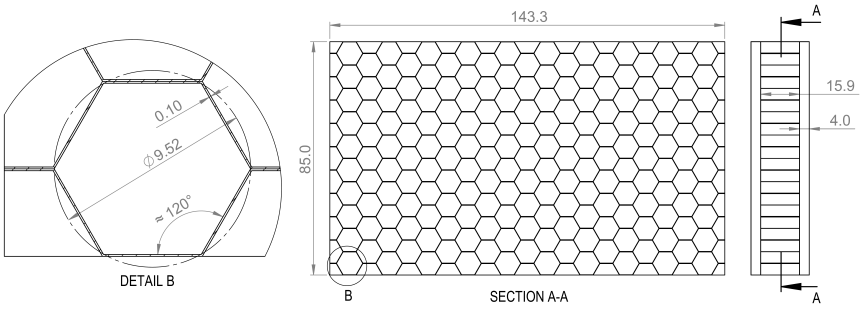

Figure 4.4.: Aluminum honeycomb panel with commercial core containing 10×10 Hexcel-3/8-5052-0.004 cells (dimensions converted to mm).

4.4.2. Existing simulation techniques for honeycomb structures

Given that for the honeycomb sandwich models the computational time increases very rapidly with the number of cells in the panel core (Burlayenko and Sadowski, 2009); in order to reduce both the pre-processing and computation time, the 3D detailed solid FE model is usually replaced by either:

- a 3D simplified model using shell elements to model face sheets, and either solid or shell elements for the actual geometry of the core cells;
- or, either a 3D or 2D equivalent three-layered continuum model based on effective orthotropic elastic constants of the honeycomb core determined by analytical/numerical approaches such that reviewed by Ali and Jun (2014); Cinar et al. (2015); Schwingshackl et al. (2006).

For the second option, the 2D models are usually preferred, requiring computer resources much lower than other options. However, its reliability is critically dependent on the prediction accuracy of the effective elastic constants of the core. Besides, the three-layer arrangements lead to the use of the various sandwich theories characterized by the wide range of assumptions concerning the through-the-thickness behavior (Burlayenko and Sadowski, 2009). The approach can be mostly used in the preliminary design stage of the design process. Even for a simple clamped honeycomb beam, significant differences (around 10% for 3^{th} natural frequency) were obtained by Boudjemai et al. (2012) between the experimental measurements and a simplified 3D one-layered model, possibly caused by ignoring the effect

of adhesive films, damping or complex boundary conditions, according to the authors; after comparing a 2D equivalent three-layered model with a 3D simplified shell model, Cinar et al. (2015) found differences around 10 to 15% in the 1^{st}, 4^{th} and 5^{th} natural frequencies of a honeycomb sandwich laminate, depending on the stacking configuration.

4.4.2.1. Effective orthotropic material properties

Schwingshackl et al. (2006) applied 15 of the existing theoretical methods to a commercial honeycomb core and compared the results to standardized experimental ASTM values. The main conclusions are the following:

- Despite the high divergence found in the values for E_x, E_y, G_{xy}, E_z, ν_{xy}, ν_{xz} and ν_{yz}, a sensitivity analysis proved that these parameters have minor influence on dynamic behavior;

- The sensitive G_{xz} and G_{yz} shear moduli predicted by majority of the analytical approaches are in good agreement with those obtained through ASTM standard methods.

Being purely analytical and providing all nine material properties, the models according to Gibson and Ashby (from 1988) and Burton and Noor (1997) were selected as references for the current research. The first, although frequently used, is limited because of the assumption of a constant cell wall thickness yields significantly low G_{xz} values. Burton and Noor (1997) would latter consider the double wall effect in all the material properties.

4.4.2.2. Effective density

In dynamic and frequency analyses the mass distribution is the most sensitive of the effective material parameters (Jiang et al., 2014). However, various aspects tend to cause the appearance of errors, namely: the (in)proper selection of a model that accurately describes the geometry of the actual structure, but mainly the (in)correct interpretation of the core dimensions in the commercial honeycoms.

Regarding the first issue, even though the geometry assumed by Gibson and Ashby (in 1988) is perfectly clear (see figure 4a from Ali and Jun (2014)), the same does not happen for the model presented by Burton and Noor (1997), where a 3D detailed geometry of the core is missing. More recently Balawi (2007) derived an expression for the effective density considering the effect of double wall thickness, based on a detailed 3D cell geometry whose mid-surface wall dimensions match those assumed by Burton and Noor (1997). Besides Balawi (2007) considered the overlapping areas, such those unfilled diamond-shaped areas in figure 4.5a, through the term $-\frac{4}{9}(\frac{t}{l})^2$ in equation (4.71c).

However, a commercial core formed by either expansion or corrugation process will more likely get closer to the figure 4.5c than the others. Indeed, Balawi (2007) has firstly considered the geometry in figure 4.5b to determine the core density, but latter (in order to derive effective elastic properties) assumed that the geometry in figure 4.5c (apart from the radios of curvature) is considered to better describe commercial hexagonal honeycombs.

Now that the differences in geometry of the various models are enlightened, another issue arises: the predicted core densities obtained from any of the previous models are quite below the values provided by the suppliers, due to a misunderstanding in the cell size definition as demonstrated below.

The cell size is consensually defined as either the "distance across flats" (Hexcel Composites, 2000; Plascore, Inc, 2014) or alternatively "the diameter of an inscribed circle within a

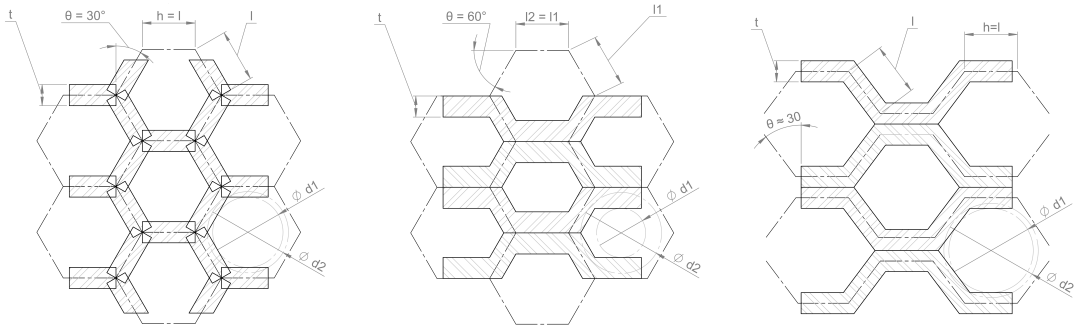

(a) Gibson and Ashby - 1988 (b) Burton and Noor (1997); Balawi (2007) (c) Assumed for the present research

Figure 4.5.: Detailed core 3D geometries according to different authors. In addition to the usual cell sides (l and h, or $l1$ and $l2$) and the foil thickness (t), it was included the dimensions of the inscribed (d_{ins}) and circumscribed diameters (d_{cir}), represented respectively as $d1$ and $d2$.

cell" (Davis, 1992), which for honeycombs with regular hexagonal cells have the same value. To correctly apply the following expressions to estimate the effective density:

$$\text{Gibson and Ashby (1988):} \quad \frac{\rho_e}{\rho_s} = \frac{6t}{3\sqrt{3}l} \tag{4.71a}$$

$$\text{Burton and Noor (1997):} \quad \frac{\rho_e}{\rho_s} = \frac{8t}{3\sqrt{3}l} \tag{4.71b}$$

$$\text{Balawi (2007):} \quad \frac{\rho_e}{\rho_s} = \frac{8t}{3\sqrt{3}l} - \frac{4}{9}\left(\frac{t}{l}\right)^2 \tag{4.71c}$$

$$\text{Proposed for figure 4.5c:} \quad \frac{\rho_e}{\rho_s} = \frac{8lt}{3\sqrt{3}l^2 + 6lt} \tag{4.71d}$$

and in order to determine the cell side dimension (l), one needs to know if the available cell size (d) was assumed as the inscribed value (d_{insc}):

- Gibson and Ashby (1988) / Proposed:

$$l = \frac{d_{insc} + t}{\sqrt{3}} \tag{4.72}$$

- Burton and Noor (1997) / Balawi (2007):

$$l = \frac{d_{insc} + 2t}{\sqrt{3}} \tag{4.73}$$

or, as the circumscribed value (d_{circ}):

$$l = \frac{d_{circ}}{2} + \frac{t}{\sqrt{3}} \tag{4.74}$$

As the values predicted with equations (4.71b) to (4.71d) are nearly the same, in figure 4.6 are plotted only those obtained according to Gibson and Ashby (1988) and Burton

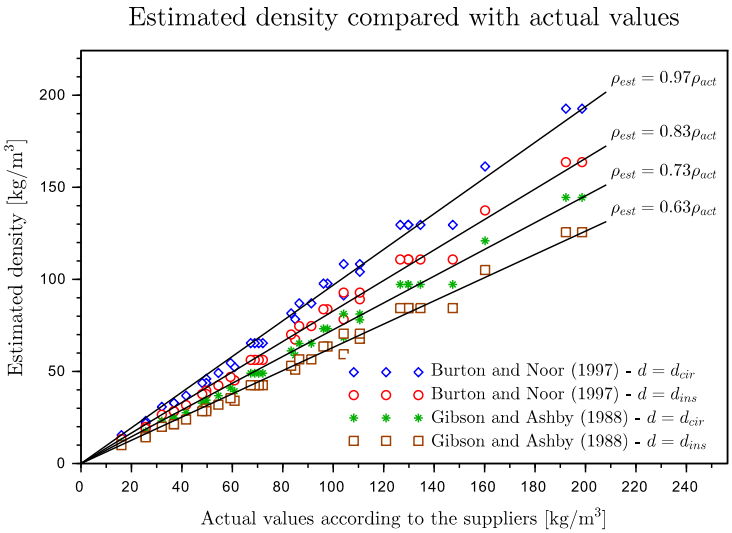

Figure 4.6.: Comparison of the estimated effective density with the actual values for 35 different cores collected from product data sheets.

and Noor (1997). In order to better compare the results obtained with equations (4.71a) to (4.71d), table 4.1 presents the overall correlation between the estimated effective density ($\rho_e^{est.}$) and the actual values ($\rho_e^{act.}$) for 35 different cores collected from product data sheets. Additionally, the same analysis is made specifically for the Hexcel 3/8-5052-0.004 aluminum core under analysis in this chapter. As previously explained, the model geometry according to Burton and Noor (1997) and Balawi (2007), as well as the assumed geometry in this chapter should incrementally describe more accurately the effective density of the commercial honeycomb cores; however the results in table 4.1 show that the tendency of increasing accuracy is precisely the opposite. Nevertheless, the differences are negligible, and the accuracy of any of them is clearly superior to that obtained from the Gibson and Ashby (1988) model.

Table 4.1.: Correlation between the estimated effective density ($\rho_e^{est.}$) and the actual values obtained from product data sheet ($\rho_e^{act.}$) for 35 different cores and in particular for the Hexcel-3/8-5052-0.004 core.

	Overall	Hexcel 3/8-5052-0.004			
	$\left(\frac{\rho_e^{est.}}{\rho_e^{act.}}\right)$	$\rho_e^{act.} \mid \rho_e^{CAE}$	$\rho_e^{est.}$	$\left(\frac{\rho_e^{est.}}{\rho_e^{act.}}\right)$	$\left(\frac{\rho_e^{est.}}{\rho_e^{CAE}}\right)$
	[%]	[kg/m^3]	[kg/m^3]	[%]	[%]
Actual value	-	86.5	-	-	-
Value from CAE Model	-	85.4	-	-	-
Gibson and Ashby (1988)	72.7	-	65.2	75.4	76.4
Burton and Noor (1997)	96.9	-	87.0	100.5	101.8
Balawi (2007)	96.3	-	86.4	99.9	101.2
Proposed (eq. (4.71d) and (4.74))	93.6	-	84.9	98.1	99.4

From figure 4.6 it is clear that the core density match the cell size (both values given by the product designation) if the cell size is assumed as the diameter of a circumscribed circumference. This was verified in the catalogs of the main honeycomb manufacturers (AlCore, HexCel, PlasCore), which does not agree with the consensual definition of cell size initially presented. For the 3003 Aluminum HexWeb 5.2-1/4-0.0025 commercial core, Schwingshackl

et al. (2006) compared the effective elastic properties obtained from 15 theoretical models considering cells with 1/4" inscribed circumference, with the results obtained experimentally from core specimens that indeed have cells with 1/4" circumscribed circumferences (as previously demonstrated). In other research presented by Xu et al. (2012), the equation $\frac{\rho_e}{\rho_s} = \frac{8t}{3\sqrt{3}l}$ was introduced from literature for perfect hexagonal honeycomb, along with a table summarizing research results where $\frac{t}{l}$ and $\frac{\rho_e}{\rho_s}$ are data columns. It can be concluded that the authors assumed $l \approx \frac{d}{\sqrt{3}}$ (inscribed cell size), but the relative density was estimated from the catalog data instead of using the equation introduced previously.

Finally, the comparative table presented by Schwingshackl et al. (2006) is partially reproduced; at table 4.2 experimental data given by several data sheets were included and the average values compared with those obtained by the Gibson and Ashby (1988) and Burton and Noor (1997) models, correctly applied to commercial honeycombs with "density"|"cell size"|"foil thickness" equal to 5.2 lb/ft^3 | 1/4" | 0.0025". The following approximated core material properties were assumed: $E = 70\,\text{GPa}$, $\nu = 0.33$, $\rho = 2680\,\text{kg/m}^3$. The main conclusions remain the same, except that the accuracy of G_{xz} is increased, as well as the overestimation of the E_z and G_{yz}.

Table 4.2.: Effective material constants for 5.2-1/4-0.025 commercial cores.

	ν_{xy} -	ν_{xz} -	ν_{yz} -	E_x [MPa]	E_y [MPa]	E_z [MPa]	G_{xy} [MPa]	G_{xz}^{low} [MPa]	G_{xz}^{up} [MPa]	G_{yz} [MPa]
	Experimental material properties									
HexWeb 3003	-	-	-	-	-	1000	-	440		220
HexWeb 5052	-	-	-	-	-	1310	-	565		244
PAMG-XR1 5052	-	-	-	-	-	1310	-	565		241
DuraCore || 5052	-	-	-	-	-	-	-	427		214
HexWeb 5056	-	-	-	-	-	1586	-	579		221
PAMG-XR1 5056	-	-	-	-	-	1586	-	579		221
DuraCore || 5056	-	-	-	-	-	-	-	427		207
AVERAGE	-	-	-	-	-	1358	-	512		224
	Theoretical material properties									
Gibson and Ashby (1988)	1	0	0	1.25	1.25	1598	0.31	300		300
Burton and Noor (1997)	0.44	0	0	1.25	1.25	2131	0.75	180	501	300

4.4.3. Experimental scaled model testing: an affordable simulation alternative

Given that some of the failures of aircrafts and helicopters are related to severe vibrations during launch, accurate prediction of the vibration parameters of honeycomb sandwich panels is very important (Sadowski and Bęc, 2011). Being capable to more properly capture the complex details of manufacturing effects, material properties and boundary conditions, the use of experimental model testing is proposed as a significantly more affordable alternative to (experimental) full scale testing. Besides, the method allows to avoid extremely detailed models and the associated pre-processing and computation time, specially in the advanced design stages were high accuracy is required.

4.4.4. Case study

The previous sections allowed the selection of two methods among those available in the literature to determine the effective material properties used in the equivalent models.

Although impractical as a design tool, the model from figure 4.7a was developed to obtain the reference values, being the model from figure 4.7c the one to which the results predicted from a reduced model may be compared properly. Similar to the detailed model regarding the processing time, the model from figure 4.7b was developed for further analysis of the results, allowing the sources of inaccuracies to be clearly identified. Unless otherwise stated, the actual honeycomb is assumed as partially clamped in the farthest edges, this is, only in the cross section belonging to the face sheets; the other edges are set free. The considered meshes using solid elements were subjected to a convergence analysis, ensuring both moderate computation time and accurate results.

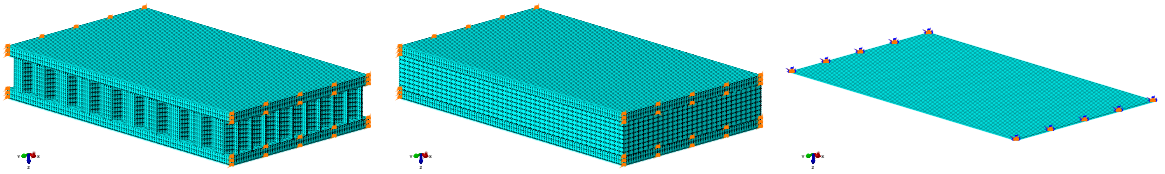

(a) Detailed model (47488 elements) (b) Solid model with equivalent core layer (32640 elements) (c) Equivalent 2D shell model (5472 elements)

Figure 4.7.: ABAQUS finite elements models using solid (C3D20R) or shell (S8R) elements.

For the reduced model, a 1:6-scale ($\lambda = 6$) was selected. To achieve complete similitude, using the same materials, the geometry has to be a replica, according to equations (4.36) and (4.49b); the frequency is given by the inverse of time scale factor (equation (4.34c)) and the accelerance function scaled by equation (4.44b). However, due to the limitations in the available standard structural elements respecting the necessary dimensions, and as one can see from table 4.3, the core and face sheet dimensions have some deviations from the geometry required for complete similitude. The -4% deviation in the face sheets thickness is due to the fact that a 0.025" is from the available standard dimensions the closest to the desired dimension. As a consequence, the scaled factor of the core thickness were set also to 6.25 in order to keep the scaling through honeycomb thickness homogeneous. Also, as a consequence of the limited available core geometries, the foil thickness and therefore the density are scaled with a positive 5% deviation. The reduced model may therefore be more correctly classified as a distorted scaled model.

Table 4.3.: Dimensions of the honeycomb prototype and its scaled model.

		Prototype	1:6-scale model			
			Complete similitude (ideal)	Partial similitude (actual)	Actual scale factor [-]	Deviation [%]
Face sheets:						
Thickness	[mm]	4.0	0.7	0.6	6.25	-4.0
Density	[kg/m^3]	2680	2680	2680	1	0
Core:						
Thickness	[mm]	15.9	2.6	2.5	6.25	-4.0
Cell size	[mm]	9.5	1.6	1.6	6	0
Foil thickness	[mm]	0.102	0.017	0.018	5.71	5.0
Density	[kg/m^3]	85.4†	89.6	89.7†	0.95	5.0

† Values obtained from the CAE model of the honeycomb core.

Analysis of catalog core dimensions

Considering that the *core mass* and *core volume* are proportional to the cell size (d_{cell}), and to the core (t_{core}) and foil (t_{foil}) thicknesses:

$$core\ mass \propto t_{core} \times d_{cell} \times t_{foil}$$
$$core\ volume \propto t_{core} \times d_{cell}^2$$

apart from minor manufacturing tolerances, the following similitude condition is derived:

$$\lambda_{\rho_{core}} = \lambda_{t_{foil}}\, \lambda_{d_{cell}}^{-1}$$

Replacing the density and foil thickness values available in the manufacturers catalog, that condition yields: $\lambda_{t_{foil}} = 4.98$. However, the direct ratio of the (foil thicknesses) catalog values is $\lambda_{t_{foil}} = 5.71$.

Such a marked difference may be explained by a lack of significant digits in catalog values; for example: assuming that the densities are accurate (2 significant digits), any of the following ordered pair: {0.0037"; 0.00075"} or {0.0035; 0.00070"} for the foil thicknesses, would respect both the similitude conditions, and the catalog values {0.004; 0.0007"}. Additionally it would also explain most of the data scattering in figure 4.6.

For the presented research, the foil thickness was assumed as accurate, and that is why the values for density in the table 4.3 are those from CAE model rather then the catalog values. For a future experimental validation, replacing the selected Hexcel-3/8-5052-0.004 commercial core by the Hexcel-3/8-5052-0.005 is recommended, matching the scaled density and ignoring the deviation in the scaled foil thickness, due to the lack of significant digits in the catalog values.

4.4.4.1. Results analysis

The natural frequencies of the prototype for the first 8 modes of vibration, which were obtained directly through numerical methods, are presented in table 4.4. It was considered a detailed model, two equivalent shell models (A_1, B_1) and two equivalent solid models (A_2, B_2). The effective properties for the models A_i and B_i are according to Gibson and Ashby (1988) and Burton and Noor (1997), respectively.

Table 4.4.: Natural vibration frequency f_i for the first 8 natural modes of the prototype, obtained using the detailed model or equivalent models. The effective properties for the models A_i and B_i are according to Gibson and Ashby (1988) and Burton and Noor (1997), respectively.

	Natural frequency (f_i) [Hz]				
	Detailed	Equiv. shell models		Equiv. solid models	
i	Model	Model A_1	Model B_1	Model A_2	Model B_2
1	2767	1989	2509	2324	2788
2	3987	3262	3639	3617	3959
3	5777	3954	4984	4938	5789
4	7031	5144	6027	6268	6990
5	8386	6034	7112	8047	8168
6	9002	6392	7669	8145	8971
7	9347	6418	8034	9046	9349
8	10387	6430	8241	9282	10307

Alternatively, the numerical validation of the scaled model testing was considered. The natural frequencies of the 1:6-scale model are presented in table 4.5 for the first 8 modes of vibration; then, applying the scaling laws (4.35) and (4.49a) to these values, the natural frequencies of the prototype were predicted, as available from table 4.6.

Table 4.5.: Natural vibration frequency f_i for the first 8 natural modes of the scaled model.

	Natural frequency (f_i) [Hz]
i	1:6-scale model
1	16721
2	23903
3	34789
4	42318
5	50554
6	53954
7	56115
8	62304

Table 4.6.: Natural vibration frequency f_i for the first 8 natural modes of the prototype, obtained using the detailed model or predicted based on the 1:6-scale model.

	Natural frequency (f_i) [Hz]	
	Detailed	Prediction based on
i	Model	the 1:6-scale model
1	2767	2787
2	3987	3984
3	5777	5798
4	7031	7053
5	8386	8426
6	9002	8992
7	9347	9352
8	10387	10384

Assumed as the most accurate, the results from the detailed model are shown as reference values in tables 4.4 and 4.6. The relative differences available from table 4.7 are obtained between the results of other models and these reference values. Besides, some frequency response functions are plotted in figures 4.9 and 4.10, obtained considering the excitation and measurement points depicted in figure 4.8.

Table 4.7.: Relative difference [%] between the natural frequencies of the prototype that were obtained using equivalent models or predicted through the scaled model (respectively, in tables 4.4 and 4.6), and those obtained from the detailed model.

	Relative difference (RD_i) [%]				
	Equiv. Shell Models		Equiv. Solid Models		Predicted based on
i	Model A_1	Model B_1	Model A_2	Model B_2	the 1:6-scale Model
1	-28.1	-9.3	-16.0	0.8	0.7
2	-18.2	-8.7	-9.3	-0.7	-0.1
3	-31.6	-13.7	-14.5	0.2	0.4
4	-26.8	-14.3	-10.9	-0.6	0.3
5	-28.0	-15.2	-4.0	-2.6	0.5
6	-29.0	-14.8	-9.5	-0.3	-0.1
7	-31.3	-14.1	-3.2	0.0	0.1
8	-38.1	-20.7	-10.6	-0.8	0.0

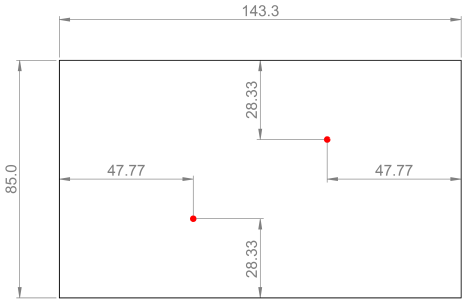

Figure 4.8.: In-plane location of the excitation and measurement points for dynamic analysis of the honeycomb panel (dimensions in mm).

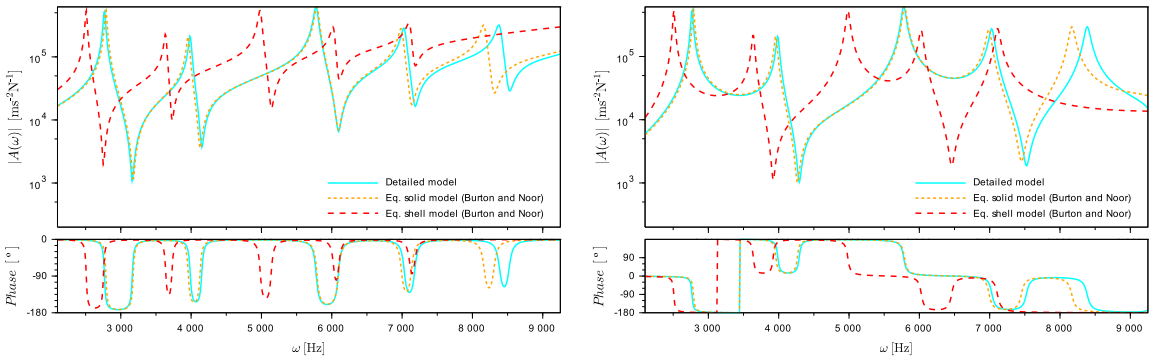

(a) Flexural point direct accelerance

(b) Flexural transfer direct accelerance

Figure 4.9.: Comparison of frequency response functions obtained from the detailed honeycomb model with those from the equivalent shell model and from the equivalent solid model, both using effective properties according to Burton and Noor (1997).

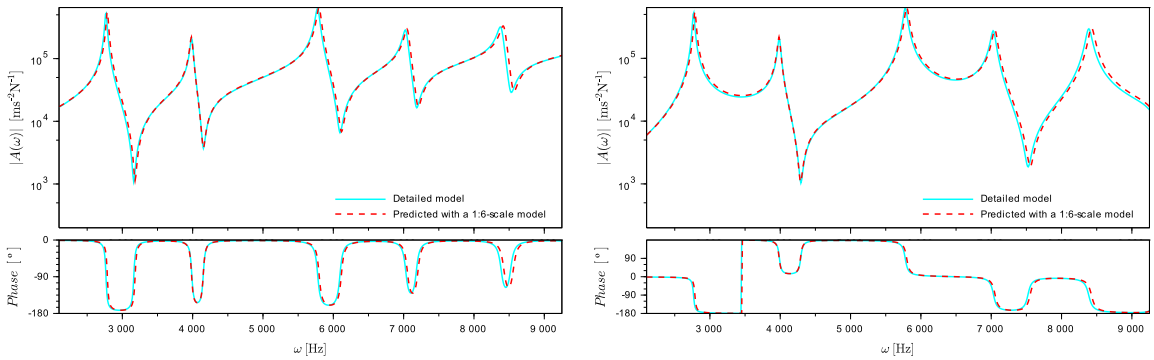

(a) Flexural point direct accelerance

(b) Flexural transfer direct accelerance

Figure 4.10.: Comparison of frequency response functions obtained from the detailed honeycomb model with those from the scaled model designed according to the similitude theory.

Numerical methods

Comparing results in table 4.4 between the models A_1 and A_2, as well as between the models B_1 and B_2 it is clear that the results significantly lose accuracy when an equivalent shell model is used. This is also clearly noticeable in figure 4.9, when comparing the frequency response functions of the detailed model with those from models B_1 and B_2.

Previously mentioned as affecting the reliability of equivalent models, the following factors will be therefore analyzed in order to understand the quantitative impact of each one:

- Prediction accuracy of the effective elastic constants;
- The influence of the wide range of assumptions concerning the through-the-thickness behavior in the equivalent layer theories;
- Ability to reproduce the loading and boundary conditions as in a detailed model.

Regarding the first factor, the low accuracy of models A_1 and A_2 is mainly due to the inaccuracies introduced by equation (4.71a) in the effective core density, as already demonstrated by the correlation values in table 4.1. On the other hand, the model B_2 although highly accurate, computationally remains very expensive. Nevertheless, it proves that the use of effective material properties according to Burton and Noor (1997) introduces an almost negligible approximation error.

In order to estimate the sensitivity of the results to the isolated effect of the second and third factors, 9 additional modal analysis were performed considering combinations of different material properties:

- (X) both the core layer and the face sheets assumed as aluminum;
- (Y) or, both the core layer and the face sheets assumed a material with the effective properties from table 4.2 according to Burton and Noor (1997);
- (Z) or, material distribution of the actual honeycomb;

with different boundary conditions, assuming the farthest panel edges:

- (1) free ($FFFF$);

- (2) or, fully clamped (C^fFC^fF);
- (3) or, partially clamped, this is, only in the face sheets cross section (C^pFC^pF).

As it can be observed from table 4.8, for panels with homogeneous material properties through the thickness and correctly reproduced boundary conditions (combinations X1, X2, Y1 and Y2), it is possible to conclude that, as expected, the difference in results obtained with solid and shell models is acceptable, taking into account the reduced computational cost of shell models.

Table 4.8.: Range of relative differences [%] for the first 8 natural vibration frequencies obtained from shell model B_1 when compared with solid model B_2, for different material combinations, considering the edges all free (FFFF) or only the farthest edges clamped (CFCF).

	Material properties		Boundary conditions					
			(1)		(2)		(3)	
	Face sheets	Core	FFFF		C^fFC^fF		C^pFC^pF	
			from	up to	from	up to	from	up to
(X)	Aluminum	Aluminum	-2.4	0.0	-2.0	-0.7	0.6	8.3
(Y)	Effective properties	Effective properties	-2.3	0.0	-1.3	0.1	-0.6	1.3
(Z)	Aluminum	Effective properties	-11.7	-2.4	-20.5	-8.8	-20.0	-8.1

However, in honeycombs where materials have significantly different mechanical properties (combinations Z1 and Z2), the assumption that planes perpendicular to the honeycomb mid-surface remain plane after bending is highly disrespected, as one can see in figure 4.11. The equivalent layer theory applied to the analysis of an honeycomb ignores a great amount of core shear deformation, which therefore is wrongly converted into bending, making the structure apparently more flexible then it really is. For the present case study, with farthest edges fully clamped, the softening effect observed in shell models reached -20.5% for the 8^{th} vibration mode.

Finally, due to the different ability to reproduce the loading and boundary conditions, differences were observed in the frequencies and in the order of the mode shapes:

- In the combination X3 the in-plane modes vibrating across the direction defined by the honeycomb supports kept their order (global modes number 3 and 7); however, from the solid to the shell model, the 2^{nd} in-plane mode (global mode 6), vibrating along the direction previously defined, changed place with global mode number 8. In comparison to combination X2 these differences are due to highly non-linear distribution of displacements through the panel thickness, previously restrained by a fully clamped cross section, which invalidates assumptions from the equivalent layer theory used in shell models. Note that differences obtained in the remaining frequencies are below 1.2%, which is in the same range as those from combination X2.
- In the combinations Y3 and Z3, comparing the shell model with the solid model, no significant changes were verified in the modes of vibration. The relative differences remained approximately in the same range as in combinations Y2 and Z2, respectively, given that the core non-linear in-plane displacements restrained by the full clamp are reduced, and so the shell model remained an approximation as good as with a full clamp;

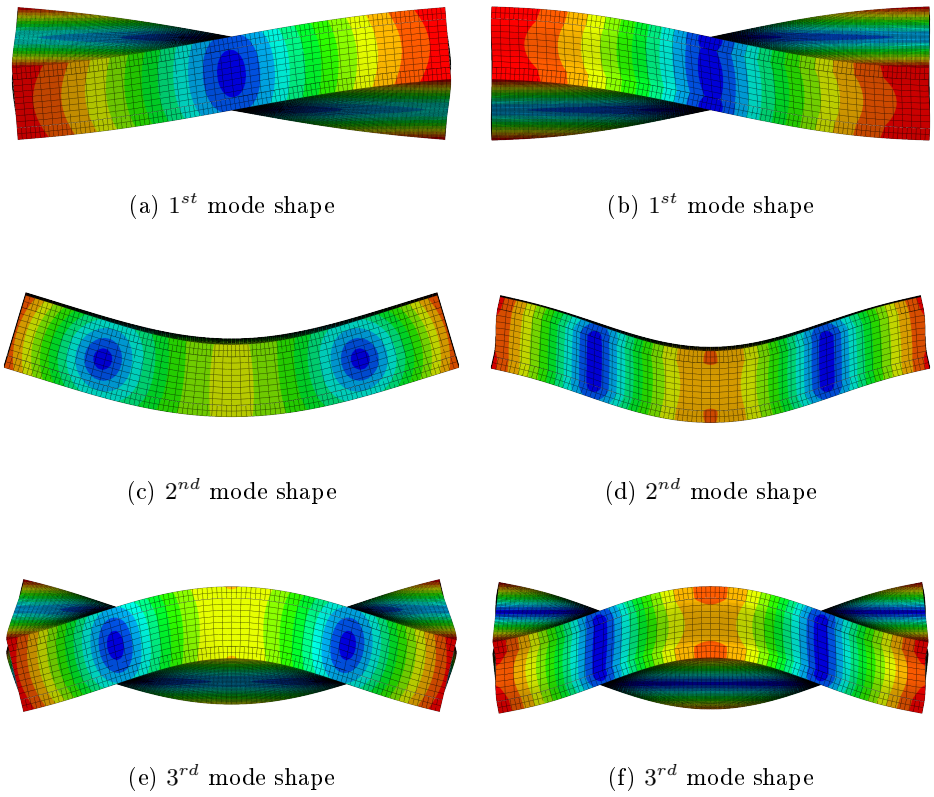

(a) 1^{st} mode shape (b) 1^{st} mode shape

(c) 2^{nd} mode shape (d) 2^{nd} mode shape

(e) 3^{rd} mode shape (f) 3^{rd} mode shape

Figure 4.11.: Comparison of the mode shapes for a laminated structure: layers with the same material properties on the left and with different material properties (as in honeycomb panels) on the right.

Scaled model testing

The 1:6-scale model is the one that performs better, keeping the $\sum_{i=1}^{i=8} \mid RD_i \mid$ as low as 2.1%, while the better alternative results obtained from a solid model with efficient properties according to Burton and Noor (1997) (model B_2) achieved 6.0%.

Finally, in figure 4.10, the frequency response functions predicted through a 1:6-scale model are compared with those obtained from the detailed honeycomb model, confirming that the results of the reduced model remain quite accurate even for higher frequencies.

The only major and potential disadvantage of a scaled model when compared to the alternative numerical methods would be that the expenses with experimental work must be incurred (Young, 1971). However, such argument is based on the premise that, using numerical simulation, no experimental testing is required which may not be true. For example, accurate damping characteristics require experimental testing. Note that, for example, a 1:5-scale model would have $\frac{1}{125}$ the mass (and volume) of the full scale structure and therefore his production would easily be included in medium to high budget projects. Eventually, any slightly expense increase is expected to be acceptable given that it allows to economically avoid the risks associated with prototyping a structure in its full size configuration without no previous testing (of the whole structure). Besides, the experimental simulation of a reduced scale model yielding accurate and reliable data could lead to one last optimization step, and therefore evolve the final design to a more efficient, economic and yet reliable solution.

4.5. Concluding remarks

A generalized procedure to obtain the scaling relationships for an anisotropic laminated plate has been presented. The overview of the equation's flow in their derivation is represented in figure 4.2. In order to correctly select the similarity conditions and scaling laws for a specific plate the considerations listed below should be followed for each set of equations used in this procedure:

- **Governing equations**: some authors neglect the effect of in-plane forces on bending, after assuming that no large membrane forces are applied or after neglecting geometric non-linearities. So, for that formulations the equations (4.5e), (4.17e) to (4.17g), (4.41), (4.43) and (4.46) will not be available;
- **Constitutive equations**:
  - Laminated plates with symmetric stacking do not exhibit membrane-bending coupling, so the equations (4.8), (4.9), (4.12), (4.13), (4.18), (4.19), (4.26) to (4.28), (4.40b), (4.40d), (4.40e) and (4.43) should not be used;
  - Cross-ply laminates ($[0/90]_n$) for which the stiffnesses A_{16}, A_{26}, D_{16} and D_{26} are zero do not have to respect any condition including scaling factors of those terms. However, the derived scaling laws for complete similitude remain the same;
  - Some laminate for which other stiffnesses are zero may exist. However, as long as the terms A_{11}, A_{12}, A_{22}, A_{66}, D_{11}, D_{12}, D_{22}, D_{66}, and any of the B_{ij} stiffnesses are not zero or negligible, all the derived scaling laws will remain unchanged.
- **Strain-displacement relations**: some authors neglect the strain components $\frac{1}{2}\left(\frac{\partial w}{\partial x}\right)^2$, $\frac{1}{2}\left(\frac{\partial w}{\partial y}\right)^2$ and $\frac{\partial w}{\partial x}\frac{\partial w}{\partial y}$, after assuming small rotations. For such formulations the equation (4.16) is not considered.

The imposition of initial similarity conditions such as the material or geometric similarity must be done carefully, and if possible, based on some theoretical foundation that classifies them as necessary, avoiding the over-constraining of the model to be designed for experiments. For example, regarding static analysis, no equality is imposed between the geometric factors λ_x and λ_y from equation (4.36) in relation to the displacement factors λ_u and λ_v from equation (4.37). Other example is the inclusion of (moderate) non-linear terms in the theory governing the plate behavior, that introduces an additional condition $\lambda_w^2 = \lambda_u \lambda_x$. It should be clear that except for (moderate) non-linear and dynamic analysis, the consequently obtained condition:

$$\lambda_x = \lambda_y = \lambda_z = \lambda_{u_0} = \lambda_{v_0} = \lambda_{w_0}$$

is overly restrictive for the scaled model design.

The ability to apply the generalized set of scaling relationships to a specific problem can be easily demonstrated deriving all the particular sets of similitude criteria proposed previously for: cylindrical bending of laminated plates (Simitses and Rezaeepazhand, 1992; Wu, 2005), vibration of elastically restrained isotropic flat plates (Simitses and Rezaeepazhand, 1993b; Wu, 2003), and buckling of laminated plates subjected to biaxial or shear loading for particular stacking configurations (Singhatanadgid and Ungbhakorn, 2002a; Ungbhakorn, 2001; Ungbhakorn and Singhatanadgid, 2003c).

In the present chapter, the experimental scaled model testing, as an alternative simulation tool, was numerically validated through the prediction of the frequency response functions of

an honeycomb panel, based on the results obtained from a distorted 1/6-scale model. Several issues arose unexpectedly during this demonstration; the presented explanation is lengthy but very interesting for any future research regarding honeycomb structures, particularly if a scaled model is required. The case study highlights are, in brief, the following:

- Due to the high pre-processing and computation time of detailed models, equivalent shell models are often proposed in the literature as an alternative;
- Such simplified models require effective properties; those obtained according to Burton and Noor (1997) are indeed highly accurate for commercial honeycomb cores;
- For future researches, determination of effective properties should take into account some considerations regarding the parameters in catalogs of the honeycomb manufacturers;
- However, being already listed in the literature as a source of inaccuracies, the characteristics assumptions of an equivalent layer model may introduce significant errors in the results due to the significantly different material properties present in an honeycomb;
- Alternatively, the reduced scale model testing was proposed, and demonstrated as an accurate simulation tool, despite the geometric distortions of the model up to 5%.

5. Modular Approach to structural similitude

Abstract

An original Modular Approach is presented. The objective is to improve how the similitude theory is applied to governing equations, overcoming both its primary and secondary identified weaknesses. The major achievement is that, with the new approach, the similitude theory can be applied to complex structures through differential equations of its simple substructures, even if the governing equations for the whole structure are not available.

A stiffened plate is selected to demonstrate the use of the Modular Approach and the accuracy of the scaled model testing. To that end, the Modular Approach has to be firstly applied to the generalized simple plate and beam. Even though the simplifying assumptions are minimized in the substructure governing equations, the Modular Approach is able to avoid the expected increase in the mathematical effort and complexity of the process of applying the similitude theory. In a second step, a relation is established between the scaling relationships derived for each simple structural element of the complex prototype.

5.1. Introduction

5.1.1. Research background

A complete perspective of the contributions to the use of scaled models based on similitude theory, ever since its establishment as a branch of engineering science was presented at the beginning of this thesis. That work reveled a significant number of publications based mainly on the dimensional analysis or alternatively on the use of differential equations.

Regarding the methodologies based on dimensional analysis, reports recently made available by the aerospace industry regarding past case studies demonstrated the applicability for complex structures. However, the correct use of dimensional analysis, although simple, requires great effort and skill.

An alternative and more intuitive approach was initially proposed by Kline applying the similitude theory through the governing equations. If directly applied to the governing equations, it is avoided the need of an exact or approximate analytical solution, valid for the geometry, boundary and loading conditions of the structure under analysis. Despite this, one still needs to know enough about the physics of the problem to be able to write down a complete set of governing equations. This primary weakness may explain why this method was rarely applied in the literature to structures more complex than plates and shells, since the governing equations were not available. Furthermore, as currently applied in the literature, the method suffers from the following secondary weaknesses:

- Lack of generality of the scaling relationships;
- Reduced insight of the meaning, origin or significance of most of the derived scaling laws and similarity conditions.

In chapter 4, regarding the structural similitude of plates, instead of simplified governing equations written in terms of displacements and stiffnesses, the similitude theory was ap-

plied to governing equations (written in terms of the force and moment resultants), strain-displacement relations and constitutive equations, whose simplifications were minimized. With this approach, generalized scaling relationships were derived allowing their quick simplification for any particular case study. Besides, some additional insight of the origin and relations between scaling laws was provided.

This type of approach (avoiding simplified governing equations) requires an increased investment of effort and time. Dividing the governing equations into (three) sub-sets, the similitude theory is applied in a simpler, more structured and straightforward manner, but still complex and unintuitive. It is highlighted that once generalized scaling relationships are derived these disadvantages are unnoticed and do not affect their virtues; nevertheless, overcoming these limitations partially motivated further research.

Lastly, despite the effort in previous chapter, the fact is that the primary weakness of the similitude theory applied to governing equations still persists, particularly for structures with complex geometry: one still needs to know enough about the physics of the problem to be able to write down a complete set of governing equations.

5.1.2. Objectives

In order to improve the direct application of the similitude theory to governing equations, overcoming both its primary and secondary weaknesses, as well as other limitations and difficulties previously identified, an original Modular Approach is presented. The objective is to achieve the following characteristics:

- **Ability to obtain scaling relationships as general and structured as possible, organized into modules.** To achieve this, the similitude theory will be applied to the most basic equations, this is, equations with simplifications or substitutions minimized:
  - Governing equations derived from the equations of elasticity, assuming plane-stress state, and written in terms of force and moment resultants;
  - Force and moment resultants written as the integral of a generic stress field;
  - Stress-strain relations;
  - Strain-displacements relations, written as derivatives of a generic displacement field;
  - Displacement field.

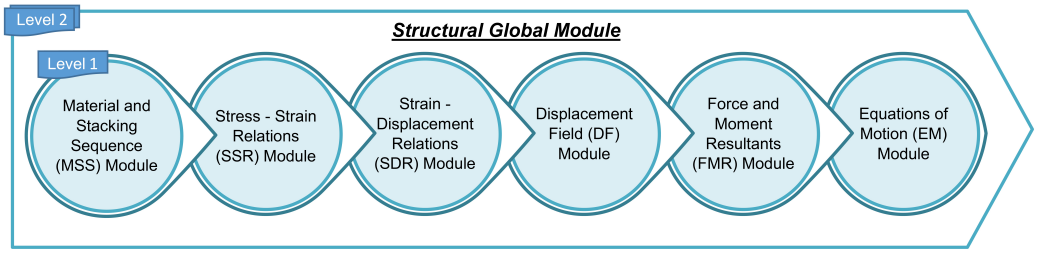

Figure 5.1.: Modules grouped by sequential substitution to create the structural global module of a simple element.

From each of these equations a module of scaling factors and similarity conditions will be derived, as illustrated in figure 5.1.

- **Flexibility of the obtained modules to be efficiently re-used in a multi-level methodology.** The 6 modules (level 1) from figure 5.1 grouped by sequential substitution create the called structural global module (level 2), that in turn, is expected to be directly applicable as one of those modules necessary for example: (1) to the analysis of a complex structure (level 3) constructed with diverse simple elements such beams, plates, shells and solid parts, or (2) to the thermo-structural analysis of a structure (level 4).

For the current manuscript, the previous application example (1) was selected to demonstrate the proposed modular methodology. The case study consists of a stiffened plate, composed by three sub-systems: a simple plate and two stiffeners, each of them assumed as a beam.

Considering a generic complex structure composed by n sub-systems, as exemplified in figure 5.2, one of the concepts behind this approach is for the first time stated in this manuscript as follows:

> *Two complex structures (systems) will be similar in relevant characteristics if simultaneously:*
>
> - *a bi-unique transformation can be derived between the characteristics of each one of its basic structural elements (sub-systems) seen as a free-body diagram;*
> - *the relation between the independent bi-unique transformations (of each of the sub-systems) imposed through additional similarity conditions (derived from the continuity of displacements and internal forces) can be respected.*

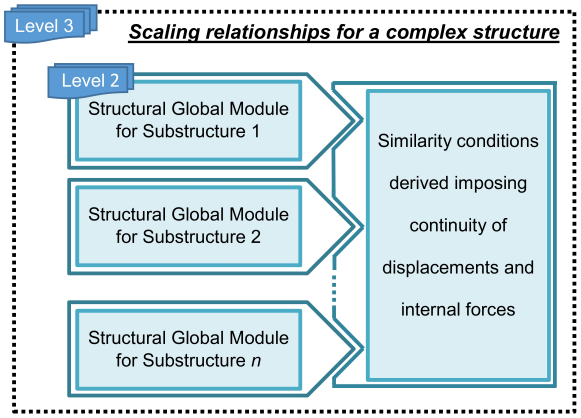

Figure 5.2.: Scaling relationships for a complex structure derived coupling the structural global modules of its n simple elements.

5.2. Structural global module for the generalized plate

A generalized plate is considered in this section, whose dimensions and coordinate system are depicted in figure 5.3.

5.2.1. Material and stacking sequence (MSS) module

Despite the lengthy mathematical deduction of the MSS module (available in B.1), from a practical viewpoint, the main conclusion to be retained is that to achieve the complete

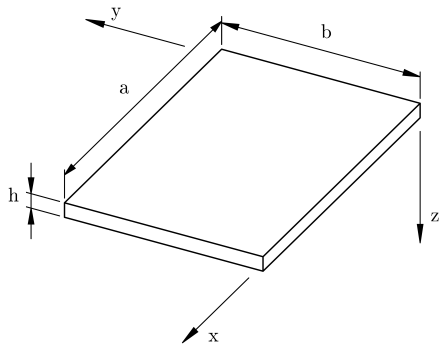

Figure 5.3.: Geometry and coordinate system of the generalized plate.

similitude between a model and a prototype made from different materials was seen to be either impossible or very unlikely to happen. Only two possible situations are considered in the following description of this methodology:

- **Complete similitude** can be used and therefore the model and prototypes are made of the same materials. When scaling laminated structures the stacking sequence and the number of plies are also to remain unchanged. All the scaling factors in this module are unitary:

$$\lambda_{E_i} = \lambda_{G_{ij}} = \lambda_{\nu_{ij}} = \lambda_\theta = \lambda_{Q_{ij}} = \lambda_{\bar{Q}_{ij}} = 1 \qquad \forall\, i,j$$

- **Partial similitude** has to be used, and therefore the ability to somehow predict or control the range of the error induced is needed.

5.2.2. Stress-strain relations (SSR) module

From the stress-strain relations (Reddy, 2004):

$$\begin{Bmatrix} \sigma_x \\ \sigma_y \\ \tau_{xy} \end{Bmatrix} = \begin{bmatrix} \overline{Q}_{11} & \overline{Q}_{12} & \overline{Q}_{16} \\ & \overline{Q}_{22} & \overline{Q}_{26} \\ sym & & \overline{Q}_{66} \end{bmatrix} \begin{Bmatrix} \epsilon_x \\ \epsilon_y \\ \gamma_{xy} \end{Bmatrix}$$

$$\begin{Bmatrix} \tau_{xz} \\ \tau_{yz} \end{Bmatrix} = \begin{bmatrix} \overline{Q}_{44} & \overline{Q}_{45} \\ \overline{Q}_{45} & \overline{Q}_{55} \end{bmatrix} \begin{Bmatrix} \gamma_{xz} \\ \gamma_{yz} \end{Bmatrix}$$

the following similarity conditions can be written:

$$\begin{aligned} \lambda_{\sigma_x} &= \lambda_{\bar{Q}_{11}}\lambda_{\epsilon_x} = \lambda_{\bar{Q}_{12}}\lambda_{\epsilon_y} = \lambda_{\bar{Q}_{16}}\lambda_{\gamma_{xy}} \\ \lambda_{\sigma_y} &= \lambda_{\bar{Q}_{12}}\lambda_{\epsilon_x} = \lambda_{\bar{Q}_{22}}\lambda_{\epsilon_y} = \lambda_{\bar{Q}_{26}}\lambda_{\gamma_{xy}} \\ \lambda_{\tau_{xy}} &= \lambda_{\bar{Q}_{16}}\lambda_{\epsilon_x} = \lambda_{\bar{Q}_{26}}\lambda_{\epsilon_y} = \lambda_{\bar{Q}_{66}}\lambda_{\gamma_{xy}} \end{aligned}$$

$$\begin{aligned} \lambda_{\tau_{xz}} &= \lambda_{\bar{Q}_{44}}\lambda_{\gamma_{xz}} = \lambda_{\bar{Q}_{45}}\lambda_{\gamma_{yz}} \\ \lambda_{\tau_{yz}} &= \lambda_{\bar{Q}_{45}}\lambda_{\gamma_{xz}} = \lambda_{\bar{Q}_{55}}\lambda_{\gamma_{yz}} \end{aligned}$$

which are equivalent to:

$$\lambda_{\sigma_x} = \lambda_{\bar{Q}_{11}} \lambda_{\epsilon_x} \tag{5.2a}$$
$$\lambda_{\sigma_y} = \lambda_{\bar{Q}_{22}} \lambda_{\epsilon_y} \tag{5.2b}$$
$$\lambda_{\tau_{xy}} = \lambda_{\bar{Q}_{66}} \lambda_{\gamma_{xy}} \tag{5.2c}$$
$$\lambda_{\tau_{xz}} = \lambda_{\bar{Q}_{44}} \lambda_{\gamma_{xz}} \tag{5.2d}$$
$$\lambda_{\tau_{yz}} = \lambda_{\bar{Q}_{55}} \lambda_{\gamma_{yz}} \tag{5.2e}$$
$$\lambda_{\bar{Q}_{11}} = \frac{\lambda_{\epsilon_y}}{\lambda_{\epsilon_x}} \lambda_{\bar{Q}_{12}} = \tag{5.2f}$$
$$= \frac{\lambda_{\gamma_{xy}}}{\lambda_{\epsilon_x}} \lambda_{\bar{Q}_{16}} = \tag{5.2g}$$
$$= \frac{\lambda_{\epsilon_y}^2}{\lambda_{\epsilon_x}^2} \lambda_{\bar{Q}_{22}} = \tag{5.2h}$$
$$= \frac{\lambda_{\epsilon_y}}{\lambda_{\epsilon_x}} \frac{\lambda_{\gamma_{xy}}}{\lambda_{\epsilon_x}} \lambda_{\bar{Q}_{26}} = \tag{5.2i}$$
$$= \frac{\lambda_{\gamma_{xy}}^2}{\lambda_{\epsilon_x}^2} \lambda_{\bar{Q}_{66}} \tag{5.2j}$$
$$\lambda_{\bar{Q}_{44}} = \frac{\lambda_{\gamma_{yz}}}{\lambda_{\gamma_{xz}}} \lambda_{\bar{Q}_{45}} = \tag{5.2k}$$
$$= \frac{\lambda_{\gamma_{yz}}^2}{\lambda_{\gamma_{xz}}^2} \lambda_{\bar{Q}_{55}} \tag{5.2l}$$

5.2.3. Strain-displacement relations (SDR) module

From the strain-displacement relations valid for small strains but moderate rotations (Reddy, 2004):

$$\epsilon_x = \frac{\partial u}{\partial x} + \frac{1}{2}\left(\frac{\partial w}{\partial x}\right)^2$$
$$\epsilon_y = \frac{\partial v}{\partial y} + \frac{1}{2}\left(\frac{\partial w}{\partial y}\right)^2$$
$$\gamma_{xy} = \frac{\partial u}{\partial y} + \frac{\partial v}{\partial x} + \frac{\partial w}{\partial x}\frac{\partial w}{\partial y}$$
$$\gamma_{xz} = \frac{\partial u}{\partial z} + \frac{\partial w}{\partial x}$$
$$\gamma_{yz} = \frac{\partial v}{\partial z} + \frac{\partial w}{\partial y}$$

applying the similitude theory to the linear terms it is possible to derive:

$$\lambda_{\epsilon_x} = \frac{\lambda_u}{\lambda_x} \tag{5.3a}$$

$$\lambda_{\epsilon_y} = \frac{\lambda_v}{\lambda_y} \tag{5.3b}$$

$$\lambda_{\gamma_{xy}} = \frac{\lambda_u}{\lambda_y} \tag{5.3c}$$

$$\lambda_{\gamma_{xy}} = \frac{\lambda_v}{\lambda_x} \implies \lambda_u \lambda_x = \lambda_v \lambda_y \tag{5.3d}$$

$$\lambda_{\gamma_{xz}} = \frac{\lambda_u}{\lambda_z} \tag{5.3e}$$

$$\lambda_{\gamma_{xz}} = \frac{\lambda_w}{\lambda_x} \implies \lambda_u \lambda_x = \lambda_w \lambda_z \tag{5.3f}$$

$$\lambda_{\gamma_{yz}} = \frac{\lambda_v}{\lambda_z} \tag{5.3g}$$

$$\lambda_{\gamma_{yz}} = \frac{\lambda_w}{\lambda_y} \implies \lambda_v \lambda_y = \lambda_w \lambda_z \tag{5.3h}$$

while from the non-linear terms the following conditions are obtained:

$$\lambda_u = \frac{\lambda_w^2}{\lambda_x} \tag{5.4a}$$

$$\lambda_v = \frac{\lambda_w^2}{\lambda_y} \implies \lambda_u \lambda_x = \lambda_v \lambda_y$$

5.2.4. Displacement field (DF) module

From the displacement field of the first-order shear deformation plate theory (Reddy, 2004):

$$\begin{aligned} u(x,y,z,t) &= u_0(x,y,t) + z\theta_y(x,y,t) \\ v(x,y,z,t) &= v_0(x,y,t) - z\theta_x(x,y,t) \\ w(x,y,z,t) &= w_0(x,y,t) \end{aligned}$$

one derives through the similitude theory:

$$\begin{aligned} \lambda_u &= \lambda_{u_0} \\ \lambda_v &= \lambda_{v_0} \\ \lambda_{\theta_y} &= \frac{\lambda_u}{\lambda_z} \\ \lambda_{\theta_x} &= \frac{\lambda_v}{\lambda_z} \end{aligned}$$

5.2.4.1. Comparison of the results obtained from the displacement field of the classical plate theory

Applying the similitude theory to the displacement field of the classical plate theory:

$$\begin{aligned} u(x,y,z,t) &= u_0(x,y,t) - z\frac{\partial w}{\partial x}(x,y,t) \\ v(x,y,z,t) &= v_0(x,y,t) - z\frac{\partial w}{\partial y}(x,y,t) \\ w(x,y,z,t) &= w_0(x,y,t) \end{aligned}$$

the similarity conditions would be:

$$\begin{aligned} \lambda_u &= \lambda_{u_0} \\ \lambda_v &= \lambda_{v_0} \\ \lambda_w &= \frac{\lambda_u}{\lambda_z}\lambda_x \\ \lambda_w = \frac{\lambda_v}{\lambda_z}\lambda_y \implies \lambda_u\lambda_x &= \lambda_v\lambda_y \end{aligned}$$

Through the classical plate theory the last two conditions would be derived here in the DF module, while applying a first-order theory they were already derived in the SDR module, applying the similitude theory to the γ_{xz} and γ_{yz} strain components. It should therefore be noted that, through a first-order theory, besides the scaling relationships obtained from the classical plate theory, some additional scaling laws are obtained for variables that were either neglected or substituted in the latter, such as: $\lambda_{\tau_{xz}}, \lambda_{\gamma_{xz}}, \lambda_{\tau_{yz}}, \lambda_{\gamma_{yz}}, \lambda_{\theta_x}, \lambda_{\theta_y}$. This was expected since the thin-plate theory can be derived as a particular case of the thick-plate theory.

5.2.5. Force and moment resultants (FMR) module

The internal force and moment resultants in a differential $dxdy$ plate element are depicted in figure 5.4; although they act all simultaneously on the same element, three sub-figures were used for the sake of simplicity.

From the definition of force and moment resultants (Ashton and Whitney, 1970; Reddy, 2004):

$$\begin{Bmatrix} N_x \\ N_y \\ N_{xy} \end{Bmatrix} = \int_{-h/2}^{h/2} \begin{Bmatrix} \sigma_x \\ \sigma_y \\ \tau_{xy} \end{Bmatrix} dz$$

$$\begin{Bmatrix} M_x \\ M_y \\ M_{xy} \end{Bmatrix} = \int_{-h/2}^{h/2} \begin{Bmatrix} \sigma_x \\ \sigma_y \\ \tau_{xy} \end{Bmatrix} z\, dz$$

$$\begin{Bmatrix} Q_x \\ Q_y \end{Bmatrix} = k \int_{-h/2}^{h/2} \begin{Bmatrix} \tau_{xz} \\ \tau_{yz} \end{Bmatrix} dz$$

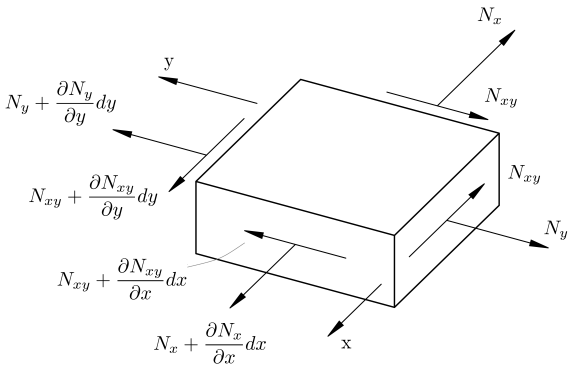

(a) In-plane forces.

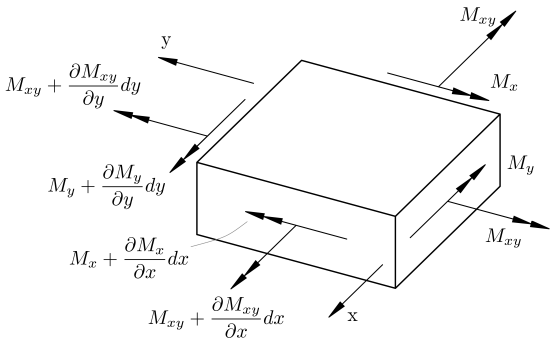

(b) Moments.

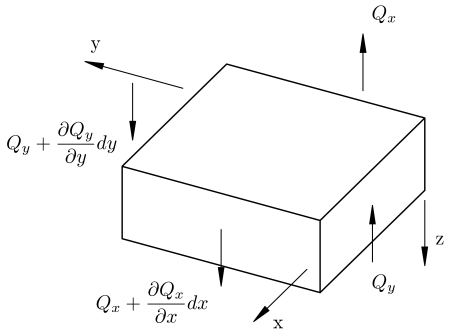

(c) Lateral forces.

Figure 5.4.: Internal force and moment resultants on a differential plate element.

their scaling factors are written as follows:

$$\begin{aligned}
\lambda_{N_x} &= \lambda_{\sigma_x} \lambda_z \\
\lambda_{N_y} &= \lambda_{\sigma_y} \lambda_z \\
\lambda_{N_{xy}} &= \lambda_{\tau_{xy}} \lambda_z \\
\lambda_{Q_x} &= \lambda_k \lambda_{\tau_{xz}} \lambda_z \\
\lambda_{Q_y} &= \lambda_k \lambda_{\tau_{yz}} \lambda_z \\
\lambda_{M_x} &= \lambda_{\sigma_x} \lambda_z^2 \\
\lambda_{M_y} &= \lambda_{\sigma_y} \lambda_z^2 \\
\lambda_{M_{xy}} &= \lambda_{\tau_{xy}} \lambda_z^2
\end{aligned}$$

5.2.6. Equations of motion (EM) module

The non-linear equations of motion (B.5) and (B.6) rewritten below:

$$\frac{\partial N_x}{\partial x} + \frac{\partial N_{xy}}{\partial y} + q_x = \int_{-\frac{h}{2}}^{\frac{h}{2}} (\rho_0 \frac{\partial^2 u}{\partial t^2}) dz$$

$$\frac{\partial N_{xy}}{\partial x} + \frac{\partial N_y}{\partial y} + q_y = \int_{-\frac{h}{2}}^{\frac{h}{2}} (\rho_0 \frac{\partial^2 v}{\partial t^2}) dz$$

$$N_x\frac{\partial^2 w}{\partial x^2}+2N_{yx}\frac{\partial^2 w}{\partial x\partial y}+N_y\frac{\partial^2 w}{\partial y^2}+\frac{\partial Q_x}{\partial x}+\frac{\partial Q_y}{\partial y}+$$
$$+\frac{\partial w}{\partial y}(\frac{\partial N_y}{\partial y}+\frac{\partial N_{xy}}{\partial x})+\frac{\partial w}{\partial x}(\frac{\partial N_x}{\partial x}+\frac{\partial N_{yx}}{\partial y})+q_z=\int_{-\frac{h}{2}}^{\frac{h}{2}}(\rho_0\frac{\partial^2 w}{\partial t^2})dz$$

$$\frac{\partial M_x}{\partial x}+\frac{\partial M_{xy}}{\partial y}-Q_x+m_x=\int_{-\frac{h}{2}}^{\frac{h}{2}}(z\rho_0\frac{\partial^2 u}{\partial t^2})dz$$

$$\frac{\partial M_{xy}}{\partial x}+\frac{\partial M_y}{\partial y}-Q_y+m_y=\int_{-\frac{h}{2}}^{\frac{h}{2}}(z\rho_0\frac{\partial^2 v}{\partial t^2})dz$$

yield the following similarity conditions, from the linear terms:

$$\lambda_{N_x}=\lambda_{N_{xy}}\frac{\lambda_x}{\lambda_y}$$
$$\lambda_{N_y}=\lambda_{N_{xy}}\frac{\lambda_y}{\lambda_x}$$
$$\lambda_{M_x}=\lambda_{M_{xy}}\frac{\lambda_x}{\lambda_y}$$
$$\lambda_{M_y}=\lambda_{M_{xy}}\frac{\lambda_y}{\lambda_x}$$
$$\lambda_{Q_x}=\frac{\lambda_{M_x}}{\lambda_x}$$
$$\lambda_{Q_y}=\frac{\lambda_{M_y}}{\lambda_y}$$
$$\lambda_{q_x}=\frac{\lambda_{N_x}}{\lambda_x}$$
$$\lambda_{q_y}=\frac{\lambda_{N_y}}{\lambda_y}$$
$$\lambda_{q_z}=\frac{\lambda_{Q_x}}{\lambda_x}$$
$$\lambda_{m_x}=\frac{\lambda_{M_x}}{\lambda_x}$$
$$\lambda_{m_y}=\frac{\lambda_{M_y}}{\lambda_y}$$
$$\frac{\lambda_u}{\lambda_t^2}=\frac{\lambda_{q_x}}{\lambda_{\rho_0}\lambda_z}$$
$$\frac{\lambda_v}{\lambda_t^2}=\frac{\lambda_{q_y}}{\lambda_{\rho_0}\lambda_z}$$
$$\frac{\lambda_w}{\lambda_t^2}=\frac{\lambda_{q_z}}{\lambda_{\rho_0}\lambda_z}$$
$$\frac{\lambda_u}{\lambda_t^2}=\frac{\lambda_{m_x}}{\lambda_{\rho_0}\lambda_z^2}$$
$$\frac{\lambda_v}{\lambda_t^2}=\frac{\lambda_{m_y}}{\lambda_{\rho_0}\lambda_z^2}$$

and from the non-linear terms:

$$\lambda_{Q_x} = \frac{\lambda_w}{\lambda_x}\lambda_{N_x}$$
$$\lambda_{Q_x} = \frac{\lambda_x}{\lambda_y}\lambda_{Q_y}$$

5.2.7. Complete similitude

From the MSS module, for complete similitude, the scaling factors for the reduced stiffnesses are unitary:

$$\lambda_{\bar{Q}_{ij}} = 1$$

Therefore from equations (5.2) on the SSR module the following similarity conditions are obtained:

$$\lambda_\epsilon = \lambda_{\epsilon_x} = \lambda_{\epsilon_y} = \lambda_{\gamma_{xy}}$$
$$\lambda_\sigma = \lambda_{\sigma_x} = \lambda_{\sigma_y} = \lambda_{\tau_{xy}}$$
$$\lambda_\sigma = \lambda_\epsilon$$

$$\lambda_\gamma = \lambda_{\gamma_{xz}} = \lambda_{\gamma_{yz}}$$
$$\lambda_\tau = \lambda_{\tau_{xz}} = \lambda_{\tau_{yz}}$$
$$\lambda_\tau = \lambda_\gamma$$

Introducing the SDR module and considering any of the following ratios derived from equations (5.3):

$$\frac{\lambda_{\gamma_{xy}}}{\lambda_{\epsilon_x}} = \frac{\lambda_x}{\lambda_u}\frac{\lambda_v}{\lambda_x} = \frac{\lambda_x}{\lambda_u}\frac{\lambda_u}{\lambda_y} = \frac{\lambda_x}{\lambda_y}$$
$$\frac{\lambda_{\epsilon_y}}{\lambda_{\gamma_{xy}}} = \frac{\lambda_v}{\lambda_y}\frac{\lambda_x}{\lambda_v} = \frac{\lambda_v}{\lambda_y}\frac{\lambda_y}{\lambda_u} = \frac{\lambda_x}{\lambda_y}$$

it is concluded that:

$$\lambda_x = \lambda_y$$

In turn equation (5.3d) yield:

$$\lambda_u = \lambda_v$$

and from equation (5.3f) the scaling law for the transverse displacement is obtained:

$$\lambda_w = \frac{\lambda_u \lambda_x}{\lambda_z}$$

Additionally the equation (5.4a) is rewritten as:

$$\lambda_w^2 = \lambda_u \lambda_x \tag{5.5}$$

allowing to concluded that for non-linear analysis the following condition has to be respected:

$$\lambda_w = \lambda_z$$

The scaling laws from the DF module remain unchanged. On the other hand, from the FMR module the scaling factors for the force and moment resultants for complete similitude are written as follows:

$$\lambda_N = \lambda_{N_x} = \lambda_{N_y} = \lambda_{N_{xy}} = \lambda_\sigma \lambda_z$$
$$\lambda_M = \lambda_{M_x} = \lambda_{M_y} = \lambda_{M_{xy}} = \lambda_\sigma \lambda_z^2$$
$$\lambda_Q = \lambda_{Q_x} = \lambda_{Q_y} = \lambda_\sigma \lambda_z = \lambda_N$$

Finally from the EM module, the scaling factors for the external loads are:

$$\lambda_q = \lambda_{q_x} = \lambda_{q_y} = \lambda_{q_z} = \frac{\lambda_N}{\lambda_x}$$
$$\lambda_m = \lambda_{m_x} = \lambda_{m_y} = \frac{\lambda_M}{\lambda_x}$$

For dynamic analysis it is derived the condition:

$$\lambda_{\ddot{u}} = \lambda_{\ddot{v}} = \lambda_{\ddot{w}} = \frac{\lambda_q}{\lambda_{\rho_0} \lambda_z}$$

which implies the following conditions for time and displacements:

$$\lambda_t^2 = \frac{\lambda_{\rho_0}}{\lambda_q} \lambda_u \lambda_z$$
$$\lambda_w = \lambda_u = \lambda_v \tag{5.6a}$$

If equation (5.6a) applies, then considering the equation (5.5):

$$\lambda_x = \lambda_y = \lambda_z$$

and for dynamic non-linear analysis an even more restrictive similarity condition is derived:

$$\lambda_x = \lambda_y = \lambda_z = \lambda_u = \lambda_v = \lambda_w$$

5.3. Structural global module for the generalized beam

A generalized beam is considered in this section, whose dimensions and coordinate system are depicted in figure 5.5.

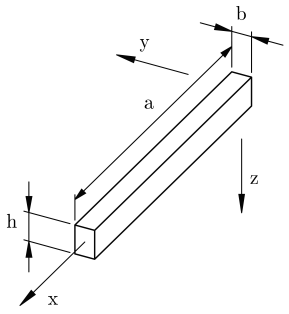

Figure 5.5.: Geometry and coordinate system of the generalized beam.

5.3.1. Material and stacking sequence (MSS) module

The scaling relationships from the MSS module derived to plates are directly applicable to beams.

5.3.2. Stress-strain relations (SSR) module

For a general (narrow) laminated beam, recurring either to a classical or first-shear deformation theory, the strains ϵ_y and γ_{yz} are zero. However, the stresses σ_y and τ_{yz} may be nonzero due to the shear coupling ($\overline{Q}_{16}$ and $\overline{Q}_{26}$) and/or to the Poisson's ratio effect ($\overline{Q}_{12}$), or even to the ply orientation ($\overline{Q}_{45}$).

Inverting the stress-strain relations (5.1), removing the negligible strains and inverting again, the following stress-strain relations are derived, as presented by Zhang et al. (2011):

$$\begin{Bmatrix} \sigma_x \\ \tau_{xy} \end{Bmatrix} = \begin{bmatrix} \overline{Q}_{11} - \dfrac{\overline{Q}_{12}^2}{\overline{Q}_{22}} & \overline{Q}_{16} - \dfrac{\overline{Q}_{12}\overline{Q}_{26}}{\overline{Q}_{22}} \\ \overline{Q}_{16} - \dfrac{\overline{Q}_{12}\overline{Q}_{26}}{\overline{Q}_{22}} & \overline{Q}_{66} - \dfrac{\overline{Q}_{26}^2}{\overline{Q}_{22}} \end{bmatrix} \begin{Bmatrix} \epsilon_x \\ \gamma_{xy} \end{Bmatrix} \tag{5.7a}$$

$$\tau_{xz} = \left(\overline{Q}_{55} - \frac{\overline{Q}_{45}^2}{\overline{Q}_{44}} \right) \gamma_{xz} \tag{5.7b}$$

the following similarity conditions can be derived:

$$\begin{aligned} \lambda_{\sigma_x} &= \lambda_{\left(\overline{Q}_{11} - \frac{\overline{Q}_{12}^2}{\overline{Q}_{22}}\right)} \lambda_{\epsilon_x} &&= \lambda_{\left(\overline{Q}_{16} - \frac{\overline{Q}_{12}\overline{Q}_{26}}{\overline{Q}_{22}}\right)} \lambda_{\gamma_{xy}} \\ \lambda_{\tau_{xy}} &= \lambda_{\left(\overline{Q}_{16} - \frac{\overline{Q}_{12}\overline{Q}_{26}}{\overline{Q}_{22}}\right)} \lambda_{\epsilon_x} &&= \lambda_{\left(\overline{Q}_{66} - \frac{\overline{Q}_{26}^2}{\overline{Q}_{22}}\right)} \lambda_{\gamma_{xy}} \\ \lambda_{\tau_{xz}} &= \lambda_{\left(\overline{Q}_{55} - \frac{\overline{Q}_{45}^2}{\overline{Q}_{44}}\right)} \lambda_{\gamma_{xz}} \end{aligned}$$

which are equivalent to:

$$\lambda_{\sigma_x} = \lambda_{\bar{Q}_{11}} \lambda_{\epsilon_x} \tag{5.8a}$$

$$\lambda_{\tau_{xy}} = \lambda_{\bar{Q}_{66}} \lambda_{\gamma_{xy}} \tag{5.8b}$$

$$\lambda_{\tau_{xz}} = \lambda_{\bar{Q}_{55}} \lambda_{\gamma_{xz}} \tag{5.8c}$$

$$\lambda_{\bar{Q}_{11}} = \frac{\lambda_{\gamma_{xy}}}{\lambda_{\epsilon_x}} \qquad \lambda_{\bar{Q}_{16}} \tag{5.8d}$$

$$= \frac{\lambda_{\gamma_{xy}}^2}{\lambda_{\epsilon_x}^2} \qquad \lambda_{\bar{Q}_{66}} \tag{5.8e}$$

$$\lambda_{\bar{Q}_{12}} = \frac{\lambda_{\gamma_{xy}}}{\lambda_{\epsilon_x}} \qquad \lambda_{\bar{Q}_{26}} \tag{5.8f}$$

$$\lambda_{\bar{Q}_{11}} \lambda_{\bar{Q}_{22}} = \lambda_{\bar{Q}_{12}}^2 \tag{5.8g}$$

$$\lambda_{\bar{Q}_{44}} \lambda_{\bar{Q}_{55}} = \lambda_{\bar{Q}_{45}}^2 \tag{5.8h}$$

It is worth noting that indeed the similarity conditions (5.8) could have been derived from those (5.2) obtained for the plate analysis. However, it is not as straightforward as

simply ignoring all the conditions containing scaling factors of non-relevant parameters; in this case, for example, the higher order non-redundant system of equations without the following scaling factors: λ_{ϵ_y}, $\lambda_{\gamma_{yz}}$, λ_{σ_y}, $\lambda_{\tau_{yz}}$ has to be obtained.

5.3.2.1. Isotropic beam analysis

Note that replacing in equation (5.7) the expressions for the reduced stiffnesses given in B.1, with $\theta = 0$, the following known stress-strain relation for isotropic material is obtained:

$$\begin{Bmatrix} \sigma_x \\ \tau_{xy} \\ \tau_{xz} \end{Bmatrix} = \begin{bmatrix} E & 0 & 0 \\ 0 & G & 0 \\ 0 & 0 & G \end{bmatrix} \begin{Bmatrix} \epsilon_x \\ \gamma_{xy} \\ \gamma_{xz} \end{Bmatrix}$$

The derived scaling relationships are the following:

$$\begin{aligned} \lambda_{\sigma_x} &= \lambda_E \lambda_{\epsilon_x} \\ \lambda_{\tau_{xy}} &= \lambda_G \lambda_{\gamma_{xy}} \\ \lambda_{\tau_{xz}} &= \lambda_G \lambda_{\gamma_{xz}} \end{aligned}$$

5.3.2.2. Stiffener analysis

For a stiffener element disposed along the x axis subjected only to bending in the xz plane only the ϵ_x and γ_{xz} strain components are considered. Through the same procedure previously referred to derive the stress-strain relations for general beams, it is possible to obtain the following relations:

$$\begin{aligned} \{\sigma_x\} &= \left[\ \widetilde{Q}_{11} \ \right] \{\epsilon_x\} \\ \{\tau_{xz}\} &= \left[\ \widetilde{Q}_{55} \ \right] \{\gamma_{xz}\} \end{aligned}$$

with:

$$\begin{aligned} \widetilde{Q}_{11} &= \overline{Q}_{11} + \frac{2\,\overline{Q}_{16}\overline{Q}_{12}\overline{Q}_{26} - \overline{Q}_{16}^2\overline{Q}_{22} - \overline{Q}_{12}^2\overline{Q}_{66}}{\overline{Q}_{22}\overline{Q}_{66} - \overline{Q}_{26}^2} \\ \widetilde{Q}_{55} &= \overline{Q}_{55} - \frac{\overline{Q}_{45}^2}{\overline{Q}_{44}} \end{aligned}$$

Therefore, applying the similitude theory to these equations, it is concluded that the following similitude conditions have to be respected:

$$\begin{aligned} \lambda_{\sigma_x} &= \lambda_{\bar{Q}_{11}} \lambda_{\epsilon_x} \\ \lambda_{\tau_{xz}} &= \lambda_{\bar{Q}_{55}} \lambda_{\gamma_{xz}} \\ \lambda_{\bar{Q}_{11}} \lambda_{\bar{Q}_{22}} &= \lambda_{\bar{Q}_{12}}^2 \\ \frac{\lambda_{\bar{Q}_{11}} \lambda_{\bar{Q}_{26}}^2}{\lambda_{\bar{Q}_{66}}} &= \lambda_{\bar{Q}_{12}}^2 \\ \lambda_{\bar{Q}_{11}} \lambda_{\bar{Q}_{66}} &= \lambda_{\bar{Q}_{16}}^2 \\ \lambda_{\bar{Q}_{12}} \lambda_{\bar{Q}_{16}} &= \lambda_{\bar{Q}_{11}} \lambda_{\bar{Q}_{26}} \end{aligned}$$

which once again could be obtained from those for the plate analysis (5.2), by obtaining the higher order non-redundant system of equations without the following scaling factors: λ_{ϵ_y}, $\lambda_{\gamma_{xy}}$, $\lambda_{\gamma_{yz}}$, λ_{σ_y}, $\lambda_{\tau_{xy}}$, $\lambda_{\tau_{yz}}$.

5.3.3. Strain-displacement relations (SDR) module

Geometrically non-linear deformation is considered and the following non-zero strain components derived from Green's strain tensor (Reddy, 2004):

$$\begin{aligned}
\epsilon_x &= \frac{\partial u}{\partial x} + \overbrace{\frac{1}{2}\left(\frac{\partial u}{\partial x}\right)^2}^{\approx 0} + \frac{1}{2}\left(\frac{\partial v}{\partial x}\right)^2 + \frac{1}{2}\left(\frac{\partial w}{\partial x}\right)^2 \\
\gamma_{xy} &= \frac{\partial u}{\partial y} + \frac{\partial v}{\partial x} + \frac{\partial u}{\partial x}\frac{\partial u}{\partial y} + \overbrace{\frac{\partial v}{\partial x}\frac{\partial v}{\partial y}}^{\approx 0} + \frac{\partial w}{\partial x}\frac{\partial w}{\partial y} \\
\gamma_{xz} &= \frac{\partial u}{\partial z} + \frac{\partial w}{\partial x} + \frac{\partial u}{\partial x}\frac{\partial u}{\partial z} + \frac{\partial v}{\partial x}\frac{\partial v}{\partial z} + \overbrace{\frac{\partial w}{\partial x}\frac{\partial w}{\partial z}}^{\approx 0} \\
\epsilon_y &= \epsilon_z = \gamma_{yz} \approx 0
\end{aligned}$$

The torsion is assumed small enough such that ϵ_y and ϵ_z are negligible (Fonseca and Ribeiro, 2006). Depending on the displacement field, this is equivalent to argue that $\frac{\partial v}{\partial y} \approx 0$ and $\frac{\partial w}{\partial z} \approx 0$, for example, such as Sharf (1996) did. In doing so, in each shear strain one non-linear term is usually neglected as indicated in the previous equations (Fonseca and Ribeiro, 2006; Sapountzakis and Dourakopoulos, 2008; Sharf, 1996); besides the quadratic term in u can be neglected without significantly change the results, as demonstrated by Stoykov and Ribeiro (2010).

From the non-negligible terms, it is concluded through the similitude theory that:

- For **uniaxial bending** (on plane xz), in a linear analysis:

$$\begin{aligned}
\lambda_{\epsilon_x} &= \frac{\lambda_u}{\lambda_x} \\
\lambda_{\gamma_{xz}} &= \frac{\lambda_w}{\lambda_x} \\
\lambda_{\gamma_{xz}} = \frac{\lambda_u}{\lambda_z} &\implies \lambda_u \lambda_x = \lambda_w \lambda_z \qquad (5.9a)
\end{aligned}$$

  and also, for moderate rotations (longitudinal geometric non-linear analysis):

$$\lambda_u = \frac{\lambda_w^2}{\lambda_x} \qquad (5.10a)$$

$$\lambda_{\gamma_{xz}} = \frac{\lambda_u^2}{\lambda_x \lambda_z} \implies \lambda_x = \lambda_u \qquad (5.10b)$$

- Additionally for **biaxial bending** (on plane xz and xy), besides the previous condi-

tions, in a linear analysis, it has to be respected:

$$\lambda_{\gamma_{xy}} = \frac{\lambda_u}{\lambda_y}$$
$$\lambda_{\gamma_{xy}} = \frac{\lambda_v}{\lambda_x} \implies \lambda_u \lambda_x = \lambda_v \lambda_y$$

and for moderate rotations (longitudinal geometric non-linear analysis):

$$\lambda_u = \frac{\lambda_v^2}{\lambda_x}$$
$$\lambda_{\gamma_{xy}} = \frac{\lambda_u^2}{\lambda_x \lambda_y} \implies \lambda_x = \lambda_u \quad \equiv (5.10\text{b})$$

- Alternatively, for **torsion** it is applied the similarity conditions:

$$\lambda_{\gamma_{xy}} = \frac{\lambda_v}{\lambda_x}$$
$$\lambda_{\gamma_{xz}} = \frac{\lambda_w}{\lambda_x}$$

which are included in those of the biaxial loading, but not in the uniaxial bending.

And, for non-linear analysis:

$$\lambda_{\gamma_{xy}} = \frac{\lambda_w^2}{\lambda_x \lambda_y} \implies \lambda_w^2 = \lambda_v \lambda_y$$
$$\lambda_{\gamma_{xz}} = \frac{\lambda_v^2}{\lambda_x \lambda_z} \implies \lambda_v^2 = \lambda_w \lambda_z$$

Note that, considering the negligible terms in the shear strains, additionally for non-linear torsion the following expressions would have been derived:

$$\lambda_{\gamma_{xy}} = \frac{\lambda_v^2}{\lambda_x \lambda_y} \implies \lambda_y = \lambda_v \tag{5.11a}$$
$$\lambda_{\gamma_{xz}} = \frac{\lambda_w^2}{\lambda_x \lambda_z} \implies \lambda_z = \lambda_w \tag{5.11b}$$

5.3.4. Displacement field (DF) module

Considering Timoshenko's theory for flexure and Saint-Venant's for torsion, the non-linear displacement field is written as (Stoykov and Ribeiro, 2010):

$$u(x,y,z,t) = u_0(x,t) + z\theta_y(x,t) - y\theta_z(x,t) + \psi(y,z)\frac{\partial \theta_x}{\partial x}(x,t)$$
$$v(x,y,z,t) = v_0(x,t) + y\cos(\theta_x(x,t)) - y - z\sin(\theta_x(x,t))$$
$$w(x,y,z,t) = w_0(x,t) + y\sin(\theta_x(x,t)) + z\cos(\theta_x(x,t)) - z$$

where θ_x, θ_y, θ_z denote rotation of the cross section about the axis indicated in subscript, and ψ is the warping function.

Regarding the warping component, it should be noted that cross section of a circular bar or a circular hollow section will remain plane, as a result of twisting but all other sections

will experience warping of the cross section, depending on the geometry of the cross section. The warping of solid, hollow, angle, tee and cruciform sections is generally very small and can be neglected. However, the warping of open double-flanged sections, such as an I or UPN section is much more significant, essentially due to the effect of the counter rotation of the flanges in their planes (Hughes et al., 2011).

The scaling relationships derived in this section are for beams where the warping effects are negligible. Given this, through the common approximation: $\sin(\theta_x) \approx \theta_x$ and $\cos(\theta_x) \approx 1$, only valid for small angles of rotation (Stoykov and Ribeiro, 2010), the previous displacement field can be rewritten as (Fonseca and Ribeiro, 2006):

$$\begin{aligned} u &= u_0(x,t) + z\theta_y(x,t) - y\theta_z(x,t) \\ v &= v_0(x,t) - z\theta_x(x,t) \\ w &= w_0(x,t) + y\theta_x(x,t) \end{aligned}$$

Applying the similitude theory, it is conclude that the scaling relationships to be respected are the following:

- For **uniaxial bending** (on plane xz):

$$\begin{aligned} \lambda_u &= \lambda_{u_0} \\ \lambda_u &= \lambda_z \lambda_{\theta_y} \\ \lambda_w &= \lambda_{w_0} \end{aligned}$$

- And additionally, for **biaxial bending** (on plane xz and xy):

$$\begin{aligned} \lambda_u &= \lambda_y \lambda_{\theta_z} \\ \lambda_v &= \lambda_{v_0} \end{aligned}$$

- Or alternatively, if **torsion** exists, the additional conditions to respect are:

$$\lambda_v = \lambda_z \lambda_{\theta_x} \implies \begin{aligned} \lambda_w &= \lambda_y \lambda_{\theta_x} \\ \lambda_v \lambda_y &= \lambda_w \lambda_z \end{aligned}$$

Once again, note that considering the displacement field with non-linearized trigonometric functions, for non-linear torsion the following expressions would have been derived:

$$\begin{aligned} \lambda_y &= \lambda_v \quad \equiv (5.11a) \\ \lambda_z &= \lambda_w \quad \equiv (5.11b) \\ \lambda_{\theta_x} &= 1 \end{aligned}$$

5.3.5. Force and moment resultants (FMR) module

The internal force and moment resultants in a differential dx beam element are depicted in figure 5.6.

The superscript ^{beam} will be used to keep in mind that the following scaling factors are relative to force and moment resultants on beams, because the standard nomenclature may be the same as that used for plates, but with different meaning. For example, λ_{N_x} and $\lambda_{N_x}^{beam}$ are both for the resultant force in the x direction, in a section yz. But, for example, for the transverse force resultant in the z direction, in a section yz, the scaling factors λ_{Q_x} and $\lambda_{Q_z}^{beam}$ are used, respectively for the plate and for the beam.

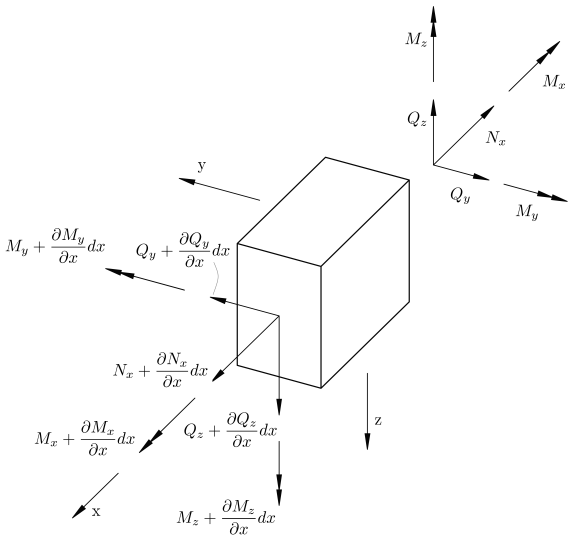

Figure 5.6.: Internal force and moment resultants on a differential beam element.

Integrating over the cross section the stresses defined by equation (5.7), yields the force and moment resultants for a general beam:

$$\left[N_x^{beam}, M_y^{beam}, M_z^{beam}\right] = \int [1, z, y]\, \sigma_x \, dA$$
$$\left[Q_y^{beam}, Q_z^{beam}\right] = k \int [\tau_{xy}, \tau_{xz}]\, dA$$
$$M_x^{beam} = \int (z\, \tau_{xy} + y\, \tau_{xz})\, dA$$

And, through the similitude theory, the following scaling relationships are obtained:

- For **uniaxial bending** (on the plane xz):

$$\lambda_{N_x}^{beam} = \lambda_y \lambda_{\sigma_x} \lambda_z \tag{5.12a}$$
$$\lambda_{M_y}^{beam} = \lambda_y \lambda_{\sigma_x} \lambda_z^2 \tag{5.12b}$$
$$\lambda_{Q_z}^{beam} = \lambda_k \lambda_y \lambda_{\tau_{xz}} \lambda_z \tag{5.12c}$$

- And additionally, for **biaxial bending** (on the planes xz and xy):

$$\lambda_{M_z}^{beam} = \lambda_y^2 \lambda_{\sigma_x} \lambda_z$$
$$\lambda_{Q_y}^{beam} = \lambda_k \lambda_y \lambda_{\tau_{xy}} \lambda_z$$

- And additionally, if the beam is subjected to **torsion**:

$$\lambda_{M_x}^{beam} = \lambda_y \lambda_{\tau_{xy}} \lambda_z^2$$
$$\lambda_{M_x}^{beam} = \lambda_y^2 \lambda_{\tau_{xz}} \lambda_z \implies \lambda_{\tau_{xz}} = \lambda_{\tau_{xy}} \frac{\lambda_z}{\lambda_y}$$

5.3.6. Equations of motion (EM) module

The non-linear equations of motion (B.7) and (B.8) rewritten below:

$$\frac{\partial N_x}{\partial x}^{beam} + q_x^{beam} = \int_A \left(\rho_0 \frac{\partial^2 u}{\partial t^2}\right) dA$$

$$\frac{\partial^2 v_0}{\partial x^2} N_x^{beam} + \frac{\partial v_0}{\partial x}\frac{\partial N_x}{\partial x}^{beam} + \frac{\partial Q_y}{\partial x}^{beam} + q_y^{beam} = \int_A \left(\rho_0 \frac{\partial^2 v}{\partial t^2}\right) dA$$

$$\frac{\partial^2 w}{\partial x^2} N_x^{beam} + \frac{\partial w}{\partial x}\frac{\partial N_x}{\partial x}^{beam} + \frac{\partial Q_z}{\partial x}^{beam} + q_z^{beam} = \int_A \left(\rho_0 \frac{\partial^2 w}{\partial t^2}\right) dA$$

$$\frac{\partial M_y}{\partial x}^{beam} - Q_z^{beam} + m_y^{beam} = \int_A \left(z\ \rho_0 \frac{\partial^2 u}{\partial t^2}\right) dA$$

$$\frac{\partial M_z}{\partial x}^{beam} - Q_y^{beam} + m_z^{beam} = \int_A \left(y\ \rho_0 \frac{\partial^2 u}{\partial t^2}\right) dA$$

$$\frac{\partial M_x}{\partial x}^{beam} - Q_y^{beam}\frac{\partial w}{\partial x} - Q_z^{beam}\frac{\partial v}{\partial x} + m_x^{beam} = \int_A \rho_0 \left(y\frac{\partial^2 w}{\partial t^2} + z\frac{\partial^2 v}{\partial t^2}\right) dA$$

yield the following similarity conditions from the linear terms:

$$\lambda_{Q_y}^{beam} = \frac{\lambda_{M_z}^{beam}}{\lambda_x} \tag{5.13a}$$

$$\lambda_{Q_z}^{beam} = \frac{\lambda_{M_y}^{beam}}{\lambda_x} \tag{5.13b}$$

$$\lambda_{q_x}^{beam} = \frac{\lambda_{N_x}^{beam}}{\lambda_x}$$

$$\lambda_{q_y}^{beam} = \frac{\lambda_{Q_y}^{beam}}{\lambda_x}$$

$$\lambda_{q_z}^{beam} = \frac{\lambda_{Q_z}^{beam}}{\lambda_x}$$

$$\lambda_{m_x}^{beam} = \frac{\lambda_{M_x}^{beam}}{\lambda_x}$$

$$\lambda_{m_y}^{beam} = \frac{\lambda_{M_y}^{beam}}{\lambda_x}$$

$$\lambda_{m_z}^{beam} = \frac{\lambda_{M_z}^{beam}}{\lambda_x}$$

$$\frac{\lambda_u}{\lambda_t^2} = \frac{1}{\lambda_y}\frac{\lambda_{q_x}^{beam}}{\lambda_{\rho_0}\lambda_z}$$
$$\frac{\lambda_v}{\lambda_t^2} = \frac{1}{\lambda_y}\frac{\lambda_{q_y}^{beam}}{\lambda_{\rho_0}\lambda_z}$$
$$\frac{\lambda_w}{\lambda_t^2} = \frac{1}{\lambda_y}\frac{\lambda_{q_z}^{beam}}{\lambda_{\rho_0}\lambda_z}$$
$$\frac{\lambda_u}{\lambda_t^2} = \frac{1}{\lambda_y}\frac{\lambda_{m_y}^{beam}}{\lambda_z^2\ \lambda_{\rho_0}}$$
$$\frac{\lambda_u}{\lambda_t^2} = \frac{1}{\lambda_y^2}\frac{\lambda_{m_z}^{beam}}{\lambda_z\ \lambda_{\rho_0}}$$
$$\frac{\lambda_v}{\lambda_t^2} = \frac{1}{\lambda_y}\frac{\lambda_{m_x}^{beam}}{\lambda_z^2\ \lambda_{\rho_0}}$$
$$\frac{\lambda_w}{\lambda_t^2} = \frac{1}{\lambda_y^2}\frac{\lambda_{m_x}^{beam}}{\lambda_z\ \lambda_{\rho_0}}$$

and from the non-linear terms:

$$\lambda_{Q_y}^{beam} = \lambda_{v_0}\frac{\lambda_{N_x}^{beam}}{\lambda_x}$$
$$\lambda_{Q_z}^{beam} = \lambda_{w}\frac{\lambda_{N_x}^{beam}}{\lambda_x}$$
$$\lambda_{M_x}^{beam} = \lambda_w\lambda_{Q_y}^{beam}$$
$$\lambda_{M_x}^{beam} = \lambda_v\lambda_{Q_z}^{beam}$$

5.3.7. Complete similitude

When establishing the structural similitude for a beam, several options may exist inside each of the modules when combining them, depending, for example, on the material properties or on the loadings acting on the beam. Any combination is possible as long as the assumptions keep valid for the structure and consistent between modules.

5.3.7.1. Laminated beam subjected to uniaxial bending

From the MSS module, for complete similitude, the scaling factors for the reduced stiffnesses are unitary:

$$\lambda_{\bar{Q}_{ij}} = 1$$

Therefore from equations (5.8) on the SSR module:

$$\lambda_\epsilon = \lambda_{\epsilon_x} = \lambda_{\gamma_{xy}}$$
$$\lambda_\sigma = \lambda_{\sigma_x} = \lambda_{\tau_{xy}}$$
$$\lambda_\sigma = \lambda_\epsilon$$

$$\lambda_\gamma = \lambda_{\gamma_{xz}}$$
$$\lambda_\tau = \lambda_{\tau_{xz}}$$
$$\lambda_\tau = \lambda_\gamma$$

Introducing the SDR module, for uniaxial bending, the similarity condition for the strains is firstly established:

$$\lambda_{\epsilon_x} = \frac{\lambda_u}{\lambda_x}$$
$$\lambda_{\gamma_{xz}} = \frac{\lambda_w}{\lambda_x}$$

as well as, for the transverse displacement w through the equation (5.9a):

$$\lambda_w = \frac{\lambda_u \lambda_x}{\lambda_z}$$

which for longitudinal geometric non-linear analysis (equation (5.10a)) can also be written as:

$$\lambda_w^2 = \lambda_u \lambda_x$$

yielding the condition:

$$\lambda_w = \lambda_z$$

The similarity conditions from DF module for uniaxial bending (5.12) remain unchanged, while from the FMR module the following are obtained:

$$\begin{aligned}
\lambda_{N_x}^{beam} &= \lambda_y \lambda_{\sigma_x} \lambda_z \\
\lambda_{M_y}^{beam} &= \lambda_y \lambda_{\sigma_x} \lambda_z^2 \quad = \lambda_{N_x}^{beam} \lambda_z \\
\lambda_{Q_z}^{beam} &= \lambda_y \lambda_{\tau_{xz}} \lambda_z \lambda_k = \lambda_y \lambda_{\sigma_x} \lambda_z \lambda_k \frac{\lambda_w}{\lambda_u} = \lambda_{N_x}^{beam} \lambda_k \frac{\lambda_w}{\lambda_u}
\end{aligned}$$

The shear correction factor k of a laminated beam is influenced by the elastic moduli ratio (E_1/E_2), number of layers (N) and fiber-angle orientation (θ). Therefore it may be significantly different from that $\frac{5}{6}$ used typically for an isotropic material (Madabhusi-Raman and Davalos, 1996). However, as the material, number of plies and stacking sequence are considered the same for complete similitude, the shear correction factor can be assumed to be the same for both the model and prototype and therefore $\lambda_k = 1$.

Finally from the EM module the expressions for the scaling factors of the external forces and moments are obtained:

$$\lambda_{q_x}^{beam} = \frac{\lambda_{N_x}^{beam}}{\lambda_x}$$
$$\lambda_{q_z}^{beam} = \frac{\lambda_{Q_z}^{beam}}{\lambda_x} = \lambda_{q_x}^{beam} \frac{\lambda_w}{\lambda_u}$$

Additionally, for dynamic analysis the expressions for the axial and transverse accelerations are obtained. The amplitude is not necessarily equal, but nevertheless both motions are scaled in time by the same scale factor:

$$\frac{\lambda_u}{\lambda_t^2} = \frac{1}{\lambda_y} \frac{\lambda_{q_x}^{beam}}{\lambda_{\rho_0} \lambda_z}$$
$$\frac{\lambda_w}{\lambda_t^2} = \frac{1}{\lambda_y} \frac{\lambda_{q_z}^{beam}}{\lambda_{\rho_0} \lambda_z} = \frac{1}{\lambda_y} \frac{\lambda_{q_x}^{beam}}{\lambda_{\rho_0} \lambda_z} \frac{\lambda_w}{\lambda_u}$$

5.3.7.2. Isotropic beam subjected to combined biaxial bending and torsion

Replacing in the SSR module the relation $\lambda_E = \lambda_G = 1$, available from the MSS module, yields:

$$\begin{aligned}\lambda_{\sigma_x} &= \lambda_{\epsilon_x}\\ \lambda_{\tau_{xy}} &= \lambda_{\gamma_{xy}}\\ \lambda_{\tau_{xz}} &= \lambda_{\gamma_{xz}}\end{aligned}$$

Considering the linear analysis of biaxial bending, one can state: $\lambda_x\lambda_u = \lambda_y\lambda_v = \lambda_z\lambda_w$ from the SDR module and $\lambda_y\lambda_{\theta_z} = \lambda_z\lambda_{\theta_y}$ from the DR module.

Finally, replacing into equations (5.13a) and (5.13b) the necessary scaling factors from the FMR and previous modules yields after simplification:

$$\begin{aligned}\lambda_x\lambda_v &= \lambda_y\lambda_u\\ \lambda_x &= \lambda_z\end{aligned}$$

which from the above scaling relationships imply that:

$$\lambda_x = \lambda_y = \lambda_z \tag{5.14}$$

$$\lambda_u = \lambda_v = \lambda_w \tag{5.15}$$

Note that so far it has not been applied any condition related to the beam torsion, but even if it had been, the results would be the same. Therefore the criteria derived in this sub-section is valid for the complete similitude of beams subjected to biaxial bending and, optionally, torsion.

The scaling factors for the force and moment resultants are obtained from the FMR module as follows:

$$\begin{aligned}\lambda_{N_x}^{beam} = \lambda_{Q_y}^{beam} = \lambda_{Q_z}^{beam} = \lambda_N^{beam} &= \lambda_u\lambda_x\\ \lambda_{M_x}^{beam} = \lambda_{M_y}^{beam} = \lambda_{M_z}^{beam} = \lambda_M^{beam} &= \lambda_u\lambda_x^2\end{aligned}$$

and the scaling factors for the time and external loads from the EM module:

$$\begin{aligned}\lambda_{q_x}^{beam} = \lambda_{q_y}^{beam} = \lambda_{q_z}^{beam} = \frac{\lambda_N^{beam}}{\lambda_x} \quad &\Leftrightarrow \quad \lambda_q^{beam} = \lambda_u\\ \lambda_{m_x}^{beam} = \lambda_{m_y}^{beam} = \lambda_{m_z}^{beam} = \frac{\lambda_M^{beam}}{\lambda_x} \quad &\Leftrightarrow \quad \lambda_m^{beam} = \lambda_u\lambda_x\\ \lambda_t^2 = \frac{\lambda_{\rho_0}}{\lambda_q^{beam}}\lambda_u\lambda_z^2 \quad &\Leftrightarrow \quad \lambda_t = \lambda_x\end{aligned}$$

Lastly, note that so far it has not been applied any scaling relationship regarding the nonlinear behavior of beams. For geometrically non-linear analysis, the relations (5.14) would be replaced by a more restrictive condition:

$$\lambda_x = \lambda_y = \lambda_z = \lambda_u = \lambda_v = \lambda_w$$

allowing some more simplifications in the previously derived scaling factors, valid for complete similitude.

5.4. Case study: Static analysis of stiffened plates

The stiffened plate represented on figure 5.7, from now on called **Prototype 1**, will be considered as a case study to demonstrate the effectiveness and simplicity of the Modular Approach establishing criteria for the complete similitude of structures without available governing equations.

A smearing technique in which the stiffened plate is converted into an equivalent orthotropic plate by "smearing out" the stiffeners could be used. However, such approximation will not be well suited to the stiffened plates in which stiffeners are large and widely spaced or unevenly distributed (Szilard, 2004).

The relevant material properties for the study are the following:

$$E = 68.7 \times 10^9 \ Pa$$
$$\nu = 0.3$$
$$\rho = 2823 \ kg/m^3$$

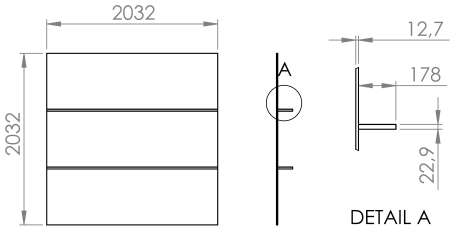

Figure 5.7.: Prototype 1 - Square plate with two parallel stiffeners (dimensions in mm).

and, as in figure 5.8, the stiffened plate is considered pinned along all edges and subjected to uniform pressure equal to 0.1 N/mm^2.

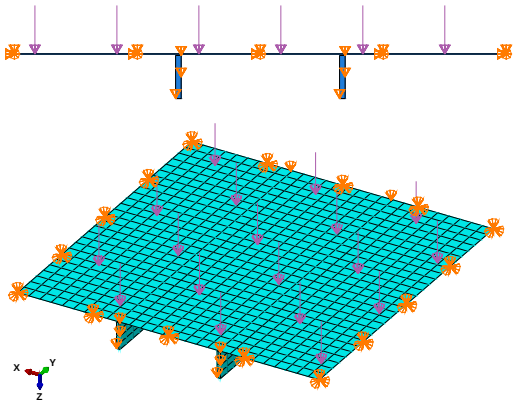

Figure 5.8.: FEM model of Prototype 1, pinned along all edges, under uniforme pressure.

It is considered the situation where the Prototype 1 is to be tested experimentally. However given the dimensions of the structure and the fact that the available facilities for the experimental analysis are limited to structures at least 10 times smaller, the experimental analysis of the prototype is not possible.

From the similitude theory one knowns that a 1/10-scale model constructed respecting all the conditions for complete similitude, from now on called **Model 1**, can be used to predict the structural behavior of Prototype 1.

The purpose of current research is to provide a preliminary numerical validation of the scaled model testing; therefore the experimental analysis of the Model 1 is replaced by numerical results. Besides, the FEM analysis results of the Prototype 1 will be considered to evaluate the accuracy of those predicted from scale models.

5.4.1. Selection of scaling criteria

Following the current manuscript, the choice of the correct similarity conditions for a linear static analysis is quite straightforward and no additional explanations will be given. For the plate alone, this is, considered as a free body diagram, it is known that:

- Equivalent points share the same material properties in both structures;
- $\lambda_x^{plate} = \lambda_y^{plate} = 0.1$
- $\lambda_u^{plate} = \lambda_v^{plate} = \left(\lambda_w \frac{\lambda_z}{\lambda_x}\right)^{plate}$
- $\lambda_\sigma^{plate} = \lambda_\epsilon^{plate} = \left(\frac{\lambda_u}{\lambda_x}\right)^{plate}$
- $\lambda_N^{plate} = (\lambda_\sigma \lambda_z)^{plate} = \left(\frac{\lambda_u}{\lambda_x}\lambda_z\right)^{plate}$
- $\lambda_q^{plate} = \left(\frac{\lambda_N}{\lambda_x}\right)^{plate} = \left(\frac{\lambda_u}{\lambda_x^2}\lambda_z\right)^{plate}$

For the stiffeners, analyzed as a beam subjected to uniaxial bending (induced by the plate) it is imposed that:

- Equivalent points share the same material properties in both structures;
- $\lambda_x^{beam} = \lambda_z^{beam} = 0.1$
- $\lambda_u^{beam} = \lambda_w^{beam}$
- $\lambda_{\sigma_x}^{beam} = \lambda_{\epsilon_x}^{beam} = \left(\frac{\lambda_u}{\lambda_x}\right)^{beam}$
- $\lambda_N^{beam} = (\lambda_{\sigma_x}\lambda_y\lambda_z)^{beam} = \left(\frac{\lambda_u}{\lambda_x}\lambda_y\lambda_z\right)^{beam} = (\lambda_u\lambda_y)^{beam}$
- $\lambda_q^{beam} = \left(\frac{\lambda_N}{\lambda_x}\right)^{beam} = \left(\frac{\lambda_u\lambda_y}{\lambda_x}\right)^{beam}$

Now, these two sets of similarity conditions have to be related imposing in the interface surface between the plate and the stiffeners:

- Continuity of displacements:

$$\lambda_u^{beam} = \lambda_u^{plate}$$
$$\lambda_v^{beam} = \lambda_v^{plate}$$
$$\lambda_w^{beam} = \lambda_w^{plate}$$

yielding the value for the thickness scale factor of the plate:

$$\lambda_z^{plate} = \lambda_x^{plate} = 0.1$$

- Continuity of the internal forces, which is equivalent to impose that the "external" forces in the free body diagrams are scaled by the same numeric factor:

$$\lambda_q^{plate} = \left(\frac{\lambda_q}{\lambda_y}\right)^{beam} \quad \Leftrightarrow \quad \left(\frac{\lambda_u \lambda_z}{\lambda_x^2}\right)^{plate} = \left(\frac{\lambda_u \lambda_y}{\lambda_x \lambda_y}\right)^{beam} \quad \Leftrightarrow \quad \lambda_x^{beam} = \lambda_x^{plate}$$

Note that internal forces on a beam are simplified as concentrated values, while in the plate they are values per unit width.

The previous sets of scaling relationships can be simplified to the following:

$$\text{Same material properties for equaivalent points} \tag{5.16a}$$

$$\lambda_x = \lambda_y = \lambda_z \tag{5.16b}$$

$$\lambda_w = \lambda_u = \lambda_v \tag{5.16c}$$

$$\lambda_\sigma = \frac{\lambda_w}{\lambda_x} \tag{5.16d}$$

$$\lambda_N^{plate} = \frac{\lambda_N^{beam}}{\lambda_y} = \lambda_w \tag{5.16e}$$

$$\lambda_q^{plate} = \frac{\lambda_q^{beam}}{\lambda_y} = \frac{\lambda_w}{\lambda_x} \tag{5.16f}$$

where, λ_x and λ_w were chosen as representative scale factors in complete similitude for all the (x, y, x) components of dimensions and displacements. Besides, a missing superscript ^{plate} or ^{beam} means that the scale factor applies to the whole stiffened plate, being the same for both plate and beam substructures.

Therefore it is concluded that the (scale) Model 1, in the figure 5.9, will have to be a replica model of the (original) Prototype 1. Dealing with a linear analysis, some freedom still exists on the choice of the scaling factor for the displacement field or for the external loadings:

$$\lambda_q = \frac{\lambda_u \lambda_z}{\lambda_x^2} = \frac{\lambda_w}{\lambda_x} \quad \Leftrightarrow \quad \lambda_q = 10\ \lambda_w$$

Otherwise, either for a dynamic analysis or for a geometric non-linear analysis the scaling factors for displacements would be equal to those of the geometry, and therefore, no free scaling factors would remain.

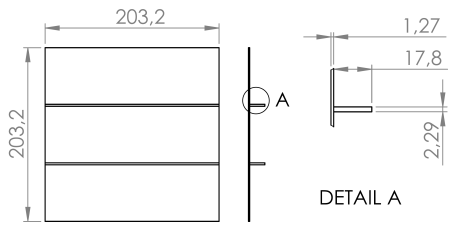

Figure 5.9.: Model 1 geometry (dimensions in mm).

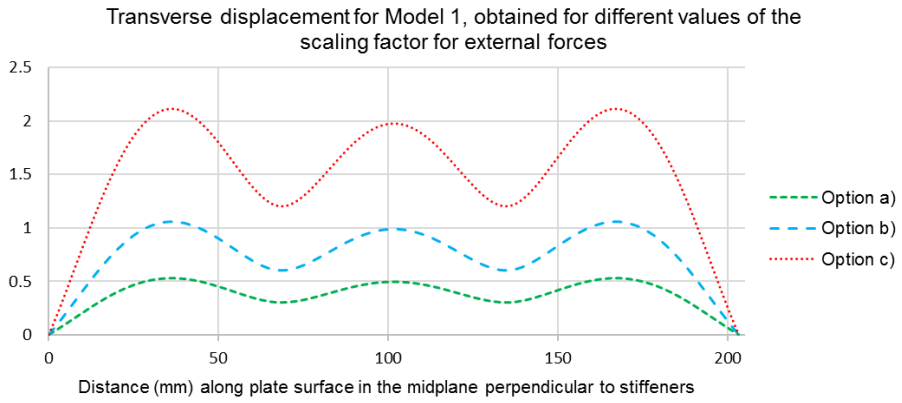

Figure 5.10.: Transverse displacement field (mm) for Model 1, obtained for different values of the scaling factor for external forces: $\lambda_q^{plate} = 0.5$, $\lambda_q^{plate} = 1$ and $\lambda_q^{plate} = 2$, respectively for option a), b) and c).

5.4.2. Analysis of results

Simulating Model 1 under an uniform pressure of 100 ($\lambda_q = 1$), 50 ($\lambda_q = 0.5$) and $200N/mm^2$ ($\lambda_q = 2$) the displacement fields represented in the figure 5.10 were obtained.

In a similar real case study, where Model 1 would be tested experimentally, the distributed load scale factor and the displacement scale factor could be chosen by a trade-off between:

- The material strength: the force scale factor may be greater than 1 if the structure keeps an elastic and linear behavior;
- The precision on experimental measurements: the load scale factor may be less than 1, if enough precision on the measurements exists, given that, for example, the amplitude of the displacement field will be smaller;
- The maximum available loading capacity: if applying the necessary distributed loading is not possible, then its amplitude may be reduced.

As depicted in figure 5.12, if the results in figure 5.10 are properly scaled with $\lambda_w = 0.05$, $\lambda_w = 0.1$, and $\lambda_w = 0.2$ (respectively for Options a), b) and c)), then the obtained predictions for the Prototype 1 transverse displacement field match perfectly its actual transverse displacement field (which is fully plotted in 5.11).

Factors such as manufacturing tolerances or statistical variation on the material properties are expected to introduce some negligible differences in predictions based on experimental analysis. Nevertheless, these are issues that arise in any simulation technique, most of them frequently neglected in numerical simulations such as those based on the finite element method.

5.5. Concluding remarks

The current research addresses the need for a methodology to design scaled models based on the similitude theory, being as intuitive as those based on the use of governing equations, but as versatile as those based on the dimensional analysis, without requiring great effort and skill for complex structures.

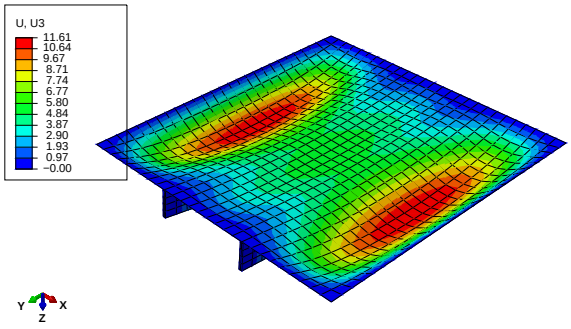

Figure 5.11.: Transverse displacement field [mm] for Prototype 1 pinned along all edges and subjected to an uniform pressure of $100kPa$.

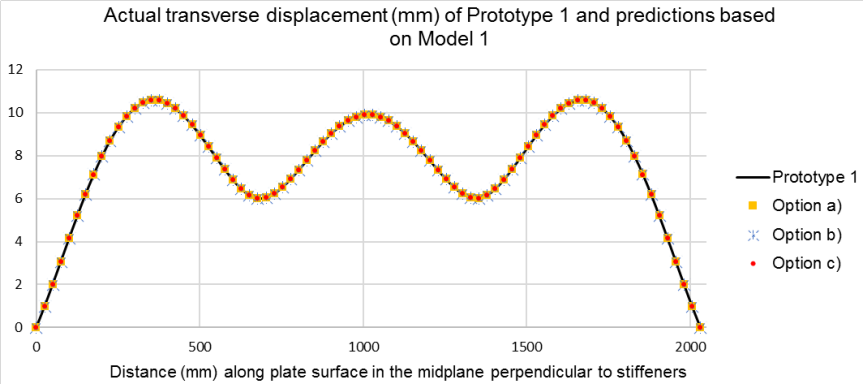

Figure 5.12.: Comparison of the actual transverse displacement field (mm) of the Prototype 1 with predictions obtained based on Model 1, for different values of the scaling factor for external forces: $\lambda_q^{plate} = 0.5$, $\lambda_q^{plate} = 1$ and $\lambda_q^{plate} = 2$, respectively for option a), b) and c).

The proposed solution is an approach based on a totally new modular concept, intended to improve how the similitude theory is applied to governing equations, and so overcoming identified limitations and difficulties.

The major achievement demonstrated in this chapter is that similitude theory can now be applied to complex structures through differential equations of its simple substructures, even if the governing equations for the whole structure are not available. To this end, the following innovative concepts are introduced:

- The structural similitude between two complex structures (systems) can be established for the relevant characteristics if the governing equations are available for each one of its basic structural elements (sub-systems) seen as a free body diagram;
- The two sets of scaling factors (such as those for the material properties and geometric dimensions) derived for two adjacent sub-systems are related between them by additional similarity conditions derived imposing displacement and force continuity inside the systems domain.

When compared to established methodologies, the strength of proposed approach lies in the possibility of combining modules of similarity conditions. No simplifying assumption is applied to the governing equations, which makes the scaling relationships in each of that modules as general as possible, but still easily adjusted to a specific application. Contrary to this, in the literature the similitude theory is applied to the governing equations simplified

for each specific application, as observed for example in researches regarding laminated plates, and therefore the obtained scaling relationships have limited range of application.

Therefore, for a given structural element, the governing equations are organized into modules of simpler equations. From each of them, a module of scaling relationships is derived. Then, by sequential substitutions all the previous modules can be grouped to create (in a second level) a global module with the scaling relationships for the structural behavior. Repeating the process for several structural elements, such as beams, plates or shells, the obtained global modules can be related to create (in a third level) a module with the scaling relationships for the structural behavior of a complex prototype.

A similar procedure can be repeated (up to the third level) to create a module with scaling relationships for any physical behavior. Ultimately relating (third-level) thermal and structural modules, for example, the thermal-structural behavior can be scaled.

A stiffened plate was selected to demonstrate the use of the Modular Approach and the accuracy of the scaled model testing. To that end, the Modular Approach had to be firstly applied to the generalized simple plate and beam. Even though the simplifying assumptions are minimized in the governing equations of both the generalized beam and plate, the Modular Approach is able to avoid the expected increase in the mathematical effort and complexity of the process of applying the similitude theory.

Scaling relationships for plates and beams had already be presented in the literature. However, apart from this work, no other research is known where:

- The scaling laws were derived depending primarily on the engineering constants E_i, G_{ij} and ν_{ij}, and not on the stiffness terms A_{ij}, B_{ij} and D_{ij};
- The scaling laws and similarity conditions for the complete similitude of the generalized beam and plate were derived without any previously assumed condition. This is, all the conditions imposing the use of the same materials or any type of geometric similarity are derived, ensuring that only the strictly necessary restrictions are imposed;
- The similitude theory was applied to the first-order shear deformation plate theory, and compared with the scaling relationships obtained from the classical plate theory;
- The difference between the similarity conditions obtained for linear or for (moderate geometric) non-linear analysis was clearly presented.

Besides, through the comparison of the actual and predicted transversal displacement field of a stiffened plate under static load, the experimental scaled model testing is numerically validated as an alternative accurate simulation tool. The predicted results matched perfectly the calculated transverse displacement of the prototype.

Lastly, it is highlighted that the true potential of the Modular Approach is beyond that demonstrated through this case study. At the moment, any structure composed from plates and beams/stiffeners could have been analyzed. Once the structural global module for other simple elements (including shells and solid parts) are available, it will be possible to establish structural similitude between scaled models and prototypes with higher diversity of structural elements. Another area of promising research is the applicability of Modular Approach to the scaling of multi-physics problems as already referred.

6. Static and dynamic experimental scaled model testing of stiffened plates

Abstract

Stiffened plates are basic sub-structures of a wide scope of structures. Their behavior can be simulated using FEM, but the models may be complex and time consuming, particularly the pre-processing of large structures.

The static and dynamic experimental scaled model testing of a large stiffened plate is demonstrated as an alternative simulation technique. A medium 2/5-scale model and the small 1/5-scale model are considered in order to compare the accuracy of different predictions for the same prototype based on reduced models of different scales.

The predictions based on experimental testing of the scaled models are compared with those obtained from finite element models, considering the experimental data directly measured in the prototype as the reference values.

Additionally, testing of the base plates and stiffeners are introduced in intermediate stages of the manufacturing process, helping to understand how the correlation between measured data and predicted results evolves for structures of increasing complexity.

6.1. Introduction

Stiffened panels represent one of the most important structural units of diverse structures, such as ships, offshore platforms, box girder bridges and stadiums (Momcilovic et al., 2016; Paik and Thayamballi, 2003).

According to Badran et al. (2013), since stiffened panels are fundamental building blocks in ships, many researchers have contributed to ship plating using stiffeners to support the plate. This structures are required to resist combined axial compressive forces, lateral loads and/or in-plane bending moments and shearing forces (Khedmati et al., 2010; Paik and Kim, 2002).

In particular, the description of the stiffened panels under predominantly lateral loads is relatively complicated due to the large number of possible combinations of plate and stiffener geometries, boundary conditions and loading (Badran et al., 2013).

A brief literature review of previous works regarding the stiffened panels subjected to lateral loads is available, for example, in a recent publication by Badran et al. (2013).

6.1.1. Simulation techniques for complex stiffened structures

Complex stiffened structures, such as ships, are made of thousands of stiffened panel units, each of which contributes to the global response of the whole structure, depending for example on other surrounding structural members (Momcilovic et al., 2016).

In order to analytically assess behavior of panels, the obstacles to be faced may be so restrictive that modeling of any structure more complex than unstiffened plates becomes impossible. Orthotropic plate theory formulations to describe stiffened panel bending can be used to obtain proper results, but only if the stiffeners are densely and evenly distributed, having less stiffness than plating (Momcilovic et al., 2016; Szilard, 2004).

Alternatively, the finite element method is widely accepted and a recognized numeric technique to model complex structures, regardless of the level of complexity and type of structural analysis (Momcilovic et al., 2016). However, structures having a large number of stiffened panel units require large numerical models. Recent emergence and routine use of extremely powerful digital computer hardware and software continuously mitigates limitations related with processing capacity and time. Despite that, FEM still requires enormous computation time, specially for nonlinear analysis (Paik and Thayamballi, 2003). Even for static and dynamic linear analysis, the method is still very limited for complex structures because of the largest part of FEM analysis is due to the pre-processing time taken modeling the geometry, preparing the model, conducting convergence analysis and/or debugging simulation errors.

Particularly for nonlinear analysis of large plated structures, the idealized structural unit method (ISUM) was firstly proposed by Ueda and Rashed, and has now been widely recognized by researchers as an efficient and accurate methodology (Paik and Thayamballi, 2003). ISUM is a simplified nonlinear FEM, whose field of application is out of the scope of the present chapter.

Alternatively to the techniques based on a mathematical models, the experimental scaled model testing can be used for diverse simulations of stiffened structures: from those as "simple" as the impact on a stiffener (Oshiro et al.) or panel unit (Mazzariol et al., 2010) to those as complex as a ship collision (Calle and Alves; Hagiwara et al., 1983; Lehmann and Peschmann, 2002; Tabri et al., 2008). Despite this, experimental research covering the use of scaled model testing for the static or dynamic simulation of stiffened panels is nonexistent or unknown.

6.1.2. Objectives

In order to improve how the similitude theory is applied to governing equations, an original Modular Approach was presented in chapter 5. Using this new approach, the similitude theory can be applied to complex structures through differential equations of its simple substructures, even if the governing equations for the whole structure are not available. In section 5.4 static response of a stiffened plate under lateral pressure was accurately predicted using the results from the analysis of a 1/10-scale model.

The main purpose of the following experimental work is to extend that preliminary numerical validation of the Modular Approach to a more comprehensive experimental program. The scaled model testing of a selected stiffened plate includes not only static but also dynamic analysis. Besides, the complexity of the panel was intentionally increased selecting one with T-stiffeners manufactured by welded construction, instead of flat bars. Therefore, between others, the experimental program has the following objectives:

1. Investigation of the influence of scale reduction in the correlation between the predicted results and the experimental data (directly) measured from the prototype, requiring:
   - Prediction of the structural behavior of a large stiffened plate, based on the experimental analysis of reduced models in different scales: the medium 2/5-scale and the small 1/5-scale;

2. Comparison of predictions for similar prototypes in different scales, whose respective scaled models have approximately the same scale reduction, requiring:
   - Prediction of the structural behavior of the medium scaled model, based on the experimental analysis of small scale stiffened plate (Scale reduction: 50%);

- Comparison of the correlation of previous prediction with that of the prototype based on the medium scaled model (Scale reduction: 40%).

3. Comparison of prediction accuracy of the experimental scaled model testing with that of numerical simulation using FE-models;

4. Assessment of how the similitude of structural behavior evolves from the simpler substructures of the stiffened plate to the final structure, requiring:

   - Scaled model testing of structures with increasing complexity, manufactured as much as possible from the same materials and by the same processes. This was achieved performing dynamic tests in intermediate stages of the stiffened plates manufacturing process;
   - Reproduction of the required research in previous items 1 to 3, and comparison of results.

6.2. Selection and description of the prototype

A total of 107 gross panels (figure 6.1), also known as grillages, which cover the full range of proportions of typical ship panels were numerically and analytically investigated by Chen (2003). All the grillages are 3600mm wide and composed (longitudinally) by three adjacent stiffened plates, supported by intermediate transverse frames. The stiffened plates have 3 stiffeners in 53 grillages and 5 in the remaining.

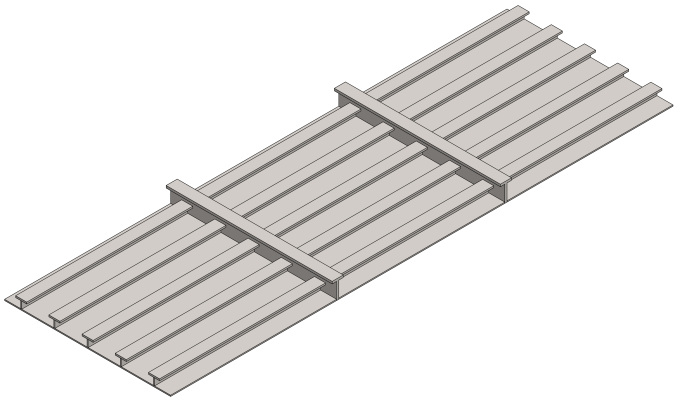

Figure 6.1.: Generic gross ship panel composed by three stiffened plates having 5 longitudinal stiffeners, and being supported transversally by two intermediate transverse frames.

For the current case study, the isolated stiffened panel P88 was firstly considered, whose geometry and dimensions are available from figure 6.2 and table 6.1, respectively. Even limiting the experimental analysis to a simple stiffened panel, the dimensions and, above all, the total mass reaching 2450 kg was prohibitive in the context of the current thesis. The expected material and manufacturing cost would exceed the available budget, the availability of facilities with required test capacities is reduced, and a lot of difficulty in ensuring personal safety conditions would be predictable.

Without compromising the research objectives, the case study was modified to a subsection of the P88 panel, comprising only 3 stiffeners. This reduced the total mass to around 1444 kg. However, some of previous concerns still prevailed. This justifies why the large

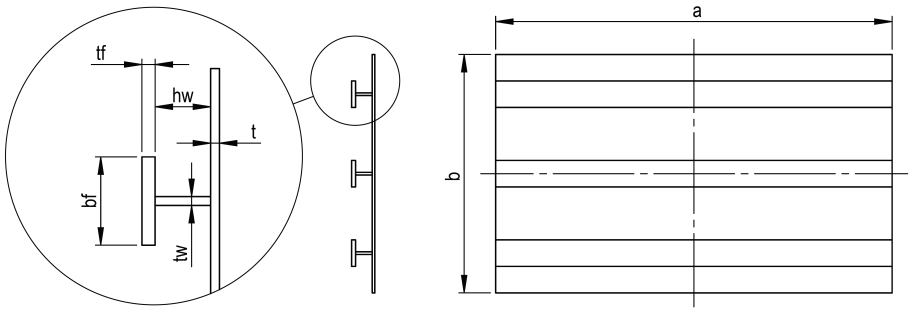

Figure 6.2.: Geometric parameters of a generic stiffened panel: length (a), breadth (b) and thickness (t) of the base plate; thickness (t_w) and height (h_w) of the stiffeners web; thickness (t_f) and breadth (b_f) of the stiffeners flange; number of stiffeners (n).

Table 6.1.: Comparison between the geometric dimensions (expressed in mm) of the original P88 panel and those of the selected prototype.

	Base plate			Stiffeners			
				Web		Flange	
	a	b	t	h_w	t_w	b_f	t_f
Original structure	3000	1800	21	126	20	200	30
(Selected) Prototype	1500	900	10	63	10	100	15

scale prototype finally chosen for experimental analysis consists of a 1/2-scale near replica of the original P88, comprising only 3 stiffeners.

6.3. Design of the scaled models

6.3.1. Selection of scaling criteria for linear dynamic analysis

The choice of the correct similarity conditions, from chapter 5, for a linear dynamic analysis is quite straightforward and no additional explanations will be given. For the base plate alone, this is, considered as a free body diagram, the imposed scaling relationships include the following:

- Equivalent points share the same material properties in both structures;
- $\lambda_x^{plate} = \lambda_y^{plate} = \lambda_z^{plate}$
- $\lambda_u^{plate} = \lambda_v^{plate} = \lambda_w^{plate}$
- $\lambda_\sigma^{plate} = \lambda_\epsilon^{plate} = \left(\frac{\lambda_u}{\lambda_x}\right)^{plate}$
- $\lambda_N^{plate} = (\lambda_\sigma \lambda_z)^{plate} = \left(\frac{\lambda_u}{\lambda_x}\lambda_z\right)^{plate} = \lambda_u^{plate}$
- $\lambda_q^{plate} = \left(\frac{\lambda_N}{\lambda_x}\right)^{plate} = \left(\frac{\lambda_u}{\lambda_x}\right)^{plate}$

- $\lambda_M^{plate} = \left(\lambda_\sigma \lambda_z^2\right)^{plate} = \left(\dfrac{\lambda_u}{\lambda_x}\lambda_z^2\right)^{plate} = \left(\lambda_u \lambda_z\right)^{plate}$
- $\lambda_m^{plate} = \left(\dfrac{\lambda_M}{\lambda_x}\right)^{plate} = \left(\dfrac{\lambda_u \lambda_z}{\lambda_x}\right)^{plate} = \lambda_u^{plate}$
- $\lambda_t^{plate} = \lambda_x^{plate}$

For the dynamic analysis of the T-stiffeners alone, analyzed as a beam subjected to bi-axial bending and torsion (induced by the plate), the following scaling relationships are imposed:

- Equivalent points share the same material properties in both structures;
- $\lambda_x^{beam} = \lambda_y^{beam} = \lambda_z^{beam}$
- $\lambda_u^{beam} = \lambda_v^{beam} = \lambda_w^{beam}$
- $\lambda_{\sigma_x}^{beam} = \lambda_{\epsilon_x}^{beam} = \left(\dfrac{\lambda_u}{\lambda_x}\right)^{beam}$
- $\lambda_N^{beam} = \left(\lambda_{\sigma_x} \lambda_y \lambda_z\right)^{beam} = \left(\dfrac{\lambda_u}{\lambda_x}\lambda_y \lambda_z\right)^{beam} = \left(\lambda_u \lambda_y\right)^{beam}$
- $\lambda_q^{beam} = \left(\dfrac{\lambda_N}{\lambda_x}\right)^{beam} = \left(\dfrac{\lambda_u \lambda_y}{\lambda_x}\right)^{beam} = \lambda_u^{beam}$
- $\lambda_M^{beam} = \left(\lambda_{\sigma_x} \lambda_y \lambda_z^2\right)^{beam} = \left(\dfrac{\lambda_u}{\lambda_x}\lambda_y \lambda_z^2\right)^{beam} = \left(\lambda_u \lambda_y \lambda_z\right)^{beam}$
- $\lambda_m^{beam} = \left(\dfrac{\lambda_M}{\lambda_x}\right)^{beam} = \left(\dfrac{\lambda_u \lambda_y \lambda_z}{\lambda_x}\right)^{beam} = \left(\lambda_u \lambda_y\right)^{beam}$
- $\lambda_t^{beam} = \lambda_x^{beam}$

Now, these two sets of similarity conditions have to be related imposing in the interface surface between the plate and the stiffeners:

- Continuity of displacements:

$$\begin{aligned} \lambda_u^{beam} &= \lambda_u^{plate} \\ \lambda_v^{beam} &= \lambda_v^{plate} \\ \lambda_w^{beam} &= \lambda_w^{plate} \end{aligned}$$

- Continuity of the internal forces, which is equivalent to impose that the "external" forces in the free body diagrams are scaled by the same numeric factor:

$$\lambda_q^{plate} = \left(\frac{\lambda_q}{\lambda_y}\right)^{beam} \quad \Leftrightarrow \quad \left(\frac{\lambda_u}{\lambda_x}\right)^{plate} = \left(\frac{\lambda_u}{\lambda_y}\right)^{beam} \quad \Leftrightarrow \quad \lambda_x^{plate} = \lambda_y^{beam}$$
$$\lambda_m^{plate} = \left(\frac{\lambda_m}{\lambda_y}\right)^{beam} \quad \Leftrightarrow \quad \lambda_x^{plate} = \lambda_y^{beam}$$

  Note that the internal forces and moments on a beam are simplified as concentrated values, while in the plates they are values per unit width.

For particular case of dynamic analysis, the previous coupling between geometric scale factors of different substructures can also be obtained imposing the same time scale during the experimental analysis of the whole structure:

$$\lambda_t^{plate} = \lambda_t^{beam} \quad \Leftrightarrow \quad \lambda_x^{plate} = \lambda_x^{beam}$$

Therefore it is concluded that any scale model have to be a replica model of the prototype. Dealing with a linear analysis, some freedom still exists on the choice of the scaling factor for the displacement field or for the external loadings of the stiffened plate:

$$\lambda_q = \frac{\lambda_w}{\lambda_x}$$

It is highlighted again that the scaling factors for displacements would be imposed equal to those of the geometry only for a non-linear analysis, in which case no free scaling factors would remain.

Additionally, from the implicit scaling laws presented in section 4.2.3.2 for frequency response analysis, which are valid regardless of the primary method applied to obtain the explicit scaling factors, it is derived:

$$\lambda_A = \frac{\lambda_w}{\lambda_t^2 \lambda_q} \tag{6.1}$$

$$\lambda_\omega = \lambda_t^{-1} \tag{6.2}$$

6.3.2. Geometric dimensions

A medium and a small scaled models were designed, whose geometric scale factors are 2/5 and 1/5, respectively. Their dimensions are available from table 6.2. Besides, from table 6.3 a comparison of the total mass of the prototype and scaled models is provided; it is notorious how even a small scale reduction is highly effective in reducing the total mass, due to the cubic relation between size and mass.

Table 6.2.: Comparison between the geometric dimensions (expressed in mm) of the prototype and those of the scaled models.

				Stiffeners			
	Base plate			Web		Flange	
	a	b	t	h_w	t_w	b_f	t_f
(Selected) Prototype	1500	900	10	63	10	100	15
2/5-scale model	600	360	4	25.2	4	40	6
1/5-scale model	300	180	2	12.6	2	20	3

6.4. Additional details

6.4.1. Selected material and manufacturing process

Both the structure and the scaled models were manufactured using the S275JR steel grade. No delivery condition was imposed, and therefore some variations exist as shown in

Table 6.3.: Total mass (expressed in kg) of the original P88 panel (encompassing only 3 stiffeners), selected prototype and scaled models.

	Total Mass
Original structure	1444
(Selected) Prototype	175
2/5-scale model	11.2
1/5-scale model	1.4

table 6.4. Additionally, some mechanical properties obtained from tensile tests and included in the quality certificates is available from table 6.5 .

Table 6.4.: Delivery conditions of the S275JR steel grade used in both the prototype and scaled models: normalized (N), as-rolled (AR), thermo-mechanical rolling (M).

		Stiffeners	
	Base plate	Web	Flange
Prototype	N / sheet	N / sheet	AR / profile
2/5-scale model	AR / sheet	AR / sheet	M / profile
1/5-scale model	AR / sheet	AR / sheet	AR / sheet

Table 6.5.: Mechanical properties according to the quality certificates of the S275JR steel grade used in the prototype and scaled models.

		Material Properties		
Thickness t [mm]	Delivery condition [–]	Yield strength R_e [MPa]	Tensile strength R_m [MPa]	Elongation A [%]
2	AR / sheet	441	496	24
3	AR / sheet	354	458	38
4	AR / sheet	347	442	35
6	M / profile	347	456	29.2
10	N / sheet	351	498	26.5
15	AR / profile	331	499	30.6

Material provided in sheet format was mechanically sheared in 4 edges, while those provided in profile format was sheared only on 2 (opposite) edges.

Lastly, the welding process and parameters are available from table 6.6. A reference value for the fillet weld size was initially obtained according to an experience based rule for full strength design: the leg size of the fillet may equal $\frac{3}{4}$ of the thiner plate thickness (Blodgett, 1963). As significant distortions would be expected, intermittent staggered weldings were designed according to EN 1993-1-2 (2005), using the previous weld size as reference. Assuming the structure as a build-up member whose welds are mostly under shear force, the selected intermittent staggered weldings are equivalent to a rigidity design having around 27% and 38% of the full strength, respectively for the web-flange and plate-web connections. The selected design according to EN 1993-1-2 (2005) have into account the loading condition, distance between stiffeners, as well as breadth and thickness of the base plate, web and flange. Alternatively, from Blodgett (1963), an experience based rule is available

for rigidity design having continuous welds with between 33% and 55% of full strength: the leg size of the fillet may equal from $\frac{1}{4}$ to $\frac{3}{8}$ of the thiner plate thickness.

Table 6.6.: Process and parameters used in the welded constructions of the stiffened plates.

	Process	Parameters	
		Voltage [V]	Current [A]
Prototype	MIG/MAG	18.5	216-220
2/5-scale model	MIG/MAG	17.0	123-125
1/5-scale model	TIG	10.0	70

6.4.2. Surface finishing

A total of 4 stiffened plates were initially planned for manufacturing: one (large scale) prototype, one medium scaled model and two small scaled models. For all of them, galvanized surface finishing was required. Due to unforeseen circumstances in the production process, only one small scaled model and the medium scaled model were galvanized. As the latter was delivered with errors in the positioning of the reinforcements, it was required the production of a new medium scaled model.

Therefore, by the end of the manufacturing process of the stiffened plates the following structures were available:

- without any surface finishing:
  - 1 prototype
  - 1 small scaled model
  - 1 medium scaled model
- with galvanized surface finishing:
  - 1 small scaled model
  - 1 medium scaled model, with some geometric distortion

6.5. Dynamic analysis

6.5.1. ABAQUS FE-model and preliminary numerical results

In order to compare the results predicted using experimental scaled model testing with those obtained from numerical simulation, the FE-models shown in figure 6.3 were created in ABAQUS.

In the mesh of the prototypes, considering the results of the convergence analysis, the global size of the elements was defined equal to 25 mm. The exception is the element size along the flange breadth and web height of the stiffeners, where the average local size is refined to approximately 12.5mm. In the medium and small scale FE-models, the global and local mesh sizes are defined according to the geometric scale factors, such that, in any scale the FE-models of the stiffeners, base plates and stiffened plates have 780, 2160 and 4500 elements of type S4R, respectively.

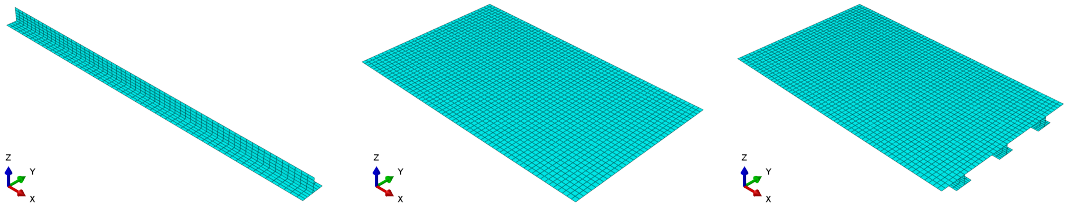

(a) Stiffener FE-model (780 S4R elements, with 5124 DOFs).

(b) Plate FE-model (2160 S4R elements, with 13542 DOFs).

(c) Stiffened plate FE-model (4500 S4R elements, with 27816 DOFs).

Figure 6.3.: ABAQUS FE-models.

6.5.1.1. Comparison with alternative ABAQUS FE-models

The selected FE-models for the current case study have already been presented. Nevertheless, some alternatives that have been discarded are discussed in this section, taking the stiffener sub-structure as example.

The mesh global size of the stiffener shell FE-model depicted in figure 6.3a was reduced 2.5 times, yielding the so called stiffener refined shell FE-model (figure 6.4a).

Four additional models using ABAQUS solid elements of type C3D8R are considered:

- the solid FE-model (figure 6.4b) with a mesh global size equal to 6.5 mm in the prototype scale, and imposing at least 4 elements through the thickness in the web and flange;
- the refined solid FE-model (figure 6.4c), corresponding to the previous model with the mesh global size reduced (approximately 2.5 times) to 2.5 mm in the prototype;
- the detailed solid FE-model with beads (figure 6.4d), which additionally to the solid FE-model includes the weld beads;
- the detailed solid FE-model with beads and material discontinuity (figure 6.4e), which additionally to the previous model includes material discontinuity between the flange and web.

The first (non-zero) 48 natural frequencies of the prototype were obtained using the models in figures 6.3a and 6.4. Taking the results from the refined shell FE-model as the reference values, the relative differences were calculated and averaged for an increasing number of considered natural frequencies, as plotted in figure 6.5. For the shell model, it is observed that the average relative difference increases from 0% up to 1% when 48 natural frequencies are considered.

On the other hand, the average relative difference of the results obtained from the solid FE-model ranges between -2.0% and 0.7%; the refined solid model improved the results, whose average relative difference ranges between -1.6 and 0.8.

One can conclude that both the shell and solid FE-models yield results that are almost but not fully converged. Besides, it is observed from figure 6.5 that both models are converging to intermediate values. Nevertheless, the possible additional convergence is so reduced that do not justify the extra computational time imposed by a refined model. Lastly, the much lower computer resources required by the shell model in comparison to a solid model with the same accuracy justifies why shell models were preferred in the current case study.

The use of detailed models was also considered. The relative differences of the results from the detailed solid model with added beads reveal that the extra mass and/or stiffness

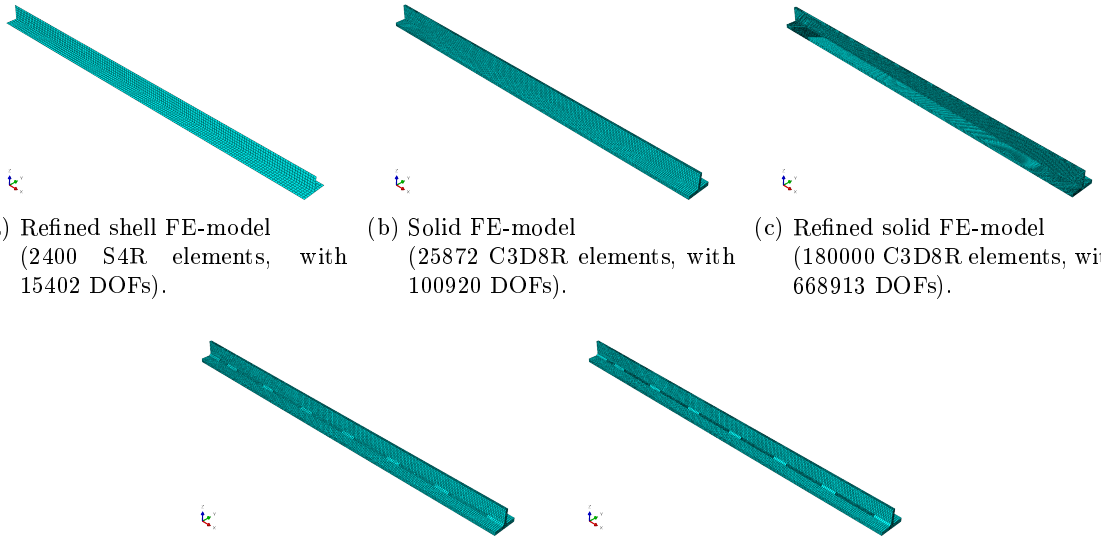

(a) Refined shell FE-model (2400 S4R elements, with 15402 DOFs).

(b) Solid FE-model (25872 C3D8R elements, with 100920 DOFs).

(c) Refined solid FE-model (180000 C3D8R elements, with 668913 DOFs).

(d) Detailed solid FE-model with beads (29212 C3D8R elements, with 112824 DOFs).

(e) Detailed solid FE-model with beads and material discontinuity (31962 C3D8R elements, with 125715 DOFs).

Figure 6.4.: Some alternative ABAQUS FE-models of the stiffener.

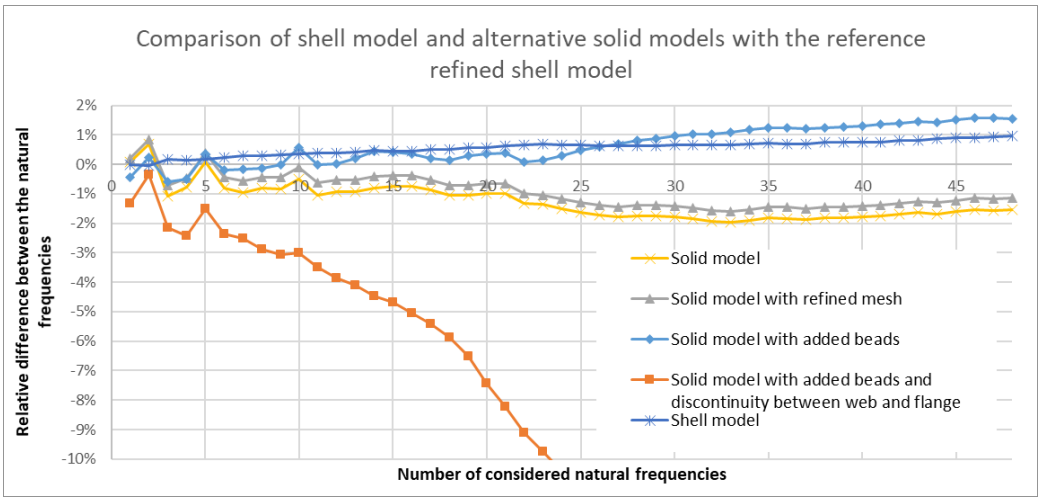

Figure 6.5.: Comparison of selected shell model and alternative solid models with the reference refined shell model.

introduced by the weld beads can have a significant effect in the obtained natural frequencies, increasing them in a generalized way. Nevertheless, such model is not practical in real applications, not only because of the required computational time but also due to the higher pre-processing time taken modeling the detailed geometry of the weld.

While a detailed solid model with added beads may be used to obtain highly accurate results, the same is not likely to happen using the model from figure 6.4e. The high loss of stiffness introduced modeling material discontinuity (between the web and flange) cause an abrupt frequency decrease in the higher modes of vibration, which is probably caused by the absence of a modeled surface-to-surface interaction for that discontinuity. Once again, that is not a plausible approach on real large scale case studies.

6.5.1.2. Effect of added masses on experimental measurements

The effect of the added mass introduced in the structure by the measurement equipment is expected to be negligible as long as the ratio between the masses of the accelerometer and the modal mass of the structure tends to zero.

Initially for experimental measurements of small scale structures, an B&K accelerometer type 4507 was selected, weighting 4.8 g. As depicted in figure 6.6, the instrumented structure can have some of its measured natural frequencies reduced up to around 1.7%.

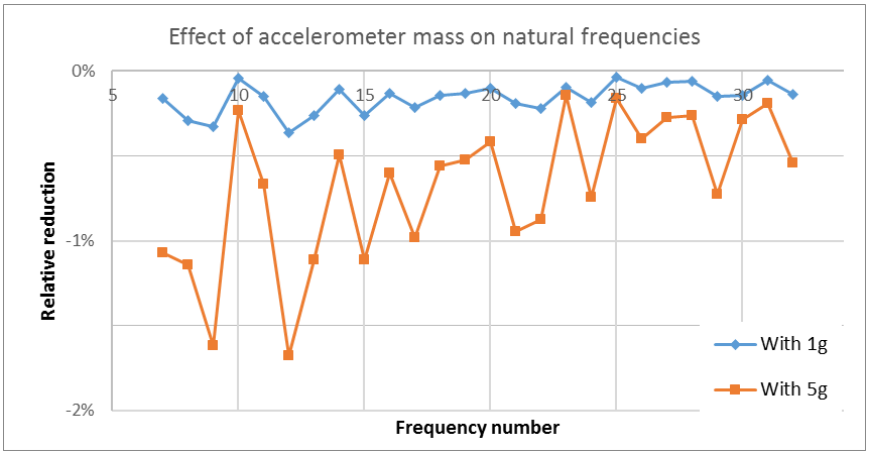

Figure 6.6.: FEM analysis of the effect of added mass introduced by different accelerometers on the value of the first 32 natural frequencies of the small scale base plate with free boundaries.

In order to ensure that the dynamic measurements are not significantly affected by added mass introduced by the measurement equipment, an Endevco accelerometer model 27A11 (weighting 1 g) was selected for measurements on the small scale experiments.

6.5.1.3. Numerical mode shapes

In order to complete the preliminary numerical results in this section, as well as to provide a better interpretation of the experimental data in the following sections, some of the modal shapes obtained with the numerical models shown in figure 6.3 are depicted in figures 6.7 to 6.9.

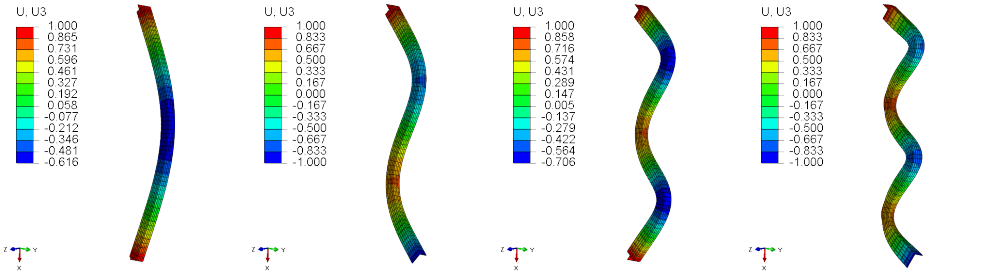

(a) 1^{st} mode shape (b) 2^{nd} mode shape (c) 3^{rd} mode shape (d) 4^{th} mode shape

Figure 6.7.: Numerical mode shapes of the stiffener.

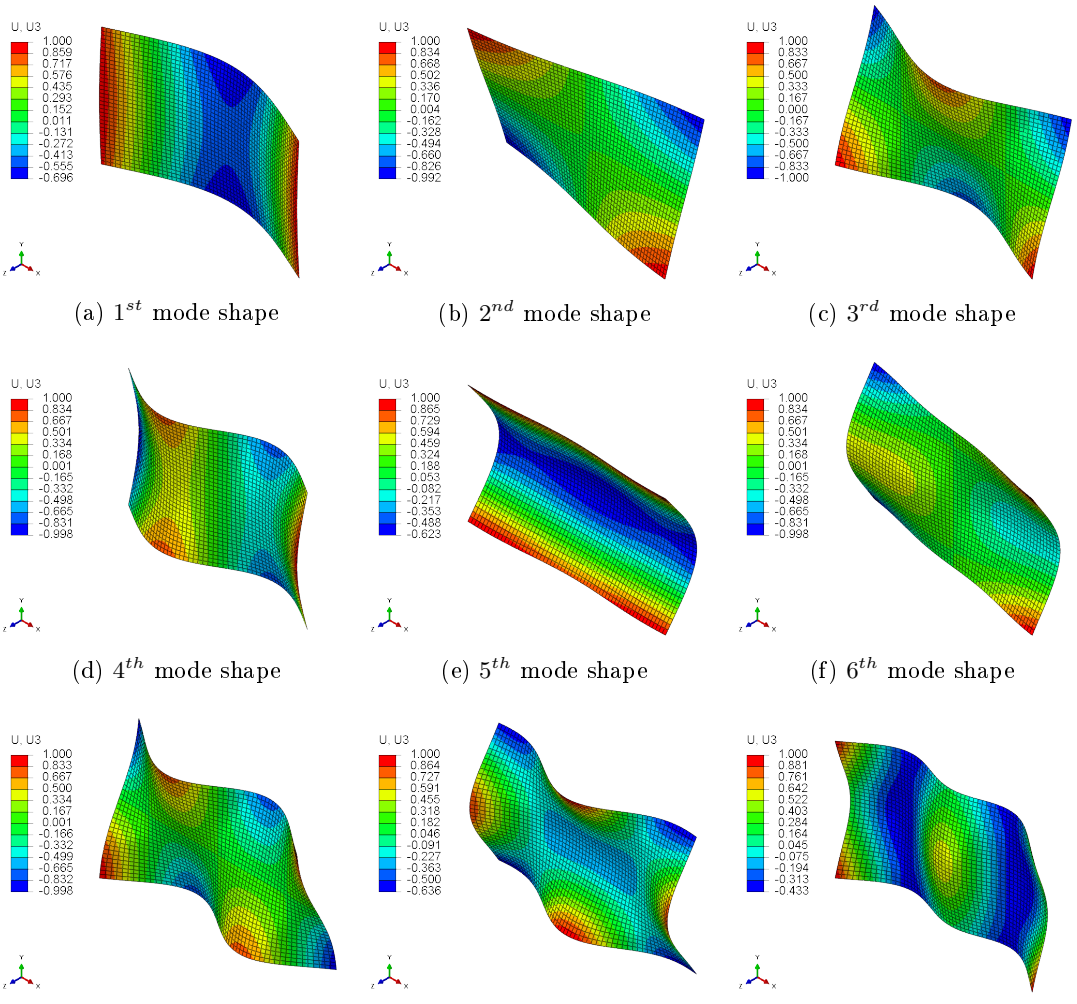

(a) 1^{st} mode shape (b) 2^{nd} mode shape (c) 3^{rd} mode shape

(d) 4^{th} mode shape (e) 5^{th} mode shape (f) 6^{th} mode shape

(g) 7^{th} mode shape (h) 8^{th} mode shape (i) 9^{th} mode shape

Figure 6.8.: Numerical mode shapes of the base plate.

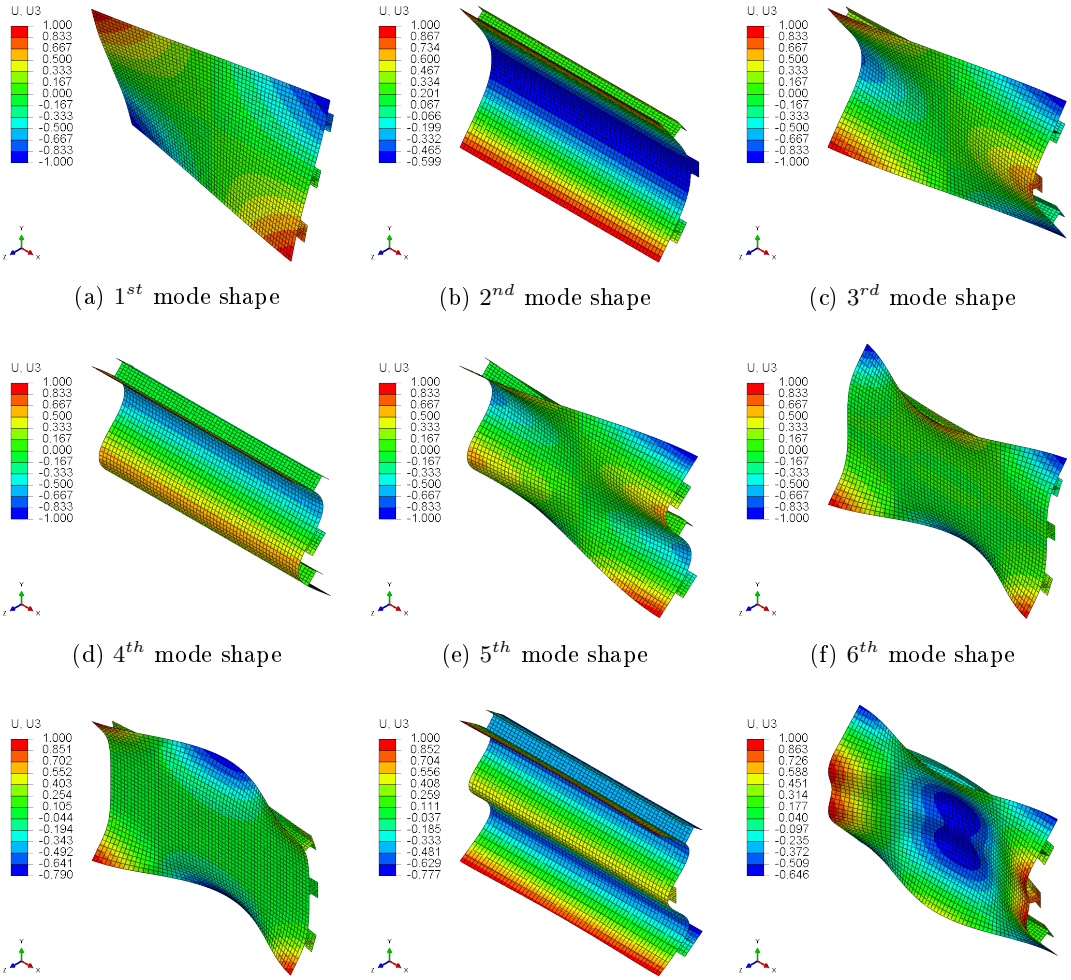

(a) 1^{st} mode shape (b) 2^{nd} mode shape (c) 3^{rd} mode shape

(d) 4^{th} mode shape (e) 5^{th} mode shape (f) 6^{th} mode shape

(g) 7^{th} mode shape (h) 8^{th} mode shape (i) 9^{th} mode shape

Figure 6.9.: Numerical mode shapes of the stiffened plate.

6.5.2. Experimental setup

The plates, stiffeners and stiffened plates were suspended vertically in order to simulate free boundary conditions, as shown in figures 6.10 and 6.11. A total of 4 points on each (base and stiffened) plate and 2 points on each stiffener were defined, as represented in figure 6.12; the parameter d is equal to 50 mm, 20 mm and 10 mm, respectively for the prototype and its medium and small scaled models, respecting therefore the geometric scaling factors.

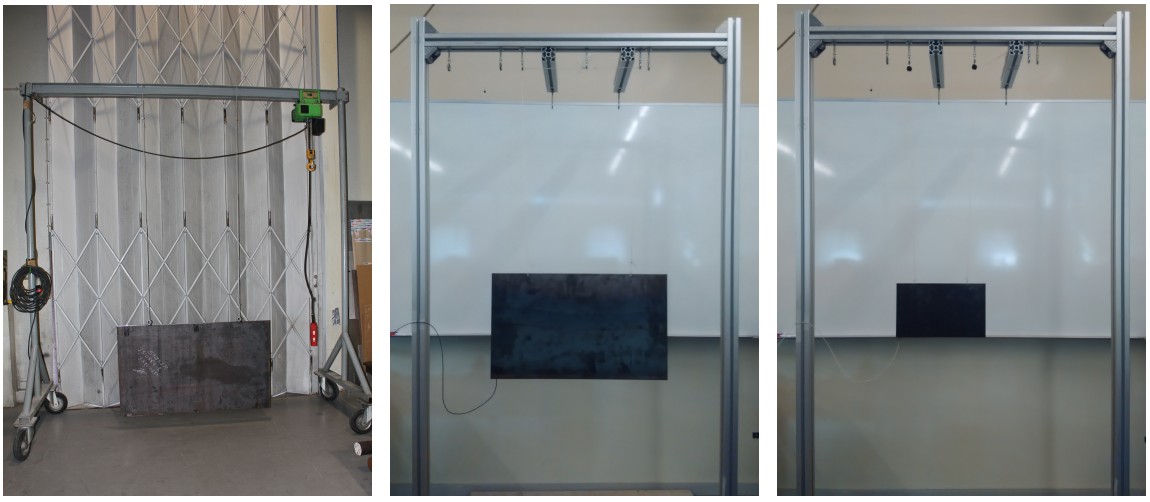

(a) Prototype (b) Medium 2/5-scale model (c) Small 1/5-scale model

Figure 6.10.: Experimental setups for frequency response analysis of the (base and stiffened) plates under simulated free boundary conditions.

(a) Prototype (b) Medium 2/5-scale model (c) Small 1/5-scale model

Figure 6.11.: Experimental setups for frequency response analysis of the stiffeners under simulated free boundary conditions.

The B&K signal analyzer unit type 2035 was used to acquire the excitation and response signals. The excitation was applied striking the structure at each point with a B&K impact hammer type 8202. The response was measured by an accelerometer placed at the versus of a fixed point: the point 4 in the (base and stiffened) plates and the point 2 in the stiffeners.

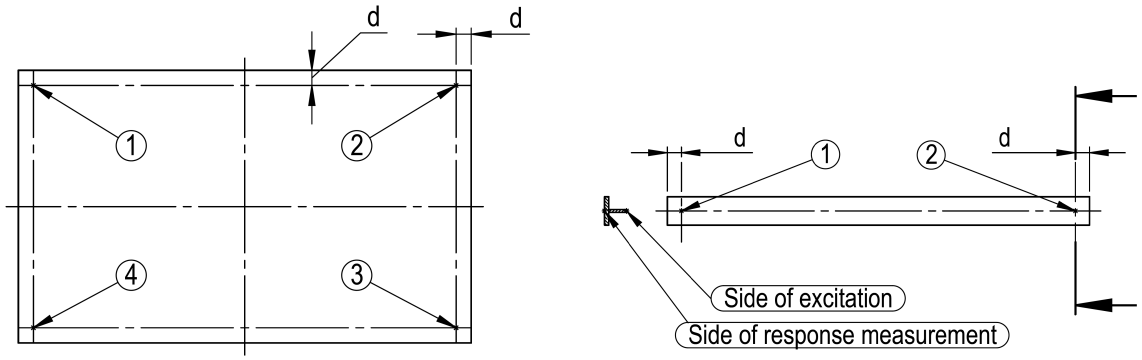

(a) Points 1 to 4 in the (base and stiffened) plates. In the stiffened plates the free surface was chosen as the side of excitation.

(b) Points 1 and 2 along the stiffener.

Figure 6.12.: Location of the measurements points for dynamic analysis.

An Endevco accelerometer model 27A11 was used for the small scale experiments and a B&K type 4371 was used for the medium scale and prototype's measurements.

6.5.3. Experimental results

6.5.3.1. Base plates

The dynamic response of the base plate prototype was analyzed up to 160 Hz, which correspond in the medium and small scaled models to similar frequency ranges up to 400 Hz and 800 Hz, respectively.

In figures 6.13 to 6.16 the accelerances measured in the prototype of the base plate are plotted along with corresponding predictions: one of them calculated through the shell FE-model of the prototype, and the other obtained applying accelerance and frequency scale factors to the measured FRFs of the scaled models.

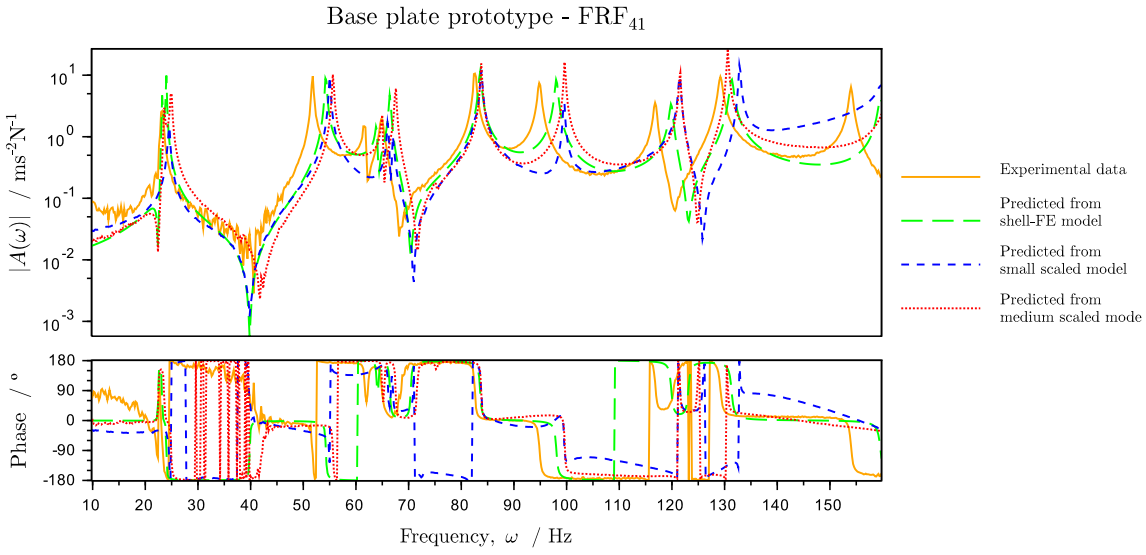

Figure 6.13.: Measured and predicted frequency response function FRF_{41} of the base plate prototype.

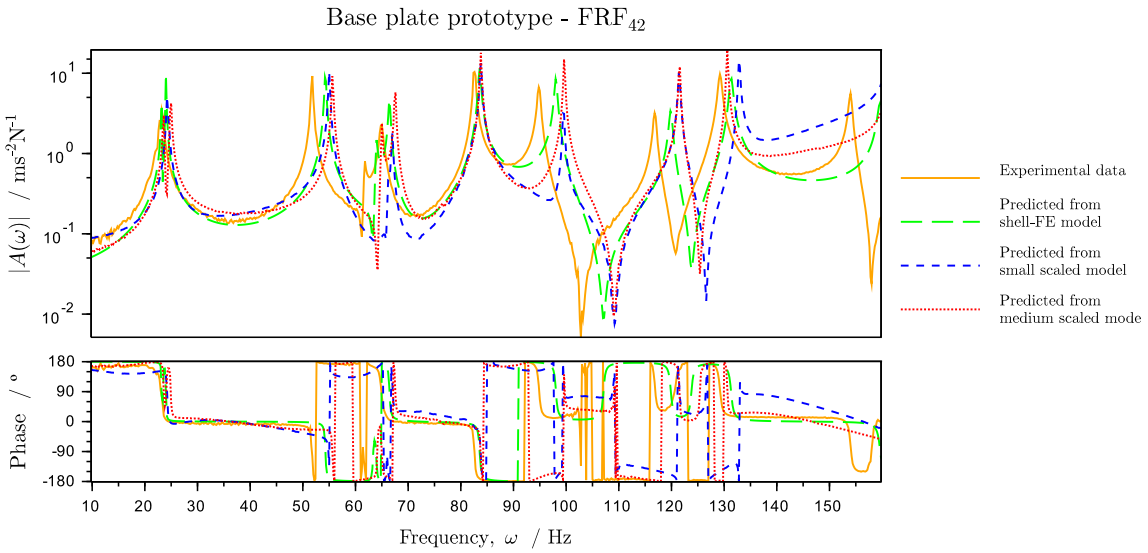

Figure 6.14.: Measured and predicted frequency response function FRF_{42} of the base plate prototype.

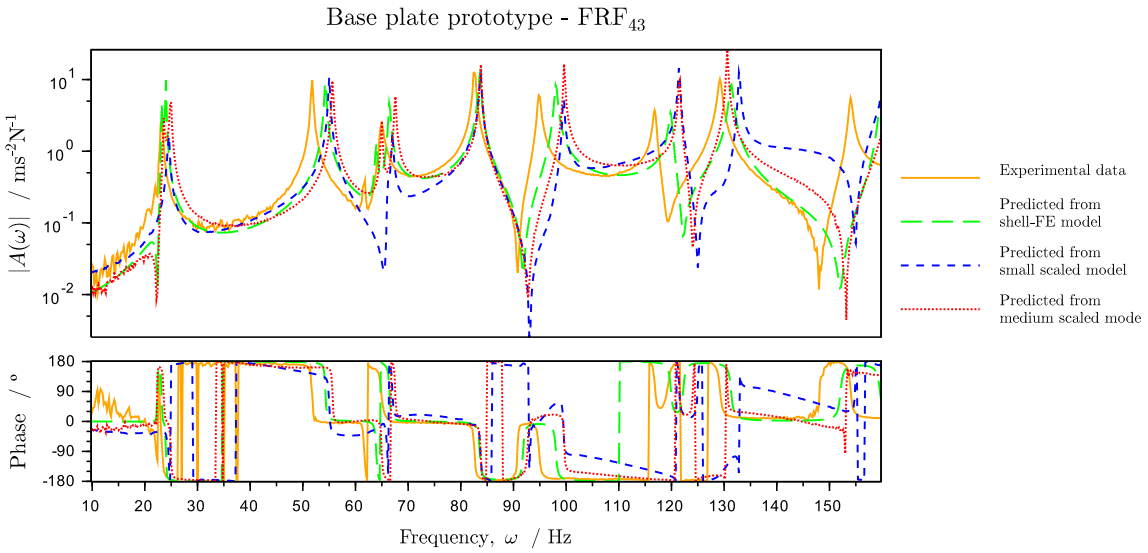

Figure 6.15.: Measured and predicted frequency response function FRF_{43} of the base plate prototype.

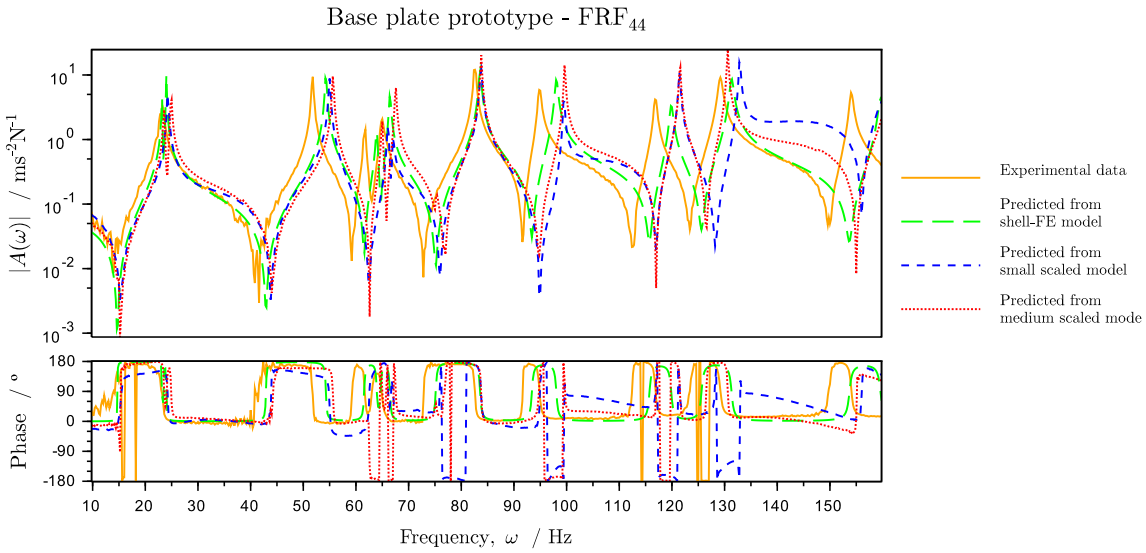

Figure 6.16.: Measured and predicted frequency response function FRF_{44} of the base plate prototype.

Evaluation of the correlation between FRFs

From visual inspection of the overlaid responses, it is possible to obtain a global idea of the correlation between the results directly measured in the prototype and those predicted by some experimental or numerical method of simulation. To avoid the subjectiveness of such qualitative evaluation, FRF-based correlation metrics are usually calculated.

The Local Amplitude Criterion (LAC) is an helpful tool to quantify the correlation between numerical results and experimental data as a frequency function for each individual degree of freedom (Moreira and Rodrigues; Zang et al., 2001). It was selected for the current results analysis, allowing to individually evaluate the frequency correlation for each FRF as follows:

$$LAC_{jk} = \frac{2\ \left|\left(FRF_{X_{jk}}(\omega)\right)^{*}\ \left(FRF_{A_{jk}}(\omega)\right)\right|}{\left(\left(FRF_{X_{jk}}(\omega)\right)^{*}\ \left(FRF_{X_{jk}}(\omega)\right) + \left(FRF_{A_{jk}}(\omega)\right)^{*}\ \left(FRF_{A_{jk}}(\omega)\right)\right)}$$

where, $FRF_{X_{jk}}(\omega)$ and $FRF_{A_{jk}}(\omega)$ stand for, respectively, the experimental and numerical frequency response functions between the degrees of freedom j and k, and * denotes the complex conjugate.

Lastly, according to Zang et al. (2001), for a given frequency range comprising N frequencies of interest ω_i, the averaged LAC can be defined as:

$$\overline{LAC_{jk}} = \frac{1}{N}\sum_{i=1}^{N} LAC_{jk}(\omega_i) \tag{6.3}$$

In table 6.7, for each frequency response function, a total of 6 independent values were calculated between the measured data and possible predictions from the scaled and FE-models. In these matrices of averaged LAC values, the acronyms P, MS, SS and FE stand for prototype, medium scaled model, small scaled model and corresponding FE-model, respectively.

A more concise overview of all those correlation values is provided by the last subtable in

table 6.7, allowing to observe that the measured predictions of the prototype accelerances are better correlated by the results from its FE-model. On the other hand, the measured FRFs of the medium scaled model are equally correlated by both the predictions from the small scaled model and the numerical results from the FE-model.

Table 6.7.: Matrices of averaged LAC correlation indicators between the measured frequency response functions of the prototype (P), medium (MS) and small (SS) scaled models and those predicted from the scaled models (MS, SS) and FE-models (FE).

	P	MS	SS	FE
P	1	0.71	0.70	0.76
MS		1	0.79	0.83
SS			1	0.79
FE	(sym.)			1

(a) $\overline{LAC_{41}}$

	P	MS	SS	FE
P	1	0.73	0.69	0.77
MS		1	0.86	0.84
SS			1	0.77
FE	(sym.)			1

(b) $\overline{LAC_{42}}$

	P	MS	SS	FE
P	1	0.72	0.69	0.78
MS		1	0.79	0.86
SS			1	0.76
FE	(sym.)			1

(c) $\overline{LAC_{43}}$

	P	MS	SS	FE
P	1	0.61	0.60	0.70
MS		1	0.83	0.78
SS			1	0.75
FE	(sym.)			1

(d) $\overline{LAC_{44}}$

	P	MS	SS	FE
P	1	0.69	0.67	0.75
MS		1	0.82	0.83
SS			1	0.77
FE	(sym.)			1

(e) Average $\overline{LAC_{jk}}$ of previous subtables

Comparison of the natural frequencies of vibration

The covered frequency ranges in the experimental analyses of the several base plates allowed to identify the first 9 natural frequencies of vibration, whose values are available in table 6.8.

Additionally the natural frequencies obtained with shell FE-models for the prototype and its scaled models are presented in table 6.9. These results can be directly compared with those obtained experimentally in table 6.8; while the natural frequencies of the prototype are over-estimated between 1.2% and 4.6%, those of the scaled models are under-predicted up to −4.1%.

Alternatively to the use of FE-models, the experimental natural frequencies of vibration of the base plate prototype can be predicted from those of its scaled models. Similarly, if the medium scaled model was considered as the large scale prototype, then its natural frequencies could be predicted from those measured in the small scale prototype (see table 6.10). In

Table 6.8.: Experimental natural frequencies of vibration of the base plate (f_i) in different scales.

mode number i	Experimental data - f_i [Hz]		
	Prototype	Medium scaled model	Small scaled model
1	22.8	59.0	121
2	23.2	62.5	123
3	51.8	139.0	275
4	61.8	162.5	330
5	65.0	169.0	335
6	82.6	209.5	419
7	94.8	249.0	497
8	116.8	304.0	607
9	129.2	326.5	664

Table 6.9.: Predicted frequencies of vibration for the base plates obtained using shell FE-models (f_i), and corresponding relative difference when compared with experimental results ($f_i^{(ref)}$).

mode number i	Numerical predictions					
	Prototype		Medium scaled model		Small scaled model	
	f_i [Hz]	$\frac{f_i - f_i^{(ref)}}{f_i^{(ref)}}$ [%]	f_i [Hz]	$\frac{f_i - f_i^{(ref)}}{f_i^{(ref)}}$ [%]	f_i [Hz]	$\frac{f_i - f_i^{(ref)}}{f_i^{(ref)}}$ [%]
1	23.2	1.8	58.0	-1.7	116	-4.1
2	24.0	3.4	60.0	-4.0	120	-2.4
3	54.2	4.6	135.5	-2.5	271	-1.5
4	64.0	3.6	159.9	-1.6	320	-3.1
5	66.4	2.2	166.0	-1.8	332	-0.9
6	83.6	1.2	209.0	-0.2	418	-0.2
7	98.0	3.4	245.0	-1.6	490	-1.4
8	119.8	2.6	299.5	-1.5	599	-1.3
9	131.4	1.7	328.5	0.6	657	-1.1

both situations, taking the experimentally measured natural frequencies of the prototypes as the reference values, the relative differences of the predicted values are plotted respectively in figure 6.17a and 6.17b.

Table 6.10.: Predicted frequencies of vibration for the base plates obtained using scaled models (f_i), and corresponding relative difference when compared with experimental results ($f_i^{(ref)}$).

mode number	Prototype				Medium scaled model	
	Predicted from medium scaled model		Predicted from small scaled model		Predicted from small scaled model	
i	f_i [Hz]	$\frac{f_i - f_i^{(ref)}}{f_i^{(ref)}}$ [%]	f_i [Hz]	$\frac{f_i - f_i^{(ref)}}{f_i^{(ref)}}$ [%]	f_i [Hz]	$\frac{f_i - f_i^{(ref)}}{f_i^{(ref)}}$ [%]
1	23.6	3.5	24.2	6.1	60.5	2.5
2	25.0	7.8	24.6	6.0	61.5	-1.6
3	55.6	7.3	55.0	6.2	137.5	-1.1
4	65.0	5.2	66.0	6.8	165.0	1.5
5	67.6	4.0	67.0	3.1	167.5	-0.9
6	83.8	1.5	83.8	1.5	209.5	0.0
7	99.6	5.1	99.4	4.9	248.5	-0.2
8	121.6	4.1	121.4	3.9	303.5	-0.2
9	130.6	1.1	132.8	2.8	332.0	1.7

Very similar results are predicted for the prototype by both the medium and small scaled models, whose associated relative differences range in the following respective intervals: [1.1%; 7.8%] and [1.5%; 6.8%]; both of them reach values higher than those corresponding to the results of the FE-model (and ranging between 1.2% and 4.6%).

On the other hand, when the medium scaled model is considered as the prototype structure, the average accuracy of the natural frequencies predicted by the small scaled model is higher that of the values predicted by a shell FE-model. The associated relative differences of results obtained through the former model are in the approximate $\pm 2.5\%$ range, while the latter model relative differences up to -4% were found. It is highlighted that the better performance of the scaled model testing (predicting natural frequencies) is not reflected by an higher average $\overline{LAC_{jk}}$ in table 6.7.

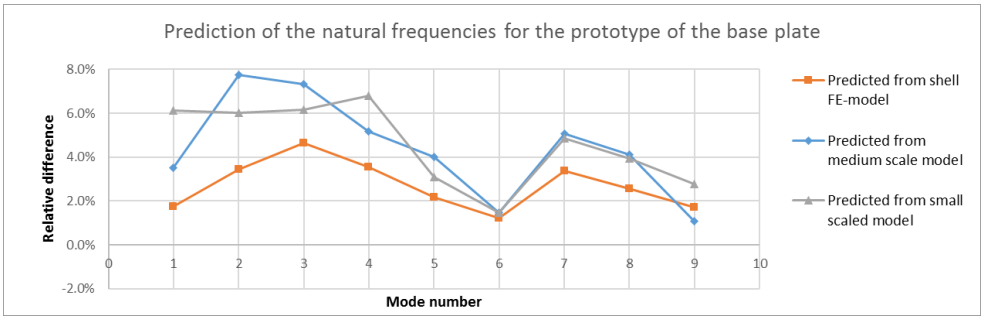

(a) Considering the prototype as the large scale structure.

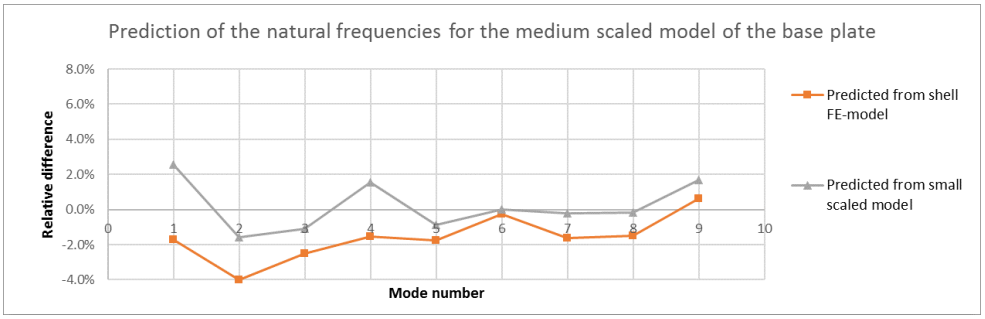

(b) Considering the medium scaled model as the large scale structure.

Figure 6.17.: Relative differences between the predicted and measured natural frequencies of the base plate.

6.5.3.2. Stiffeners

The dynamic response of the stiffener prototype was analyzed up to 1280 Hz, which correspond in the medium and small scaled models to similar frequency ranges up to 3200 Hz and 6400 Hz, respectively.

In figures 6.18 and 6.19 the accelerances measured in the prototype of the stiffener are plotted along with corresponding predictions: one of them calculated through the shell FE-model of the prototype, and the other obtained applying accelerance and frequency scale factors to the measured FRFs of the scaled models.

Evaluation of the correlation between FRFs

Following a procedure similar to that described for the base plate analyses, the averaged LAC values given by equation (6.3) were calculated and made available in table 6.11. The observed average $\overline{LAC_{jk}}$ values are between 0.84 and 0.94, which are quite high in comparison with those obtained for the base plate prototype, ranging between 0.67 and 0.83.

When compared with the simple base plates, the stiffeners have a more complex geometry whose manufacturing processes additionally include a welding process. Therefore, the stiffeners are more prone to distortions which affect the similarity between different structures, and which if not considered by the FE-models may also affect their prediction accuracy. Due to these reasons, and contrary to what was observed and described, lower LAC values would be expected.

Very similar average $\overline{LAC_{jk}}$ values were obtained for both the predictions based on scaled models and FE-models; however, only the FRFs predicted by the medium scaled model for the prototype stiffener correlated better than the results from FE-models with the experimental data of the large and medium scale structures.

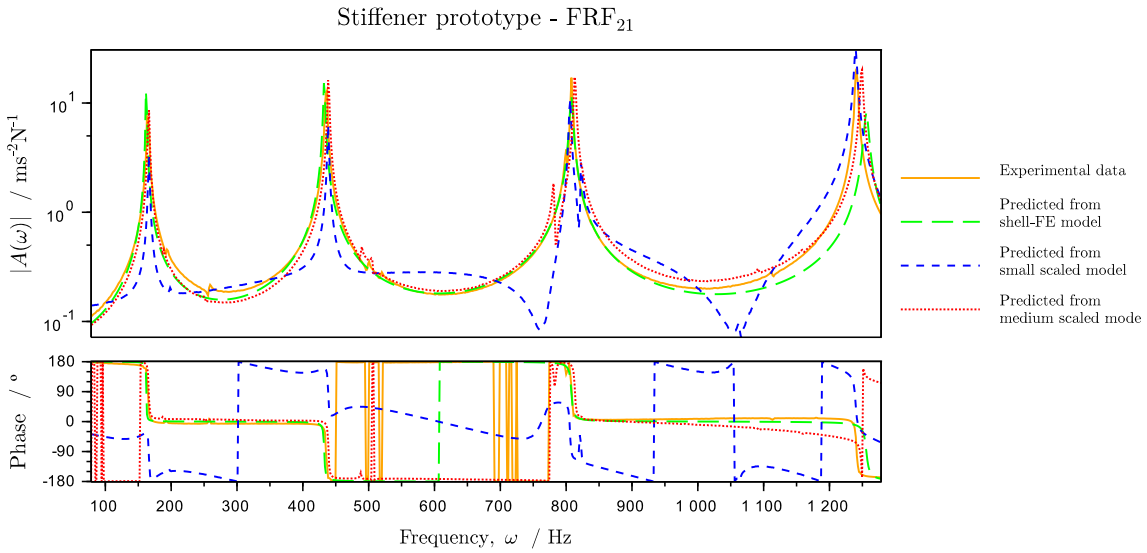

Figure 6.18.: Measured and predicted frequency response function FRF_{21} of the stiffener prototype.

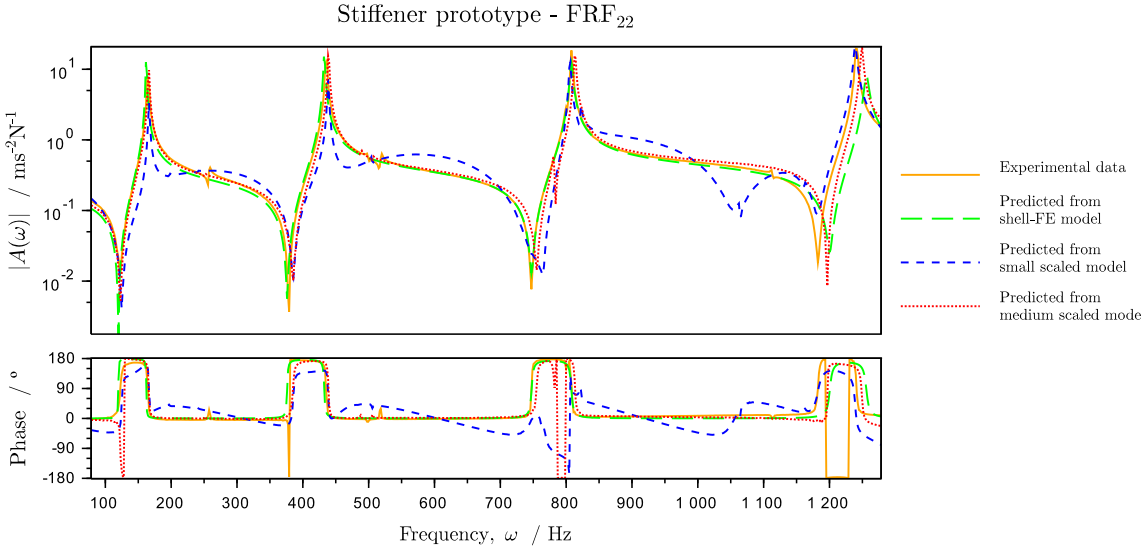

Figure 6.19.: Measured and predicted frequency response function FRF_{22} of the stiffener prototype.

Table 6.11.: Matrices of averaged LAC correlation indicators between the measured frequency response functions of the prototype (P), medium (MS) and small (SS) scaled models and those predicted from the scaled models (MS, SS) and FE-models (FE).

	P	MS	SS	FE
P	1	0.93	0.84	0.93
MS		1	0.88	0.95
SS			1	0.86
FE	(sym.)			1

(a) $\overline{LAC_{21}}$

	P	MS	SS	FE
P	1	0.90	0.83	0.87
MS		1	0.86	0.93
SS			1	0.83
FE	(sym.)			1

(b) $\overline{LAC_{22}}$

	P	MS	SS	FE
P	1	0.92	0.84	0.90
MS		1	0.87	0.94
SS			1	0.85
FE	(sym.)			1

(c) Average $\overline{LAC_{jk}}$ of previous subtables

Comparison of the natural frequencies of vibration

The frequency ranges covered in the experimental analyses of the stiffeners allowed to identify the first 4 natural frequencies of vibration in the web plane (oXZ), whose values are available in table 6.12.

Regarding the comparison between the experimental results in table 6.12 and those from the FE-models presented in table 6.13, excellent correlation is observed for the first 4 transverse vibration frequencies of the prototype, predicted with relative differences from -1.1% up to 0%. For the stiffeners in the other scales, the relative differences are higher, ranging in the following intervals: $[-2.5\%,\ -0.6\%]$ and $[-2.5\%,\ 0.2\%]$, respectively for the medium and small scaled model.

Alternatively, the use of scaled models provides an equally accurate tool to predict the transverse frequencies of vibration, presented in table 6.14. With regard to predictions for the prototype, the relative differences in relation to experimental data range in the following intervals: $[0.6\%,\ 1.4\%]$ and $[-0.2\%,\ 1.4\%]$, respectively for the use of medium and small scaled models. For the medium scaled model, the referred natural frequencies were predicted from the small scaled model with relative differences between -0.8% and 0.0% which is accurate, considering that these results are obtained experimentally from different (although similar) structures.

Table 6.12.: Experimental natural frequencies of vibration of the stiffener (f_i) in different scales.

transverse mode number i	Experimental data - f_i [Hz]		
	Prototype	Medium scaled model	Small scaled model
1	164	416	832
2	436	1096	2192
3	808	2032	4032
4	1242	3124	6199

Table 6.13.: Predicted frequencies of vibration for the stiffeners obtained using shell FE-models (f_i), and corresponding relative difference when compared with experimental results ($f_i^{(ref)}$).

transverse mode number i	Numerical predictions					
	Prototype		Medium scaled model		Small scaled model	
	f_i [Hz]	$\frac{f_i - f_i^{(ref)}}{f_i^{(ref)}}$ [%]	f_i [Hz]	$\frac{f_i - f_i^{(ref)}}{f_i^{(ref)}}$ [%]	f_i [Hz]	$\frac{f_i - f_i^{(ref)}}{f_i^{(ref)}}$ [%]
1	162	-1.1	405	-2.5	811	-2.5
2	432	-0.8	1081	-1.3	2162	-1.3
3	808	0.0	2020	-0.6	4039	0.2
4	1235	-0.6	3087	-1.2	6174	-0.4

Table 6.14.: Predicted frequencies of vibration for the stiffeners obtained using scaled models (f_i), and corresponding relative difference when compared with experimental results ($f_i^{(ref)}$).

transverse mode number i	Prototype				Medium scaled model	
	Predicted from medium scaled model		Predicted from small scaled model		Predicted from small scaled model	
	f_i [Hz]	$\frac{f_i - f_i^{(ref)}}{f_i^{(ref)}}$ [%]	f_i [Hz]	$\frac{f_i - f_i^{(ref)}}{f_i^{(ref)}}$ [%]	f_i [Hz]	$\frac{f_i - f_i^{(ref)}}{f_i^{(ref)}}$ [%]
1	166	1.4	166	1.4	416	0.0
2	438	0.6	438	0.6	1096	0.0
3	813	0.6	806	-0.2	2016	-0.8
4	1250	0.6	1240	-0.2	3100	-0.8

6.5.3.3. Stiffened plates (without surface finishing)

The dynamic response of the stiffened plates was analyzed up to 320 Hz, which correspond in the medium and small scaled models to similar frequency ranges up to 800 Hz and 1600 Hz, respectively.

In figures 6.20 to 6.23 the accelerances measured in the prototype of the stiffened plate are plotted along with corresponding predictions: one of them calculated through the shell FE-model of the prototype, and the other obtained applying accelerance and frequency scale factors to the measured FRFs of the scaled models.

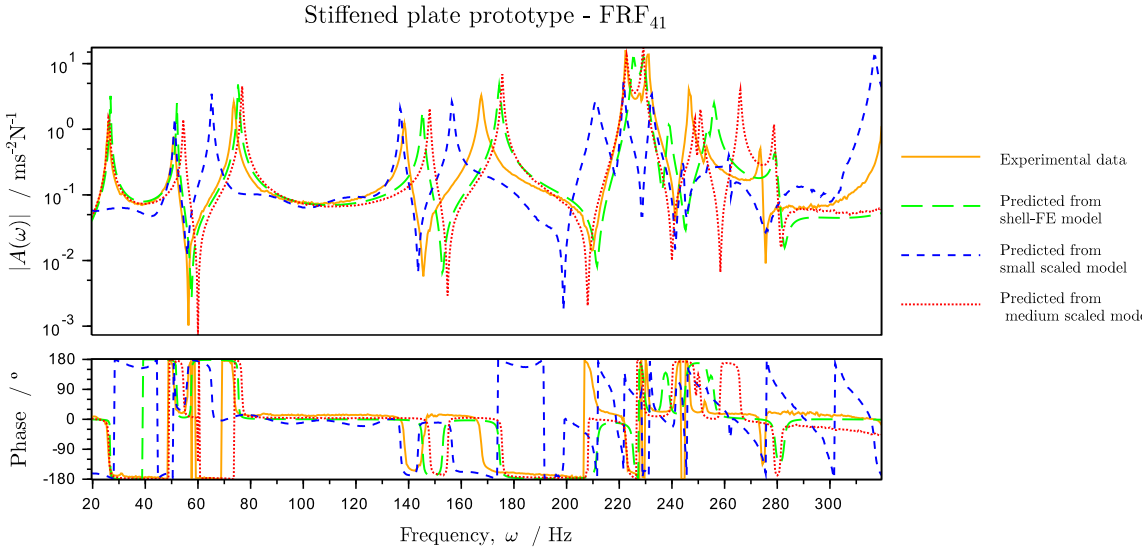

Figure 6.20.: Measured and predicted frequency response function FRF_{41} of the stiffened plate prototype.

Evaluation of the correlation between FRFs

The averaged LAC values were calculated according to equation (6.3) in order to evaluate the correlation of measured data and predicted accelerances of the stiffened plates, and are presented in table 6.15. It can be seen that the average $\overline{LAC_{jk}}$ ranges between 0.59 and 0.85, demonstrating the worst correlated results presented until now, particularly when experimental data or predicted results of the small scaled model are involved.

The scaled model testing was able to produce predictions as accurate as those of the FE-model only when predicting the accelerance of the prototype, based on the measured data from the medium scaled model.

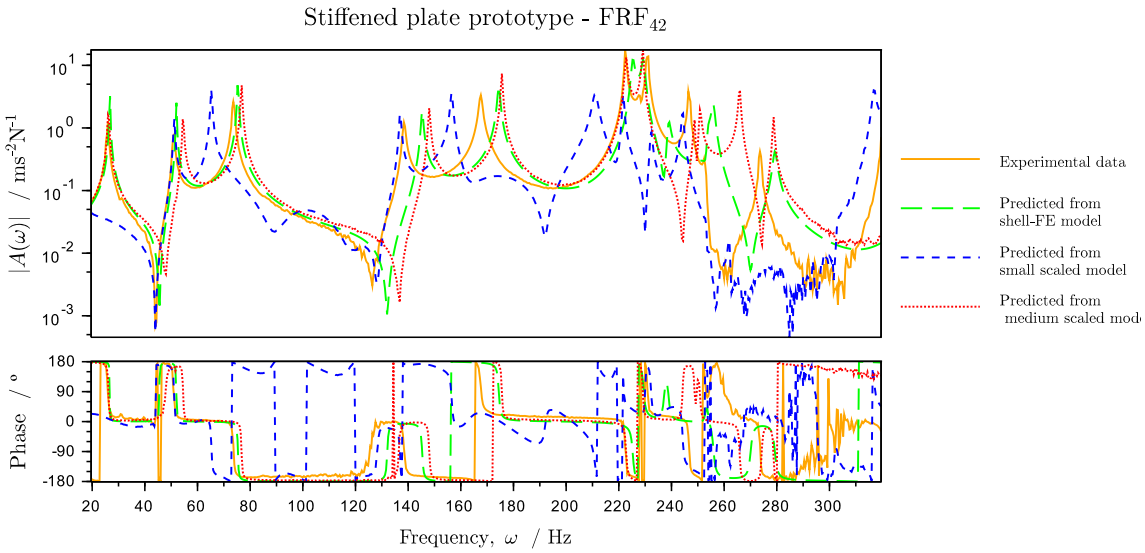

Figure 6.21.: Measured and predicted frequency response function FRF_{42} of the stiffened plate prototype.

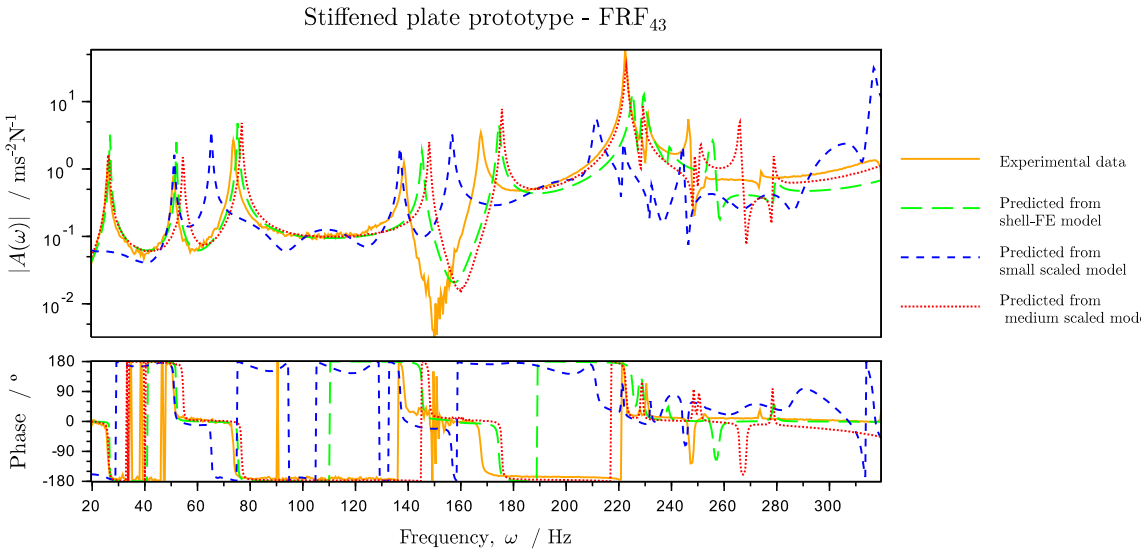

Figure 6.22.: Measured and predicted frequency response function FRF_{43} of the stiffened plate prototype.

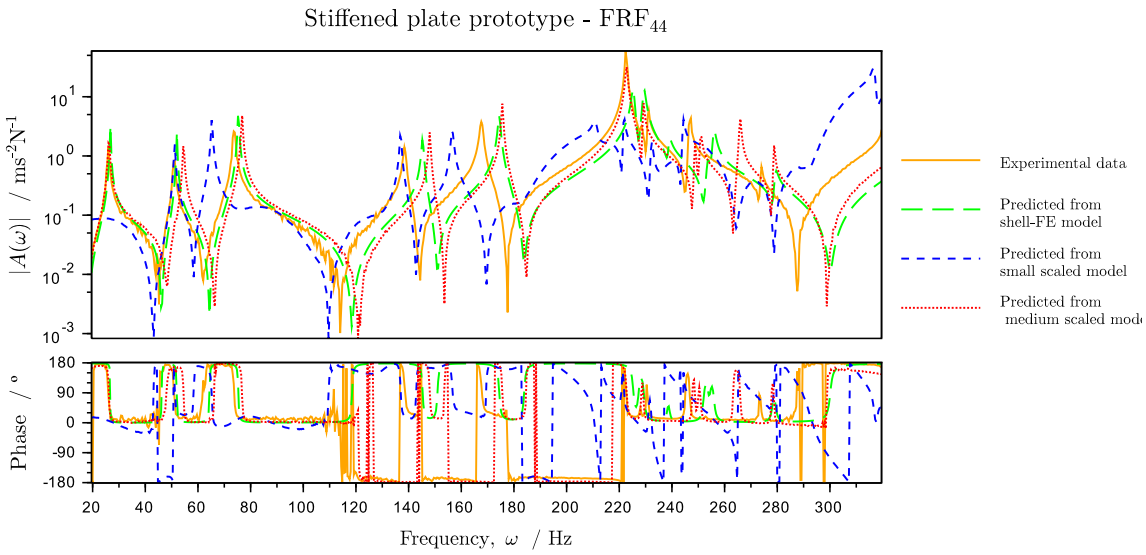

Figure 6.23.: Measured and predicted frequency response function FRF_{44} of the stiffened plate prototype.

Table 6.15.: Matrices of averaged LAC correlation indicators between the measured frequency response functions of the prototype (P), medium (MS) and small (SS) scaled models and those predicted from the scaled models (MS, SS) and FE-models (FE).

	P	MS	SS	FE
P	1	0.76	0.72	0.78
MS		1	0.60	0.83
SS			1	0.62
FE	(sym.)			1

(a) $\overline{LAC_{41}}$

	P	MS	SS	FE
P	1	0.67	0.64	0.73
MS		1	0.51	0.84
SS			1	0.55
FE	(sym.)			1

(b) $\overline{LAC_{42}}$

	P	MS	SS	FE
P	1	0.83	0.74	0.83
MS		1	0.70	0.89
SS			1	0.72
FE	(sym.)			1

(c) $\overline{LAC_{43}}$

	P	MS	SS	FE
P	1	0.69	0.67	0.72
MS		1	0.54	0.84
SS			1	0.55
FE	(sym.)			1

(d) $\overline{LAC_{44}}$

	P	MS	SS	FE
P	1	0.74	0.69	0.76
MS		1	0.59	0.85
SS			1	0.61
FE	(sym.)			1

(e) Average $\overline{LAC_{jk}}$ of previous subtables

Comparison of the natural frequencies of vibration

The FE-models predicted the experimentally measured natural frequencies of the stiffened plate prototype with relative differences ranging from −3.2% to 5.1%. Alternatively, through experimental scale models testing, the predictions based on the medium scaled model yielded relative differences ranging between −0.8% and 7.1%, oscillating very similarly to those of the FE-model. The performance of predictions based on the small scaled model is clearly the worst, with the fundamental frequency being under-predicted almost 45%, while the relative error in the following 8 identified natural frequencies ranges between −11.3% and 0.4%.

Regarding the prediction of the natural frequencies of the medium-scaled model, it is observed that predictions from its FE-model keep the relative differences in the ±5% range. Once again the fundamental frequency is under-predicted almost 45% by the small scaled model, and the following predicted 9 natural frequencies yielded relative differences between −15.1% and −1.6%.

It is highlighted that the FE-model of the small scaled model has also an inaccurate performance when predicting its natural frequencies of vibration: the fundamental frequency is over-predicted around 85% and for the following 9 frequencies, relative differences were found between −2.2% and 15.4%. Therefore, it can be concluded that the manufacturing process of the small plate somehow affected its behavior, such that:

- the shell FE-model of the small scale stiffened panel made inaccurate predictions due to some effect of the manufacturing process that became not negligible;
- the referred not negligible effect of the manufacturing process caused a distortion to the similarity between the small scaled model and the other larger stiffened plates.

Table 6.16.: Experimental natural frequencies of vibration of the stiffened plate (f_i) in different scales.

mode number i	Experimental data - f_i [Hz]		
	Prototype	Medium scaled model	Small scaled model
1	26.0	65	72
2	51.0	136	256
3	73.5	192	326
4	138.3	370	685
5	166.0	439	783
6	222.3	557	1055
7	231.0	573	1109
8	246.8	622	1161
9	253.0	628	1221
10	(n.i.)	665	1309
11	273.5	697	(n.i.)

Table 6.17.: Predicted frequencies of vibration for the stiffened plates obtained using shell FE-models (f_i), and corresponding relative difference when compared with experimental results ($f_i^{(ref)}$).

mode number	Numerical predictions					
	Prototype		Medium scaled model		Small scaled model	
i	f_i [Hz]	$\frac{f_i - f_i^{(ref)}}{f_i^{(ref)}}$ [%]	f_i [Hz]	$\frac{f_i - f_i^{(ref)}}{f_i^{(ref)}}$ [%]	f_i [Hz]	$\frac{f_i - f_i^{(ref)}}{f_i^{(ref)}}$ [%]
1	26.7	2.6	67	2.6	133	85.3
2	52.0	1.9	130	-4.5	260	1.5
3	75.3	2.5	188	-1.9	377	15.5
4	145.3	5.1	363	-1.8	727	6.1
5	174.4	5.1	436	-0.7	872	11.4
6	225.3	1.4	563	1.1	1126	6.8
7	229.4	-0.7	573	0.1	1147	3.4
8	238.9	-3.2	597	-4.0	1195	2.9
9	253.7	0.3	634	1.1	1269	3.9
10	255.9	(n.i.)	640	-3.8	1280	-2.2
11	279.3	2.1	698	0.2	1396	(n.i.)

Table 6.18.: Predicted frequencies of vibration for the stiffened plates obtained using scaled models (f_i), and corresponding relative difference when compared with experimental results ($f_i^{(ref)}$).

mode number	Prototype				Medium scaled model	
	Predicted from medium scaled model		Predicted from small scaled model		Predicted from small scaled model	
i	f_i [Hz]	$\frac{f_i - f_i^{(ref)}}{f_i^{(ref)}}$ [%]	f_i [Hz]	$\frac{f_i - f_i^{(ref)}}{f_i^{(ref)}}$ [%]	f_i [Hz]	$\frac{f_i - f_i^{(ref)}}{f_i^{(ref)}}$ [%]
1	26.0	0.0	14	-44.6	36	-44.6
2	54.4	6.7	51	0.4	128	-5.9
3	76.8	4.5	65	-11.3	163	-15.1
4	148.0	7.1	137	-0.9	343	-7.4
5	175.6	5.8	157	-5.7	392	-10.8
6	222.8	0.2	211	-5.1	528	-5.3
7	229.2	-0.8	222	-4.0	555	-3.2
8	248.8	0.8	232	-5.9	581	-6.7
9	251.0	-0.8	244	-3.5	611	-2.7
10	266.0	0.0	262	(n.i.)	655	-1.6
11	278.8	1.9	(n.i.)	(n.i.)	(n.i.)	(n.i.)

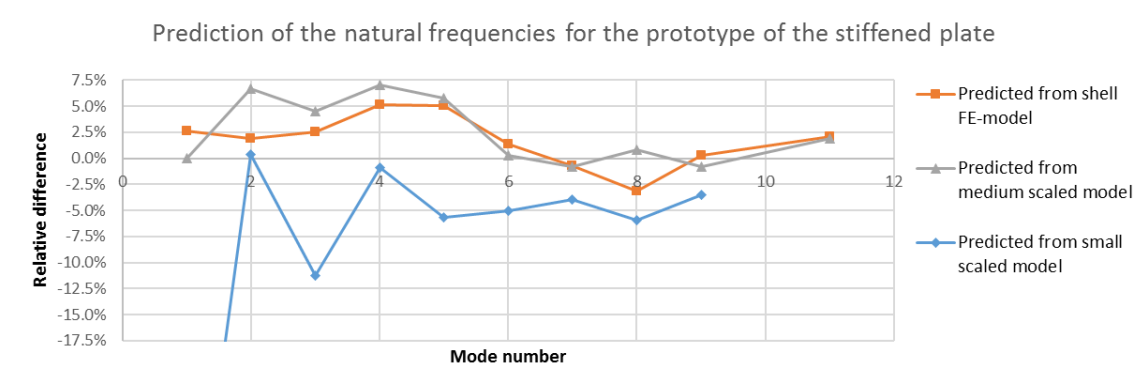

Figure 6.24.: Relative differences between predicted and experimental natural frequencies of the stiffened plate prototype.

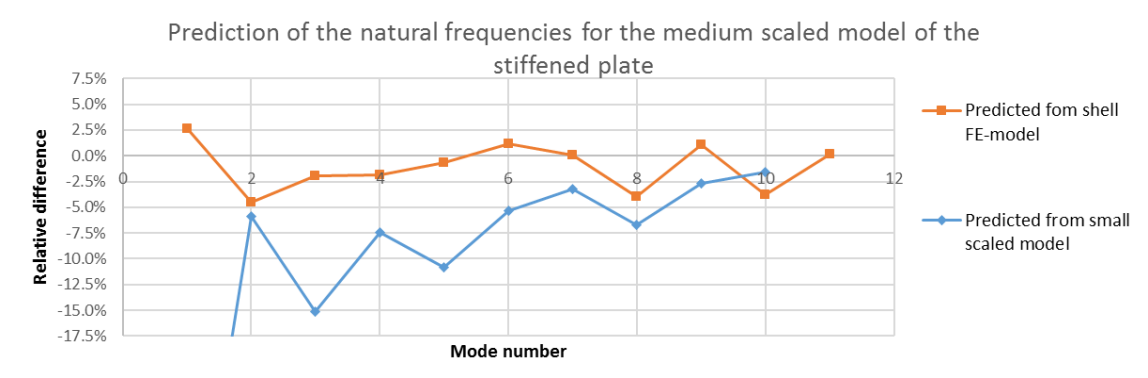

Figure 6.25.: Relative differences between predicted and experimental natural frequencies of the medium scaled model of the stiffened plate.

6.5.3.4. Galvanized scaled models of the stiffened plate prototype

Experimental results of the galvanized scaled models are presented below. Despite the small distortion of the medium scaled model geometry (depicted in figure 6.26), interesting additional results were provided by their experimental analysis.

The FE-models used to simulate the galvanized models are the same, except for the medium scaled model whose FE-model geometry was modified to respect the distorted geometry of the actual (physical) structure. According to the numerical results, the geometric changes caused a variation of -3.9% and 1.2% in the 6^{th} and 11^{th} natural frequencies, respectively. For all the other frequencies, the variation of results remained in the negligible $\pm 1\%$ range, and therefore, it is assumed that a valid comparison can be made for these frequencies between the galvanized and not galvanized stiffened plates.

In figures 6.27 to 6.30 the accelerances measured in the prototype of the stiffened plate are plotted along with corresponding predictions. Some improvements in the correlation between experimental data of the prototype and the accelerances predicted from the (galvanized) scaled models is readily noticeable at first glance.

Evaluation of the correlation between FRFs

Analyzing the calculated averaged LAC values in table 6.19 and comparing them with those in table 6.15, it is observed that:

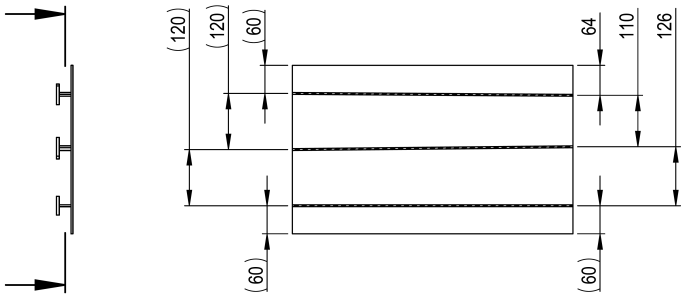

Figure 6.26.: Geometric distortion caused by two errors in the parallelism between stiffeners and their position in relation to the base plate.

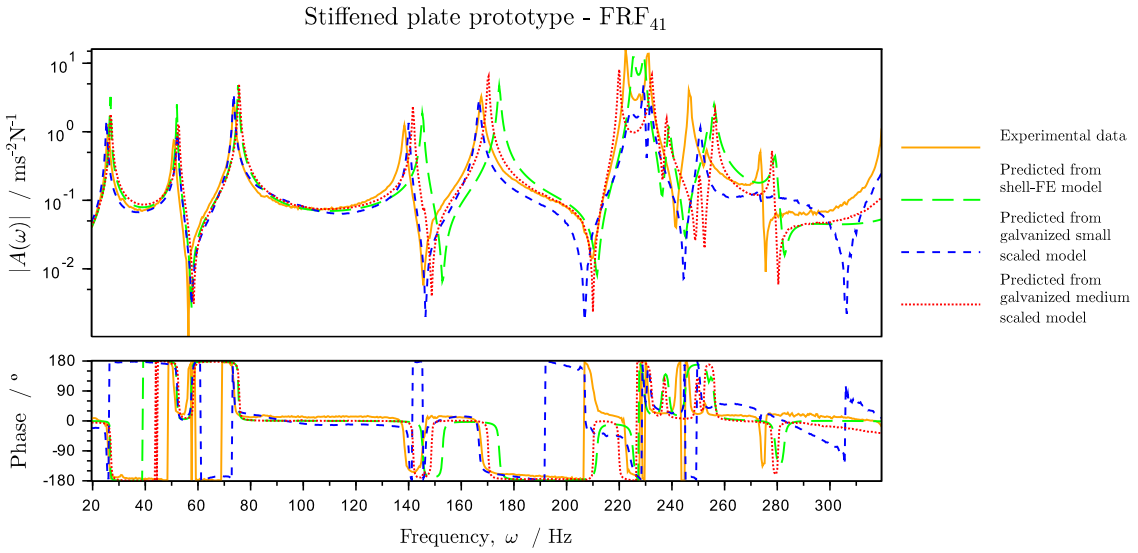

Figure 6.27.: Measured and predicted frequency response function FRF_{41} of the stiffened plate prototype, whose scaled models were galvanized.

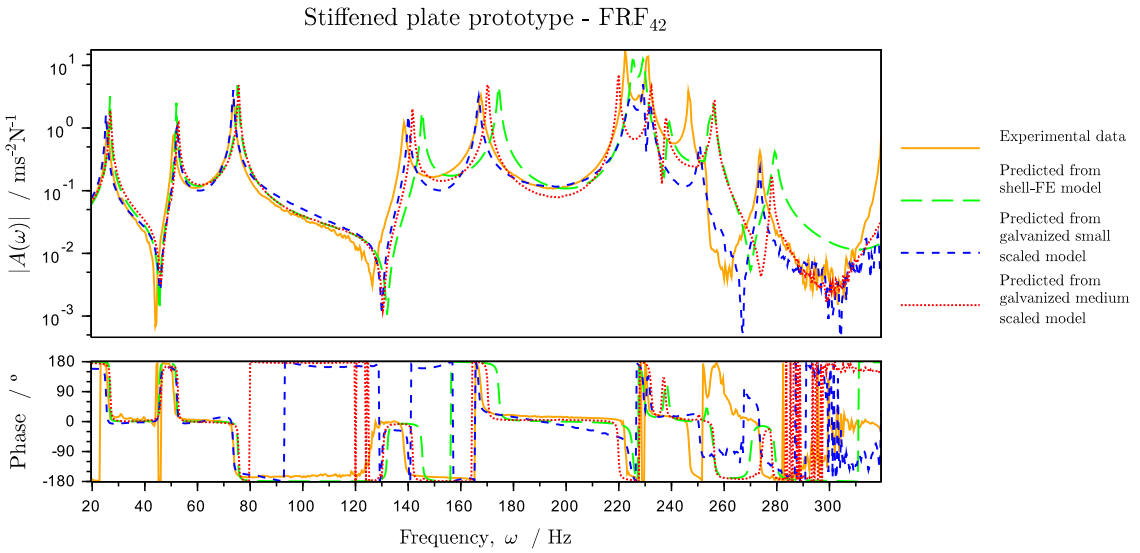

Figure 6.28.: Measured and predicted frequency response function FRF_{42} of the stiffened plate prototype, whose scaled models were galvanized.

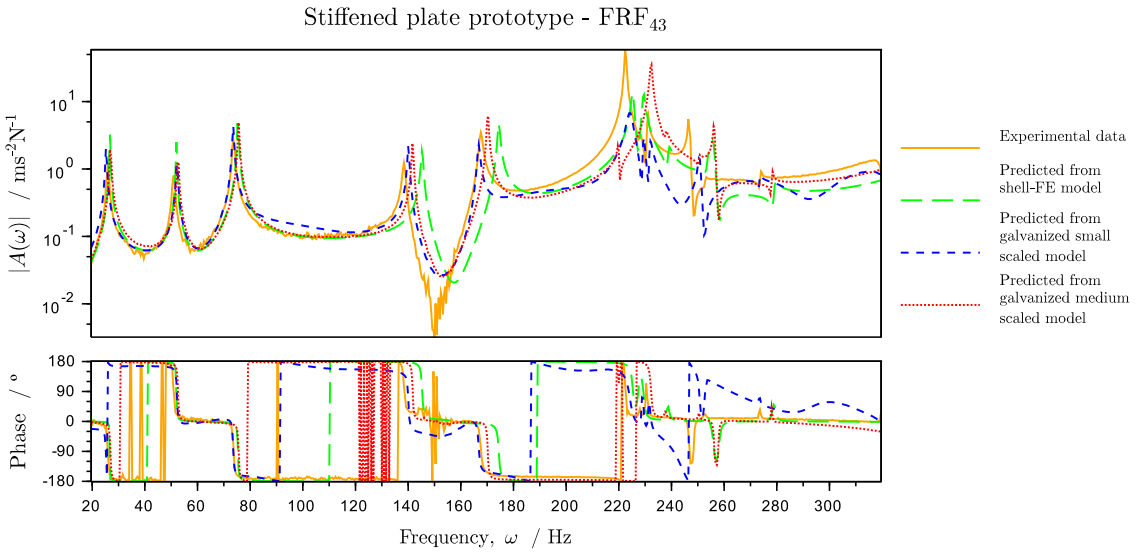

Figure 6.29.: Measured and predicted frequency response function FRF_{43} of the stiffened plate prototype, whose scaled models were galvanized.

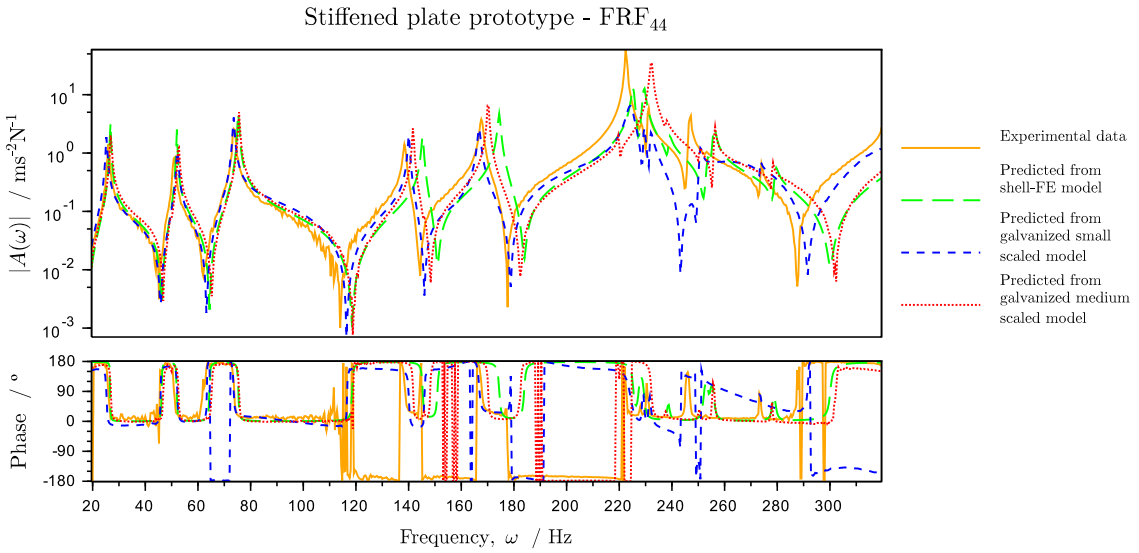

Figure 6.30.: Measured and predicted frequency response function FRF_{44} of the stiffened plate prototype, whose scaled models were galvanized.

- The correlation between the experimental data of the prototype and the results from its FE-model is the same, given that none of those FRFs suffered changes;
- The prediction of the experimental data of medium scaled model by its FE-model, as well as the prediction of the prototype behavior based on the medium scaled model suffered residual improvements of their correlation. The justification for that improvement is expected to be mostly due to the effect of the galvanizing process on the medium scaled model, given that the remaining results remained unchanged[1];
- The most significant increase of the averaged LAC values was verified for correlations involving the small scaled model. Given that the considered experimental data of the (not galvanized) prototype remained unchanged, and considering that the effect of the galvanizing process caused residual improvements of the LAC values involving the medium scaled model, it may also be concluded that the significant improvements in the LAC values of correlations involving the small scaled model are due to effects of the galvanizing process.

From a generic point of view, the predictions using the galvanized scaled model correlated the experimental data of the prototype better then its FE-model. Even the prediction using the galvanized small scaled model reached a level of correlation of the experimental data from the medium scaled model, that in an average manner is as good as that of the numerical results.

[1]For the purpose of LAC calculation, the distortions of the medium scaled model were not considered in the FE-model, and therefore in the predicted FRFs.

Table 6.19.: Matrices of averaged LAC correlation indicators between the measured frequency response functions of the prototype (P), medium (MS) and small (SS) scaled models and those predicted from the scaled models (MS, SS) and FE-models (FE).

	P	MS	SS	FE
P	1	0.82	0.85	0.78
MS		1	0.81	0.85
SS			1	0.79
FE	(sym.)			1

(a) $\overline{LAC_{41}}$

	P	MS	SS	FE
P	1	0.79	0.83	0.73
MS		1	0.83	0.82
SS			1	0.76
FE	(sym.)			1

(b) $\overline{LAC_{42}}$

	P	MS	SS	FE
P	1	0.86	0.87	0.83
MS		1	0.88	0.90
SS			1	0.86
FE	(sym.)			1

(c) $\overline{LAC_{43}}$

	P	MS	SS	FE
P	1	0.70	0.82	0.72
MS		1	0.88	0.88
SS			1	0.77
FE	(sym.)			1

(d) $\overline{LAC_{44}}$

	P	MS	SS	FE
P	1	0.79	0.84	0.76
MS		1	0.85	0.86
SS			1	0.79
FE	(sym.)			1

(e) Average $\overline{LAC_{jk}}$ of previous subtables

Comparison of the natural frequencies of vibration

Comparing the experimental results from the galvanized scaled models (in table 6.20) with the numerical predictions in table 6.21, it is observed that the interval of relative differences between those results (also included in the latter table) is reduced from $[-4.5\%, 2.6\%]$ to $[-2.0\%, 2.6\%]$ in the medium scaled and from $[-2.2\%, 85.3\%]$ to $[-0.4\%, 5.9\%]$ in the small scale. Similarly to the LAC values, these results demonstrate that the galvanizing process may have a significant effect in the dynamic response of a structure, which in this case are stiffened plates.

Table 6.20.: Experimental natural frequencies of vibration of the stiffened plate (f_i) in different scales.

mode number i	Experimental data - f_i [Hz]	
	Galvanized medium scaled model	Galvanized small scaled model
1	67	126
2	132	261
3	189	368
4	354	700
5	426	834
6	550	1122
7	581	1147
8	595	1160
9	627	1253
10	641	(n.i.)
11	696	1368

Regarding the prediction of the natural frequencies for the large scale stiffened panel using scaled models, it is observed that the relative differences between the predictions and the experimental data is in the interval $[-3.5\%,\ 3.1\%]$, narrower than that of the results obtained by the FE-model, as shown by figure 6.31. The small scaled model, apart from the 8^{th} mode frequency, also predicted quite accurate results with relative differences in a range slightly larger than $\pm 2.5\%$.

Lastly, with regard to the predictions of the natural frequencies of the medium scaled structure, it is verified from table 6.22 or from figure 6.32 that both the FE-model and small scaled model provided good results, with relative differences approximately in the range of $\pm 2.5\%$, except for the fundamental frequency predicted by the scaled model that reached a relative difference of -6%.

Table 6.21.: Predicted frequencies of vibration for the stiffened plates obtained using shell FE-models (f_i), and corresponding relative difference when compared with experimental results ($f_i^{(exp)}$).

mode number	Numerical predictions			
	Galvanized medium scaled model		Galvanized small scaled model	
i	f_i [Hz]	$\frac{f_i - f_i^{(ref)}}{f_i^{(ref)}}$ [%]	f_i [Hz]	$\frac{f_i - f_i^{(ref)}}{f_i^{(ref)}}$ [%]
1	67	0.3	133	5.9
2	131	-0.5	260	-0.4
3	190	0.3	377	2.4
4	363	2.6	727	3.8
5	434	2.1	872	4.6
6	541	-1.5	1126	0.4
7	569	-2.0	1147	0.0
8	600	0.8	1195	3.0
9	635	1.4	1269	1.3
10	640	0.0	1280	(n.i.)
11	706	1.6	1396	2.1

Table 6.22.: Predicted frequencies of vibration for the stiffened plates obtained using scaled models (f_i), and corresponding relative difference when compared with experimental results ($f_i^{(exp)}$).

mode number	Prototype				Medium scaled model	
	Predicted from medium scaled model		Predicted from small scaled model		Predicted from small scaled model	
i	f_i [Hz]	$\frac{f_i - f_i^{(ref)}}{f_i^{(ref)}}$ [%]	f_i [Hz]	$\frac{f_i - f_i^{(ref)}}{f_i^{(ref)}}$ [%]	f_i [Hz]	$\frac{f_i - f_i^{(ref)}}{f_i^{(ref)}}$ [%]
1	27	3.1	25	-3.1	63	-6.0
2	53	3.1	52	2.4	131	-0.8
3	76	2.9	74	0.1	184	-2.6
4	142	2.4	140	1.3	350	-1.1
5	170	2.5	167	0.5	417	-2.0
6	220	-1.1	224	1.0	561	2.1
7	232	0.5	229	-0.7	574	-1.2
8	238	-3.5	232	-6.0	580	-2.5
9	251	-0.9	251	-0.9	627	0.0
10	256	0.0	(n.i)	(n.i.)	(n.i)	(n.i.)
11	278	1.7	274	0.0	684	-1.7

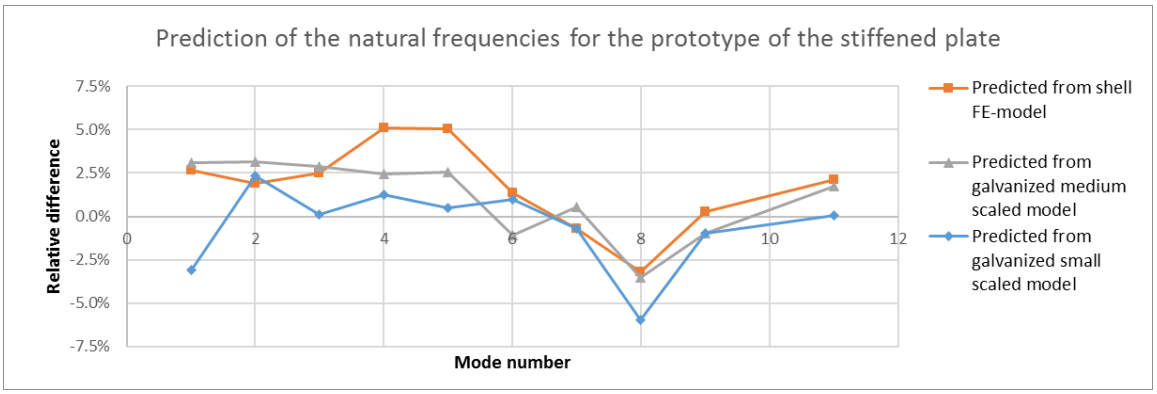

Figure 6.31.: Relative differences of the predicted natural frequencies for the stiffened plate prototype when compared with the experimentally (directly) obtained results.

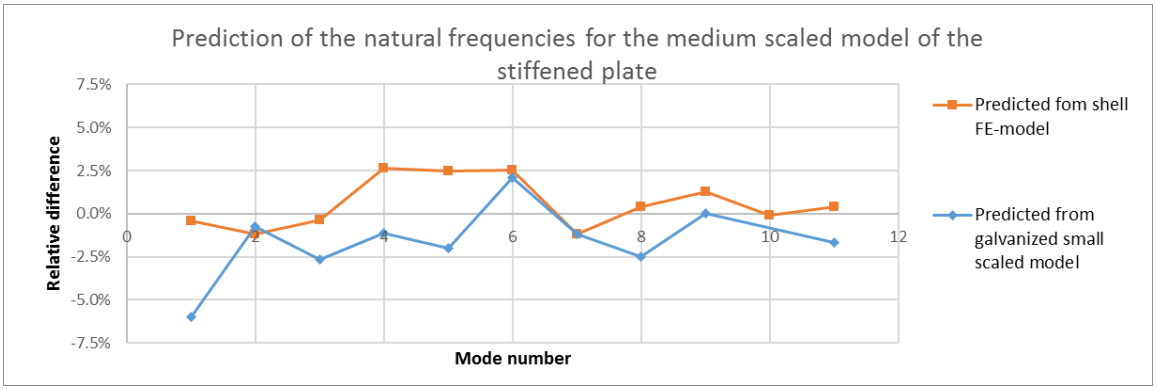

Figure 6.32.: Relative differences of the predicted natural frequencies for the small scaled model of the stiffened plate when compared with the experimentally (directly) obtained results.

6.5.4. Overview of results

An overview of the main results regarding the prediction of accelerance frequency response functions, and particularly, the prediction of natural frequencies is presented in figures 6.33 to 6.36, respectively.

In following concluding remarks, the superscripts (SS⇔P), (MS⇔P) and (SS⇔MS) stand for correlations between experimentally predicted and experimentally measured accelerances (EXP⇔EXP) of the small scaled model (SS), medium scaled model (MS) and prototype (P). Similarly, (FE⇔P), (FE⇔MS) and (FE⇔SS) are superscripts for correlations between numerically simulated and experimentally measured accelerances (NUM⇔EXP), where FE stands for FE-model of the experimentally measured structure.

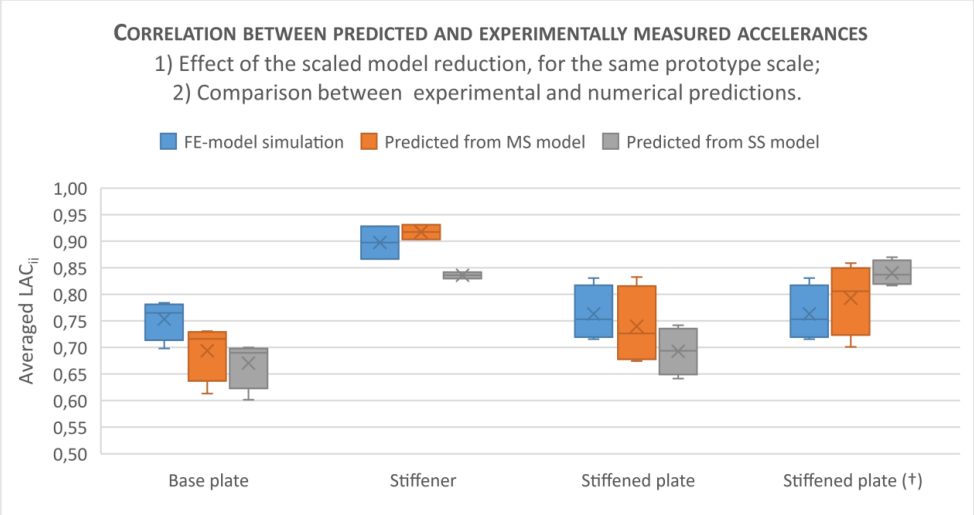

Figure 6.33.: Overview of $\overline{LAC_{jk}}$ between predicted and measured accelerances, for large scale prototypes of increasing complexity. Predictions were calculated using numerical FE-model simulation and experimental scaled model testing. Series marked with (†) includes the predictions based on the galvanized scaled models. MS and SS refers to medium scaled and small scaled, respectively.

Effects of the scale reduction

Analyzing the effect of scale reduction (for fixed prototype scale), from the comparison of $\overline{LAC_{jk}}^{(MS\Leftrightarrow P)}$ and $\overline{LAC_{jk}}^{(SS\Leftrightarrow P)}$ plotted in figure 6.33, a consistent decrease is observed in the correlation values corresponding to accelerances predicted from not-galvanized scaled models.

However, and unexpectedly, for experimental scaled model testing using galvanized scaled models, the results from the small scale model correlate with the experimental data better than those from the medium scaled model: $\overline{LAC_{jk}}^{(SS\Leftrightarrow P)} > \overline{LAC_{jk}}^{(MS\Leftrightarrow P)}$. These results suggest that the observed changes in the correlation metric are not primarily driven by scale reduction differences. Further explanations are given below under the topic covering effects of residual stresses.

In the absence of consistent scale reduction effects, it makes no sense to analyze the evolution of that effect with the increasing complexity of the tested structure, which nevertheless is also not observed.

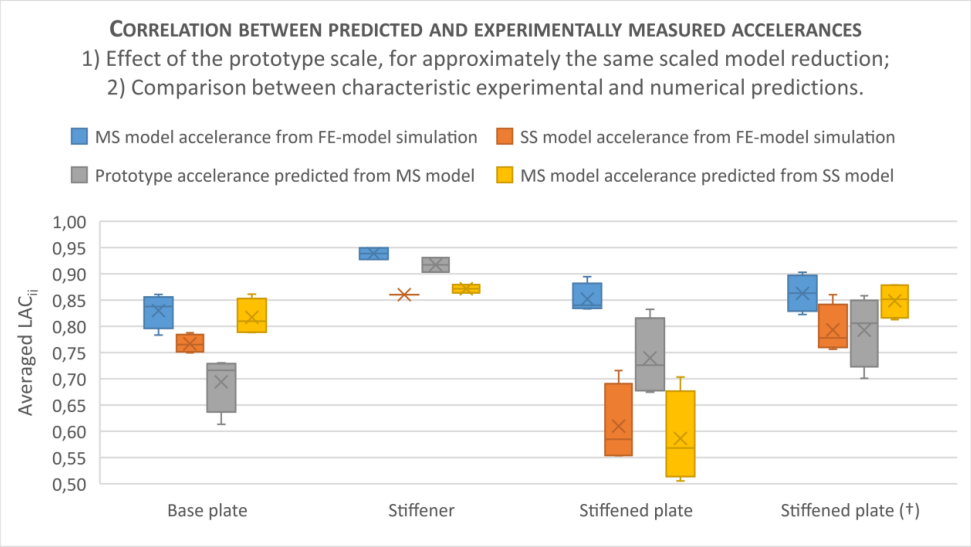

Figure 6.34.: Overview of $\overline{LAC_{jk}}$ between measured accelerances of large scale and medium scale prototypes and those measured from medium scaled (MS) and small scaled (SS) models, respectively. Series marked with (†) includes the predictions based on the galvanized scaled models. Correlations between calculated results from FE-model simulation of the selected scaled models and theirs experimental data allow to compare how scale variation affects both the simulations techniques.

On the other hand, from the analysis of the relative differences plotted in figure 6.35 and obtained predicting natural frequencies of the large scale prototypes, from the analysis of their medium and small scaled models, similar conclusions are taken.

Smaller scaled models does not imply higher relative difference between predicted natural frequencies and measured data. In the base plate and stiffeners the same average value was observed for scaled models of different sizes. Indeed, with regard to the galvanized stiffened plates, more accurate predictions were obtained from the small scaled model.

Effects of the prototype scale

The comparison between $\overline{LAC_{jk}}^{(MS \Leftrightarrow P)}$ and $\overline{LAC_{jk}}^{(SS \Leftrightarrow MS)}$, plotted in figure 6.34, allows to analyze possible effects on the correlation metric values when prototypes with different scales are experimentally analyzed by scaled models with the same or near scale reductions.

The observed changes are not consistent; when the prototype scale is reduced 60% both significant increase ($\overline{LAC_{jk}}^{(SS \Leftrightarrow MS)} >> \overline{LAC_{jk}}^{(MS \Leftrightarrow P)}$) and decrease ($\overline{LAC_{jk}}^{(SS \Leftrightarrow MS)} << \overline{LAC_{jk}}^{(MS \Leftrightarrow P)}$) are observed in their values, respectively, for the base plate and stiffened plate, while comparatively both minor decrease and increase are observed, respectively, for the stiffener and galvanized scaled stiffened plates.

Similarly, no consistent relation was observed between the prototype scale and the relative differences between obtained natural frequencies and experimental data.

Effect of structural increasing complexity in structural similitude

The Modular Approach considers that for a generic complex structure composed by n sub-systems two complex structures will be similar in relevant characteristics if a bi-unique

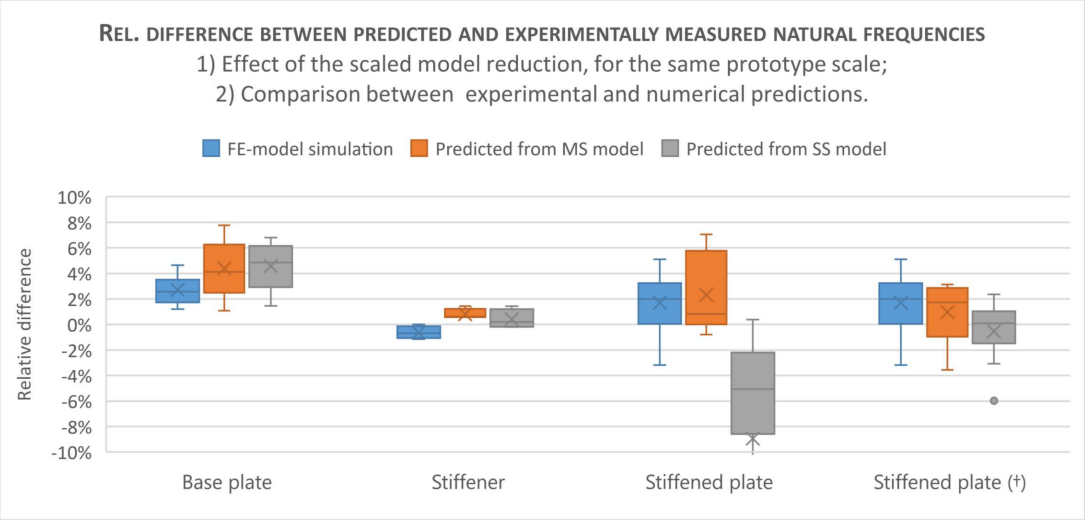

Figure 6.35.: Overview of relative differences between predicted and measured natural frequencies, for large scale prototypes of increasing complexity. Predictions were calculated using numerical FE-model simulation and experimental scaled model testing. Series marked with (†) includes the predictions based on the galvanized scaled models. MS and SS refers to medium scaled and small scaled, respectively.

transformation can be derived between the characteristics of each one of its basic structural elements seen as a free-body diagram. This means that each of the sub-structures of a complex structure has to be similar to the equivalent substructure of the scaled model, and that additional similarity conditions are imposed in order to relate the scaling relationships of each sub-structure.

An alternative perspective is that if any of the substructures of the complex structure is distorted, the similitude of the whole complex structure will be distorted as well, depending on the influence that the substructure has in the full structure.

The analysis of the results in figures 6.33 and 6.34 reveals that the maximum value for any $\overline{LAC_{jk}}^{(EXP \Leftrightarrow EXP)}$ metric of the stiffened plates are outlined by the upper limit obtained for its simpler substructures, regardless of the scale reduction and prototype scale effects or even the effect of the galvanization.

In addition, it is notorious that the galvanization process significantly increased the maximum LAC of the stiffened plate to a value closer to that of its simpler substructure, which in this case is the stiffener.

Effect of residual stresses

Lastly, some research is introduced that, although covering topics that are out of the initial scope of this experimental program, may help understanding some of the obtained results.

One of the most unexpected effects are those of the galvanization process. For the tested stiffened plates, cold-galvanization technology was employed, requiring the parts to be shot-blasted or sandblasted prior to dipping bath.

Although residual stresses induced by manufacturing processes are often neglected in structural analysis due to challenging aspects associated with their simulation, the fact is that their effect has long been noticed and documented.

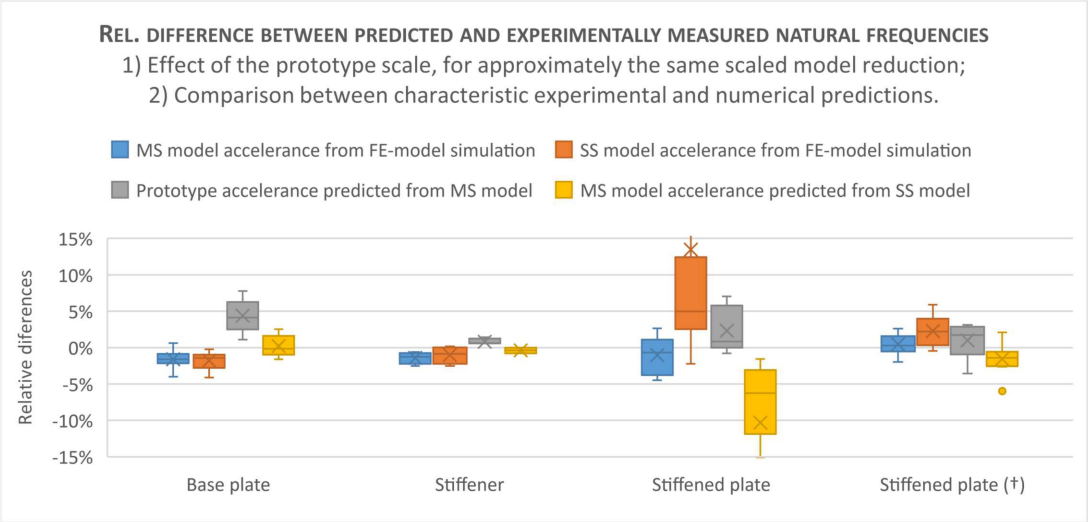

Figure 6.36.: Overview of relative differences between measured natural frequencies of large scale and medium scale prototypes and those measured from medium scaled (MS) and small scaled (SS) models, respectively. Series marked with (†) includes the predictions based on the galvanized scaled models. Correlations between calculated results from FE-model simulation of the selected scaled models and theirs experimental data allow to compare how scale variation affects both the simulations techniques.

Regarding the fatigue behavior, Lessells and Murray (1941) concluded in their research that shot-blasting process produces a cold working of the surface which is the main contributing factor to increase in fatigue strength. The measured depth of cold working is around 0.15 mm, which is in the same order of magnitude of the values measured by the same authors for cold rolled specimens (0.15 mm-0.38 mm). As the depth of cold working is independent of the part thickness, it can be inferred that the effect of the same shot-blasting process is higher for smaller scaled models.

More recently, Galtier and Statnikov (2003) referred that the sand blasting operation gives a significant fatigue improvement by the introduction of residual stresses similar to shot penning. Also Kim and Jeong (2013) experimentally concluded that blast cleaning for subsequent painting can result in a significant decrease in tensile residual stress and the introduction of compressive residual stress.

Unexpected results were also obtained for the base plates, particularly for predictions of the prototype based on the medium and small scaled models. Considering the simplicity of the base plates when compared with stiffeners and stiffened plates, higher correlations and lower relative differences were expected.

Once again this is likely to be explained by the residual stresses induced by the manufacturing process of steel plates, including: uneven cooling after hot-rolling, plastic deformation caused by cold-straightening (uncoiling process) and/or cutting operations (such as shearing) (Abambres and Quach, 2016).

Lieven and Greening (2001) experimentally measured the natural frequencies of a 1 mm-thick sheet plate (measuring 290 mm by 150 mm) suspended vertically in a free-free boundary conditions. In comparison with the experimental data, the relative differences of the first 10 FE predicted frequencies are negative except for the 3^{rd} and 9^{th} mode, ranging between -10% and 6.1%. After annealing, the plates revealed curvatures that according

to the authors are caused by the stresses induced during the manufacturing process of the plates, particularly in the uncoiling process.

The results of current case study are similar to those obtained by Lieven and Greening (2001). As referred in table 6.4, the small and medium scaled base plates share the same (as rolled) delivery condition while the material for the prototype base plate was delivered in the normalized rolling condition (which is a type of annealing); as expected, the natural frequencies of the as rolled plates are higher due to stress stiffening effects. Besides it is highlighted that having the same delivery condition, and therefore more similar state of residual stresses, the most accurate predictions for the natural frequencies of the medium scaled plate were obtained from the experimental analysis of the small scaled plate.

6.6. Static three point bending

The not-galvanized scaled stiffened plates were subjected to a static test, whose configuration is quite similar to that of a three point bending. As depicted in the exploded view from figure 6.37, an actuation block transfers the loading from the hydraulic actuator to the square loading bar. The stiffened plates are simply supported along the shorter edges on the stiffeners side and loaded at the mid-length.

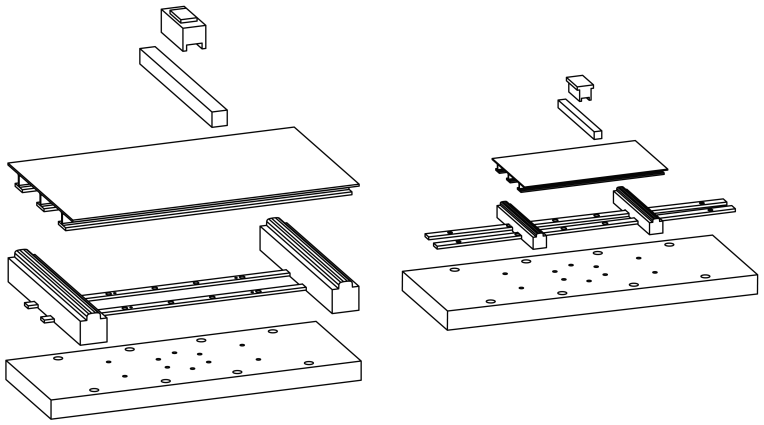

(a) Medium 2/5-scale model (b) Small 1/5-scale model

Figure 6.37.: Exploded view of the experimental setups for the static analysis. From top to bottom: actuation block, loading bar, stiffened plate, supports connected by fixing bars, (fixed) base of the (INSTRON 4208) testing machine.

The loading bar is designed to have higher rigidity than that of the plate, but even so its deformation is not negligible. Indeed, the system under analysis is intended to be the stiffened plate plus its elastic loading structural element.

The actuation blocks and loading bars used for the small stiffened plate are scaled replicas of those used for the medium stiffened plate. Apart from some distortions, their geometry is based in that initially planned for the prototype testing, which was not performed due to safety issues. For example, the upper part of the supports contacting with the stiffeners is similar to that of the rail profile 54E1 (prEN 13674-1, 2002).

The distance between the supports of the prototype is 1320 mm. According to the geometric scale factors, in the medium and small scale that distance is 528 mm and 264 mm, respectively. The positioning, spacing and centering of the supports in relation to the hydraulic actuator is guaranteed mechanically by fixing bars screwed to both the supports and

the base of testing machine.

The scaled model testing was performed mounting the previous setups on an INSTRON 4208 universal testing machine, which was equipped with an INSTRON 2518-805 load cell (with 100 kN static rating), as shown in figures 6.38.

(a) Medium 2/5-scale model (b) Small 1/5-scale model

Figure 6.38.: Experimental setups for static three point bending of the stiffened plates.

Additionally to the load and displacement data directly acquired from the testing machine, the outer flanges of each panel were instrumented at the mid-length, as shown in figure 6.39, with Vishay Micro-Measurements strain gauges of type CEA-06-125UR-120 (with gage factor equal to 2.095).

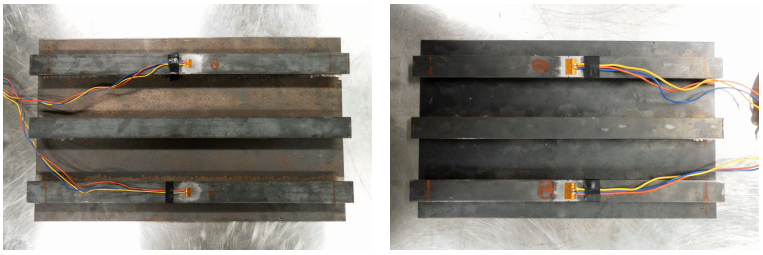

(a) Medium 2/5-scale model (b) Small 1/5-scale model

Figure 6.39.: Scaled models of the stiffened plate prototype instrumented at mid-length with strain gauges type CEA-06-125UR-120.

6.6.1. ABAQUS FE-models and preliminary numerical results

In order to obtain a preliminary simulation of the stiffened plate, two numerical models using ABAQUS solid elements of type C3D8R are considered:

- simplified solid FE-model (92036 elements, from which 64800 in the plate), with a mesh global size equal to 5 mm in the medium scaled model, and imposing at least 4 elements through any thickness;

- detailed solid FE-model (107112 elements, from which 79876 in the plate), which additionally includes the intermittent staggered weld beads and material discontinuity (0.1 mm gap) between base plate and stiffener web, as well between this and the stiffener flange.

Both models have surface-to-surface interactions simulating the normal behavior as an "hard contact" (with allowed separation) in the following interfaces: actuation block /

loading bar, loading bar / base plate, stiffeners web / supports. The detailed solid FE-model additional considers that interaction between the surfaces created by the 0.1 mm gaps.

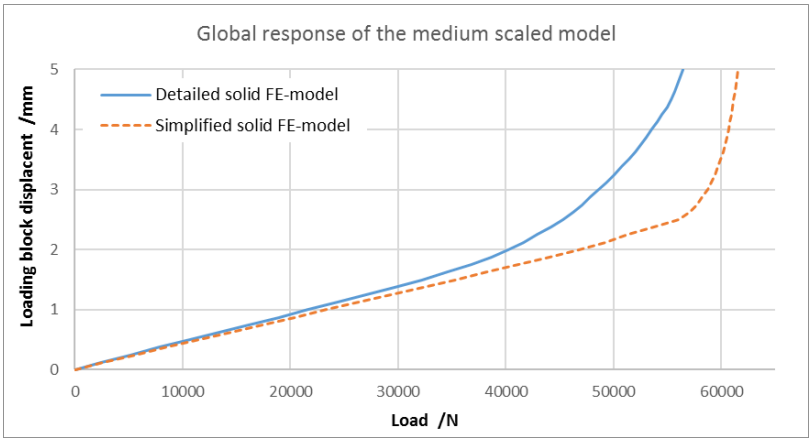

(a) Global load-displacement behavior.

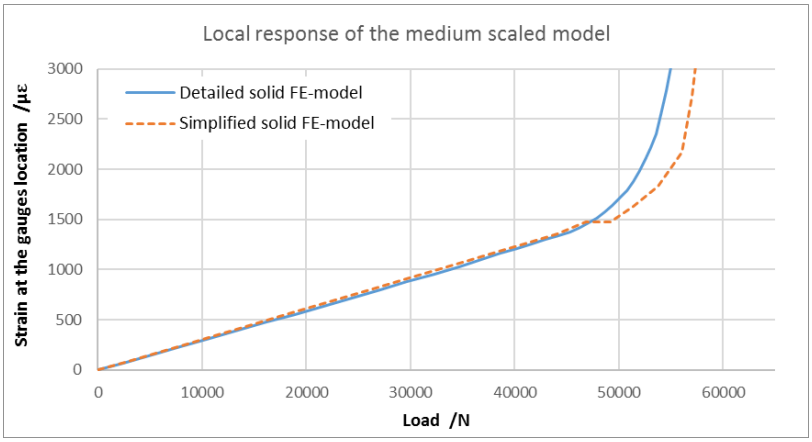

(b) Local load-strain behavior.

Figure 6.40.: Predicted displacement of the loading block and predicted strain at the mid-length measured in the gauges locations (depicted in figure 6.39a).

The load-displacement and load-strain curves obtained from both numerical FE-models are plotted in figure 6.40. It is observed that for the considered gauge locations, quite similar strain predictions were obtained for loads under 40 kN; only one curve was plotted because the model yields the same results for both points, due to its symmetry. On the other hand significant differences are observed for the predicted load-displacement curves, particularly for loads higher than 30 kN. As expected, the detailed model has lower rigidity and predicts a significantly lower yielding load: around 30 kN, while in the simplified model it is around 45 kN.

Given these preliminary results, and in order to ensure that through the experimental testing the base material is kept in linear elastic domain, 20 kN was defined as the maximum testing load.

6.6.2. Experimental results

A total of 5 tests were performed sequentially in each stiffened plate. For the large and small scaled models, those results are plotted in figures 6.41 and 6.42. No mechanical pre-

loading was applied. Alternatively, and unless another value is identified, the presented data were truncated for loads under 300 N and 88 N, in the medium and small scale experiments respectively, and reinitialized from that point.

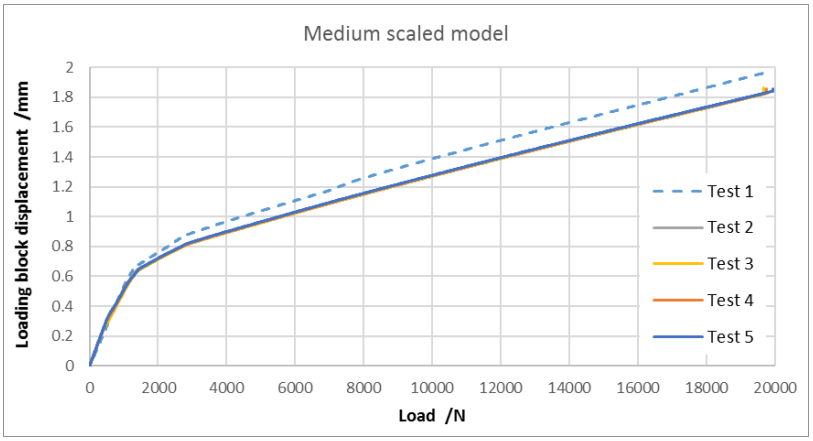

(a) Global load-displacement behavior.

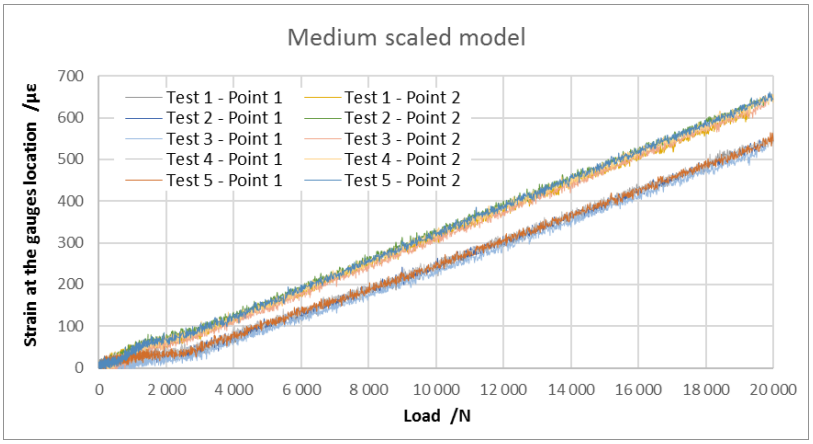

(b) Local load-strain behavior.

Figure 6.41.: Experimental load-displacement and load-strain curves measured from the medium scaled model.

Regarding the medium scale experiments, excellent reproducibility was obtained for the load-displacement curves after the first test. Besides, no significant changes between tests were observed in load-strain curves, apart from some expected measurements noise.

On the other hand, regarding the small scale experiments, the same observations remain valid for the load-displacement data. However, there are more scatter in the measured load-strain data. Particularly, from the analysis of the load-strain curves for pre-loads between 200 N to 400 N it was observed that the data of the first test is the only which tends to deviate from the average value of the remaining tests.

6.6.2.1. Analysis of the load-displacement behavior

The apparently non-linear behavior of the stiffened plates is caused by geometric imperfections (mostly induced by the welding process). In the medium scaled model, visual inspection during the experimental tests allowed to divide the curve into three approximately linear sections:

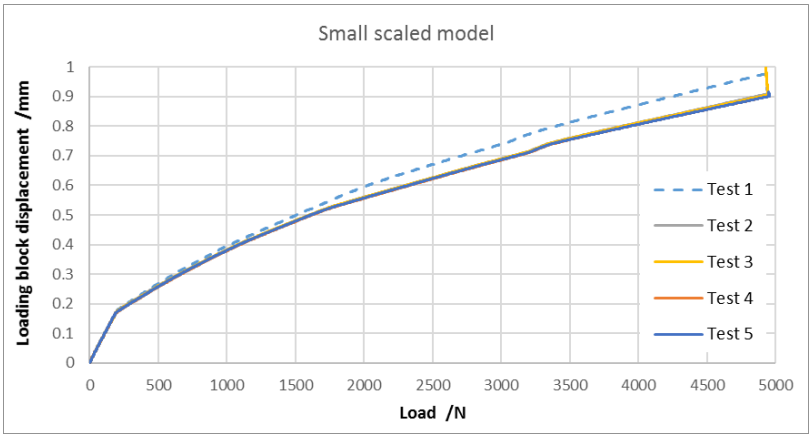

(a) Global load-displacement behavior.

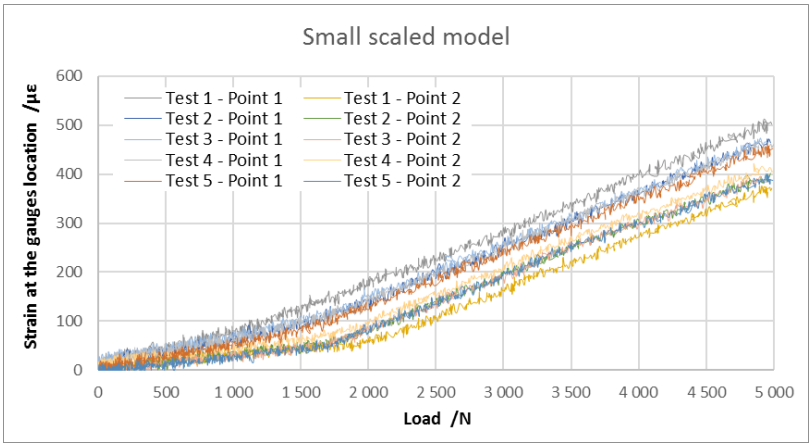

(b) Local load-strain behavior.

Figure 6.42.: Experimental load-displacement and load-strain curves measured from the small scaled model.

- loads up to 1400 N: as the plate residual twisting is removed, the number of contacts (between the stiffeners web and the supports) increases from 2 (instable) to 4;
- loads from 1400 N up to 2800 N: as the residual deformation along the shortest edge of the plate is removed, the clearance between the middle stiffener and the supports is reduced; the number of contacts evolves from 4 to 6;
- loads higher than 2800 N: the geometry of the model and the loading conditions are very close to the theoretical ones.

Visual inspection of the small scale experiment did not disclose relevant information, but the similarities between the experiments allow to equally identify the following three regions:

- loads up to 200 N;
- loads from 200 N up to 1750 N;
- loads higher than 1750 N: additional load increments are distributed equally by both outer stiffeners, given that the strain value start increasing equally in both measurement points.

Shakedown of welding-induced residual stress

Other aspect deserving further explanations is the observed difference between the first and the subsequent measured load-displacement behaviors in both scaled models.

Although this phenomenon was unexpected in the scope of this thesis, and unknown for many other researchers who are not specialists in the field, the fact is that similar behaviors are referred in the literature as the shakedown of welding-induced residual stress. It was recently the target of scientific research by Gannon (2011) in his Ph.D. thesis, which by numerical simulation concluded that reduction in residual stress of T-stiffened plates due to shakedown occurs entirely during the first load cycle provide that the magnitude of that load is no subsequently exceeded. These conclusions are in perfect accordance with the measured load-displacement curves in figures 6.41a and 6.42a.

Lastly, as a complementary information, Gannon (2011) concluded that both the tensile and compressive welding residual stress are reduced as much as 40% when the applied load causes an average stress equal to 50% of the yield stress, which was exceeded in the presented load conditions.

6.6.2.2. Analysis of the load-strain behavior

No significant and consistent difference is observed between tests for the acquired load-strain data. These are expected results, given that the strain gauges are re-calibrated prior to each test and the instrumented points of the structure are in the elastic domain. It can be argued that in the small scale testing the measured strain in point 1 reached $370\,\mu\epsilon$ in the 1^{st} test and $380\,\mu\epsilon$ to $420\,\mu\epsilon$ in the following; and that point 2 reached $500\,\mu\epsilon$ in the first test and $480\,\mu\epsilon$ to $440\,\mu\epsilon$ in the following. However the average of values measured in both points is around $430\,\mu\epsilon$ to $435\,\mu\epsilon$, allowing to conclude that the referred differences are mostly due to variations in the distribution of load between stiffeners, which in turn has several causes including initial non-perfect centering of the plate or even minor variations between tests of plate position (given that its low weight may not be totally effective in keeping it fixed).

6.6.2.3. Comparison of predictions for the medium scaled model

In the absence of experimental data for the stiffened plate prototype, alternatively, the medium scaled model is considered as the prototype. Predictions of its (global) load-displacement behavior before and after the shakedown of residual stresses are plotted in figures 6.43a and 6.43b, where they can be compared with experimentally measured data.

After the shakedown, it is observed an increase in the correlation between the experimental data and the prediction from the small scaled model, with significant deviation of results restricted to loads between 800 N and 1700 N. In turn, the results from FE-models (plotted in the same figures) where unable to predict the non-linear load-displacement behavior induced by geometric imperfections, mostly generated by the welding process.

Contrary to these results, in the predictions of the load-strain behavior (after shake-down), the FE-model simulations clearly outperformed the predictions from experimental scaled model testing, as demonstrated by the results plotted in figure 6.44 for each of the measurement points.

Lastly, the previous comparison (after the shakedown) is repeated considering the medium scaled model pre-loaded with 800 N and 8000 N, whose results are plotted in figures 6.45 and 6.46. This is equivalent to consider the experimental analysis of stiffened plates whose distortions are reduced artificially by the pre-loading. It is observed that regardless of the pre-loading, the predictions of load-displacement behavior from the small scaled model

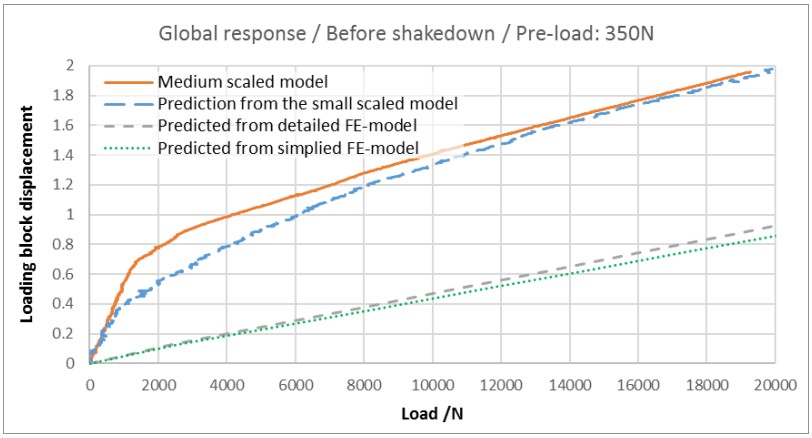

(a) Before shakedown.

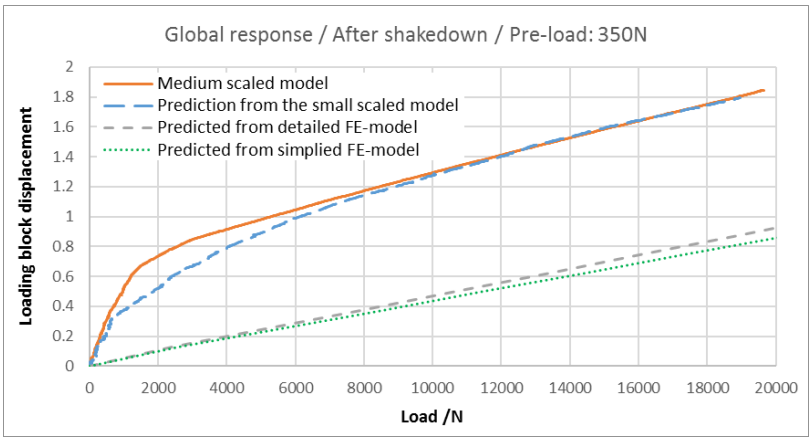

(b) After shakedown.

Figure 6.43.: Comparison of experimental and predicted load-displacement curves.

outperforms those from FE-models. On the other hand, for the load-strain behavior the FE-models provide always better predictions, particularly for pre-loadings up to 7 kN.

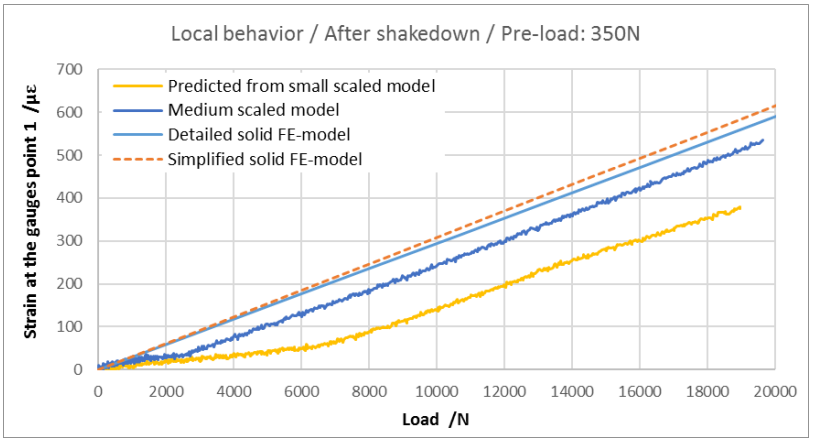

(a) Point 1.

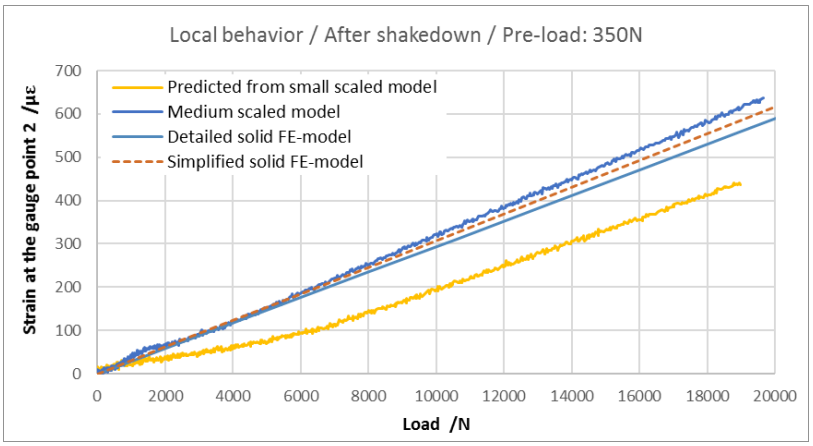

(b) Point 2.

Figure 6.44.: Comparison of experimental and predicted load-strain curves for each of the measurement points.

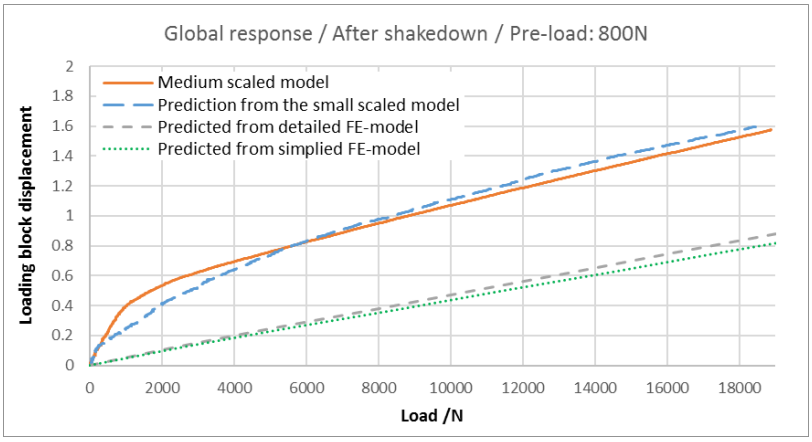

(a) Global behavior.

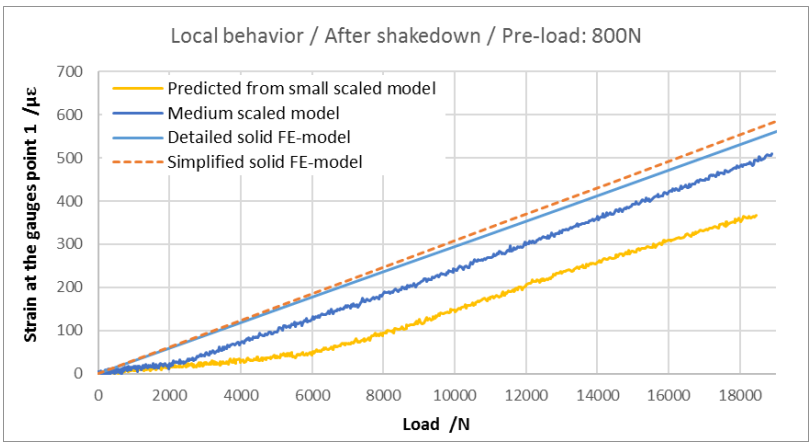

(b) Local behavior at point 1.

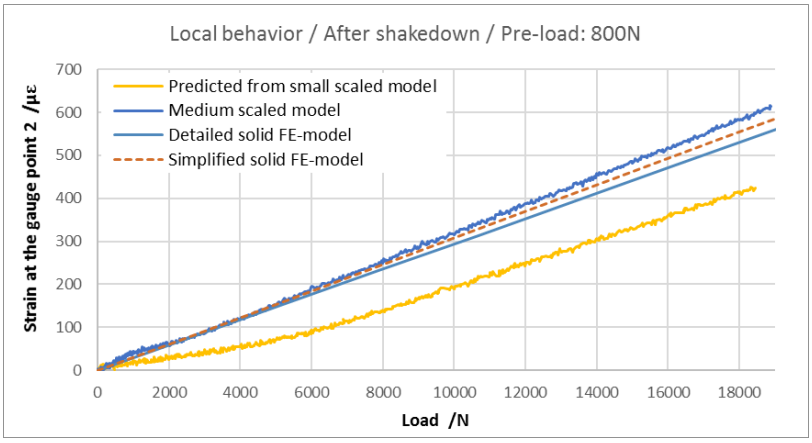

(c) Local behavior at point 2.

Figure 6.45.: Comparison of experimental and predicted behaviors of the medium scaled model, pre-loading the structure with 800N.

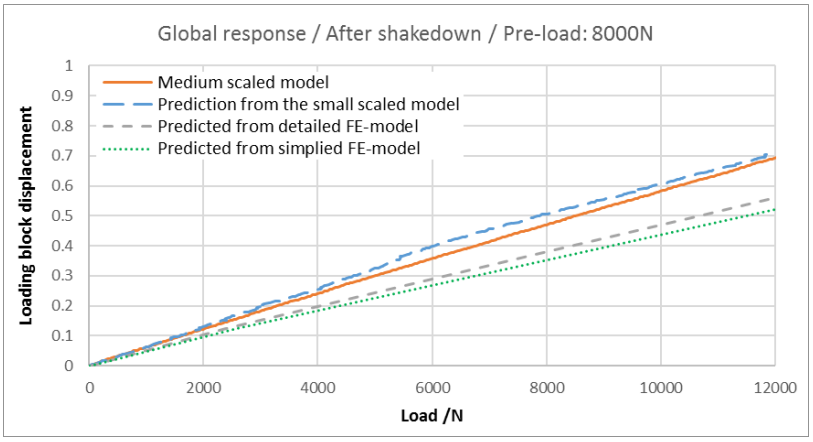

(a) Global behavior.

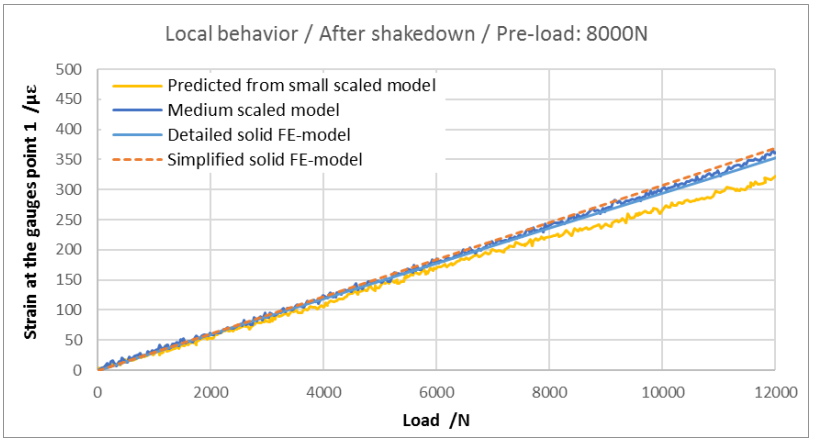

(b) Local behavior at point 1.

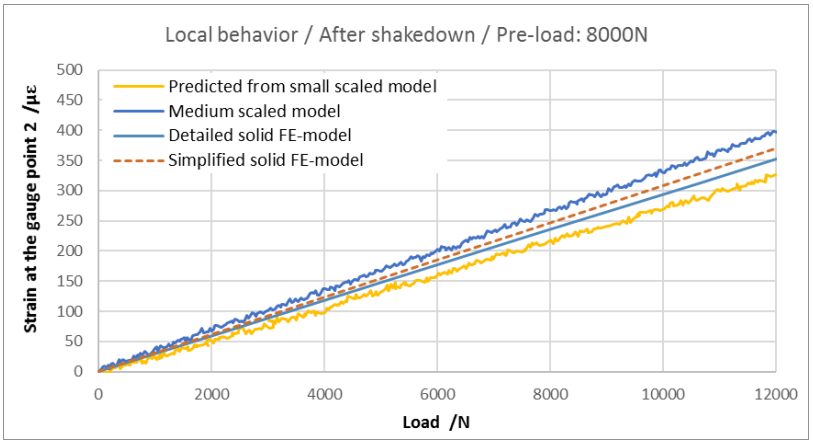

(c) Local behavior at point 2.

Figure 6.46.: Comparison of experimental and predicted behaviors of the medium scaled model, pre-loading the structure with 8000N.

6.7. Concluding remarks

In order to provide a more comprehensive validation of the Modular Approach to structural similitude, the current experimental program was carried out with objectives which can be succinctly summarized as follows:

- Investigation of the effect of the scaled model reduction, for the same prototype;
- Investigation of the effect of the prototype scale, for approximately the same scaled model reduction;
- Comparison between the experimental scaled model testing and the FE-model simulation;
- Assessment of how the similitude of structural behavior evolves for structures of increasing complexity.

The obtained results did not reveal significant effect on the correlation between experimentally predicted and experimentally measured results when the scale reduction increased from 60% to 80%. Similarly, consistent effects were not observed due to a 60% variation in the scale of different prototypes, experimentally analyzed by scaled models with approximately the same scale reduction (50% and 60%).

Despite this absence of observable consistent effects, the basic assumption of the Modular Approach was consistently verified as valid. For diverse ranges of $\overline{LAC_{jk}}$ values, the maximum value for any metric correlating experimentally predicted values and experimentally measured data of the stiffened plates is outlined by the upper limit obtained for its simpler substructures, regardless of the scale reduction and prototype scale effects or even the effect of the residual stresses.

Other of the most notorious results is that the sandblasting prior to galvanization process significantly increased the maximum LAC of the stiffened plate to a value closer to that of its simpler substructure. Similarly, the accuracy of the experimentally predicted natural frequencies was also significantly increased. It is a very strong hypothesis that the sandblasting removed the effect of excessive residual stresses in the scaled models, particularly in the small scale, where the effect of the cold working is more effective (due to an 100% higher ratio between deep of cold working and plate thickness).

Therefore, future research on the topic of dynamic experimental scaled model testing should devote special attention to the importance of correct scaling of residual stresses induced by the manufacturing processes.

On the other hand, the static tests allowed to demonstrate how the experimental scaled model testing is effective in the detection of unforeseen or unknown phenomena.

The small scaled model testing was quite effective in accurately reproducing the global force-displacement behavior of the stiffened plate prior and after the shakedown of welding-induced residual stresses.

The reduced scaled model testing was equally effective in predicting the non-linear load-displacement behavior, regardless of the pre-loading value.

Part III.

New approaches to Thermal-Structural and Constitutive Similitude

7. Modular Approach to the thermal-structural similitude

Abstract

The Modular Approach is extended in order to allow the thermal-structural similitude to be established. Difficulties associated with the experimental scale model testing of conductive-convective-radiate systems are highlighted.

7.1. Introduction

7.1.1. Research background and objectives

The Modular Approach and its structural global modules for plates and beams/stiffeners were presented in chapter 5. The applicability of the approach to the scaling of multi-physics problems was then suggested.

The present chapter is therefore devoted to deriving the similarity conditions and scaling laws needed to predict the thermal behavior of a prototype, based on the experimental analysis of a scaled model. To this end, the similitude theory will be applied to the heat transfer governing equations, as well as to the boundary conditions of the general problem. The modules of scaling laws derived in this chapter may be integrated in the previously derived Modular Approach for structural analysis, with the purpose to design a scaled model thermo-mechanically similar to the prototype under analysis.

7.2. Heat transfer theory

7.2.1. Heat transfer theory

Heat is thermal energy in transit due to a spacial temperature difference, and it may be transfered in a *medium* through conduction or between *media* through convection or radiation.

Considering the conduction as the transfer mode, the temperature distribution as a function of time $T(x, y, z, t)$ in a stationary medium (solid or fluid) is governed by the heat equation:

$$\rho c_p \frac{\partial T}{\partial t}(x, y, z, t) = -\nabla \vec{q}\,(x, y, z, t) + \dot{q}_g(x, y, z, t) \tag{7.1}$$

with the conduction heat flux $\vec{q}\,(W/m^2)$ in an isotropic material evaluated by Fourier's law:

$$\vec{q} = -k\nabla T \tag{7.2}$$

where, ρ (kg/m^3) is the density of the materials, c_p $(J/kg/K)$ is the specific heat capacity, $\dot{q}_g$ (W/m^3) is the volumetric rate of thermal energy generation, k $(W/m/K)$ is the temperature-dependent thermal conductivity and ∇ is the spacial gradient operator.

On the other hand, the convective flux $\dot{q_c}$ (W/m^2) from a surface to a moving fluid is governed by Newton's law of cooling:

$$\dot{q_c} = h(T_s - T_\infty) \tag{7.3}$$

where T_s and T_∞ are surface and fluid temperature respectively, and the parameter h $(W/m^2/K)$ is the convection heat transfer coefficient, which depends on conditions in the boundary layer, influenced for example by the surface geometry or the nature of the fluid motion.

Finally, the difference between thermal energy that is released due to radiation emission and that gained due to radiation absorption may be expressed as:

$$\dot{q_r} = \varepsilon\sigma(T_s^4 - T_{sur}^4) \tag{7.4}$$

where, ε is the emissivity (radiative property) of the surface, σ is the Stefan Boltzmann constant ($\sigma = 5.67 \times 10^{-8} W/m^2/K^4$), T_s is the absolute temperature of the small surface and T_{sur} is the absolute temperature of the much larger, isothermal surface that completely surrounds the smaller one (Bergman et al., 2011).

7.3. Thermal global module

7.3.1. Conductive heat transfer (CHT) module

Applying the similitude theory to the conductive heat transfer governing equations (7.1) and (7.2), the following similarity conditions are obtained:

$$\lambda_\rho \lambda_{c_p} \frac{\lambda_T}{\lambda_t} = \frac{\lambda_{\dot{q}_x}}{\lambda_x} = \frac{\lambda_{\dot{q}_y}}{\lambda_y} = \frac{\lambda_{\dot{q}_z}}{\lambda_z} = \lambda_{\dot{q}_g} \tag{7.5}$$

$$\lambda_{\dot{q}_x} = \lambda_{k_x} \frac{\lambda_T}{\lambda_x} \tag{7.6}$$

$$\lambda_{\dot{q}_y} = \lambda_{k_y} \frac{\lambda_T}{\lambda_y} \tag{7.7}$$

$$\lambda_{\dot{q}_z} = \lambda_{k_z} \frac{\lambda_T}{\lambda_z} \tag{7.8}$$

7.3.1.1. Material with isotropic thermal conductivity

If both the model and prototype are constructed with isotropic materials (but not necessarily the same), then $\lambda_{k_x} = \lambda_{k_y} = \lambda_{k_z} = \lambda_k$, yielding the geometric similarity condition:

$$\frac{\lambda_{\dot{q}_x}}{\lambda_x} = \frac{\lambda_{\dot{q}_y}}{\lambda_y} = \frac{\lambda_{\dot{q}_z}}{\lambda_z} \implies \lambda_k \frac{\lambda_T}{\lambda_x^2} = \lambda_k \frac{\lambda_T}{\lambda_y^2} = \lambda_k \frac{\lambda_T}{\lambda_z^2} \implies \boxed{\lambda_x = \lambda_y = \lambda_z} \tag{7.9}$$

and the same scaling factor for the conductive heat flux in all directions, represented simply by $\lambda_{\dot{q}}$:

$$\lambda_{\dot{q}_x} = \lambda_{\dot{q}_y} = \lambda_{\dot{q}_z} = \lambda_{\dot{q}}$$

where,

$$\boxed{\lambda_{\dot{q}} = \lambda_k \frac{\lambda_T}{\lambda_x}} \tag{7.10}$$

Additionally, for complete similitude, the following scaling laws are obtained:

- Time:

$$\lambda_\rho \lambda_{c_p} \frac{\lambda_T}{\lambda_t} = \frac{\lambda_{\dot{q}_x}}{\lambda_x} \implies \lambda_\rho \lambda_{c_p} \frac{\lambda_T}{\lambda_t} = \lambda_k \frac{\lambda_T}{\lambda_x^2} \implies \boxed{\lambda_t = \lambda_x^2 \frac{\lambda_\rho \lambda_{c_p}}{\lambda_k}} \tag{7.11}$$

- Generated heat:

$$\boxed{\lambda_{\dot{q}_g} = \lambda_\rho \lambda_{c_p} \frac{\lambda_T}{\lambda_t}} \tag{7.12}$$

7.3.1.2. Same isotropic material in both structures

If both the prototype and its scaled model are of the same isotropic material, then:

$$\lambda_\rho = \lambda_{c_p} = \lambda_k = 1$$

and so, the scaling laws are rewritten as follows:

- Conductive heat flux:

$$\lambda_{\dot{q}} = \frac{\lambda_T}{\lambda_x} \tag{7.13}$$

- Time:

$$\lambda_t = \lambda_x^2 \tag{7.14}$$

- Generated heat:

$$\lambda_{\dot{q}_g} = \frac{\lambda_T}{\lambda_x^2} \tag{7.15}$$

The obtained scale factors and similarity conditions allow to conclude how conductive thermal behavior can be predicted from a scaled model.

Regardless of how the thermal and structural relationships are to be coupled, from these results it can already be pointed out that it is not possible to simulate strongly coupled transient thermal and dynamic structural behaviors; their time scale are affected differently by the geometric scale factor: $\lambda_t^{(struc.)} = \lambda_x$ and $\lambda_t^{(thermal)} = \lambda_x^2$.

7.3.2. Radiative/Convective heat transfer (RCvHT) module

The term "convective heat transfer" in the following sections refers only to the natural mechanism. Research regarding the similitude of forced convection would require at least some of the governing equations of the fluid dynamics to be considered, in order to derive a scaling factor to the forced heat transfer coefficient expressed in terms of the scaling factors for the flow parameters. Such research, however, is beyond the scope of this thesis. For example, it is known that dimensional analysis applied to those equations yield dimensionless groups such as the Nusselt number (Nu), the Reynold number (Re) and the Prandtl number (Pr).

Additional difficulties are found to respect the complete similitude if the heat transfered by convection and radiation significantly affect the temperature field and therefore cannot be neglected. From equations (7.3) and (7.4) the following similarity conditions are derived:

$$\lambda_{\dot{q}_c} = \lambda_h \lambda_{T_s} = \lambda_h \lambda_{T_\infty} \tag{7.16}$$

$$\lambda_{\dot{q}_r} = \lambda_\varepsilon \lambda_{T_s}^4 = \lambda_\varepsilon \lambda_{T_{sur}}^4 \tag{7.17}$$

If the temperature distribution is respected in both the scale model and its surrounding environment, then:

$$\lambda_{T_s} = \lambda_{T_\infty} = \lambda_{T_{sur}} = \lambda_T \tag{7.18}$$

and assuming that the values for the parameters h and ε remain approximately the same:

$$\lambda_h = \lambda_\varepsilon = 1 \tag{7.19}$$

the scaling laws (7.16) and (7.17) can be rewritten as:

$$\boxed{\lambda_{\dot{q}_c} = \lambda_T} \tag{7.20}$$

$$\boxed{\lambda_{\dot{q}_r} = \lambda_T^4} \tag{7.21}$$

On the other side, as in the boundary between *media* the conducted heat flux perpendicular to the surface has to equal the heat flux exchanged by convection and radiation:

$$\dot{q} = \dot{q}_c + \dot{q}_r$$

then:

$$\lambda_{\dot{q}} = \lambda_{\dot{q}_c} = \lambda_{\dot{q}_r} \tag{7.22}$$

which however cannot be fully respected because:

$$\left(\lambda_{\dot{q}} = \frac{\lambda_T}{\lambda_x}\right) \neq \left(\lambda_{\dot{q}_c} = \lambda_T\right) \neq \left(\lambda_{\dot{q}_r} = \lambda_T^4\right) \tag{7.23}$$

These limitations in achieving the fully thermal similitude between conductive-convective-radiative systems has long been noticed. In one of the first known publications, related to aeronautic applications, O'Sullivan (1957) introduce his research stating that:

> A structural model geometrically similar to the aircraft and constructed of the same materials as the aircraft will be thermally similar to the aircraft with respect to the flow of the heat through the structure.

The author would latter refer, as an assumption, that:

> (...) the flow of heat inside the structure is predominantly by the process of thermal conduction through the solid material so that the transfer of heat by radiation from one part to another and convective transfer of heat through the air inside the structure from one part to another are negligible.

which indeed may be misleading for those without experience on the thermal similitude of structures. Indeed, neglecting the heat transfer by convection and/or radiation, for most of the aeronautic and space applications is a valid assumption. However, for a more general problem, it becomes a restriction to the accurate use of scaled model testing.

Concluding, unless the conduction and radiation are negligible, the complete similitude between conductive-convective-radiative systems cannot be established.

After the research of O'Sullivan (1957) on the transient aerodynamic heating of conductive systems, Katzoff (1963); Maples and Scogin (1970); Marshall et al. (1969) studied similitude between conduction-radiation coupled space environments. Katzoff (1963) gave some additional discussion of similitude criteria for the convective heat transfer inside manned spacecrafts.

The report present by Shannon (1972) was the first to develop thermal scale modeling techniques applicable to radiation-conduction-convection systems:

- Modified material preservation: based on the "material preservation technique" used for conduction-radiation systems, it is limited to scaled models greater than 1/2 due to the increased model temperature and required high pressure increase in the model environment;

- Temperature preservation: although used successfully for radiation-conduction systems at various scale ratios, the application of this technique to systems involving convective heat transfer depends on the availability of gas with substantially lower thermal conductivities than that of the prototype, such as Freon 11, Krypton or Xenon, leading to several practical limitations;

- Scaling comprises: the degree of similitude is approximate, depending on the scaling comprise used and on the system being scaled;

- Nusselt number preservation: its investigation was not completed due to a lack of time and funds. According to the authors, although the technique is workable, it is costly and difficult to implement.

Based on Dimensional Analysis, those approaches are partially dedicated to fluid dynamics, which is out of the scope of this thesis as previously refereed.

7.4. Thermal-Structural global module

In the elastic domain, the relationship between stress tensor and strain tensor of an anisotropic body is given by Hooke's Law. The constitutive equation can be represented in contracted notation as:

$$\sigma_i = D_{ij}\,\epsilon_j^{el} \qquad (i,\ j\ =\ 1,\ 2,\ 3,\ 4,\ 5,\ 6) \tag{7.24}$$

where D_{ij}, σ_i and ε_j^{el} are the contracted form of the elasticity, stress and strain tensors.

When the material is loaded beyond its yield strength, plastic deformation occurs. An increase in stress results in incremental increase in plastic strain $d\epsilon_j^{pl}$, and upon unloading the plastic behavior is unrecoverable. Therefore, the total strain tensor can be decomposed into two part: the elastic tensor and the plastic tensor, as follows:

$$\epsilon_j = \epsilon_j^{el} + \epsilon_j^{pl} \tag{7.25}$$

Besides, when subjected to a change in temperature, isotropic materials expand/contract equally in all direction. The change in dimensions due to temperature changes is called thermal strain ϵ^{th} which is function of the initial T_0 and applied T temperatures:

$$\epsilon_j^{th} = \alpha(T)(T - T_0) \tag{7.26}$$

where α is the temperature dependent thermal expansion coefficient. If the material is free to move, internal stresses due to thermal strains are not produced, unlike mechanical strains which are related to internal stresses by material constitutive law (Aziz and Tao, 2012).

Therefore, if thermal stresses are considered, the total stain tensor can be decomposed as follows:

$$\epsilon_j = \epsilon_j^{el} + \epsilon_j^{pl} + \epsilon_j^{th} \tag{7.27}$$

7.4.1. Thermal-Structural (TS) coupling module

The scaling factor for thermal strain is defined applying the similitude theory to equation (7.26):

$$\lambda_{\epsilon_j^{th}} = \lambda_\alpha \, \lambda_T \tag{7.28}$$

On the other hand from equation (7.27), the following scaling relationships are obtained:

$$\lambda_{\epsilon_j} = \lambda_{\epsilon_j^{el}} = \lambda_{\epsilon_j^{pl}} = \lambda_{\epsilon_j^{th}} \tag{7.29}$$

Equating the scale factors for thermal strain in relations (7.28) and (7.29), the desired connection between structural modules, as those presented in chapter 5, and the previously derived thermal modules is obtained:

$$\boxed{\lambda_{\epsilon_j} = \lambda_{\epsilon_j^{th}} = \lambda_\alpha \, \lambda_T} \tag{7.30}$$

The result is the global module for thermal-structural similitude represented in figure 7.1.

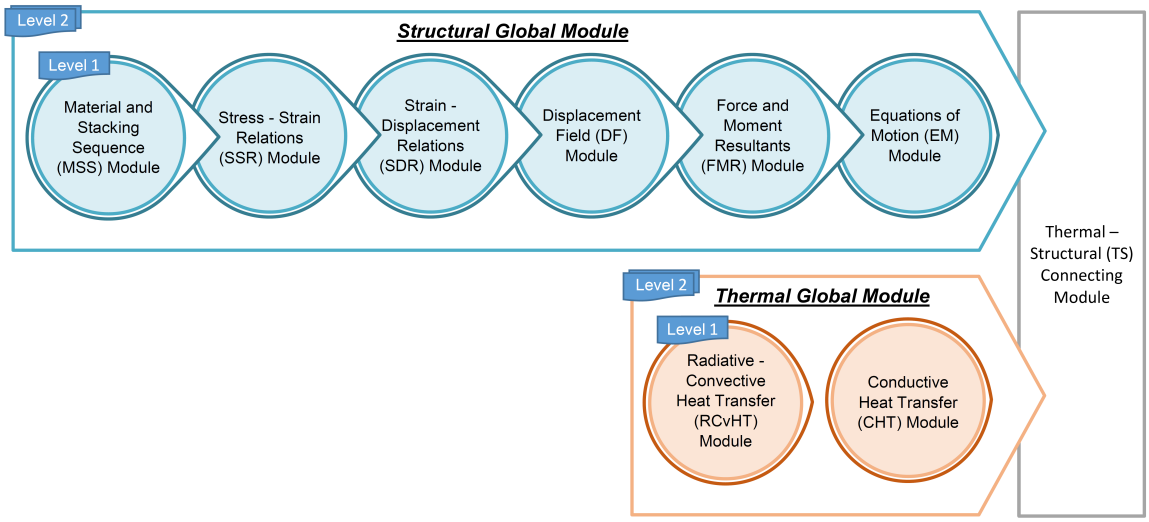

Figure 7.1.: Coupled Thermal-Structural Global Module containing the scaling relationships required to establish thermal-structural similitude.

7.5. The structural - thermal analogy

The experimental analysis of an analog system has long been known as a simulation technique (Young, 1971). The most commonly known analogies are those with electrical systems: *structural* $\Leftrightarrow$ *electrical* (either the *force* $\Leftrightarrow$ *current* or the *force* $\Leftrightarrow$ *voltage* analogy), *fluid* $\Leftrightarrow$ *electrical* or *thermal* $\Leftrightarrow$ *electrical*.

Instead of being used to simulate a phenomenon, the *structural* $\Leftrightarrow$ *thermal* is used as a tool to more easily understand and clarify the similarity conditions for thermal similitude, particularly useful for those with more experience in structural analysis than in thermal problems.

As one can see in table 7.1, for any variable used in the thermal analysis there is an analog variable in the structural analysis (Ahmad, 1996). The methodology transcribed below was presented by Ahmad (1996) to solve a thermal problem, using a 2D structural analysis software:

- Let the X displacement = temperature

  Set all other displacements = 0

- Define the material properties as:

  Young's modulus (E) = thermal conductivity (k)

  Shear modulus (G) = thermal conductivity (k)

  Poisson's ratio (ν) = 0

- Apply fixed temperatures as fixed X displacement BC.

  Insulated boundaries = free displacement = no BC

- Apply point heat input as forces in the X direction.

  Apply distributed flux as distributed X traction pressure.

- Convection can be treated as springs to the ground (ambient point).

- Structural strain output = thermal gradient output

- Structural stress = Negative thermal flux

According to the author, this methodology is extensible to 3D solids, and, if both the thermal and structural elements use the same standard formulations, the results will compare exactly.

Indeed, replacing the nodal displacements by the nodal temperatures, the general conduction equation in matrix form:

$$[B]\{\dot{T}\} + [K]\{T\} = \{P\} + \{N\}$$

is directly obtained from the general structural analysis equation:

$$[M]\{\ddot{u}\} + [B]\{\dot{u}\} + [K]\{u\} = \{P\} + \{N\}$$

where $[B]$ represent both the thermal capacity and damping matrices, $[K]$ represents both the conductivity and stiffness matrix, and the vectors $\{P\}$ and $\{N\}$ respectively the linear and nonlinear applied heat sources and forces. Finally the term containing the nodal accelerations $\{\ddot{u}\}$ has no meaning in thermal analysis (Brauer, 1993).

Besides, the convective and radiative heat transfer being a surface phenomena need to be accommodated as thermal boundary conditions. The convection matrix is directly assembled to the conduction matrix considering additional nodes for the surrounding fluid temperatures. However the radiative heat flux depending on the fourth power of absolute temperature, yields a nonlinear finite element model:

$$[B]\{\dot{T}\} + [K]\{T\} + [R]\{T\}^4 = \{P\} + \{N\}$$

where $[R]$ is a linear radiation matrix, with the nodal temperatures expressed in Kelvins (Brauer, 1993).

The nonlinear term $[R]\{T\}^4$ can be rewritten as $[R_{NL}]\{T\}$, and therefore assembled to the conduction-convection matrix, considering the following expression:

$$\dot{q}_r = \varepsilon\sigma(T^4 - T_{surr}^4) = h_r(T - T_{surr})$$

where h_r is the radiation heat transfer coefficient(Bergman et al., 2011):

$$h_r = \varepsilon\sigma(T - T_{surr})(T^2 - T_{surr}^2)$$

Although it was not presented by Ahmad (1996), the concept that is worth bearing in mind is that a radiative heat flow is analog to a nonlinear elastic foundation with stiffness k equal to h_r.

Therefore, according to the previous analogies, the requirements to achieve the thermal similitude for a conductive-convective-radiative system are similar to those that would be imposed to the scale model of a structure having distributed linear and non-linear springs, whose module is respectively the parameters h and h_r.

However, available technologies allow you to easily customize the stiffness of a spring, but hardly the convection heat transfer coefficient or the emissivity of the surface in the range it would be required by the scaling relationships.

Table 7.1.: Analogy table for thermal and structural problems.

	Structural		Thermal	
Unknown	X displacement	u	Temperature	T
Gradient	X normal strain	$\epsilon_x = \frac{\partial u}{\partial x}$	Temperature gradient	$\frac{\partial T}{\partial x}$
	XY shear strain	$\epsilon_{xy} = \frac{\partial u}{\partial y}$		$\frac{\partial T}{\partial x}$
Material property	Young modulus	E	thermal conductivity	k_x
	shear modulus	G		k_y
Fluxes	X normal stress	$E\frac{\partial u}{\partial x}$	X thermal flux	$-k_x\frac{\partial T}{\partial x}$
	XY shear stress	$G\frac{\partial u}{\partial y}$	Y thermal flux	$-k_y\frac{\partial T}{\partial y}$
Body force	gravity		volume heat generation	
Surface force	pressure		surface flux	
Point force	force		point flux	
Dirichlet BC	fixed displacement		fixed temperature	
Newman BC	free edge		insulated BC	
Cauchy BC	elastic foundation		convection coefficient	

7.6. Case study: V-groove repair welding of plates

7.6.1. Introduction

The objective of this case study is to provide an illustrative example of the accuracy and limitations of scaled models designed based on the scaling relationships derived by the Modular Approach to thermal-structural similitude.

The V-groove repair welding of plates was selected due to the complex coupling between structural and thermal behaviors, in which heat is simultaneously transferred by conduction, convection and radiation. The focus is on the thermal-structural similitude of the welding process, and therefore, considerations regarding welding metallurgy or welding feasibility issues are not relevant for the referred objective of the case study.

7.6.2. Considerations regarding the ABAQUS Welding Interface

The ABAQUS Welding Interface (AWI) was used in the present research. This Plug-In was introduced by Shubert et al., which additionally provided a detailed explanation regarding the methodology applied to perform the 2D welding simulation. As previously referred, the strict objectives of this research are focused on the similitude of coupled thermal-structural behaviors. Related parallel discussions or further considerations about specific issues of the welding simulation is out of the intended scope of this research, and will be addressed later in chapter 8.

The relevant information regarding the transient heat transfer analysis is the following:

- Time intervals are defined for the torch application phase (Δt^{torch}) and cool down phase ($\Delta t^{cooling}$), in order to simulate the torch movement (along the weld line) through the considered cross section;
- The heat input provided by the weld torch is simulated prescribing linear increase of temperature up to a value slightly above the assumed melting temperature (T^{torch}), at the boundary between the weld metal of the current pass and the neighboring base metal;
- The bead associated with the current pass is activated immediately after the torch application phase and prior to the start of the respective cool down step. All the other subsequent passes are not present.

7.6.3. Description of the prototypes geometry and material properties

The AWI Plug-In provides several welding models for validation tasks, workshop sessions or benchmarking purposes. According to Shubert et al., those models were validated through the comparison between results produced by the AWI GUI and an in-house GUI that Bechtel Marine Propulsion Corporation (BMPC) uses to support welding simulations.

The entitled verification model 2.2 (Plane Strain, Ramp, model-level bead removal, without sensors), whose mesh and boundary conditions are depicted in figure 7.2, inspired (after minor modifications) the large scale prototypes considered in this research:

- Prototype A: a (narrower) plate whose weld width is 20% of the plate width.
- Prototype B: a wider plate whose weld width represent only 5% of the plate width.

The geometry and boundary conditions of both the analyzed prototypes are depicted in figure 7.3. On the other hand the refinement of the mesh was as much as possible kept

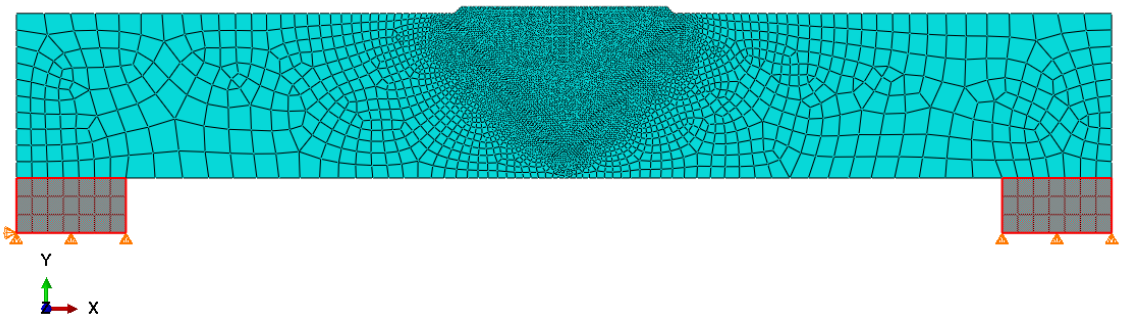

Figure 7.2.: Mesh and boundary conditions of the selected ABAQUS Verification 2D Weld Model included in the AWI Plug-In (excluding highlighted sections, 5451 elements: 5389 DCC2D4/CPE4 + 62 DC2D3/CPE3).

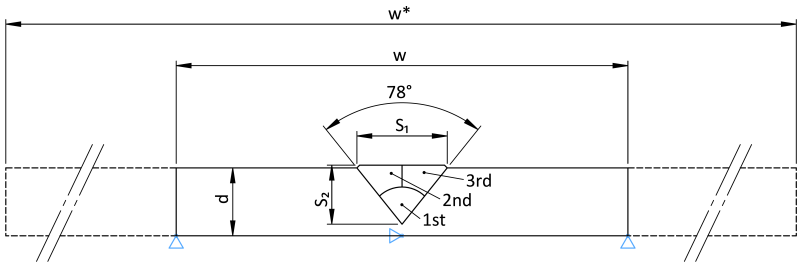

Figure 7.3.: Relevant geometry parameters and welding sequence of the studied prototypes. The dashed lines represent the extended width ($w*$) of the Prototype B in relation to that of the prototype A (w). The plate thickness (d), characteristic weld dimensions (S_1 and S_2) and boundary conditions are preserved.

similar to that adopted in the original ABAQUS model, as observed by comparison of figures 7.4 and 7.5 with figure 7.2.

Besides, both prototypes A and B were simulated assuming different boundary conditions for radiation ($\varepsilon = 0.9$) and convection ($h = 25\,\mathrm{W/m^2/K}$):

- Case A: Fully convective-radiative model. Heat losses are considered in all the surfaces, this is, in the groove and beads surfaces, when applicable, as well as in the top and bottom faces.
- Case B: Partially convective-radiative model. Heat losses are considered only in the groove and beads surfaces, when applicable, and neglected in the remaining faces.

Unless stated otherwise, the parameters defined by the AWI Plug-In for the sequentially coupled thermal-structural simulation were accepted and have not been modified in any simulation of the large scale prototypes, including the prescribed temperatures and time intervals, temperature dependent thermal and structural material properties as in tables 7.2 and 7.3, and the assumed isotropic hardening and plane strain state (finite elements of type CPE4 and CPE3).

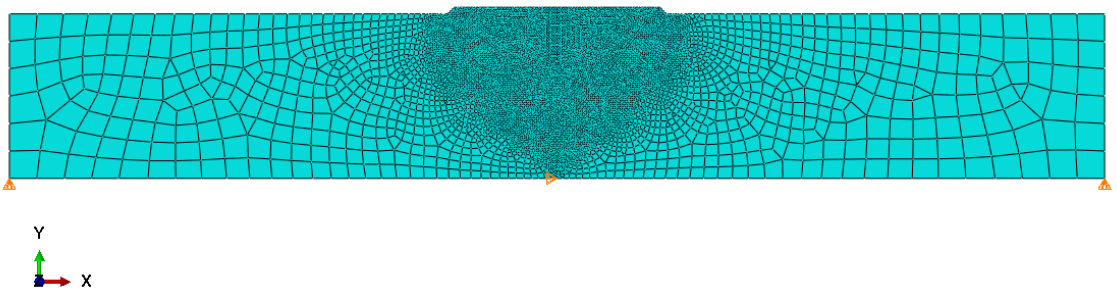

Figure 7.4.: Mesh and boundary conditions of the narrower plate, entitled Prototype A (5608 elements: 5520 DCC2D4/CPE4 + 88 DC2D3/CPE3).

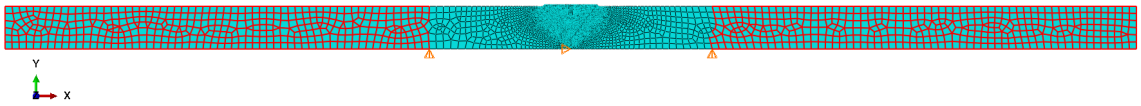

Figure 7.5.: Mesh and boundary conditions of the narrower plate, entitled Prototype B (excluding highlighted sections, 5637 elements: 5540 DCC2D4/CPE4 + 97 DC2D3/CPE3).

Table 7.2.: Thermo-mechanical properties of the base and filler material.

Temperature [°C]	Density [kg/m^3]	Conductivity [J/m/C]	Specific heat [J/kg/C]	Expansion coeff. $\times 10^{-6}$ [–]
20	7150	55	501	11.7
100	7100	51	561	11.7
200	7050	50	590	11.8
300	7000	46	619	12.2
400	6950	42	669	12.9
500	6900	39	719	13.2
600	6850	34	784	13.6
700	6800	30	855	13.8
1500	-	-	-	0

Table 7.3.: Mechanical properties of the base and filler material; additionally, the Poisson's ratio ($\nu = 0.27$) is assumed temperature-independent.

Temperature [°C]	Young Modulus [MPa]	Yield Stress at 0 plastic strain [MPa]	Yield Stress at 0.25 plastic strain [MPa]
20	93500	153	19278
100	89250	153	18747
200	85000	153	18216
300	78200	129	17129
400	66300	119	9682
500	51000	85	1998
600	40800	68	174
700	100	68	174
1500	-	5	10

7.6.4. Derivation of scaling relationships for thermal-structural similitude

From the scaling relationships obtained by the Modular Approach for complete similitude of the non-linear structural behavior of plates, the following similarity conditions apply:

- The same material properties in both the prototype and its scaled model
- $\lambda_x = \lambda_y = \dfrac{1}{5}$
- $\lambda_u = \lambda_v = \dfrac{\lambda_w \lambda_z}{\lambda_x}$
- $\lambda_z = \lambda_w$
- $\lambda_\sigma = \lambda_\epsilon = \dfrac{\lambda_u}{\lambda_x}$

Additionally from the scaling relationships obtained by the Modular Approach for thermal behavior of structures sharing the same material properties ($\lambda_\rho = \lambda_{c_p} = \lambda_k = \lambda_\alpha = 1$), convection heat transfer ($\lambda_h = 1$) and surface emissivity ($\lambda_\varepsilon = 1$), the following similarity conditions apply:

- $\lambda_x = \lambda_y = \lambda_z$
- $\lambda_t = \lambda_x^2$
- $\lambda_{\dot{q}} = \dfrac{\lambda_T}{\lambda_x}$
- $\lambda_{\dot{q}_c} = \lambda_T \neq \lambda_{\dot{q}}$ (distortion of heat losses)
- $\lambda_{\dot{q}_r} = \lambda_T^4 \neq \lambda_{\dot{q}}$ (distortion of heat losses)

Lastly, from the thermal-structural coupling module:

- $\lambda_\epsilon = \lambda_{\epsilon^{th}} = \lambda_T$

The previous sets of scaling relationships can be reduced to the following:

- The same material properties in both the prototype and its scaled model
- $\lambda_x = \lambda_y = \lambda_z = \lambda_u = \lambda_v = \lambda_w = \dfrac{1}{5}$
- $\lambda_\sigma = \lambda_\epsilon = \lambda_{\epsilon^{th}} = \lambda_T = 1$
- $\lambda_t = \lambda_x^2 = \dfrac{1}{25}$
- $\lambda_{\dot{q}} = \dfrac{\lambda_T}{\lambda_x} = 5$
- $\lambda_{\dot{q}_c} = \lambda_{\dot{q}_r} = 1 << \lambda_{\dot{q}}$ (distortion of heat losses)

7.6.5. Description of the scaled models

For the scaled model analysis of the structural-thermal behavior of each of the previous prototypes, a 1/5-scaled model is considered. This is equivalent to an 80% scale reduction, that is quite effective in reducing the overall dimension of large scale structures, as demonstrated by the visual comparison in figure 7.6.

Besides, detailed values of the characteristic geometric dimensions, time intervals and prescribed temperatures are provided in tables 7.4 and 7.5 for both the prototypes and theirs scaled models.

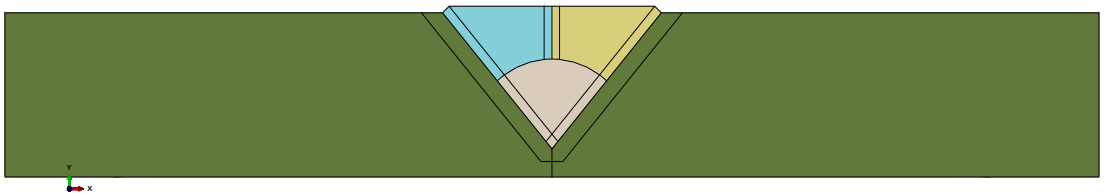

(a) Prototype A

(b) 1/5-scale model of prototype A

Figure 7.6.: Visual comparison of the Prototype A and its scaled model.

Table 7.4.: Characteristic dimensions (expressed in mm) of the prototypes and their respective scale models.

	d	w	w*	S1	S2
Prototype A	30	200	-	40	40
1/5-scale model A	6	40	-	8	40
Prototype B	30	-	800	40	40
1/5-scale model B	6	-	160	8	40

Table 7.5.: Characteristic prescribed temperatures and time intervals of the prototypes and their respective scale models.

	Δt^{torch} [s]	$\Delta t^{cooling}$ [s]	T^{amb} [°C]	T^{torch} [°C]
Prototypes (A/B)	10	150	21.1	1500
1/5-scale models (A/B)	0.4	6	21.1	1500

7.6.6. Results

The temperature and Von Mises stress were obtained in the node highlighted (in red) on the figure 7.7.

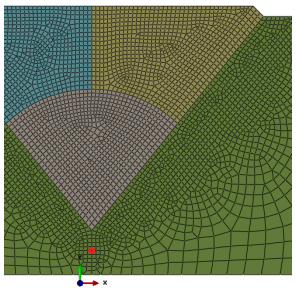

Figure 7.7.: Selected node for results.

Then, prediction for the results of the prototypes were made applying the scaling laws to the results obtained for the models. In order to analyze the accuracy of those predictions, both the absolute and relative differences are plotted in figures 7.8 and 7.9.

From the analysis of those results it is concluded that the temperature predictions based on a scaled model tend to diverge from the actual prototype temperature. This behavior is explained because while the convection and radiation heat fluxes are scaled by a unitary factor, the conduction heat flux in the scaled model is 5 times greater then in the prototype. This is: for the present case study, the model heat losses are 4 times lower than they should be in order to achieve complete similitude of structural and thermal behaviors.

Considering fully convective-radiative specimens, the results demonstrate that for a prototype where the size of the weld relatively to the specimen is significantly lower, the obtained absolute difference will be also significantly lower; however the relative prediction difference remains almost unchanged.

Finally, and as expected it is also observed that for specimens with lower radiative and convective surface areas, both the absolute and relative differences are quite low, corresponding to a satisfying accuracy of predictions obtained by reduced scale modeling.

7.7. Concluding remarks

This chapter extended the Modular Approach allowing the scaling relationships for thermal and thermal-structural similitude to be derived. Some difficulties dealing with conductive-convective-radiative systems were highlighted.

Additionally the structural-thermal analogy was used to provide further understanding of the referred difficulties. It was observed that scaling the convective and radiative heat losses on thermal models is similar to scaling non-linear distributed springs in structures.

Lastly, these limitations are further exposed considering the thermal-structural simulation of the welding process in specimens of different scales. It was concluded that the experimental scale model testing provide acceptable accuracy for structures whose heat transfer is mostly conductive.

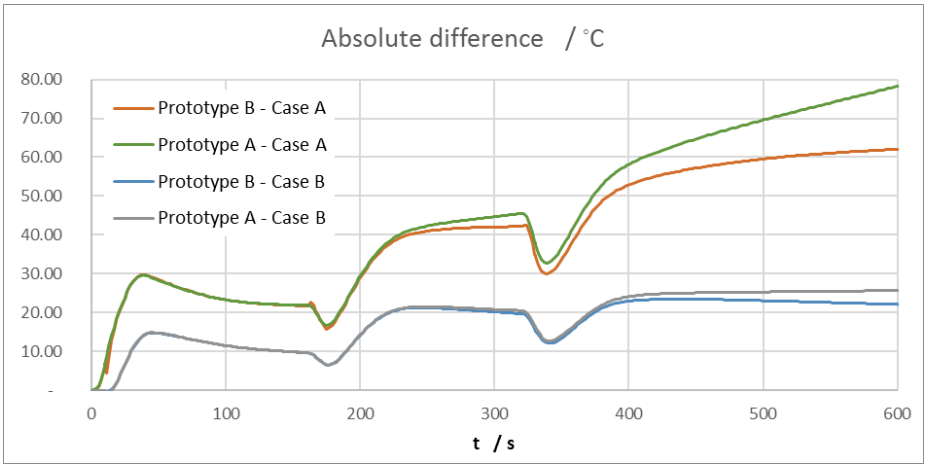

(a)

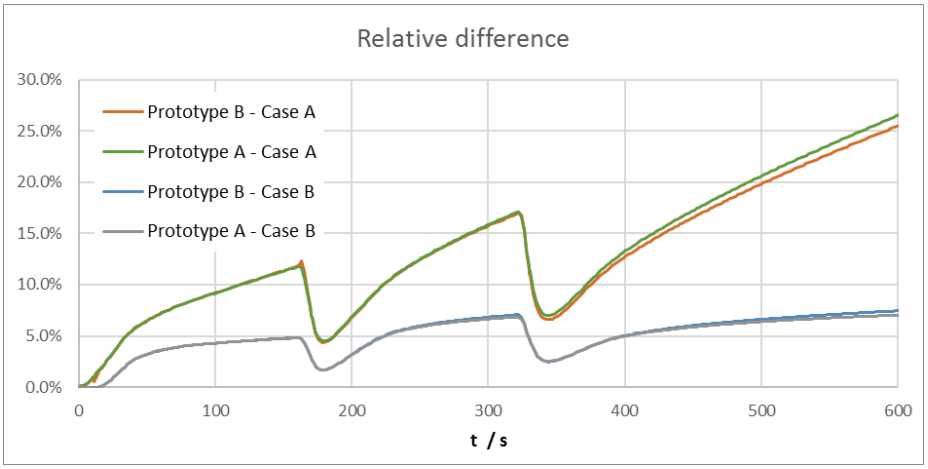

(b)

Figure 7.8.: Absolute and relative differences obtained predicting the temperature of the prototype in the point of interest.

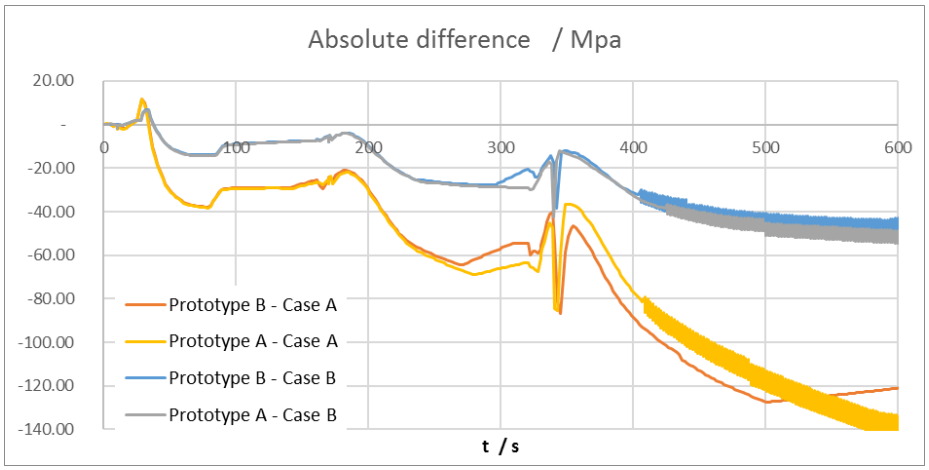

(a)

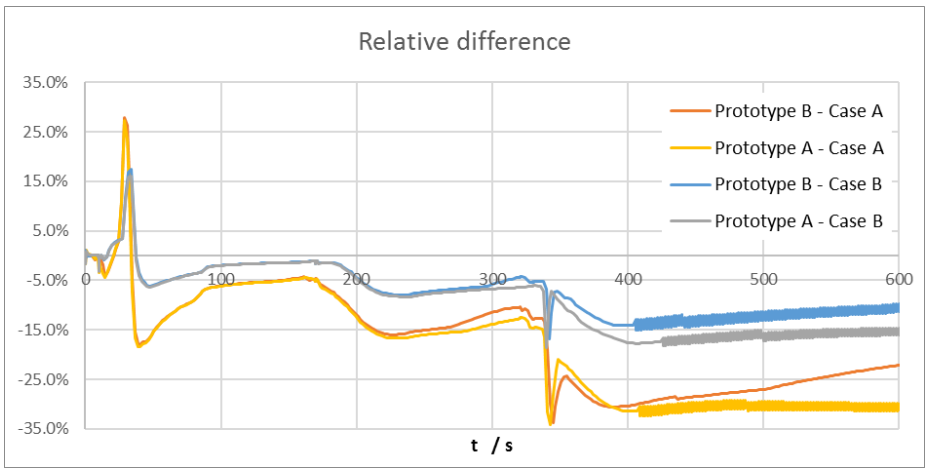

(b)

Figure 7.9.: Absolute and relative differences obtained predicting the Von Mises stress of the prototype in the point of interest.

8. Constitutive similitude of welded joints in scaled models

Abstract

The shipping, civil or metalworking machinery industry represent some examples where engineers rely heavily on expensive experimental tests. These are at the same time industries with several examples of heavy duty welded structures. However, no known study addresses how structural similitude is affected by differences between the welding procedures used for the prototype and for its scaled model.

Taking into account that material constitutive similarity is one of the requisites to achieve similitude of structural behavior, the focus of this research is in establishing similarity conditions regarding relevant welding parameters, such that the constitutive similarity is improved as much as possible.

Alternatively to the use of dimensional analysis, the similitude theory is directly applied to generalized equations predicting heat input and relevant cooling parameters. A total of 164 gas metal arc welding (GMAW) procedures are analyzed in order to assess the practical feasibility of the derived scaling relationships. Finally, the T-joint fillet welding of a prototype and its scaled model is presented as a demonstration of the application and effectiveness of the proposed scaling relationships.

8.1. Introduction

8.1.1. State of the art

The shipping, civil or the metalworking machinery industry represent some examples where engineers rely heavily on expensive experimental tests in order to verify the component's and system's analytical predictions, as well as the performance requirements of the design before going into production. These are at the same time industries with several examples of heavy duty welded structures.

An extensive literature review was recently presented by Coutinho et al. (2016), focused on the establishment of structural and/or thermal similitude. Complementary, from Mendez it is available a detailed overview of scaling laws in welding modeling. Despite the wide range of reviewed publications in each of the referred topics, no known study addresses how structural similitude is affected by differences between the welding procedures used for the prototype and for its scaled model. Still, Kim et al. (2004) referred excessive welding in the scaled model as possible cause for observed reduction in the stiffness scale factor, while Endo et al. (2002) referred the higher vulnerability of thinner shells to the welding heat input as a factor affecting the characteristics of peak force.

8.1.2. Objectives and chapter layout

Taking into account that material constitutive similarity is one of the requisites to achieve similitude of structural behavior and that from the welding metallurgy it is known that the constitutive behavior of material located on the heat affected zone (HAZ) and weld metal is dependent on the welding procedures (Blondeau, 2013), the focus of this research

is in establishing similarity conditions regarding relevant welding parameters, such that the constitutive similarity is improved as much as possible. According to Baker et al. (1991), constitutive similarity requires that at homologous locations (including weldments) the prototype ans its scaled model have to be fabricated from homologous materials, this is, materials with similar nondimensional stress-strain curves. Therefore, in opposition to the available researches in the literature, distorting the complete similitude of the welding process is not a concern, as long as the material constitutive similarity is improved.

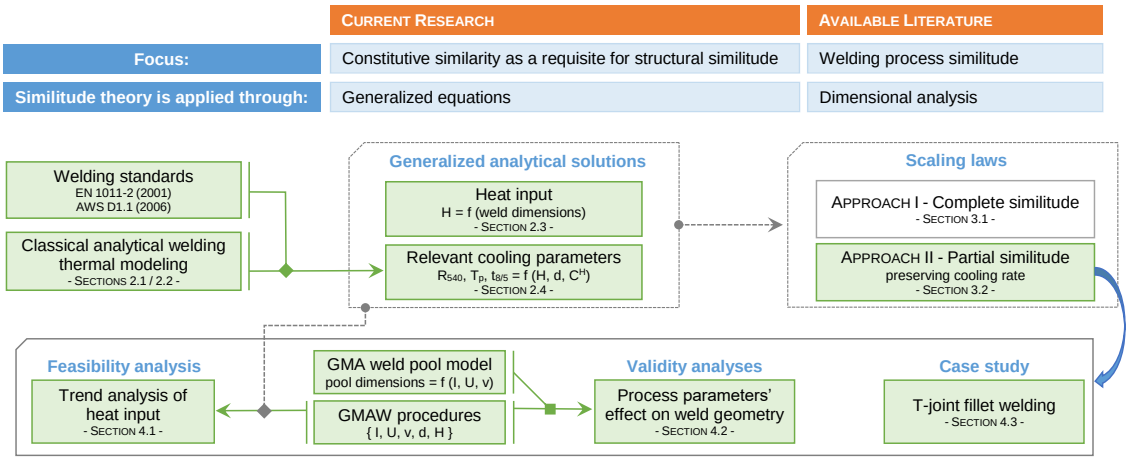

Figure 8.1.: Research overview

As outlined in figure 8.1, the present manuscript is structured as follows:

- In section 8.2 the classical analytical thermal modeling of welding based on Rosenthal's solutions (sections 8.2.1 and 8.2.2) is introduced, along with known experimentally determined relations between heat input and weld dimensions (section 8.2.3).

  The referred classical modeling is valid only for bi-thermal heat flow conditions. Therefore, heat input correction factors are derived in section 8.2.4 with the dual purpose of overcoming this limitation and better match both the analytical expressions (for colling time) in EN 1011-2 (2001) and the graphical data (for colling rate) in AWS D1.1 (2006).

- In section 8.3, scaling relationships are derived applying the similitude theory to generalized equations predicting heat input and relevant cooling parameters. Alternatively, in available literature, scaling relationships are derived through the use of dimensional analysis (Mendez).

  If all the derived scaling relationships were respected, then complete similitude of the thermal behavior would be achieved. This approach (simply entitled Approach I) was presented in section 8.3.1, having been shown to be incompatible with the intention of achieving material constitutive similarity.

  Therefore, in section 8.3.2 the Approach II is presented in which, based on metallurgical considerations, an increase of the level of constitutive similarity is sought preserving the cooling rate.

- In section 8.4, some analyses are presented with regard to the scaling laws' validity and feasibility, followed by the numerical modeling of the T-joint fillet welding.

  Section 8.4.1 presents the inverse analysis of 164 Gas Metal Arc Welding (GMAW) procedures proposed by the main filler manufacturers. The scaling relationships from

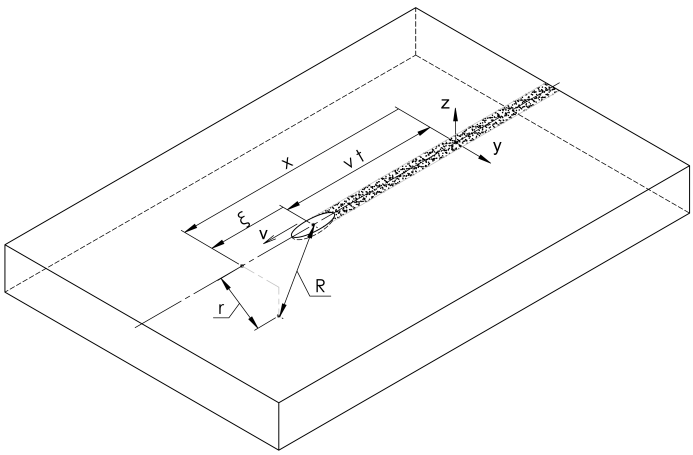

Figure 8.2.: Fixed and mobile coordinate systems considered in weld modeling.

Approach II are considered as feasible in practice if they are shown to be compatible with the assessed trend of predicted heat input in function of plate thickness.

Section 8.4.2 assesses trends in the process parameters prescribed in collected GMAW procedures. Then, through an available Gas Metal Arc (GMA) weld pool model it is evaluated the validity of scaling the weld geometry based on approximate correlations between heat input and weld dimensions (from section 8.2.3).

Lastly, section 8.4.3 covers the numerical simulation of T-joint fillet welding of a prototype and its scaled model, whose process parameters are established according to scaling relationships from Approach II. Theirs effectiveness in preserving the cooling rate is evaluated through the comparison of results.

8.2. Analytical thermal model for structural welding

Although in most fusion welding processes the heat source does not remain stationary, the following analytical formulation assumes that the source moves at a constant speed along a straight line, with constant net power supply from the source (Grong, 1997).

In those conditions, a quasi-stationary mode is achieved, and the temperature distribution around the source adopts a stable form in relation to time, that can be determined (Blondeau, 2013).

Through a system of mobile coordinates: $\xi = x - v\,t$, with the origin at a source point, moving with a constant velocity v (as in figure 8.2), the simplified heat equation:

$$k\left(\frac{\partial^2 T}{\partial x^2}+\frac{\partial^2 T}{\partial y^2}+\frac{\partial^2 T}{\partial z^2}\right)=\rho c\,\frac{\partial T}{\partial t}$$

is rewritten for a stationary state as:

$$k\left(\frac{\partial^2 T}{\partial \xi^2}+\frac{\partial^2 T}{\partial y^2}+\frac{\partial^2 T}{\partial z^2}\right)=-\rho c\,v\,\frac{\partial T}{\partial \xi}$$

whose solution was proposed as early as 1935 by Rosenthal for "thin" and "thick" plates, and latter extended by a number of other investigators (such as Rykalin, Christensen or Adams) (Blondeau, 2013; Grong, 1997).

Although numeric methods allow to avoid many of the assumptions in which the following

analytical calculations are based, experience shows that this simplified approaches solve the majority of the problems with satisfactory precision (Blondeau, 2013).

8.2.1. Temperature distribution

Based on the following simplifying assumptions (Kou, 2003):

- Steady-state heat flow;
- Point heat source;
- Negligible heat of fusion;
- Constant thermal properties;
- No heat losses from the workpiece surface;
- No convection in the weld pool.

the Rosenthal's solutions are written for thick plates assuming 3D heat flow (as in 8.3a):

$$(T - T_0)_{3D} = \frac{\dot{Q}}{2\pi\, k\, R}\, e^{\frac{-v\xi}{2\alpha}}\, e^{\frac{-vR}{2\alpha}} \tag{8.1a}$$

and for thin plates assuming 2D heat flow (as in 8.3b):

$$(T - T_0)_{2D} = \frac{\dot{Q}}{2\pi\, k\, d}\, e^{\frac{-v\xi}{2\alpha}}\, K_0\left(\frac{vR}{2\alpha}\right) \tag{8.1b}$$

where, $\dot{Q} = \eta\, U\, I$ is the net power expressed as a function of the welding voltage (U) and current (I) multiplied by the thermal efficiency (η), $R = \sqrt{\xi^2 + y^2 + z^2}$ is the distance to source point, $\alpha = \frac{k}{\rho\, c}$ is the base material diffusivity, d is the thickness of a thin plate, and $K_0\left(\frac{vR}{2\alpha}\right)$ is the modified Bessel function of the second kind and zero order (Easterling, 2013; Grong, 1997; Poorhaydari et al., 2005).

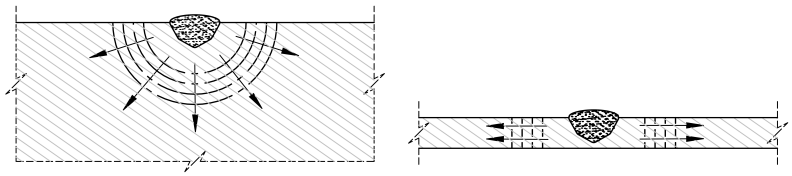

(a) Three-dimensional (3D) heat flow (b) Two-dimensional (2D) heat flow

Figure 8.3.: Assumed isothermal lines and heat flow conditions generated during a bead deposition in (a) relatively thick and (b) relatively thin plates (Blondeau, 2013; EN 1011-2, 2001; Lundberg, 2014)

8.2.1.1. Cooling rate

The cooling rate is defined through the time derivative of temperature, evaluated at T_i:

$$R_{T_i} = -\left.\frac{\partial T}{\partial t}\right|_{T=T_i} \tag{8.2}$$

and so, it can be obtained from equations (8.1), considering a point along the central axis ($y = z = 0$) at the rear of the weld pool ($\xi < 0$), as follows (Lancaster, 1999):

$$R_{T_i\,3D} = \frac{2\pi\, k}{\dot{Q}/v}\,(T_i - T_0)^2 \tag{8.3a}$$

and

$$R_{T_i\,2D} = \frac{v^2\,(T_i - T_0)}{2\alpha}\left(\frac{K_1(\frac{vR}{2\alpha})}{K_0(\frac{vR}{2\alpha})} - 1\right) \tag{8.3b}$$

According to Signes (1972), latter Adams presented the following simplified expression for the cooling rate of thin plates:

$$R_{T_i\,2D} = \frac{2\pi\, k\, \rho c\, d^2}{\left(\dot{Q}/v\right)^2}\,(T_i - T_0)^3 \tag{8.4}$$

Omitted by most of the authors, the previous equation is obtained expressing the Bessel function K_0 as follows:

$$K_0\left(\frac{vR}{2\alpha}\right) \approx e^{-\frac{vR}{2\alpha}}\sqrt{\frac{\pi\alpha}{vR}} \tag{8.5}$$

which is a fair approximation for $\frac{vR}{2\alpha} > 1$ (Grong, 1997). So, equation (8.4) is obtained through the time derivative of the temperature distribution resulting from the substitution of expression (8.5) in equation (8.1b), for $R = \xi$:

$$(T - T_0)_{2D} = \frac{\dot{Q}}{2\pi\, k\, d}\sqrt{\frac{\pi\alpha}{vR}} = \frac{\dot{Q}}{d\,\sqrt{4\pi k\, \rho c\, vR}}$$

In line with AWS D1.1 (2006), the cooling rate in the remaining of this work is evaluated at $T_i = 540°C$.

8.2.2. Time-temperature distribution

Blondeau (2013) presented in a simple and objective way the relevant aspects in the thermal cycle:

- A very fast heating phase, ranging from $10^{2°}C/s$ (arc welding) to $10^{4°}C/s$ for processes such as laser welding;
- A passage at the peak temperature T_p, during shorter time periods for higher T_p;
- A fast cooling phase, whose intensity is characterized by the time $\Delta t_{T_2}^{T_1}$ passing between two given temperatures T_1 and T_2, expressed in Celsius degrees. Usually Δt_{500}^{800} or Δt_{300}^{700} are chosen because the majority of metallurgical transformations in carbon-manganese steels occur in these two temperature ranges.

The referred peak temperature and cooling time can be derived considering the following time-temperature variations:

$$(T - T_0)_{3D} = \frac{\dot{Q}/v}{2\pi\, k\, t}\, e^{\frac{-r^2}{4\alpha t}} \tag{8.6a}$$

$$(T - T_0)_{2D} = \frac{\dot{Q}/v}{d\sqrt{4\pi\, k\, \rho c\, t}}\, e^{\dfrac{-y^2}{4\alpha t}} \tag{8.6b}$$

which are valid, respectively, for points in thick plates at the radial distance $r = \sqrt{y^2 + z^2}$ and for points in thin plates at the lateral distance y, both measured from the weld centerline (Blondeau, 2013; Poorhaydari et al., 2005).

From all the analyzed literature, only Grong (1997) stated that these simplified solutions proposed by Rykalin for fast moving high power sources, are valid within a limited range of the more general Rosenthal's equations. Through the analysis of the graphical representation of dimensionless equations, the following conditions are obtained as necessary to achieve good accuracy, for thick plates:

$$\frac{4\pi\, \alpha^2\, \rho c}{\dot{Q}\, v}\,(T_p - T_0) \leq 0.1 \tag{8.7a}$$

and for thin plates:

$$\frac{2\pi\, \alpha\, \rho c}{\dot{Q}}\, d\,(T_p - T_0) \leq 0.1 \tag{8.7b}$$

8.2.2.1. Peak temperature in the HAZ

Equating the time derivative of equations (8.6) to zero, the following expressions for the peak temperature reached in the HAZ are obtained (Poorhaydari et al., 2005):

$$(T_p - T_0)_{3D} = \frac{2}{\pi e}\frac{\dot{Q}/v}{\rho c\, r^2} \tag{8.8a}$$

and

$$(T_p - T_0)_{2D} = \sqrt{\frac{2}{\pi e}}\frac{\dot{Q}/v}{2d\, \rho c\, r} \tag{8.8b}$$

Blondeau (2013) additionally imposed the melting temperature T_f as the (upper) limiting condition, with $r = r_f$ being the radius of molten metal deposit. Thereby it is avoided the singularity ($T_p \to \infty$) when ($r \to 0$).

8.2.2.2. Cooling time

For welding of low alloy steel, the cooling time from 800 to 500°C is widely accepted as an adequate index for the thermal conditions under which the austenite to ferrite transformation takes place (Grong, 1997). Also represented by $t_{8/5}$ (EN 1011-2, 2001), this parameter is obtained from equations (8.6), for points located on the weld centerline ($r^2 = y^2 + z^2 = 0$):

$$t_{8/5\,3D} = \frac{\dot{Q}/v}{2\pi\, k}\left(\frac{1}{500 - T_0} - \frac{1}{800 - T_0}\right) \tag{8.9a}$$

and

$$t_{8/5\,2D} = \frac{(\dot{Q}/v)^2}{4\pi\, k\, \rho c\, d^2}\left(\frac{1}{(500 - T_0)^2} - \frac{1}{(800 - T_0)^2}\right) \tag{8.9b}$$

However, as several experimental readings of thermal cycles taken for welding joints shown that the cooling time varies very little within the same welded joint, it can be considered that the various zones of a weld deposit can be characterized by this single cooling time obtained for the weld axis (Blondeau, 2013).

For a given heat input, the heat flow is considered to change from the three-dimensional (3D) to the two-dimensional (2D) condition, both sketched in figure 8.3, at the following critical thickness (Easterling, 2013; Poorhaydari et al., 2005):

$$d_c = \sqrt{\frac{\dot{Q}/v}{2\rho c}\left(\frac{1}{500 - T_0} + \frac{1}{800 - T_0}\right)}$$

8.2.3. Heat input concept

The heat input affects the cooling rate, the cooling time as well as the peak temperature in the weld deposit and HAZ, being defined as follows (EN 1011-1, 1998):

$$H = \frac{\dot{Q}}{v} = \frac{\eta\, U\, I}{v} \quad [J/m] \tag{8.10}$$

in function of thermal efficiency (η), average linear torch velocity (v), welding voltage (U) and current (I).

Being a relative measure of the energy transferred per unit length of weld, the heat input is directly proportional to the (effective) bead cross-sectional area (A) (Miller and Funderburk, 2001):

$$H \approx \frac{A}{16.39} \tag{8.11}$$

where H and A are expressed in kJ/mm and mm^2, respectively.

Considering generalized weld beads, such as in figure 8.4, whose cross section is described by the characteristic dimensions s_1 and s_2, then:

$$H \propto s_1 \times s_2 \tag{8.12}$$

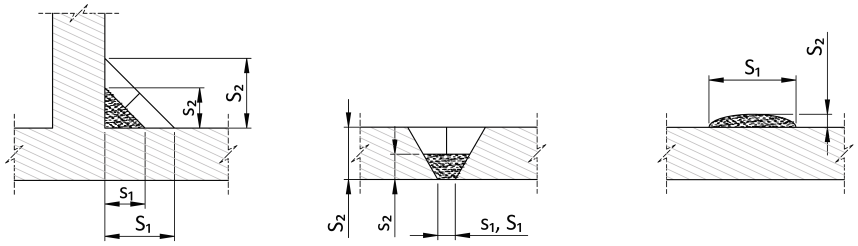

(a) Root bead of fillet and groove welds, and run on plate

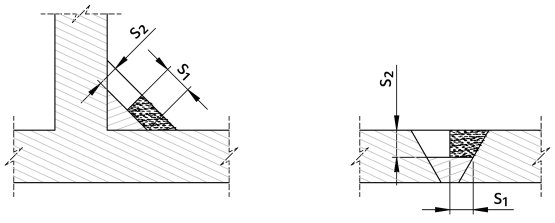

(b) Second pass of fillet and groove welds

Figure 8.4.: Examples of theoretical cross-sectional geometries for different bead passes where S_1 and S_2 are the final weld's characteristic dimensions, while s_1 and s_2 are the bead's characteristic dimensions.

The proportionality expressed by (8.12) can be also extended for multi-pass welding, as

follows:

$$H^{total} = \sum_{\text{bead 1}}^{\text{bead n}} H \;\propto\; S_1 \times S_2 \tag{8.13}$$

where S_1 and S_2 are the characteristic dimensions of the multi-pass weld, and H^{total} is the total weld heat input obtained summing the heat input H of each bead pass.

8.2.3.1. Groove welds

Defining α and β as the bevel angles, for the root pass of V-groove welds ($\alpha \neq 0, \beta \neq 0$), bevel welds ($\alpha = 0 \;\vee\; \beta = 0$) or square-groove welds ($\alpha = \beta = 0$) with no reinforcement, equation (8.11) yields:

$$H \approx \frac{1}{32.77}\left(2\,h\,R + h^2 \tan\alpha + h^2 \tan\beta\right) \tag{8.14}$$

where h and R are the root pass thickness and root opening, both expressed in mm, and H is expressed in kJ/mm (Miller and Funderburk, 2001).

8.2.3.2. Fillet welds

For rounded fillet weld beads ($s_1 = s_2 = w$) the following expression is typically accurate (Funderburk, 1999; Miller and Funderburk, 2001):

$$H \approx \left(\frac{w}{5.5}\right)^2 \tag{8.15}$$

where w is the weld leg size in mm. This approximation is based on 270 different documented welding procedures, including diverse welding methods.

8.2.4. Influence of bi- and tri-thermal heat flow conditions

According to Blodgett (1966) the analytical solutions in sections 8.2.1 and 8.2.2 are based upon bi-thermal heat flow, created for example during a run on plate.

For tri-thermal heat-flow there are three avenues (instead of two) for the heat to escape, such as in a single run fillet weld on a T-joint (see figure 8.5). Therefore, in these conditions, analytical solutions as those given by equations (8.3a) and (8.4) for the cooling rate have to be modified, using either:

- (Option A) 1/2 of the three thicknesses summed, or
- (Option B) 2/3 of the actual applied heat input.

8.2.4.1. Equivalent concepts from the EN 1011-2 (2001)

Option A is equivalent to the combined thickness concept applied in Method A for the avoidance of hydrogen cracking, given in EN 1011-2 (2001, Annex C.2).

A concept equivalent to Option B is available on the informative Annex D from the same welding standard, where besides equations (8.9) and (8.9), the following approximations for unalloyed and low alloyed steels are presented:

$$t_{8/5\,3D} = F_3 \times (6700 - 5T_0)\,H \times 10^{-6} \times \left(\frac{1}{500 - T_0} - \frac{1}{800 - T_0}\right) \tag{8.16a}$$

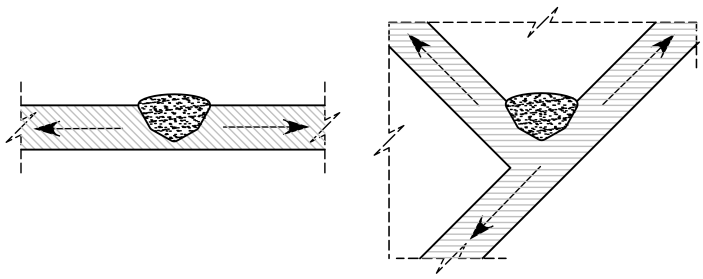

(a) Bi-thermal heat flow (b) Tri-thermal heat flow

Figure 8.5.: Bi and tri-thermal heat flow created into joints, respectively, with two and three avenues for the heat to escape.

Table 8.1.: Shape factors from the EN 1011-2 (2001), and equivalent heat input correction factors proposed for model generalization.

	Shape factor (EN 1011-2:2001 Table D.1)		Proposed heat input correction factor	
	F_2	F_3	C_H^{2D}	C_H^{3D}
Single run fillet weld on a T-joint	0.45 to 0.67	0.67	0.66 to 0.81	1.47
Between runs in butt welds	0.9	0.9	0.93	1.98
Run on plate	1	1	0.98	2.20

$$t_{8/5\,2D} = F_2 \times (4300 - 4.3T_0)\left(\frac{H}{d}\right)^2 \times 10^{-13} \times \left(\frac{1}{(500 - T_0)^2} - \frac{1}{(800 - T_0)^2}\right) \tag{8.16b}$$

In previous equations, modified for SI units, the two-dimensional F_2 and three-dimensional F_3 shape factors (see table 8.1) take into account the influence of the form of weld on the cooling time.

The ratio between $\sqrt{F^{(\text{run on plate})}}$ and $\sqrt{F^{(\text{fillet weld})}}$ ranges from 1.5 to 1.2 for 2D heat flow conditions, while for 3D heat flow conditions it is equal to 1.2.

8.2.4.2. Generalized heat input correction factors

In order to continue using the more general equations (8.3a), (8.4), (8.8) and (8.9), with improved accuracy, equivalent heat input correction factors (see table 8.1) were introduced as follows for:

- cooling rate prediction:

$$R_{540\,3D} = \frac{2\pi\, k}{C_{3D}^H \times H}\,(540 - T_0)^2 \tag{8.17a}$$

$$R_{540\,2D} = \frac{2\pi\, k\, \rho c\, d^2}{\left(C_{2D}^H \times H\right)^2}\,(540 - T_0)^3 \tag{8.17b}$$

- peak temperature prediction:

$$(T_p - T_0)_{3D} = \frac{2}{\pi e}\frac{C_{3D}^H \times H}{\rho c\, r^2} \tag{8.18a}$$

$$(T_p - T_0)_{2D} = \sqrt{\frac{2}{\pi e}}\frac{C_{2D}^H \times H}{2d\, \rho c\, r} \tag{8.18b}$$

- cooling time prediction:

$$t_{8/5\,3D} = \frac{C_{3D}^H \times H}{2\pi\, k} \times \left(\frac{1}{500 - T_0} - \frac{1}{800 - T_0}\right) \tag{8.19a}$$

$$t_{8/5\,2D} = \frac{(C_{2D}^H \times H)^2}{4\pi\, k\, \rho c\, d^2} \times \left(\frac{1}{(500 - T_0)^2} - \frac{1}{(800 - T_0)^2}\right) \tag{8.19b}$$

Equations (8.16) and (8.19) are approximately equivalent when:

$$\frac{C_{3D}^H}{F_3} \approx 2\pi\, k\ \times (6700 - 5T_0) \times 10^{-6}$$
$$\frac{\left(C_{2D}^H\right)^2}{F_2} \approx 4\pi\, k\, \rho\, c \times (4300 - 4.3T_0) \times 10^{-13}$$

Considering the simplifying assumption of constant thermal properties (in page 188), that for carbon steels (at room temperature $T_0 = 20°C$) are equal to: $\rho = 7850\ kg/m^3$, $k = 53\ J/m/°C$, $c = 440\ J/kg/°C$ (Acevedo, 2011), then:

$$C_{3D}^H \approx 2.20\ F_3 \tag{8.20a}$$
$$C_{2D}^H \approx \sqrt{0.97\ F_2} \tag{8.20b}$$

AWS D1.1 (2006) provides graphical representation of the required heat input for fillet welds, as function of the cooling rate and plate thicknesses ($H = f\,(R_{540}, d)$); however, no analytical relation is included. Equations (8.17) obtained improving equations (8.3a) and (8.4) through the heat input correction factors in table 8.1 (derived from EN 1011-2 (2001)) allows to bridge this lack of analytical model. As demonstrated in figure C.1, cooling rate prediction based on equations (8.17) match the normative data in AWS D1.1 (2006, Figure I-3a) with acceptable accuracy. The arithmetic mean $C_{2D}^H = 0.74$ was considered (for single run fillet weld on a T-joint).

Several predictions of the transition thickness were plotted in figure 8.6 in order to briefly compare the use of the heat input correction factors in table 8.1 (similar to Option B) with alternative Option A proposed by Blodgett (1966). It is observed that the equations obtained either equating:

- the cooling rate given by equations (8.17):

$$d_c^{(1)} = \sqrt{\frac{H}{\rho c\,(540 - T_0)}\frac{\left(C_H^{2D}\right)^2}{C_H^{3D}}} \tag{8.21}$$

- or the cooling time given by equations (8.19):

$$d_c^{(2)} = \sqrt{\frac{H}{2\rho c}\left(\frac{1}{500-T_0}+\frac{1}{800-T_0}\right)\frac{\left(C_H^{2D}\right)^2}{C_H^{3D}}} \tag{8.22}$$

yield approximately the same values for the transition thickness, both for groove and fillet welds.

On the other hand, if the combined thickness concept (Option A) is applied to equations (8.9) instead of a corrected heat input, the following equations are obtained:

$$d_c^{(3)-\text{butt weld}} = \sqrt{\frac{H}{2\rho c}\left(\frac{1}{500-T_0}+\frac{1}{800-T_0}\right)} \tag{8.23a}$$

$$d_c^{(3)-\text{fillet weld}} = \frac{2}{3}\sqrt{\frac{H}{2\rho c}\left(\frac{1}{500-T_0}+\frac{1}{800-T_0}\right)} \tag{8.23b}$$

through which similar transition thickness values are predicted for fillet welds, but clearly not for butt welds (see figure 8.6). This is a consequence of the correction term $\sqrt{\left(C_H^{2D}\right)^2/C_H^{3D}}$ appearing in equation (8.22) but not in equation (8.23a).

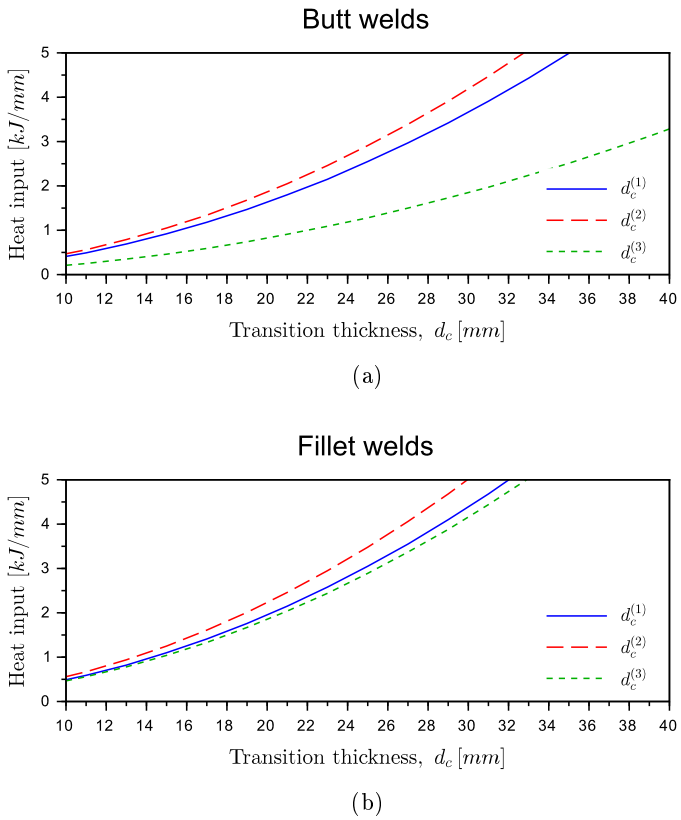

Figure 8.6.: Transitions thickness for (a) multi-pass butt welds and (b) single run fillet welds on T-joints, according to equations (8.21), (8.22) and (8.23).

8.3. Derivation of similarity conditions

Following the steps described by Simitses and Rezaeepazhand (1992), the similitude theory can be applied to equations (8.12), (8.13) and (8.17) to (8.19), yielding the following scaling laws:

- Heat input (per bead):

$$\lambda_H = \lambda_{s_1}\lambda_{s_2} \tag{8.24}$$

- Total heat input:

$$\lambda_{H^{total}} = \lambda_{S_1}\lambda_{S_2} \tag{8.25}$$

- Cooling rate:

$$\lambda_{R_{540}\,3D} = \lambda_k \frac{1}{\lambda_{C_{3D}^H}\lambda_H} \tag{8.26a}$$

$$\lambda_{R_{540}\,2D} = \lambda_k\lambda_\rho\lambda_c\left(\frac{\lambda_d}{\lambda_{C_{2D}^H}\lambda_H}\right)^2 \tag{8.26b}$$

- Peak temperature:

$$\lambda_{T_p\,3D} = \frac{1}{\lambda_\rho\lambda_c}\frac{\lambda_{C_{3D}^H}\lambda_H}{\lambda_r^2} \tag{8.27a}$$

$$\lambda_{T_p\,2D} = \frac{1}{\lambda_\rho\lambda_c}\frac{\lambda_{C_{2D}^H}\lambda_H}{\lambda_d\lambda_y} \tag{8.27b}$$

- Cooling time:

$$\lambda_{t_{8/5}\,3D} = \frac{1}{\lambda_k}\lambda_{C_{3D}^H}\lambda_H \tag{8.28a}$$

$$\lambda_{t_{8/5}\,2D} = \frac{1}{\lambda_k\lambda_\rho\lambda_c}\left(\frac{\lambda_{C_{2D}^H}\lambda_H}{\lambda_d}\right)^2 \tag{8.28b}$$

For the sake of simplicity, the prototype and its scaled model are assumed at the same initial temperature T_0.

8.3.1. Approach I: Complete similitude

Considering that:

- the same materials are used for both structures, and so, for equivalent points at the same temperature ($\lambda_T = 1$):

$$\lambda_k = \lambda_\rho = \lambda_c = 1 \tag{8.29}$$

- the following geometric similarity condition is valid:

$$\lambda_x = \lambda_d = \lambda_{S_1} = \lambda_{S_2} = \lambda_{s_1} = \lambda_{s_2} = \lambda_r = \lambda_y \tag{8.30}$$

- equivalent weld passes have the same shape factor:

$$\lambda_{C_{3D}^H} = 1, \quad \lambda_{C_{2D}^H} = 1$$

then, for complete similitude, the scaling laws are simplified as follows:

- Heat input:
$$\lambda_{H^{total}} = \lambda_H = \lambda_x^2 \tag{8.31}$$
- Cooling rate:
$$\lambda_{R_{540}} = \lambda_x^{-2}$$
- Peak temperature:
$$\lambda_{T_p} = 1$$
- Cooling time:
$$\lambda_{t_{8/5}} = \lambda_x^2$$

The thermal cycle during welding have a significant effect on the mechanical properties of a welded joint. According to Blondeau (2013), the final metallurgical structure at any point of the heat affected zone (HAZ) depends almost entirely on the peak temperature and on the cooling time Δt_{500}^{800} (or equivalent cooling rate). Increasing cooling speeds generally leads to increased toughness and hardness, but lower impact transition temperature of the HAZ.

The contradictory usual requirements for maximum hardness and minimum toughness define a metallurgical weldability field (in terms of cooling rate or time) (Blondeau, 2013; EN 1011-2, 2001) which is easily disrespected applying the scaling relationships here derived.

8.3.2. Approach II: Partial similitude with cooling rate preservation

Given the limitations of the scaling relationships derived in Approach I, a partial reduction of the thermal similitude during the welding process is proposed in this section, in order to obtain an increased level of constitutive similarity between the deposited filler metal and the HAZ of both structures. To that end, the cooling rate reached in the model's welding should be, as much as possible, preserved equal to that of the prototype's welding.

8.3.2.1. Cooling rate, heat input and number of passes

The previous requisite regarding the cooling rate preservation is mathematically stated as:

$$\lambda_{R_{540\,3D}} = \lambda_{R_{540\,2D}} \approx 1 \tag{8.32}$$

Accordingly, the following scaling relationships are derived from (8.26):

$$\lambda_{C_{3D}^H} \lambda_{H_{3D}} \approx \lambda_k \tag{8.33a}$$

$$\left(\lambda_{C_{2D}^H} \lambda_{H_{2D}}\right)^2 \approx \lambda_k \lambda_\rho \lambda_c \, \lambda_d^2 \tag{8.33b}$$

Considering:

- the prototype and its scaled model made of the same materials, and so, for equivalent points at the same temperature ($\lambda_T = 1$):
$$\lambda_k = \lambda_\rho = \lambda_c \approx 1 \tag{8.34}$$
- the following geometric similarity condition as valid:
$$\lambda_x = \lambda_d = \lambda_{S_1} = \lambda_{S_2} \tag{8.35}$$

- and approximately the same shape factors:

$$\lambda_{C_{3D}^H} \approx 1, \quad \lambda_{C_{2D}^H} \approx 1 \tag{8.36}$$

then, in order to preserve the cooling rate, it is concluded from (8.33) that the heat input has to be scaled as follows:

$$\lambda_{H_{3D}} \approx 1 \tag{8.37a}$$
$$\lambda_{H_{2D}} \approx \lambda_x \tag{8.37b}$$

On the other hand, the scaling relationship (8.25) yields:

$$\lambda_{H^{total}} = \lambda_x^2$$

which implies that, if all the bead passes has the same heat input H, then the required number of passes n has to be modified as follows:

$$\lambda_{n_{3D}} = \lambda_x^2 \tag{8.38a}$$
$$\lambda_{n_{2D}} = \lambda_x \tag{8.38b}$$

8.3.2.2. Peak temperature and HAZ size

Replacing similarity conditions (8.34) (that requires $\lambda_{T_p} = 1$), (8.35) and (8.36) into the scaling relationships (8.27), the following scale factors are obtained:

$$\lambda_r \approx 1 \tag{8.39}$$
$$\lambda_y \approx 1 \tag{8.40}$$

respectively for $3D$ and $2D$ heat flow conditions.

This means that, if the assumption of point heat source is valid, then the distance (measured relatively to the bead axis) at which a given peak temperature is achieved in the prototype remains unchanged in its scaled model.

Therefore, as the HAZ begins where the peak value T_p exceeds the lower critical temperature A_1 (Blondeau, 2013), the size of the HAZ created by a bead pass in the prototype will be approximately as big as that created by a bead in its scaled model, both measured relatively to the bead axis.

8.3.2.3. Cooling time

Replacing similarity conditions (8.34) to (8.36) into the scaling relationships (8.28) yields an unitary scale factor for the cooling time:

$$\lambda_{t_{8/5}\,3D} = \lambda_{t_{8/5}\,2D} \approx 1 \tag{8.41}$$

which is in accordance with the concept of cooling rate preservation.

8.4. Feasibility and validity analyses

In the following sections some feasibility and validity analyses are presented with regard to the scaling laws from Approach II. Besides, the numerical modeling of the T-joint fillet welding is included.

Section 8.4.1 presents the inverse analysis of GMAW procedures proposed by the main filler manufacturers. The scaling relationships are considered as feasible in practice if they are shown to be compatible with the assessed trend of predicted heat input in function of plate thickness.

Section 8.4.2 assesses trends in the process parameters prescribed in collected GMAW procedures. Then, through an available GMA weld pool model it is evaluated the validity of scaling the weld geometry based on approximate correlations between heat input and weld dimensions (from section 8.2.3).

Lastly, section 8.4.3 covers the numerical simulation of T-joint fillet welding of a prototype and its scaled model, whose process parameters are established according to scaling relationships. Theirs effectiveness in preserving the cooling rate is evaluated through the comparison of results.

8.4.1. Inverse analysis of welding procedures

Three of the main filler metal manufacturers: ESAB, Lincoln Eletric and PRAXAIR provide customers with recommended general welding conditions for low-carbon mild steels. Changes may be necessary to achieve the optimum welding condition, depending on the welder's experience, joint design and/or on the available equipment. Nevertheless, the proposed process parameters yield good and stable welding conditions, that can be applied in many situations (Fortes and Vaz, 2005).

In this section, a total of 164 collected procedures were analyzed. The trend in predicted heat input is assessed as a function of the plate thickness. If the scaling relationships (8.37) are shown to be compatible with the observed trends, then they are considered as feasible in practice. Besides, it is also indirectly evaluated the compatibility between the collected welding procedures and the scaling relationships (8.32) and (8.41) derived for the cooling rate and cooling time.

8.4.1.1. Heat input

Considering the transition thickness d_c given by equation (8.21), in table 8.2 welding procedures are distributed for each filler metal manufacturer according to the different heat flow conditions. From the total number of collected procedures, 154 generate 2D heat flow conditions and only 6 yield 3D heat flow. The remaining 4 procedures apply to plate thickness values in the $\pm 5\%$ range around the transition thickness.

Due to the reduced number of procedures yielding 3D heat flow conditions, they were not included in this analysis. Therefore, for the remaining welding procedures, and according to (8.35) and (8.37b), a linear relation is required between (scale factors for) the average heat input and the plate thickness.

Table 8.2.: Welding procedures' distribution according to three different heat flow conditions, defined through the ratio between plate thickness d and transition thickness d_c given by equation (8.21).

	$\frac{d}{d_c} < 0.95$	$0.95 < \frac{d}{d_c} < 1.05$	$\frac{d}{d_c} > 1.05$
ESAB	52	4	4
Lincoln Electric	32	0	0
PRAXAIR	70	0	2
Total	154	4	6

After averaging the torch velocity, arc current and voltage recomended by each procedure, given the thermal efficiency of GMAW process $\eta = 0.8$ (AWS D1.1, 2006; EN 1011-1, 1998), the heat input is determined by equation (8.10). The effect of different joint geometries is considered applying the correction factor C_H^{2D} equal to 0.93 and 0.74, respectively for butt and fillet welds (see table 8.1). As observed in the semi-log plot from figure 8.7, different filler metal manufacturers may diverge significantly regarding the proposed ideal welding conditions.

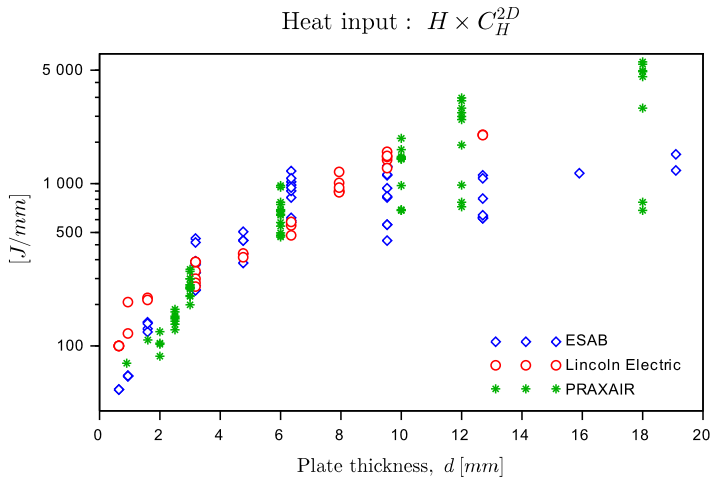

Figure 8.7.: Predicted heat input H for each welding procedure.

Additionally, the predicted heat inputs are averaged for each thickness, as represented in the semi-log plot from figure 8.8, and then fitted by the following power law:

$$H(d) = a_H \times d^{n_H} \tag{8.42}$$

Values obtained for a_H, n_H and R-squared parameter are available from table 8.3.

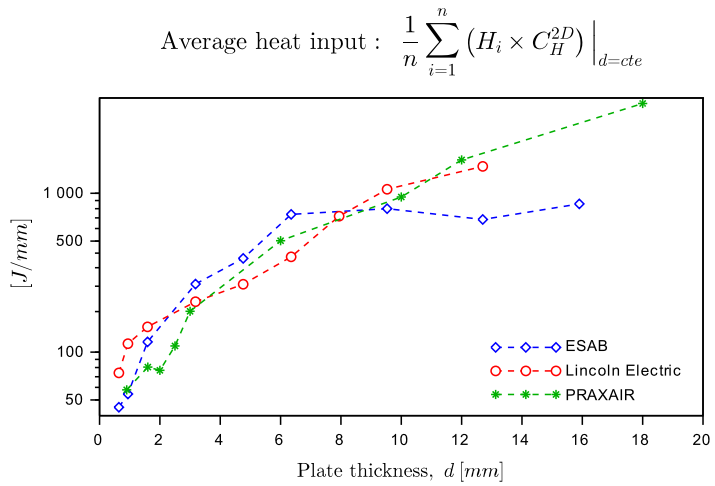

Figure 8.8.: Average predicted heat input H for each plate thickness.

Applying the similitude theory to power law (8.42) the following scaling law is obtained:

$$\lambda_H = \lambda_d^{n_H} \tag{8.43}$$

So, the scaling law (8.31) from approach I requires $n_H = 2$ (from now on referred to as square scaling), while the scaling laws (8.37b) from approach II, applicable only for welding procedures yielding 2D heat flow conditions, requires $n_H = 1$ (from now on referred to as linear scaling).

Table 8.3.: Values for the n_H exponent and the R-squared parameter obtained fitting a power law $H(d) = a_H \times d^{n_H}$ to the data points in figure 8.8.

	a_H	n_H	R^2
ESAB	73.3	1.00	0.90
Lincoln Electric	96.4	0.93	0.96
PRAXAIR	39.6	1.45	0.99

The obtained n_H values in table 8.3 show that the welding procedures proposed by Lincoln Electric and particularly by ESAB are in an average manner compatible with a linear scaling. On the other hand, for the PRAXAIR procedures, the average heat input evolves in function of the plate thickness raised to 1.45 which corresponds to an intermediate scaling between those required by Approach I and II.

The conclusion to retain is that the linear scaling proposed in Approach II is feasible according to the welding procedures proposed by two of the main filler metal manufacturers.

8.4.1.2. Cooling rate, peak temperature and cooling time

The previous type of analysis ca not be performed for a parameter X being non-linear function of its dependent variables, given that:

$$\frac{(X_n)^a}{n} \neq \left(\frac{X_n}{n}\right)^a \quad \forall \quad a \neq \{0, 1\}$$

To clarify this, a specific example is presented. Consider a set of n dependent variables $\{d_i, H_i\}$ and the correspondent n cooling rate values CR_i, whose average values are respectively $\overline{d_i}, \overline{H_i}, \overline{CR_i}$. Besides, from equation (8.17b), the average dependent parameters $\left(\overline{d_i}, \overline{H_i}\right)$ yield the following cooling rate CR_{n+1}.

The scaling law (8.26b) is correctly applied if used to relate any par of operating points given by equation (8.17b) which, besides $\{d_i, H_i, CR_i\}$, includes $\left(\overline{d_i}, \overline{H_i}, CR_{n+1}\right)$ but not $\left(\overline{d_i}, \overline{H_i}, \overline{CR_i}\right)$.

This limitation is overcome searching procedures for different thicknesses with the same value for $\frac{H \times C_H^{2D}}{d}$, and so, with the same cooling rate, peak temperature and cooling time. Figure 8.9 demonstrates that particularly for $50 \leq \frac{H \times C_H^{2D}}{d} \leq 150\ J/mm^2$, several similar welding procedures from as low as $0.6\ mm$ up to $19\ mm$ respect the similarity conditions (8.32) and (8.41).

As one can see from table 8.4 those values are compatible with the maximum cooling rates imposed by AWS D1.1 (2006) for structural steel grades such as the S235JR, S275JR and S355JR.

The procedures proposed by PRAXAIR, although do not respect the linear scaling of heat input from Approach II, were included in figure 8.9 to highlight that flexibility exist beyond the procedures proposed by ESAB and Lincoln Eletric. This is, given that all the procedures yield good and stable welding conditions regardless of the manufacturer which recommended them, any sub-set crossed by an horizontal line yield improved constitutive similarity of the weldments.

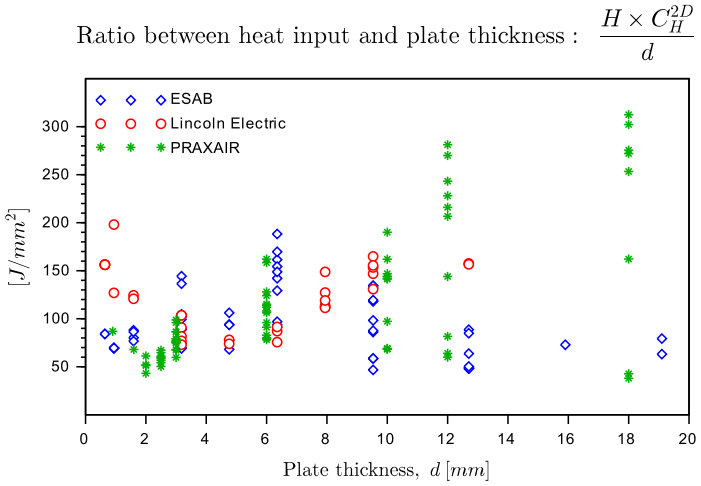

Figure 8.9.: Ratio between heat input and plate thickness, $\frac{H \times C_H^{2D}}{d}$.

Table 8.4.: Minimum $\frac{H \times C_H^{2D}}{d}$ required not to exceed the estimated critical cooling rate R^c_{540} from table C.4.

	$\frac{H \times C_H^{2D}}{d}\,[J/mm^2]$ for maximum hardness:	
	$\leq$ 400 HV	$\leq$ 350 HV
S235JR	40	54
S275JR	56	70
S355JR	75	89

8.4.2. Process parameters' effect on weld geometry

In the root pass of groove and rounded fillet welds, being partially defined by the joint surfaces, the bead cross section has only one variable characteristic dimension: the root pass thickness and the leg size (see equations (8.14) and (8.15)), respectively. Therefore, in those cases, through the heat input not only the bead (effective) cross-sectional area is (approximately) imposed, but also its characteristic dimension.

However, during multi-pass welding some beads may be deposited over the previous without its geometry being constrained by the joint boundaries (see figure 8.4). Even in single pass welding, depositing a bead-on-plate is an extreme case study where that kind of freedom is observed, requiring the process parameters to be known in order to predict the bead cross section.

A further analysis of the process parameters' effect on weld geometry is considered in this section and structured as follows:

- Firstly, it is evaluated how does voltage, current and welding velocity evolve as a function of the plate thickness, in the procedures proposed by ESAB and Lincoln Electric, where approximated linear scaling of the heat input (in relation to the plate thickness) was observed in section 8.4.1.1.

- The assessed trends are then introduced on available relationships between the weld pool geometry and the process parameters. This allows to characterize how relevant

weld geometric parameters are scaled if the heat input increases linearly with the plate thickness.

- Lastly, scaling relationships between the weld pool geometry and the plate thickness are derived applying the similitude theory.

8.4.2.1. Relationships between the process parameters and the plate thickness

A further analysis of the welding procedures proposed by ESAB and Lincoln Electric allows to assess the possibilities for proper scaling of the process parameters, that still respect the approximated linear scaling of the heat input, as identified in section 8.4.1.1. After averaging the voltage, current and welding velocity for each plate thickness, the following power laws are fitted:

$$U(d) = a_U \times d^{n_U} \tag{8.44a}$$
$$I(d) = a_I \times d^{n_I} \tag{8.44b}$$
$$v(d) = a_v \times d^{n_v} \tag{8.44c}$$

The exponents n_U, n_I, n_v are available in table 8.5. As demonstrated by the R-squared parameter values in the same table, only the voltage and current are well correlated through power laws (8.44). The overall trend of average welding velocity is moderately described by power law (8.44c) in the procedures by ESAB, but not in those proposed by Lincoln Electric. The observed lack of correlation should be taken into account but do not invalidate the conclusions of a feasibility analysis.

Table 8.5.: Values of the exponents n_U, n_I, n_v and the R-squared parameter obtained fitting power laws (8.44) to the process parameters of the welding procedures proposed by ESAB and Lincoln Eletric.

		ESAB	Lincoln Electric
Voltage (U)	a_U	14.9	15.8
	n_U	0.20	0.21
	R^2	0.95	0.97
Current (I)	a_I	71.2	61.3
	n_I	0.56	0.70
	R^2	0.99	0.95
Velocity (v)	a_v	10.0	6.0
	n_v	-0.24	-0.01
	R^2	0.88	0.00

Applying the similitude theory to power laws (8.44), the following scaling laws are obtained:

$$\lambda_U = {\lambda_d}^{n_U} \tag{8.45a}$$
$$\lambda_I = {\lambda_d}^{n_I} \tag{8.45b}$$
$$\lambda_v = {\lambda_d}^{n_v} \tag{8.45c}$$

8.4.2.2. Relationships between the weld pool geometry and the process parameters

The relationship between the welding process variables (voltage, current, speed and shielding gas composition) and the weld pool geometry are available in the form of power laws for the GMAW process (Wahab and Painter, 1997), as follows:

width:

$$\mathrm{wd} = 10^{2.02953} \times U^{0.48843} \times I^{0.65068} \times v^{-0.53419} \times (1 - CO_2)^{-0.97075}$$

bead height:

$$\mathrm{h} = 10^{-2.2526} \times U^{-0.0203} \times I^{0.65062} \times v^{-0.38287} \times (1 - CO_2)^{1.12987}$$

penetration:

$$\mathrm{p} = 10^{1.87816} \times U^{1.47845} \times I^{0.97853} \times v^{-0.53027} \times (1 - CO_2)^{-2.32128}$$

These power laws are based on experimentally determined weld pool shapes obtained with voltage, current and speed values in the following respective ranges: $17 - 31\,V$, $125 - 235\,A$ and $100 - 500\,mm/min$.

If the composition of protection gas remains unchanged, application of the similitude theory to previous correlations yields:

$$\lambda_{\mathrm{wd}} = {\lambda_U}^{0.4884} \times {\lambda_I}^{0.6507} \times {\lambda_v}^{-0.5342} \tag{8.46a}$$

$$\lambda_{\mathrm{h}} = {\lambda_U}^{-0.0203} \times {\lambda_I}^{0.6506} \times {\lambda_v}^{-0.3829} \tag{8.46b}$$

$$\lambda_{\mathrm{p}} = {\lambda_U}^{1.4784} \times {\lambda_I}^{0.9785} \times {\lambda_v}^{-0.5303} \tag{8.46c}$$

8.4.2.3. Scaling relationships between the weld pool geometry and the plate thickness

Replacing the scale factors (8.45) into (8.46), yields the scale factor for the weld pool geometry in function of the plate thickness scale factor (λ_d):

$$\lambda_{\mathrm{wd}} = {\lambda_d}^{n_{wd}} \tag{8.47a}$$

$$\lambda_{\mathrm{h}} = {\lambda_d}^{n_h} \tag{8.47b}$$

$$\lambda_{\mathrm{p}} = {\lambda_d}^{n_p} \tag{8.47c}$$

with:

$$n_{wd} = \ 0.4884\ n_U\ +\ 0.6507\ n_I\ -\ 0.5342\ n_v \tag{8.48a}$$

$$n_h = -0.0203\ n_U\ +\ 0.6506\ n_I\ -\ 0.3829\ n_v \tag{8.48b}$$

$$n_p = \ 1.4784\ n_U\ +\ 0.9785\ n_I\ -\ 0.5303\ n_v \tag{8.48c}$$

In a bead deposited on the plate, weld cross-sectional area (A) above the plate surface is proportional to the product of pool width by bead height. Therefore, the following scaling relationship applies:

$$\lambda_{\mathrm{A}} = \lambda_{\mathrm{width}} \times \lambda_{\mathrm{height}} \Leftrightarrow$$
$$\Leftrightarrow \lambda_{\mathrm{A}} = {\lambda_d}^{n_A} \tag{8.49}$$

with

$$n_A = n_{wd} + n_h \tag{8.50}$$

The exponents n_{wd}, n_h, n_p and n_A are available in table 8.6, describing how relevant geometric dimensions are scaled using the welding procedures proposed by ESAB and Lincoln Electric.

Table 8.6.: Exponent values in the scaling laws (8.47) and (8.49) regarding the weld pool geometry.

		ESAB	Lincoln Electric
pool width	n_{wd}	0.59	0.57
bead heigth	n_h	0.45	0.46
penetration	n_p	0.97	1.00
cross-sectional area	n_A	1.04	1.02

If the characteristic dimensions were scaled similarly, from equations (8.12), (8.35) and (8.37b), it would be expected that:

$$\lambda_{s_1} = \lambda_{s_2} = \lambda_d^{0.5}$$

However, in table 8.6 it is observed that the bead width and height are scaled in relation to the plate thickness with an exponent different from the expected 0.5 value: the width reduces slower ($n_{wd} < 0.5$) while the bead height reduces quicker ($n_h > 0.5$). Nevertheless, it is verified that the heat input is approximately proportional to the effective cross-sectional area: $n_H \approx n_A \approx 1$. Besides, it is demonstrated that the weld penetration is scaled by the same factor as the plate thickness ($n_p \approx 1$).

8.4.2.4. Generalization of scaling relationships

From the three process parameters under analysis, the arc voltage is the only one for which ESAB and Lincoln Electric proposed consensual values, approximately given by power law (8.44a) with $a_U = 15$ and $n_U = 0.2$:

$$U(d) = 15\ d^{0.2} \tag{8.51}$$

Even so, the power laws obtained for the arc current can also be approximately generalized averaging the obtained a_I values (in table 8.5) and considering a variable exponent n_I ranging between 0.56 and 0.70:

$$I(d) = 66\ d^{n_I} \tag{8.52}$$

On the other hand, considering the similitude theory applied to equation (8.10), yields:

$$\lambda_H = \lambda_\eta \lambda_U \lambda_I \lambda_v^{-1}$$

Assuming the same efficiency $\lambda_\eta = 1$ and after replacing the power laws (8.43) and (8.45), the following relation is obtained:

$$n_v = n_U + n_I - n_H \tag{8.53}$$

This relation allows to avoid the direct use of the power law (8.44c) for welding velocity, that as observed from table 8.5 has low R-squared parameter values. Therefore, the

expressions (8.48) for exponents n_{wd}, n_h and n_p are rewritten as follows:

$$n_{wd} = -0.0458\ n_U\ +\ 0.1165\ n_I\ +\ 0.5342\ n_H \tag{8.54a}$$

$$n_h = -0.4032\ n_U\ +\ 0.2677\ n_I\ +\ 0.3829\ n_H \tag{8.54b}$$

$$n_p = \ \ 0.9482\ n_U\ +\ 0.4483\ n_I\ +\ 0.5303\ n_H \tag{8.54c}$$

where the unknown n_v is replaced by n_H, fixed equal to 1 by approach II.

So, the only remaining unknown in previous expressions is n_I. Figure 8.10 allows to clarify how exponents n_{wd}, n_h, n_p and n_A evolve for values of n_I ranging from 0.56 to 0.70, as observed in the ESAB and Lincoln Electric procedures, respectively. The results are similar to those observed in table 8.6.

In the same figure, its observed that n_v values given by (8.53) range between -0.25 and -0.10, which is compatible with values from table 8.5.

The most unexpected result in figure 8.10 is that, if a perfect linear scaling of heat input is achieved ($n_H = 1$), the effective weld cross-sectional area will decrease more than expected: $n_A \in [1.04;\ 1.10]$, particularly for higher n_I values. In table 8.6, the analysis of welding procedures proposed by Lincoln Electric (having $n_I = 0.7$) yiels $n_A \approx 1$, beacuse the n_H value is slightly under 1 ($n_H = 0.93$).

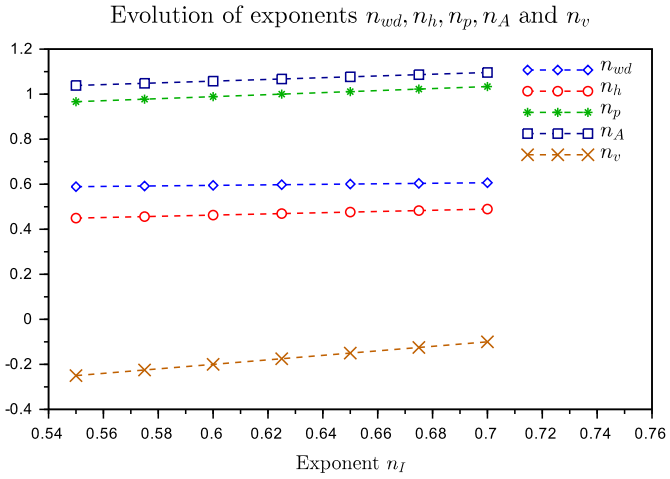

Figure 8.10.: Evolution of exponents n regarding the weld cross-sectional geometry (n_{wd}, n_h, n_p, n_A) and welding velocity (n_v), given by equations (8.50), (8.53) and (8.54).

8.4.3. Numerical simulation of T-joint fillet welding

In this section the fillet welding of a prototype is numerically simulated. Besides, its 1/3-scale model is considered, whose process parameters were defined according to the scaling approach II proposed in this manuscript, in order to improve the constitutive similarity between both structures. Lastly, to support the discussion of results, the 2/3-scale model is also simulated.

8.4.3.1. Modeling approaches

Firstly presented by Shubert et al., the ABAQUS Welding Interface (AWI) was used in the present research. Its application in the simulation of multi-pass welding, as well as, the available modeling approaches are briefly discussed by Dassault Systèmes (2013). A further

explanation and detailed review of these and other state-of-the-art approaches is presented by Lindgren (2001).

Regarding the modeling of the addition of the filler material, the quiet element approach was preferred instead of the inactive element approach. According to Lindgren (2001), both approaches can give the same results, and so, the choice of method is more a matter of what is more practical. In the quiet element approach, the non-laid welds are present in the model; its elements should be given material properties so that they do no affect the rest of the model (Lindgren, 2001).

The modeling of the heating phase is another topic subjected to different approaches in the literature. Prescribing the temperature in the weld during an appropriate torch step time is easier than directly prescribing the heat input. This time interval is defined based on the chunk length and average welding speed (Lindgren, 2001).

Concluding, weld beads for each pass are deposited in discrete chunks at the target torch temperature, through the quiet element approach. In the heat transfer analysis, the "ramp and hold option" was selected. This is, before activating the chunk, the temperature in the interface between the chunk and the base metal is linearly increased up to the torch temperature during the ramp time (t_1) and then it is prescribed at that temperature for the remaining duration of the hold time (t_2) (Dassault Systèmes, 2013). Although these simplifications reduce accuracy in the heating phase, the cooling will be computed correctly given that the temperature is no longer prescribed (Lindgren, 2001).

8.4.3.2. Prototype's geometry and material properties

As represented in figure 8.11, the prototype is obtained joining a plate attachment of nominal dimensions $300\,mm \times 150\,mm \times 15\,mm$ to a main plate of nominal dimensions $300\,mm \times 200\,mm \times 15\,mm$ by a fillet weld with $12\,mm$ of leg size. The welding sequence is according to figure 8.11.

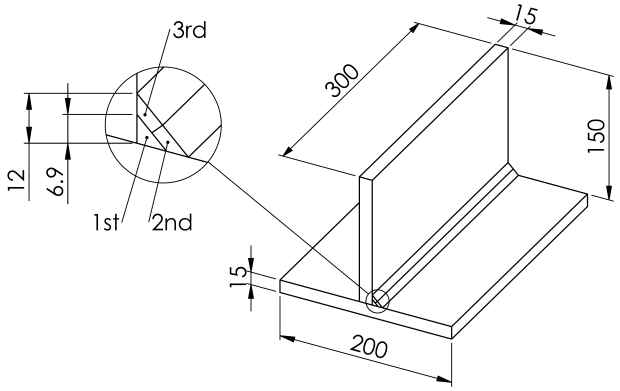

Figure 8.11.: Prototype's geometry and welding sequence.

Both plates are made of steel grade S235JR, whose material properties are discussed in appendix C.2. Assuming the selection of a mismatch filler metal, the weld metal properties are considered the same as those of the base metal (Dassault Systèmes, 2013).

8.4.3.3. Prototype's welding procedure

The prototype's welding procedure is established based on equations (8.10), (8.15), (8.44b) and (8.51).

Considering three beads with equal cross-sectional area, according to equation (8.15), a weld leg equal to 12 mm requires (per bead) an heat input of around 1590 J/mm. On the other hand, the required arc voltage and current are estimated equal to $25\,V - 26\,V$ and 325 A, using the current power law (8.44b) adjusted to the ESAB welding procedures ($a_I = 71.2, n_I = 0.56$), and the generalized voltage power law (8.51) ($a_U = 15, n_U = 0.2$). With $\eta = 0.8$ (AWS D1.1, 2006; EN 1011-1, 1998), equation (8.10) imposes the average welding velocity equal to $5.2\,mm/s$.

Lastly, it is verified that the welding procedure creates a 2D heat flow condition in the base material, given that the estimated transition thickness is between $d_c^{(1)} = 16.3\,mm$ and $d_c^{(2)} = 15.2\,mm$, obtained respectively through equations (8.21) and (8.22).

8.4.3.4. Scaled model's description

The 1/3-scale model ($\lambda_x = 3$) of the structure's prototype is described below. In order to improve the constitutive similarity between both structures, the welding procedure and process parameters were defined according to the scaling approach II proposed in section 8.3.2.

The scaled model's geometry represented in figure 8.12 is a replica of the prototype ($\lambda_x = \lambda_d = \lambda_{S_1} = \lambda_{S_2}$) and material properties are the same as those described in section 8.4.3.2.

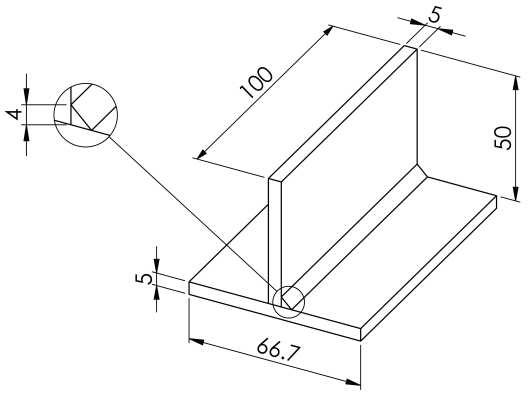

Figure 8.12.: Geometry of the 1/3-scale model.

Table 8.7.: Welding process parameters of the prototype and its 1/3-scale model

		Prototype (Fig. 8.11)	1/3-scale Model (Fig. 8.12)
Heat input, H	$[J/mm]$	1590	530
Arc voltage, U	$[V]$	25-26	20-21
Arc current, I	$[A]$	325	176
Welding velocity, v	$[mm/s]$	5.2	6.8

Regarding the welding procedure, as imposed by (8.38b), the 3 passes in the prototype's weld are lumped into a single pass, whose process parameters are available in table 8.7. Those values were obtained as follows, scaling the prototype's process parameters through (8.37b) and (8.45). The heat input scale factor is defined by equation (8.37b) ($\lambda_H = 3$), which, as explained in section 8.4.1.1, corresponds to a linear scaling of the heat input in relation to the plate thickness scaling ($n_H = 1$). Besides, replacing $n_U = 0.20$ and $n_I = 0.56$

into equations (8.45a) and (8.45b) yields the scale factors for the arc voltage ($\lambda_U = 1.25$) and current ($\lambda_I = 1.85$). Lastly, the average welding velocity can be either scaled through the factor ($\lambda_v = 0.77$) given by (8.45c), replacing the exponent n_v obtained from (8.53), or directly calculated from (8.10) using the scaled process parameters.

Furthermore it is verified that, with estimated transition thickness between $d_c^{(1)} = 9.4mm$ and $d_c^{(2)} = 8.8\,mm$, obtained respectively through equations (8.21) and (8.22), this welding procedure generates 2D heat flow condition in the base material.

8.4.3.5. Specific details of the simulations

Each bead in both the prototype and its 1/3-scale model is divided longitudinally into 15 chunks, each having $20\,mm$ and $6.7\,mm$ in length, respectively.

For the average welding velocities specified into table 8.7, each chunk takes $3.85\,s$ and $0.98\,s$ to be deposited, respectively for the prototype and scaled model. Automatic time stepping is used (with maximum time step equal to $0.4\,s$ and $0.1\,s$). The previous time interval is divided into the ramp time (t_1) and the hold time (t_2), with $\frac{t_1}{t_1+t_2} = 80\%$. In both models the initial temperature is $21°C$ and the target torch temperature is set to $1550°C$.

Other relevant parameter is the the maximum allowed temperature increment per step time, given that it controls the accuracy of the thermal analysis solution (Deng et al., 2008). In both simulations, this parameter is set to $50°C$.

For the prototype, the mesh elements globally have $5mm$ through the thickness and along the weld axis. In the remaining transversal directions they have a biased sized distribution ranging between $5\,mm$ and $18\,mm$, with additional refinement provided in the weld. The mesh is replicated 3 times smaller for the scaled model.

Both thermal analyses use 11340 first-order brick elements of type DC3D8.

8.4.3.6. Results

Description

The 8^{th} chunk in the weld mid-length was selected in the prototype, as well as, in its 1/3-scale model. For nodes 862 to 865 in the weld root, and for nodes 356, 604 and 3666, distributed in the weld cross section passing through node 863 (see figure 8.13), the cooling rate R_{540} and cooling time $t_{8/5}$ were calculated and made available in table 8.8. The relative differences for each node (in relation to the average values) are included in table 8.9. Besides, the cooling phase of nodes 862 and 865 was plotted in figure 8.14.

Discussion

A further analysis of the simulation results shows that a quasi-stationary mode is achieved, with the temperature distribution around the source adopting a stable form in relation to time for equivalent nodes in successive chunks. This is, nodes 861, 865 and 869 have the same stable time-temperature distribution, as well as nodes 862, 866 and 870, and so on.

However, analyzing the results in table 8.8, it is observed that the weld discretization into chunks may cause some variations of the cooling parameters along the nodes 862 to 865 of the chunk's length. Even if only (these) nodes along the weld root was considered, the relative differences would reach up to ±8% for the prototype's simulation, while in the scaled model's simulations they are negligible (±1%).

On the other hand Blondeau (2013) states that, according to several experimental readings of thermal cycles, the various zones of a weld deposit can be characterized by a single cooling

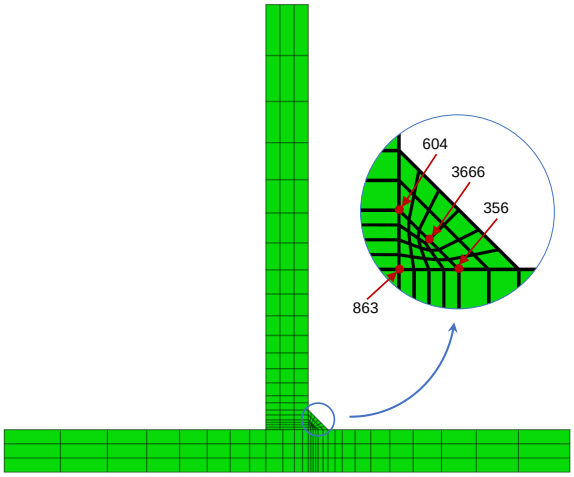

Figure 8.13.: Position of nodes 356, 604 and 3666 in the section passing through node 863.

Table 8.8.: Cooling rate R_{540} and cooling time $t_{8/5}$ for nodes of the 8^{th} chunk. Nodes 862 to 865 are located in the weld root and nodes 356, 604 and 3666 are distributed in the weld cross section passing through node 863.

	Prototype		1/3-scale Model	
Node	R_{540} [°C/s]	$t_{8/5}$ [s]	R_{540} [°C/s]	$t_{8/5}$ [s]
862	33.9	6.6	40.9	4.5
863	32.2	6.8	41.0	4.6
864	33.9	6.2	40.8	4.6
865	35.7	5.8	40.9	4.6
356	34.3	6.4	41.4	4.4
604	30.8	6.9	40.5	4.7
3666	33.2	6.4	41.1	4.5
Average:	33.4	6.5	41.0	4.5

time obtained for the weld axis. As one can see from figure 8.14 significant differences are found in time-temperature distribution of nodes 862 and 865. However, considering only the nodes 863, 356, 604 and 3666 from the same section, the relative differences of both the cooling rate and cooling time are reduced, falling in the ±7% and ±3% range, respectively in the prototype's and scaled model's simulation.

Taking both the variations of the cooling parameters into account, this is, variations along the weld axis and along the weld cross section, the relative differences (in table 8.9) obtained for all the 7 analyzed nodes reach up to ±9% and ±3%, respectively in the prototype's and scaled model's simulation.

An overview of the averaged numerical results is presented in table 8.10 along with the analytical predictions given by (8.17b) and (8.19b). The effective scale factors $\lambda_{R_{540}} = 0.8$ and $\lambda_{t_{8/5}} = 1.4$ derived from the numerical simulation are significantly different from the expected unitary values. The causes for relative differences reaching −18% for $\lambda_{R_{540}}$ and +42% for $\lambda_{t_{8/5}}$ are explained below, introducing the concept of 2.5D heat flow conditions.

Table 8.9.: Relative differences of the cooling rate R_{540} and cooling time $t_{8/5}$ values from table 8.8 in relation to the averaged values in the same table.

Node	Prototype		1/3-scale Model	
	R_{540}	$t_{8/5}$	R_{540}	$t_{8/5}$
862	1.5%	1.7%	-0.1%	-0.1%
863	-3.6%	5.6%	0.1%	0.2%
864	1.4%	-3.7%	-0.4%	0.9%
865	6.8%	-9.4%	-0.1%	0.5%
356	2.5%	-1.4%	1.2%	-3.4%
604	-8.0%	7.4%	-1.0%	2.7%
3666	-0.6%	-0.1%	0.4%	-0.8%

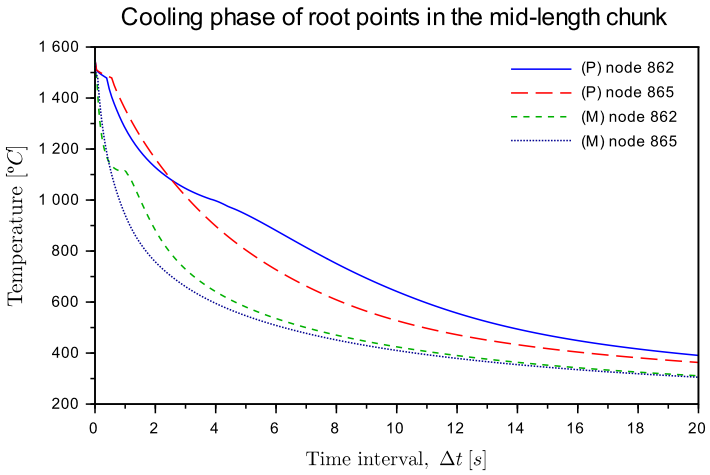

Figure 8.14.: Comparison of cooling phase of nodes 862 and 865 from prototype (P) and its 1/3-scale model (M).

Justification of the observed relative differences

Analytical solutions based only on pure 2D and 3D heat flow conditions are widely implemented. Examples of these models are the equations (8.16) used by EN 1011-2 (2001) or the equations (8.17) matching normative data in AWS D1.1 (2006, Figure I-3a). However, as the transition between extreme 2D and 3D heat flow condition is progressive rather than discrete, some authors (including Blodgett (1966) and Signes (1972)) proposed the concept of an intermediate 2.5D heat flow condition.

Blodgett (1966) introduced the traditional equations for extreme heat flow conditions:

$$R_{T_{2D}} = K_1 \frac{d^2 \, (T - T_0)^3}{H^2}$$

$$R_{T_{3D}} = K_2 \frac{(T - T_0)^2}{H}$$

where for mild steel $K_1 = 161.48$ and $K_2 = 5.961$, with T and R_T expressed in $°F$ and $°F/s$, respectively.

Table 8.10.: Comparison between the average cooling rate R_{540} [°C/s] and cooling time $t_{8/5}$ [s] values obtained from ABAQUS (in table 8.8) and the analytical predictions given by equations (8.17b) and (8.19b).

		Prototype	1/3-scale Model	λ
R_{540}	eq. (8.17b)	41.2	41.2	1.00
	ABAQUS	33.4	41.0	0.82
	Rel. difference	-18.9%	-0.6%	-18.4%
$t_{8/5}$	eq. (8.19b)	4.6	4.6	1.00
	ABAQUS	6.5	4.5	1.42
	Rel. difference	40.3%	-1.2%	42.0%

As these are the same equations as (8.3a) and (8.4), it can be deduced that:

$$K_1 = 2\pi\, k\, \rho c$$
$$K_2 = 2\pi\, k$$

Additionally, in order to take into account the transition between the extreme 2D and 3D heat flows conditions, Blodgett (1966) proposed the following model:

$$R_{572\,2D} = 161.48\,\frac{d^2\,(572 - T_0)^3}{H^2} \tag{8.55a}$$

$$R_{572\,2.5D} = -161.48\,\frac{d^2\,(T - T_0)^3}{H^2} + 87.75\,d\sqrt{\frac{(572 - T_0)^2}{H^3}} - 5.961\frac{(572 - T_0)^2}{H} \tag{8.55b}$$

$$R_{572\,3D} = 5.961\,\frac{(572 - T_0)^2}{H} \tag{8.55c}$$

where once again T and R_T are expressed in $°F$ and $°F/s$, respectively.

For the present research, in order to generalize the model for any material properties, as well as, to allow the use of SI units, the following generalized equations were derived through the reverse analysis of equations (8.55). Besides, the heat correction factors given by equations (8.20) were introduced:

$$R_{T\,2D} = \frac{K_1}{\left(C^H_{2D}\right)^2}\,\frac{d^2\,(T - T_0)^3}{H^2} \tag{8.56a}$$

$$R_{T\,2.5D} = -\frac{K_1}{\left(C^H_{2D}\right)^2}\,\frac{d^2\,(T - T_0)^3}{H^2} + \\ + 2\sqrt{2\frac{K_1}{\left(C^H_{2D}\right)^2}\,\frac{K_2}{C^H_{3D}}\,\frac{d^2\,(T - T_0)^5}{H^3}} - \frac{K_2}{C^H_{3D}}\,\frac{(T - T_0)^2}{H} \tag{8.56b}$$

$$R_{T\,3D} = \frac{K_2}{C^H_{3D}}\,\frac{(T - T_0)^2}{H} \tag{8.56c}$$

The transition thicknesses between the three considered heat flow conditions are the following:

$$d_c^{(2D-2.5D)} = \sqrt{\frac{1}{2}\,\frac{K_2}{K_1}\,\frac{\left(C_{2D}^H\right)^2}{C_{3D}^H}\,\frac{H}{(T-T_0)}} \tag{8.57a}$$

$$d_c^{(2.5D-3D)} = \sqrt{2\,\frac{K_2}{K_1}\,\frac{\left(C_{2D}^H\right)^2}{C_{3D}^H}\,\frac{H}{(T-T_0)}} \tag{8.57b}$$

Taking the cooling rate predicted by equations (8.56a) and (8.56b), the relative differences in table 8.10 were recalculated and are available in table 8.11. The main change is that both the (analytically predicted) prototype's cooling rate and its scale factor reduced about 11.4%.

The discrepancies between the analytically and numerically predicted cooling rates is reduced by the same amount to only −8.5%, and are now likely to be justified by differences between the analytical and numerical models. The Rosenthal's equations assume point heat source, negligible heat of fusion and constant thermal properties, whereas in numerical modeling: finite chunks are used, the heat of fusion is considered and the thermal properties are temperature-dependent.

Table 8.11.: Comparison between the average cooling rate R_{540} [°C/s] values obtained from ABAQUS (in table 8.9) and the analytical predictions given by equations (8.56a)/(8.56b).

		Prototype	1/3-scale Model	λ
R_{540}	eq. (8.56a)/(8.56b)	36.5	41.2	0.89
	ABAQUS	33.4	41.0	0.82
	Rel. difference	-8.5%	-0.6%	-8.0%

Range of applicability of scaling laws based on 2D heat flow conditions

The analytical solutions of cooling parameters derived based on extreme 2D heat flow conditions may yield inaccurate predictions for welding procedures in which 2.5D heat flow conditions are generated. Therefore, the use of scaling laws derived in section 8.3.2 for 2D heat flow conditions should be avoided if the 2.5D heat flow conditions are achieved through the prototype's welding process.

Applying the similitude theory to equation (8.57a) and after considering the similarity conditions given by (8.34) and (8.36), yields:

$$\lambda_{d_c} = \sqrt{\lambda_H} \tag{8.58}$$

that through scaling law (8.37b) is equivalent to:

$$\lambda_{d_c} = \sqrt{x} \tag{8.59}$$

So, by an inverse analysis, the maximum prototype's plate thickness still yielding 2D heat

flow conditions is given in function of a scaled model's characteristics as follows:

$$\begin{aligned} & d^{(p)} \leq d_c^{(p)} \quad \Leftrightarrow \\ \Leftrightarrow \quad & d^{(m)} \times \lambda_x \leq d_c^{(m)} \times \sqrt{\lambda_x} \quad \Leftrightarrow \\ \Leftrightarrow \quad & \lambda_x \leq \left(\frac{d_c^{(m)}}{d^{(m)}} \right)^2 \end{aligned} \tag{8.60}$$

The latter expression allows to conclude that for the scaled model analyzed in section 8.4.3 the maximum scale factor, corresponding to a prototype's whose welding process still yields 2D heat flow conditions, is approximately equal to:

$$\lambda_x \leq \left(\frac{6.6}{5} \right)^2 = 1.8 \tag{8.61}$$

Rounding up this value to $\lambda_x = 2$, yields the intermediate prototype in figure 8.15. The geometry is a 2/3-replica of the initially considered prototype (in figure 8.11), and, a 2/1-replica of the scaled model (in figure 8.12). Once again, the material properties are the same as those described in section 8.4.3.2.

Regarding the welding procedure, as imposed by (8.38b), the weld in this intermediate prototype has 2 passes, whose process parameters in table 8.12 were calculated following exactly the same procedure as used in section 8.4.3.4.

Table 8.12.: Welding process parameters of the intermediate prototype and its 1/2-scale model

		Intermediate Prototype (Fig. 8.15)	1/2-scale Model (Fig. 8.12)
Heat input, H	$[J/mm]$	1060	530
Arc voltage, U	$[V]$	23-24	20-21
Arc current, I	$[A]$	259	176
Welding velocity, v	$[mm/s]$	5.7	6.8

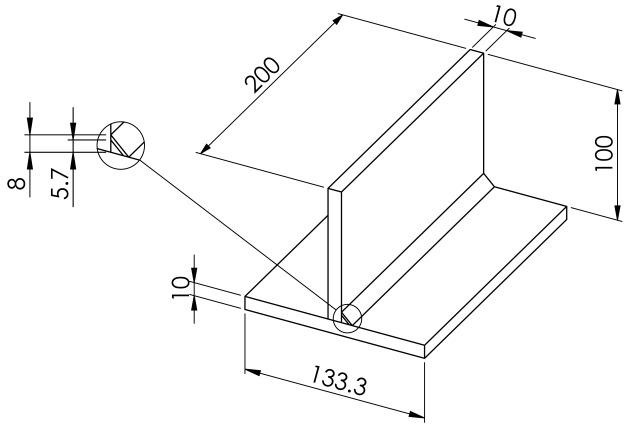

Figure 8.15.: Geometry of intermediate prototype.

The cooling rate and cooling time were calculated based on the time-temperature dis-

tribution taken from 7 nodes in the 8^{th} chunk (4 along the weld root and 3 in the cross section). The averaged results are presented in table 8.13 along with the reference values obtained from equations (8.56a) and (8.56b) for the cooling rate.

Table 8.13.: Comparison between the average cooling rate R_{540} [°C/s] values obtained from ABAQUS and the analytical predictions given by equations (8.56a)/(8.56b), for nodes of the 8^{th} chunk in the intermediate prototype and its 1/2-scale model.

		Intermediate Prototype	1/2-scale Model	λ
R_{540}	eq. (8.56a)/(8.56b)	40.8	41.2	0.99
	ABAQUS	39.4	41.0	0.96
	Rel. difference	-3.5%	-0.6%	-3.8%

The plate thickness in the intermediate prototype ($d = 10\,mm$) is about 14% higher than then the transition thickness between the 2D and 2.5D heat flow conditions, given by equation (8.57a). Even so, as one can see in table 8.13, the analytically determined scale factor for the cooling rate is only 1% lower than the required unitary value. On the other hand the same scale factor predicted through numerical simulations is about 4% lower than the unitary value. This level of relative difference is quite acceptable, and justified by the differences between the analytical and numerical models listed in the end of section 8.4.3.6.

8.5. Concluding remarks

This chapter covers the lack of research discussing how structural similitude is affected by differences between the welding procedures used for the prototype and its scaled models.

The classical thermal modeling of structural welding is introduced (sections 8.2.1 and 8.2.2) and related with the weld cross-sectional dimensions through the heat input, using available experimentally determined relations (section 8.2.3). Through the heat input correction factors C_{3D}^{H} and C_{2D}^{H} derived in section 8.2.4, the previous thermal modeling is extended from bi-thermal to tri-thermal heat flow conditions. Besides, these factors allow to better match both the analytical expressions (for colling time) in EN 1011-2 (2001) and the graphical data (for colling rate) in AWS D1.1 (2006).

Applying the similitude theory to equations (8.12), (8.13) and (8.17) to (8.19) (predicting the heat input, cooling rate, peak temperature and cooling time), a set of similarity conditions are derived, including those given by equations (8.24) to (8.28).

Complete (thermal) similitude is achieved if all the similarity conditions are respected. However, this is incompatible with metallurgical weldability field defined by the contradictory usual requirements for maximum hardness and minimum toughness. Alternatively, seeking constitutive similarity, the use of partial similitude with cooling rate preservation (entitled Approach II) is proposed in section 8.3.2. To achieve the unitary scaling factor (equation (8.32)) required for cooling rate, the heat input has to be scaled according to the relationships (8.37) and the number of passes has to be distorted according to scale factors (8.38). As expected, the derived scaling factor for cooling time (8.41) is also unitary.

A total of 164 GMAW procedures proposed by ESAB, Lincoln Electric and PRAXAIR were collected and analyzed. In section 8.4.1, the assessed trends of predicted heat input in function of plate thickness allow to conclude that the scaling relationship (8.37b) is compatible only with the welding procedures proposed by ESAB and Lincoln Electric. Including also the welding procedures proposed by PRAXAIR, it is visualized in figure 8.9 that, from

as low as 0.3 mm up to 19 mm, several similar welding procedures respect the similarity conditions (8.32) and (8.41).

In section 8.4.2, equations (8.45) and table 8.5 provided scale factors for the arc voltage, current and velocity given in function of the scale factor for the plate thickness, obtained for the welding procedures proposed by ESAB and Lincoln Electric. Additionally, applying the similitude theory to available weld pool geometry model, the scaled factors (8.46) for bead width, height and penetration are derived in function of the previous process parameters. After replacing (8.45) into (8.46) it is concluded that:

- For a bead-on-plate, although the ratio between the bead width and height is slightly modified when scaling the plate thickness, relation (8.12) between the heat input and the bead cross-sectional area remains approximately valid;
- Depositing a bead-on-plate, weld penetration is scaled by the same scale factor as the plate thickness.

Lastly, the scaling laws for arc voltage (U) and current (I) and velocity are generalized as follows:

$$\lambda_U = \lambda_d^{n_U}$$
$$\lambda_I = \lambda_d^{n_I}$$
$$\lambda_v = \lambda_d^{n_U+n_I-n_H}$$

where $n_U = 0.2$ and n_I ranges between 0.56 and 0.70 for currently proposed welding procedures, while n_H is required by Approach II to be equal to 1. However, from figure 8.10 is observed that if a perfect linear scaling of heat input is achieved ($n_H = 1$), the effective weld cross sectional area (A) will decrease more than expected, particularly for higher n_I values. This is, n_A ranges between 1.04 and 1.10 in the generalized scale factor:

$$\lambda_A = \lambda_d^{n_A}$$

Section 8.4.3 covers the numerical simulation of T-joint fillet welding of a prototype and its 1/3-scale model. The results exposed significant relative differences between the analytically and numerically predicted cooling rate and time, with average relative differences of -19% and $+40\%$, respectively.

The cause for these differences was explained introducing the concept of $2.5D$ heat flow condition, that consist of a transition state between extreme $2D$ and $3D$ heat flow conditions. It is demonstrated that, although widely implemented, analytical solutions of cooling parameters derived based on extreme $2D$ heat flow condition may yield inaccurate predictions for welding procedures in which $2.5D$ heat flow condition is achieved.

To demonstrate this, an intermediate prototype (the 2/3-scale model of original prototype) is considered and numerically simulated. Comparing the obtained results with those from its 1/2-scale model, a relative difference below -4% is obtained between the analytically and numerically determined cooling rates. Similar relative difference is observed between the required unitary value and the numerically determined scale factor for cooling rate.

This results validate the effectiveness of derived scaling relationships in preserving the cooling rate, as long as 2D heat flow conditions are generated during welding in the prototype and its scaled model.

Part IV.

Conclusion

9. Conclusion

Abstract

The use of scientific models based on dimensional analysis was firstly proposed by Rayleigh a century ago. However the value and virtues of the reduced scale model testing got more attention of the general scientific community only in the last three decades.

The presented work aimed at the development of an intuitive methodology, able to take advantage of the known potential of the experimental scaled model testing.

Generalized scaling relationships for anisotropic plates were presented, allowing to improve how their structural similitude is established.

Additionally, the new Modular Approach was presented in order to address the structural similitude of complex structures. The methodology was demonstrated and validated through numerical and experimental analysis of stiffened plates.

Lastly, some attention was given to the manufacturing process, particularly to the constitutive similarity of welded joints in scaled models.

All the relevant conclusions of the research carried out in this thesis are summarized in this chapter, followed by suggestion of required future work.

9.1. Conclusions

9.1.1. Introductory sections

Chapter 1 introduced the model analysis as a simulation technique. The development of the X-48 BWB aircraft, the Aurora Borealis icebreaker and diverse civil structures are given as iconic examples where the use of scaled models were undoubtedly advantageous. Unfortunately, for such case studies the details of the applied methodology in the creation and use of scaled models are not available.

In order to give the theoretical basis necessary to correctly understand the literature review presented in chapter 3, the Similarity Theory was introduced in **chapter 2** along with its main concepts and definitions. The Empirical Similarity Method (ESM), the Traditional Similarity Method (TSM) and the Similitude Theory applied to Governing Equations (STAGE) are presented and briefly compared in their scope, advantages and disadvantages.

9.1.2. Literature review

In **chapter 3**, a detailed and extensive analysis of the state of the art revealed a significant number of publications based mainly on the dimensional analysis (TSM) or alternatively on the use of differential equations (STAGE).

Although the most recent books and manuals covering the use of Dimensional Analysis had been published mainly with an academic purpose, including only simple examples, the published aerospace industry case studies demonstrated the applicability for complex structures. However, the correct use of dimensional analysis requires great effort and skill. When selecting the complete and independent set of quantities affecting the structural behavior, not even the smallest detail can be overlooked, while irrelevant quantities should be avoided as much as possible. Besides, the obtained pi-terms are not unique; although

following well defined steps the construction of the most adequate set of pi-terms is made by trial-and-error.

On the other hand, the STAGE is a more intuitive approach because the governing equations explicitly define the response of the system as a function of its independent variables. The two main approaches developed since then were the use of the solution for the differential equations and the direct use of that equations. Although the last avoid the need to solve the equation explicitly, one still needs to know enough about the physics of the problem to be able to write down a complete set of governing equations. This primary weakness may explain why this method was rarely applied in the literature to structures more complex than plates and shells, since the governing equations were not available.

In order to give a complete perspective of the state-of-the-art approaches and available literature, other relevant methodologies were reviewed. Additionally, the rapid prototyping of models and the analysis of impacted structures are two other areas of research, where very interesting and inspiring work has been done, continuously improving existing methods.

Despite the broad spectrum of this chapter, the remaining thesis research was focused on structural and thermal scaled model analysis, with special attention given to the constitutive similitude in the last part. From all the reviewed methodologies, the STAGE was selected as primary method for further improvements. Sporadically, dimensional analysis was applied as secondary method, for example deriving implicit scaling factors.

9.1.3. Generalized scaling relationships

Work in **chapter 4** investigated the potential advantages in applying the similitude theory to the governing equations of plates, minimizing the simplifications. As a result, a generalized procedure to obtain the scaling relationships for an anisotropic laminated plate have been created for static, dynamic and stability analysis, with the intention to more easily derive the scaling laws for any laminated anisotropic plate. Therefore instead of applying the similitude theory to the governing equations with specific simplifications related to the plate being studied, the scaling laws are quickly derived from a generalized set of similarity conditions.

Other achieved objective was the reduction of the assumed similarity conditions when deriving the complete similitude. Only the in-plane geometric similitude was assumed, ensuring that all the other derived conditions (such as the use of the same materials for both systems) are not over-constraining the scale model.

The ability to apply the generalized set of scaling relationships to a specific problem was demonstrated deriving all the particular sets of similitude criteria proposed previously for cylindrical bending of laminated plates, vibration of elastically restrained isotropic flat plates, and buckling of laminated plates subjected to biaxial or shear loading.

Besides, the experimental scaled model testing, as an alternative simulation tool, was numerically validated through the prediction of the frequency response functions of an honeycomb panel, based on the results obtained from a distorted 1/6-scale model.

9.1.4. Modular Approach to structural similitude

Even if the applied methodology to derive the generalized scaling laws is more structured and straightforward, its application is neither simple nor intuitive.

The research presented in **chapter 5** addressed the need for a methodology to design scaled models based on the similitude theory, being as intuitive as those based on the use of governing equations, but as versatile as those based on the dimensional analysis, without requiring great effort and skill for complex structures.

The proposed solution is an approach based on a new modular concept, intended to improve how the similitude theory is applied to governing equations, and so overcoming identified limitations and difficulties.

The major achievement demonstrated in this chapter is that similitude theory can be applied to complex structures through differential equations of its simple substructures, even if the governing equations for the whole structure are not available. When compared to established methodologies, the strength of proposed approach lies in the possibility of combining modules of similarity conditions. No simplifying assumption is applied to the governing equations, which makes the scaling relationships in each of that modules as general as possible, but still easily adjusted to a specific application.

Therefore, for a given structural element, the governing equations are organized into modules of simpler equations. From each of them, a module of scaling relationships is derived. Then, by sequential substitutions all the previous modules can be grouped to create (in a second level) a global module with the scaling relationships for the structural behavior. Repeating the process for several structural elements, such as beams, plates or shells, the obtained global modules can be related to create (in a third level) a module with the scaling relationships for the structural behavior of a complex prototype.

A similar procedure can be repeated (up to the third level) to create a module with scaling relationships for any physical behavior. Ultimately relating (third-level) thermal and structural modules, for example, the thermal-structural behavior can be scaled.

A stiffened plate was selected to demonstrate the use of the Modular Approach and the accuracy of the scaled model testing. Through the comparison of the actual and predicted transversal displacement field of a stiffened plate under static load, the experimental scaled model testing is numerically validated as an alternative accurate simulation tool. The predicted results matched perfectly the calculated transverse displacement of the prototype.

Finally, it was highlighted that the truly potential of this Modular Approach is beyond that demonstrated through this case study. At the moment, any structure composed from plates and beams/stiffeners could have been analyzed. Once the structural global module for other simple elements (including shells and solid parts) are available, it will be possible to establish structural similitude between scaled models and prototypes with higher diversity of structural elements. Another referred area of promising research is the applicability of Modular Approach to the scaling of multi-physics problems.

9.1.5. Experimental research

In order to provide a more comprehensive validation of the Modular Approach to structural similitude, an experimental program was carried out and presented in **chapter 6**. Its objectives can be succinctly summarized as follows:

- Investigation of the effect of the scaled model reduction, for the same prototype;
- Investigation of the effect of the prototype scale, for approximately the same scaled model reduction;
- Comparison between the experimental scaled model testing and the FE-model simulation;
- Assessment of how the similitude of structural behavior evolves for structures of increasing complexity.

To achieve them, a T-stiffened plate was selected as a case study. Through the Modular Approach to structural similitude, scaling relationships were obtained in order to design two reduced models with different scale reduction: 1/5 and 2/5.

In intermediate stages of the manufacturing process, the base plates and one stiffener of each scale were dynamically tested. Once the stiffened plates were available, they were also dynamically tested. Due to some unforeseen circumstances in the manufacturing process, galvanized scaled stiffened plates were dynamically tested in addition to the remaining large, medium and small scale structures.

No significant and consistent size effects were detected in the measured experimental data. In light of this research, it is suggested that the observed changes in the $\overline{LAC_{jk}}$ values are not primarily driven by the scale of the specific prototype under analysis, neither by differences in the scale reduction; they are in this research suggested as a consequence of distorted scaling effects.

According to the literature, residual stresses induced by manufacturing processes are often neglected in structural analysis due to challenging aspects associated with their simulation, which may cause inaccurate numerical results to be calculated. Even though the reduced scale modeling is an alternative experimental simulation technique, its predictions are equally affected when significant effects are neglected, including those of the residual stresses. Future research on the topic of dynamic experimental scaled model testing should devote special attention to the importance of correct scaling of residual stresses induced by the manufacturing processes.

Besides, the basic assumption of the Modular Approach was consistently verified as valid. Despite the wide diversity of observed ranges of $\overline{LAC_{jk}}$ values, the maximum value for any metric correlating experimentally predicted values and experimentally measured data of the stiffened plates is outlined by the upper limit obtained for its simpler substructures, regardless of the scale reduction and prototype scale effects or even the effect of the residual stresses.

On the other hand, the static tests allowed to demonstrate how the experimental scaled model testing is effective in the detection of unforeseen or unknown phenomena. The small scaled model testing was quite effective in accurately reproducing the global force-displacement behavior of the stiffened plate prior and after the shakedown of welding-induced residual stresses.

9.1.6. Modular Approach to thermal-structural similitude

In **chapter 7**, the Modular Approach was extended allowing thermal and thermal-structural similitude to be established. Difficulties dealing with conductive-convective-radiative systems were highlighted and explained through the structural-thermal analogy.

Lastly, through the thermal-structural simulation of the welding process in specimens of different scales, it was concluded that the experimental scale model testing provide acceptable accuracy for structures whose heat transfer is mostly conductive.

9.1.7. Constitutive similitude of welded joints

The work presented in **chapter 8** covers the lack of research discussing how structural similitude is affected by differences between the welding procedures used for the prototype and its scaled models.

The classical thermal modeling of structural welding is introduced and related with the weld cross-sectional dimensions through the heat input, using available experimentally determined relations. Through derived heat input correction factors, the previous thermal modeling is extended from bi-thermal to tri-thermal heat flow conditions.

Applying the similitude theory to equations predicting the heat input, cooling rate, peak temperature and cooling time, a set of similarity conditions are derived.

Complete (thermal) similitude is achieved if all the similarity conditions are respected. However, this (Approach I) is incompatible with metallurgical weldability field defined by the contradictory usual requirements for maximum hardness and minimum toughness. Alternatively, seeking constitutive similarity, the use of partial similitude with cooling rate preservation (Approach II) is proposed.

A total of 164 GMAW procedures proposed by ESAB, Lincoln Electric and PRAXAIR were collected and analyzed. The assessed trends of predicted heat input in function of plate thickness allow to conclude that the proposed scaling relationship are compatible only with the welding procedures by ESAB and Lincoln Electric. Besides, it is demonstrated that, from as low as $0.3\,mm$ up to $19\,mm$, several similar welding procedures respect the derived similarity conditions.

The numerical simulation of T-joint fillet welding of a prototype and its 1/3-scale model was presented for further validation. The results exposed significant relative differences between the analytically and numerically predicted cooling rate and time, with average relative differences of -19% and $+40\%$, respectively.

The cause for these differences was explained introducing the concept of $2.5D$ heat flow condition, that consist of a transition state between extreme $2D$ and $3D$ heat flow conditions. It is demonstrated that, although widely implemented, analytical solutions of cooling parameters derived based on extreme $2D$ heat flow condition may yield inaccurate predictions for welding procedures in which $2.5D$ heat flow condition is achieved.

To demonstrate this, an intermediate prototype (the 2/3-scale model of original prototype) is considered and numerically simulated. Comparing the obtained results with those from its 1/2-scale model, it is observed a relative difference below -4% between the analytically and numerically determined cooling rates. Similar relative difference is observed between the required unitary value and the numerically determined scale factor for cooling rate.

These results validate the effectiveness of derived scaling relationships in preserving the cooling rate, as long as 2D heat flow conditions are generated during welding in the prototype and its scaled model.

9.2. Future Developments

In line with the research presented in this thesis, the following topics are highlighted as requiring incremental developments or additional research:

- The Modular Approach was developed to the point of being able to be applied to complex structures obtained by the assembly of plates and beams/stiffeners. In order to further unlock its potential for other applications, the development of structural global modules for other simple elements such as shells are required;

- The experimental testing of stiffened plates provided results demonstrating that residual stresses due to several operations through the manufacturing processes may have a significant impact on the dynamic structural response.

  Further research is required to fully understand which scaling relationships have to be imposed through the manufacturing processes, in order to ensure confidence on the accuracy of the dynamic experimental scaled model testing as a simulation tool;

- The presented experimental testing of steel stiffened plates was devoted to static testing in elastic regime and frequency response analysis by impact testing. The available experimental data is intended to be complemented with:

  - Shaker-forced frequency response analysis of the prototypes and theirs scaled models;
  - Dynamic testing of rapid prototyped 1/5-scaled models, obtained by different 3D printing technologies: the fused deposition method (cheap and commonly available) and the stereolithography process (providing outperforming quality).

- Accurate static scale model testing of welded structures in the plastic regime raises additional difficulties due to aspects that, contrary to what happens in elastic regime, are no longer negligible. The constitutive similarity of welded joints addressed in the final part of this thesis is one of those aspects. Scaling relationships were provided and analytically/numerically validated for 2D and 2.5D heat flow conditions generated in the base material during welding. The following complementary research may be performed in future developments:
  - Derivation of similarity conditions for welding processes whose parameters induce 3D heat flow conditions in the base material of the prototype;
  - Implementation of an experimental campaign to verify the numerical validations already presented regarding constitutive similitude of welded joints.

9.3. Scientific publications

Through the course of this thesis the author has published some of his work in peer reviewed journals as well as international conferences:

- Coutinho, C. P., A. J. Baptista and J. Dias Rodrigues (2016). "Reduced scale models based on similitude theory: A review up to 2015." Engineering Structures 119: 81-94
- Coutinho, C. P., A. J. Baptista and J. Dias Rodrigues (2016). Generalized scaling relationships for the complete similitude of plates. The BSSM's 11th International Conference on Advances in Experimental Mechanics. University of Exeter, UK
- Coutinho, C. P., A. J. Baptista and J. Dias Rodrigues (2018). "Modular Approach to structural similitude." International Journal of Mechanical Sciences 135: 294-312.

References

Abambres, M., Quach, W.M., 2016. Residual stresses in steel members: a review of available analytical expressions. International Journal of Structural Integrity 7, 70–94.

Acevedo, C., 2011. Influence of residual stresses on fatigue response of welded tubular K-joints. Ph.D. thesis.

Adelman, H.M., Steeves, E.C., 1968. Vibration analysis of a 1/40 scale dynamic model of Saturn V – launch-platform – umbilical-tower configuration. Report NASA TN-D-4871. National Aeronautics and Space Administration.

Ahmad, A., 1996. Handbook of optomechanical engineering. CRC Press.

Akhlaghi, F.Z., 2014. Welding Simulation and Fatigue Assessment of Tubular K-Joints in High-Strength Steel. Ph.D. thesis.

Ali, I., Jun, Y.J., 2014. Mathematical models for in-plane moduli of honeycomb structures - a review. Research Journal of Applied Sciences, Engineering and Technology 7, 581–592.

Alves, M., Oshiro, R.E., 2006a. Scaling impacted structures when the prototype and the model are made of different materials. International Journal of Solids and Structures 43, 2744–2760.

Alves, M., Oshiro, R.E., 2006b. Scaling the impact of a mass on a structure. International Journal of Impact Engineering 32, 1158–1173.

Ambur, D.R., B., C.P., Rose, C.A., Feraboli, P., Jackson, W.C., 2005. Scaling the non-linear impact response of flat and curved composite panels.

Anderson, Charles E., J., Mullin, S.A., Kuhlman, C.J., 1992. Strain-rate effects in replica scale model penetration experiments. Report SwRI 3593/002. Defense Advanced Research Projects Agency.

Ashton, J.E., Whitney, J.M., 1970. Theory of laminated plates. Technomic Publishing Company, Inc.

ASME, 1963. Use of models and scaling in shock and vibrations.

Atkins, A.G., 1988. Scaling in combined plastic flow and fracture. International Journal of Mechanical Sciences 30, 173–191.

Atkins, A.G., 1999. Scaling laws for elastoplastic fracture. International Journal of Fracture 95, 51–65.

Attarha, M.J., Sattari-Far, I., 2011. Study on welding temperature distribution in thin welded plates through experimental measurements and finite element simulation. Journal of Materials Processing Technology 211, 688–694.

AWS D1.1, 2006. Structural welding code - steel.

Aziz, A., Tao, J., 2012. Simulation of thermal stresses in a disc brake. M.Sc. thesis.

Badran, S.F., Saddek, A.B., Leheta, H.W., 2013. Ultimate strength of y and t stiffeners subjected to lateral loads with three different levels of initial imperfection. Ocean Engineering 61, 12–25.

Bailey, N., 1994. Weldability of ferritic steels. Woodhead Publishing.

Baker, W.E., Westine, P.S., Dodge, F.T., 1991. Similarity methods in engineering dynamics: Theory and practice of scale modeling. Revised ed., Elsevier.

Balawi, S.O.M., 2007. Effective Mechanical Behavior of Honeycombs: Theoretical and Experimental Studies. Ph.D. thesis.

Bazant, Z.P., 1993. Scaling laws in mechanics of failure. Journal of Engineering Mechanics 119, 1828–1844.

Belvin, W.K., Edighoffer, H.E., 1986a. 15 meter hoop-column antenna dynamics: Test and analysis, in: Wright, R.L. (Ed.), First NASA/DOD CSI Technology Conference, Norfolk, Virginia. pp. 167–185.

Belvin, W.K., Edighoffer, H.E., 1986b. Experimental and analytical generic space station dynamic models. Report NASA TM-87696. National Aeronautics and Space Administration.

Bergman, T.L., Lavine, A.S., Incropera, F.P., DeWitt, D.P., 2011. Fundamentals of heat and mass transfer. 7 ed., John Wiley & Sons.

Bernstein, M., Coppolino, R., Zalesak, J., Mason, P.W., 1974. Development of technology for fluid-structure interaction modeling of a 1/8-scale dynamic model of shuttle External Tank (ET) - Volume I: Technical report. Report NASA CR-132549-1. National Aeronautics and Space Administration.

Blanchard, U.J., 1968. Evaluation of a full-scale lunar-gravity simulator by comparison of landing-impact tests of a full-scale and a 1/6-scale model. Report NASA TN-D-4474. National Aeronautics and Space Administration.

Blanchard, U.J., Miserentino, R., Leadbetter, S.A., 1977. Experimental investigation of the vibration characteristics of a model of an asymmetric multielement space shuttle. Report NASA TN-D-8448. National Aeronautics and Space Administration.

Blodgett, O.W., 1963. Design of Weldments. James F. Lincoln Arc Welding Foundation.

Blodgett, O.W., 1966. Design of Welded Steel Structures. 3 ed., James F. Lincoln Arc Welding Foundation.

Blok, J.J., Dekker, J.N., 1979. On hydrodynamic aspects of ship collision with rigid or non-rigid structures.

Blondeau, R., 2013. Metallurgy and mechanics of welding. John Wiley & Sons.

Boudjemai, A., Amri, R., Mankour, A., Salem, H., Bouanane, M.H., Boutchicha, D., 2012. Modal analysis and testing of hexagonal honeycomb plates used for satellite structural design. Materials & Design 35, 266–275.

Brauer, J., 1993. What every engineer should know about finite element analysis. CRC Press.

Bridgman, P.W., 1922. Dimensional Analysis. Yale University Press, New Haven.

Brush, D.O., Almroth, B.O., 1975. Buckling of bars, plates, and shells.

Buckingham, E., 1914. On physically similar systems; illustrations of the use of dimensional equations. Physical Review 4, 345–376.

Burlayenko, V.N., Sadowski, T., 2009. Analysis of structural performance of sandwich plates with foam-filled aluminum hexagonal honeycomb core. Computational Materials Science 45, 658–662.

Burton, W.S., Noor, A.K., 1997. Assessment of continuum models for sandwich panel honeycomb cores. Computer Methods in Applied Mechanics and Engineering 145, 341–360.

Calle, M.A.G., Alves, M., . Ship collision: A brief survey, in: 21st Brazilian Congress of Mechanical Engineering - COBEM 2011.

Canfield, S.L., Beard, J.W., Peddieson, J., Ewing, A., Garbe, G., 2004. Similarity rules for scaling solar sail systems.

Canfield, S.L., Peddieson, J., Garbe, G., 2010. Similarity rules for scaling solar sail systems. Report M10-0055. National Aeronautics and Space Administration.

Carden, H.D., Herr, R.W., 1964. A study of the effectiveness of various methods of vibration reduction on simplified scale models of the Nimbus spacecraft. Report NASA TN-D-2418. National Aeronautics and Space Administration.

Carrillo, J.G., Cantwell, W.J., 2008. Scaling effects in the low velocity impact response of fiber-metal laminates. Journal of Reinforced Plastics and Composites 27, 893–907.

Cartmell, M.P., Ziegler, S.W., Neill, D.S., 2003. On the performance prediction and scale modelling of a motorised momentum exchange propulsion tether, in: American Institute of Physics (AIP) Conference, pp. 571–579.

Catherine, J.J., 1965. Torsional vibration characteristics of a 1/5-scale model of Saturn SA-1. Report NASA TN-D-2745. National Aeronautics and Space Administration.

Catherine, J.J., 1968. Experimental vibration characteristics of a 1/40-scale dynamic model of the Saturn V – launch-umbilical-tower configuration. Report NASA TN-D-4870. National Aeronautics and Space Administration.

Chambers, J.R., 2009. Modeling flight: The role of dynamically scaled free flight models in support of NASA's aerospace programs. Report NASA SP-2009-575. National Aeronautics and Space Administration.

Charlton, T.M., 1954. Model analysis of structures. E. & F. N. Spon, London.

Chen, Y., 2003. Ultimate strength analysis of stiffened panels using a beam column method. Ph.D. thesis.

Chia, C.Y., 1980. Nonlinear analysis of plates. McGraw Hill, New York.

Cho, U., Dutson, A.J., Wood, K.L., Crawford, R.H., 2005. An advanced method to correlate scale models with distorted configurations. Journal of Mechanical Design 127, 78.

Cho, U., Wood, K., 1997. Empirical similitude method for the functional test with rapid prototypes.

Cho, U., Wood, K., Crawford, R.H., 1999. Error measures for functional product testing, in: 1999 ASME Design Engineering Technical Conferences.

Cho, U., Wood, K.L., Crawford, R.H., . Novel empirical similarity method for the reliable product test with rapid prototypes, in: 1998 ASME Design Engineering Technical Conferences.

Cho, U., Wood, K.L., Crawford, R.H., 1998. Online functional testing with rapid prototypes: a novel empirical similarity method. Rapid Prototyping Journal 4, 128–138.

Chouchaoui, C.S., Ochoa, O.O., 1999. Similitude study for laminated cylindrical tube under tension, torsion, bending, internal and external pressure - part i: governing equations. Composite Structures 44, 221–229.

Chouchaoui, C.S., Parks, P., Ochoa, O.O., 1999. Similitude study for a laminated cylindrical tube under tension, torsion, bending, internal and external pressure - part ii: scale models. Composite Structures 44, 231–236.

Christoforou, A.P., Yigit, A.S., 1998. Effect of flexibility on low velocity impact response. Journal of Sound and Vibration 217, 563–578.

Christoforou, A.P., Yigit, A.S., 2009. Scaling of low-velocity impact response in composite structures. Composite Structures 91, 358–365.

Chuk, R.N., Thomson, V.J., 1998. A comparison of rapid prototyping techniques used for wind tunnel model fabrication. Rapid Prototyping Journal 4, 185–196.

Chung, W.J., Yun, C.B., Kim, N.S., Seo, J.W., 1999. Shaking table and pseudodynamic tests for the evaluation of the seismic performance of base isolated structures. Engineering Structures 21, 365–379.

Cinar, O., Erdal, M., Kayran, A., 2015. Accurate equivalent models of sandwich laminates with honeycomb core and composite face sheets via optimization involving modal behavior. Journal of Sandwich Structures and Materials , 1–28.

Cosentino, G.B., 2010. Flight Testing the X-48B at the NASA Dryden Flight Research Center. Report DFRC-E-DAA-TN1299. NASA Dryden Flight Research Center.

Coutinho, C.P., Baptista, A.J., Dias Rodrigues, J., 2016. Reduced scale models based on similitude theory: A review up to 2015. Engineering Structures 119, 81–94.

Cruz, P.J.S., 2016. Edgar Cardoso: a tribute to a brilliant bridge engineer. Structure and Infrastructure Engineering , 1–20.

Dang-guo, Y., Yan, S., Zheng-yu, Z., Chao, W., Wei-jun, Z., 2013. Design and manufacture methods of rapid prototyping wind-tunnel models based on photopolymer-resin. Rapid Prototyping Journal 19, 20–27.

Dang-guo, Y., Zheng-yu, Z., Yan, S., Wei-jun, Z., 2011. A preliminary design and manufacturing study of hybrid lightweight high-speed wind-tunnel models. Rapid Prototyping Journal 17, 45–54.

Dassault Systèmes, 2013. Multi-pass pipe welding analysis using the Abaqus Welding Interface. Report TB-13-AWI-1.

Davis, D.A., Gronet, M.J., Tan, M.K., Thorne, J., 1994. Conceptual design and analysis of a dynamic scale model of the space station freedom. Report NASA CR-4598. National Aeronautics and Space Administration.

Davis, J.R., 1992. ASM Materials Engineering Dictionary. ASM International.

De Rosa, S., Franco, F., 2008. A scaling procedure for the response of an isolated system with high modal overlap factor. Mechanical Systems and Signal Processing 22, 1549–1565.

De Rosa, S., Franco, F., 2010. On the use of the asymptotic scaled modal analysis for time-harmonic structural analysis and for the prediction of coupling loss factors for similar systems. Mechanical Systems and Signal Processing 24, 455–480.

De Rosa, S., Franco, F., Li, X., Polito, T., 2012. A similitude for structural acoustic enclosures. Mechanical Systems and Signal Processing 30, 330–342.

De Rosa, S., Franco, F., Polito, T., 2011. Structural similitudes for the dynamic response of plates and assemblies of plates. Mechanical Systems and Signal Processing 25, 969–980.

Deng, D., Murakawa, H., Liang, W., 2008. Numerical and experimental investigations on welding residual stress in multi-pass butt-welded austenitic stainless steel pipe. Computational Materials Science 42, 234–244.

Dornfeld, W.H., 1994. Direct dynamic testing of stereolithographic models.

Dutson, A.J., Wood, K., Beaman, J.J., Crawford, R.H., Bourell, D.L., 2003. Application of similitude techniques to functional testing of rapid prototypes. Rapid Prototyping Journal 9, 6–13.

Dutson, A.J., Wood, K.L., 2002. Foundations and applications of the empirical similitude method (esm). Retrieved from the Singapore University of Technology and Design (`www.sutd.edu.sg/cmsresource/idc/papers/2002-_Foundations_and_Applications_of_the_Empirical_Similitude_Method_%28ESM%29.pdf`) .

Easterling, K., 2013. Introduction to the physical metallurgy of welding. Elsevier.

Emori, R.I., 1973. Scale models of automobile collisions with breakaway obstacles. Experimental Mechanics , 63–69.

EN 10025-2, 2004. Hot rolled products of structural steels, part 2: technical delivery conditions for non-alloy structural steels.

EN 1011-1, 1998. Welding - recommendations for welding of metallic materials - part 1: General guidance for arc welding.

EN 1011-2, 2001. Welding - recommendations for welding of metallic materials - part 2: Arc welding of ferritic steels.

EN 1993-1-2, 2005. Eurocode 3: Design of steel structures - part 1-2: General rules - structural fire design.

Endo, H., Yamada, Y., Kitamura, O., Suzuki, K., 2002. Model test on the collapse strength of the buffer bow structures. Marine Structures 15, 365–381.

Ewins, D.J., 2000. Modal Testing: Theory, Practice and Application. 2 ed., Research Studies Press Ltd., Great Britain.

Ezra, A.A., 1962. Similitude requirements for scale model determination of shell buckling under impulsive pressures. Report NASA TN-D-1510. National Aeronautics and Space Administration.

Fasanella, E.L., Jackson, K.E., 2002. Impact testing and simulation of a crashworthy composite fuselage section with energy-absorbing seats and dummies.

Feblowitz, J.C., 2010. Confusing the wind: The burj khalifa, mother nature, and the modern skyscraper. Inquiries Journal 2.

Ferguson, G.L., 1995. Replica model scaling for high strain-rate events. International Journal of Impact Engineering 16, 571–583.

Fonseca, J.R., Ribeiro, P., 2006. Beam p-version finite element for geometrically non-linear vibrations in space. Computer Methods in Applied Mechanics and Engineering 195, 905–924.

Fortes, C., Vaz, C.T., 2005. Soldagem mig/mag.

Fralich, R.W., Green, C.E., Rheinfurth, M.H., 1972. NASA Space Shuttle Technology Conference: Dynamics and aeroelasticity; Structures and materials. Report NASA TM-X-2570. National Aeronautics and Space Administration.

Frostig, Y., Simitses, G.J., 2004. Similitude of sandwich panels with a "soft" core in buckling. Composites Part B: Engineering 35, 599–608.

Fujino, M., Oyama, H., Omotani, H., 2003. Flutter characteristics of an over the wing engine mount business jet configuration.

Funderburk, R.S., 1999. Key concepts in welding engineering - a look at heat input. Welding Innovation 16.

Galtier, A., Statnikov, E., 2003. The influence of ultrasonic impact treatment on fatigue behaviour of welded joints in high-strength steel. Report IIW/IIS Document XIII-1976-03. International Institute of Welding / Institut International de la Soudure.

Gang, X., Wang, D., Su, X., 2010. A new similitude analysis method for a scale model test. Key Engineering Materials 439-440, 704–709.

Gannon, L., 2011. Effect of welding residual stress and distortion on ship hull structural performance. Ph.D. thesis.

Gaspar, J.L., Behun, V., T., M., Murphy, D.M., Macy, B.D., 2005. Testing of a 20-meter solar sail system.

Gaspar, J.L., Mann, T., Behun, V., Macy, B., Barker, P., Murphy, D.M., 2006. Testing of a 10-meter quadrant solar sail.

Goldak, J., Chakravarti, A., Bibby, M., 1984. A new finite element model for welding heat sources. Metallurgical Transactions B 15, 299–305.

Goodier, J.N., 1950. Dimensional analysis. John Wiley & Sons, New York. book section Appendix II. pp. 1035–1045.

Goodier, J.N., Thomson, W.T., 1944. Applicability of similarity principles to structural models. Report NACA TN-933. National Advisory Committee for Aeronautics.

Granta Design Limited, 2013. CES Edupack 2013.

Grimes, P.J., McTigue, L.D., Riley, G.F., 1970. Advancements in structural dynamic technology resulting from Saturn V programs - Volume I. Report NASA CR-1539. National Aeronautics and Space Administration.

Gronet, M.J., Pinson, E.D., Voqui, H.L., Crawley, E.F., Everman, M.R., 1987. Preliminary design, analysis, and costing of a dynamic scale model of the NASA space station. Report NASA CR-4068. National Aeronautics and Space Administration.

Grong, Ø., 1997. Metallurgical modelling of welding. 2 ed., Institute of Materials.

Grumman Aerospace Corporation, 1972. Design of a space shuttle structural dynamics model. Report NASA CR-112205. National Aeronautics and Space Administration.

Gukhman, A.A., 1965. Introduction to the theory of similarity. Academic Press, New York.

Hagiwara, K., Takanabe, H., Kawano, H., 1983. A proposed method of predicting ship collision damage. International Journal of Impact Engineering 1, 257–279.

Hamada, H., Ramakrishna, S., 1995. Scaling effects in the energy absorption of carbon-fiber/peek composite tubes. Composites Science and Technology 55, 211–221.

Harris, H.G., Sabnis, G.M., 1999. Structural modeling and experimental techniques. 2 ed., CRC Press.

Harrison, J.K., Jones, B.P., 1965. A set of experiments in thermal similitude. Report NASA TM-X-53346. National Aeronautics and Space Administration.

Herr, R.W., Leonard, H.W., 1967. Dynamic model investigation of touchdown stability of lunar-landing vehicles. Report NASA TN-D-4215. National Aeronautics and Space Administration.

Hexcel Composites, 2000. Hexweb honeycomb sandwich design technology. (Pamphlet AGU 075b). Duxford.

Hilburger, M.W., Lovejoy, A.E., Thornburgh, R.P., Rankin, C., 2012. Design and analysis of subscale and full-scale buckling-critical cylinders for launch vehicle technology development.

Hilburger, M.W., Rose, C.A., Starnes, J. H., J., 2001. Nonlinear analysis and scaling laws for noncircular composite structures subjected to combined load.

Hodges, D.H., Dowell, E.H., 1974. Nonlinear equations of motion for the elastic bending and torsion ot twisted nonuniform rotor blades. Report NASA TN D-7818. National Aeronautics and Space Administration.

Horta, L.G., Kvaternik, R.G., 2000. A historical perspective on dynamics testing at the Langley Research Center. Report NASA TM-2000-210295. National Aeronautics and Space Administration.

Hsu, C.S., Griffin, J.H., Bielak, J., 1989. How gravity and joint scaling affect dynamic response. AIAA Journal 27, 1280–1287.

Hughes, A.F., Iles, D.C., Malik, A.S., 2011. Design of steel beams in torsion. volume SCI P385. The Steel Construction Institute.

Jackson, K.E., 1990. Scaling effects in the static and dynamic response of graphite-epoxy beam-columns. Ph.D. thesis.

Jackson, K.E., 1994. Workshop on scaling effects in composite materials and structures. Report NASA CP-3271. National Aeronautics and Space Administration.

Jackson, K.E., Fasanella, E.L., 1989. Scaling effects in the static large deflection response of graphite-epoxy composite beams. Report NASA TM-101619. National Aeronautics and Space Administration.

Jackson, K.E., Fasanella, E.L., 1999. Crashworthy evaluation of a 1/5-scale model composite fuselage concept. Report NASA TM-1999-209132. National Aeronautics and Space Administration.

Jackson, K.E., Fasanella, E.L., Knight, N.F., . Demonstration of a crashworthy composite fuselage concept, in: 22nd Army Science Conference, pp. 183–184.

Jackson, K.E., Fasanella, E.L., Lyle, K.H., 2003. Comparisons of the impact responses of a 1/5-scale model and a full scale crashworthy composite fuselage section.

Jaszlics, I.J., Park, A.C., 1969. Use of dynamic scale models to determine launch vehicle characteristics - Volume 1: Analytical Investigation. Report NASA CR-102272. National Aeronautics and Space Administration.

Javeed, M., Edighoffer, H.E., McGowan, P.E., 1993. Correlation of ground tests and analyses of a dynamically scaled Space Station model configuration. Report NASA TM-107729. National Aeronautics and Space Administration.

Jha, A., 2004. Dynamic testing of structures using scale models. M.Sc. thesis.

Jiang, D., Zhang, D., Fei, Q., Wu, S., 2014. An approach on identification of equivalent properties of honeycomb core using experimental modal data. Finite Elements in Analysis and Design 90, 84–92.

Jiang, P., Tian, C.J., Xie, R.Z., Meng, D.S., 2006a. Experimental investigation into scaling laws for conical shells struck by projectiles. International Journal of Impact Engineering 32, 1284–1298.

Jiang, P., Wang, W., Zhang, G.J., 2006b. Size effects in the axial tearing of circular tubes during quasi-static and impact loadings. International Journal of Impact Engineering 32, 2048–2065.

Jones, N., 1989. Structural Impact. Cambridge University Press, United Kingdom.

Jones, R., Chen, B., Pitt, S., 2007. Similitude: Fatigue cracking in steels. Theoretical and Applied Fracture Mechanics 48, 161–168.

Kasivitamnuay, J., Singhatanadgid, P., 2005. Application of an energy theorem to derive a scaling law for structural behaviors. Thammasat International Journal of Science and Technology 10, 33–40.

Katzoff, S., 1963. Similitude in thermal models of spacecraft. Report NASA TN-D-1631. National Aeronautics and Space Administration.

Kellas, S., Morton, J., 1992. Scaling effects in angle-ply laminates. Report NASA CR-4423. National Aeronautics and Space Administration.

Khedmati, M.R., Zareei, M.R., Rigo, P., 2010. Empirical formulations for estimation of ultimate strength of continuous stiffened aluminium plates under combined in-plane compression and lateral pressure. Thin-Walled Structures 48, 274–289.

Kim, I.T., Jeong, Y.S., 2013. Fatigue strength improvement of welded joints by blast cleaning for subsequent painting. International Journal of Steel Structures 13, 11–20.

Kim, N.S., Kwak, Y.H., Chang, S.P., 2004. Pseudodynamic tests on small scale steel models.

Kim, N.S., Lee, J.H., Chang, S.P., 2009. Equivalent multi-phase similitude law for pseudodynamic test on small scale reinforced concrete models. Engineering Structures 31, 834–846.

Kline, S.J., 1965. Similitude and approximation theory. Springer-Verlag, New York.

Kou, S., 2003. Welding Metallurgy. John Wiley & Sons.

Kumar, S., Itoh, Y., Saizuka, K., Usami, T., 1997. Pseudodynamic testing of scaled models. Journal of Structural Engineering 123, 524–526.

Lancaster, J.F., 1999. Metallurgy of Welding. Springer Science & Business Media.

Langhaar, H.L., 1951. Dimensionless analysis and theory of models. John Wiley & Sons, New York.

Laue, G., Case, D., Moore, J., 2005. Fabrication and deployment testing of solar sail quadrants for a 20-meter solar sail ground test system demonstration.

Leadbetter, S.A., 1970. Application of analysis and models to structural dynamic problems related to the Apollo-Saturn V launch vehicle. Report NASA TN-D-5831. National Aeronautics and Space Administration.

Leadbetter, S.A., Kiefling, L.A., 1971. NASA Space Shuttle Technology Conference - Volume III: Dynamics and aeroelasticity. Report NASA TM-X-2274. National Aeronautics and Space Administration.

Leadbetter, S.A., Leonard, H.W., Brock, E. John, J., 1967. Design and fabrication considerations for a 1/10-scale replica model of the Apollo/Saturn V. Report NASA TN-D-4138. National Aeronautics and Space Administration.

Leadbetter, S.A., Stephens, W.B., Sewall, J.L., Majka, J.W., Barrett, J.R., 1976. Vibration characteristics of 1-8-scale dynamic models of the space-shuttle solid-rocket boosters. Report NASA TN-D-8158. National Aeronautics and Space Administration.

Lehmann, E., Peschmann, J., 2002. Energy absorption by the steel structure of ships in the event of collisions. Marine Structures 15, 429–441.

Lembke-Jene, L., Biebow, N., Thiede, J., 2011. The european research icebreaker aurora borealis: Conceptual design study - summary report. Berichte zur Polar-und Meeresforschung (Reports on Polar and Marine Research) 637.

Leonard, H.W., Morgan, H.G., 1970. Space transportation system technology symposium - Volume II: Dynamics and aeroelasticity. Report NASA TM-X-52876 Volume II. National Aeronautics and Space Administration.

Lessells, J.M., Murray, W.M., 1941. Effect of shot blasting on strength of metals - part ii and iii. Heat Treating and Forging , 516–568.

Letchworth, R., McGowan, P.E., Gronet, M.J., 1988. Space station: A focus for the development of structural dynamics scale model for large flexible space structures.

Levy, A., Zalesak, J., Bernstein, M., Mason, P.W., 1974. Development of technology for modeling of a 1/8-scale dynamic model of the shuttle solid rocket booster (SRB). Report NASA CR-132492. National Aeronautics and Space Administration.

Li, Q.M., Jones, N., 2000. On dimensionless number of dynamic plastic response of structural members. Archive of Applied Mechanics 70, 245–254.

Liang, Z., Reinhorn, A.M., 2011. Experimental Methods in Structural Engineering - Chapter 2: Modeling and Similitude. Retrieved from the State University of New York (`civil.eng.buffalo.edu/cie616/2-LECTURES/Lecture%202%20-%20Modeling%20and%20Scaling/Chapter2.pdf`).

Lieven, N.A.J., Greening, P.D., 2001. Effect of experimental pre-stress and residual stress on modal behaviour. Philosophical Transactions of the Royal Society A 359, 97–111.

Lindgren, L.E., 2001. Finite element modeling and simulation of welding - part 1: Increased complexity. Journal of Thermal Stresses 24, 141–192.

Lister, J.M., 2014. Study the effects of core orientation and different face thickness on mechanical behavior of honeycomb sandwich structures under three point bending. M.Sc. thesis.

Lundberg, A., 2014. Temperature profiles and hardness estimation of laser welded heat affected zone in low carbon steel. M.Sc. thesis.

Macagno, E.O., 1971. Historico-critical review of dimensional analysis. Journal of the Franklin Institute 292, 391–402.

Mace, B., 2003. Statistical energy analysis, energy distribution models and system modes. Journal of Sound and Vibration 264, 391–409.

Madabhusi-Raman, P., Davalos, J.F., 1996. Static shear correction factor for laminated rectangular beams. Composites Part B: Engineering 27B, 285–293.

Mahn, J.P., Bayly, P.V., 1999. Impact testing of stereolithographic models to predict natural frequencies. Journal of Sound and Vibration 224, 411–430.

Maples, D., Scogin, J.V., 1970. Thermal modeling with internal generation. Report NASA CR-109987. National Aeronautics and Space Administration.

Marshall, K.N., Foster, W.G., 1973. Space shuttle thermal scale modeling application study. Report NASA CR-128849. National Aeronautics and Space Administration.

Marshall, K.N., Murray, D.O., Rolling, R.E., 1969. Limitations in thermal modeling. Report NASA CR-102566. National Aeronautics and Space Administration.

Mason, P.W., Harris, H.G., Zalesak, J., Bernstein, M., 1974a. Analytical and experimental investigation of a 1/8 scale dynamic model of the shuttle orbiter: Volume I - Summary report. Report NASA CR-132488. National Aeronautics and Space Administration.

Mason, P.W., Harris, H.G., Zalesak, J., Bernstein, M., 1974b. Analytical and experimental investigation of a 1/8 scale dynamic model of the shuttle orbiter: Volume II - Technical report. Report NASA CR-132489. National Aeronautics and Space Administration.

Mazzariol, L.M., Alves, M., 2013. Experimental study on scaling of circular tubes subjected to dynamic axial crushing using models of different materials.

Mazzariol, L.M., Alves, M., 2014. Scaling the impact of a mass on a plate using models of different materials.

Mazzariol, L.M., Calle, M.A.G., Oshiro, R.E., Alves, M., 2010. Scaling of stiffened panels subjected to impact loading.

McGehee, J.R., Stubbs, S.M., 1973. Experimental validation of a landing-dynamics computer program for legged spacecraft landers. Report NASA TN-D-7301. National Aeronautics and Space Administration.

McGowan, P.E., Edighoffer, H.E., Wallace, J.W., 1990. Development of an experimental space station model for structural dynamics research. Report NASA TM-102601. National Aeronautics and Space Administration.

McGowan, P.E., Javeed, M., Edighoffer, H.H., 1991. Status of DSMT research program. Report NASA TM-102764. National Aeronautics and Space Administration.

McKown, S., Cantwell, W.J., Jones, N., 2008. Investigation of scaling effects in fiber-metal laminates. Journal of Composite Materials 42, 865–888.

Me-Bar, Y., 1997. A method for scaling ballistic penetration phenomena. International Journal of Impact Engineering 19, 821–829.

Mendez, P.F., . Scaling laws in welding modeling, in: 7th International Conference on Trends in Welding Research, pp. 103–108.

Miller, D.K., Funderburk, R.S., 2001. Tools for reviewing welding procedures. Welding Journal 80, 40–43.

Mixson, J.S., Catherine, J.J., 1964a. Comparison of experimental vibration characteristics obtained from a 1/5-scale model and from a full-scale Saturn SA-1. Report NASA TN-D-2215. National Aeronautics and Space Administration.

Mixson, J.S., Catherine, J.J., 1964b. Experimental lateral vibration characteristics of a 1/5-scale model of Saturn SA-1 with an eight-cable suspension system. Report NASA TN-D-2214. National Aeronautics and Space Administration.

Momcilovic, N., Motok, M., Maneski, T., 2016. Simplified numerical analysis of stiffened panels.

Moreira, R., Rodrigues, J.D., . The modelisation of constrained damping layer treatment using the finite element method: Spatial and viscoelastic behavior, in: International Conference on Structural Dynamics Modelling, Test, Analysis, Correlation and Validation.

Morgan, G.W., 1964. Scaling techniques for orthotropic cylindrical aerospace structures.

Morosow, G., Jaszlics, I.J., 1966. TitanIII 20 percent dynamic model characteristics - Comparison of theory and experiment. Report AFFDL-TR-66-80. Air Force Flight Dynamics Laboratory.

Morton, J., 1988. Scaling of impact loaded carbon fiber composites. AIAA Journal 26, 989–994.

Murphy, D.M., Macy, B.D., Gaspar, J.L., 2004. Demonstration of a 10-m solar sail system.

Na Songkhla, A., Singhatanadgid, P., 2005. Accuracy of the scaling law for experimental natural frequencies of rectangular thin plates.

Nadooshan, A.A., Daneshmand, S., Aghanajafi, C., 2007. Application of rp technology with polycarbonate material for wind tunnel model fabrication. International Journal of Mechanical, Industrial Science and Engineering 1.

Nettles, A.T., Douglas, M.J., Estes, E.E., 1999. Scaling effects in carbon/epoxy laminates under transverse quasi-static loading. Report NASA TM-1999-209103. National Aeronautics and Space Administration.

Neuberger, A., Peles, S., Rittel, D., 2007. Scaling the response of circular plates subjected to large and close-range spherical explosions. part i: Air-blast loading. International Journal of Impact Engineering 34, 859–873.

Oshiro, R.E., Alves, M., 2004. Scaling impacted structures. Archive of Applied Mechanics 74, 130–145.

Oshiro, R.E., Alves, M., 2007. Scaling of cylindrical shells under axial impact. International Journal of Impact Engineering 34, 89–103.

Oshiro, R.E., Alves, M., 2009. Scaling of structures subject to impact loads when using a power law constitutive equation. International Journal of Solids and Structures 46, 3412–3421.

Oshiro, R.E., Alves, M., 2012. Predicting the behaviour of structures under impact loads using geometrically distorted scaled models. Journal of the Mechanics and Physics of Solids 60, 1330–1349.

Oshiro, R.E., Calle, M.A.G., Mazzariol, L.M., Alves, M., . Experimental study of scaled t cross-section beams subjected to impact load, in: 21st Brazilian Congress of Mechanical Engineering - COBEM 2011.

O'Sullivan, William J., J., 1957. Theory of aircraft structural models subject to aerodynamic heating and external loads. Report NACA TN-4115. National Aeronautics and Space Administration.

Paik, J.K., Kim, B.J., 2002. Ultimate strength formulations for stiffened panels under combined axial load inplane bending and lateral pressure. Thin-Walled Structures 40, 45–83.

Paik, J.K., Thayamballi, A.K., 2003. A concise introduction to the idealized structural unit method for nonlinear analysis of large plated structures and its application. Thin-Walled Structures 41, 329–355.

Pankhurst, R.C., 1964. Dimensional analysis and scale factors. Chapman And Hall, London.

Peele, E.L., Leonard, H.W., Leadbetter, S.A., 1970. Lateral vibration characteristics of the 1/10-scale Apollo/Saturn V replica model. Report NASA TN-D-5778. National Aeronautics and Space Administration.

Peele, E.L., Thompson, William M., J., 1968. A theoretical and experimental investigation of the three-dimensional vibration characteristics of a scaled model of an asymmetrical launch vehicle. Report NASA TN-D-4707. National Aeronautics and Space Administration.

Penning, F.A., 1969. Use of dynamic scale models to determine launch vehicle characteristics - Volume II: experimental investigation. Report NASA CR-102280. National Aeronautics and Space Administration.

Petrescu, F.I.T., Petrescu, R.V., 2012. New Aircraft II. Books on Demand GmbH, Germany, Norderstedt.

Pinson, L.D., 1975. Analytical and experimental vibration studies of a 1/8 scale shuttle orbiter. Report NASA TN-D-7964. National Aeronautics and Space Administration.

Pinson, L.D., Leonard, H.W., 1969. Longitudinal vibration characteristics of 1/10-scale Apollo/Saturn V replica model. Report NASA TN-D-5159. National Aeronautics and Space Administration.

Plascore, Inc, 2014. Core terminology. (Pamphlet v03.28.14).

Poorhaydari, K., Patchett, B.M., Ivey, D.G., 2005. Estimation of cooling rate in the welding of plates with intermediate thickness. Welding Journal 84, 149–155.

prEN 13674-1, 2002. Railway applications - track - rails - part 1: Vignole railway rails 46 kg/m and above.

Qian, Y., Swanson, S.R., Nuismer, R.J., Bucinell, R.B., 1971. An experimental study of scaling rules for impact damage in fiber composites. Composite Materials 24, 559–570.

Ramu, M., Prabhu Raja, V., Thyla, P.R., 2013. Establishment of structural similitude for elastic models and validation of scaling laws. KSCE Journal of Civil Engineering 17, 139–144.

Rao, N.N., 1996. Dimensional analysis - keeping track of length, mass, time... Resonance 1, 29–41.

Rayleigh, L., 1915. The principle of similitude. Nature 95, 66–68.

Reddy, J.N., 2004. Mechanics of laminated composite plates and shells: theory and analysis. 2 ed., CRC Press.

Rezaeepazhand, J., Simitses, G.J., 1993. Design of scaled down models for stability and vibration studies. Report NASA CR-194687. National Aeronautics and Space Administration.

Rezaeepazhand, J., Simitses, G.J., 1997. Structural similitude for vibration response of laminated cylindrical shells with double curvature. Composites Part B: Engineering 28B, 195–200.

Rezaeepazhand, J., Simitses, G.J., Starnes, J. H., J., 1995. Use of scaled-down models for predicting vibration response of laminated plates. Composite Structures 30, 419–426.

Rezaeepazhand, J., Simitses, G.J., Starnes, J. H., J., 1996a. Design of scaled down models for predicting shell vibration response. Journal of Sound and Vibration 195, 301–311.

Rezaeepazhand, J., Simitses, G.J., Starnes, J. H., J., 1996b. Scale models for laminated cylindrical shells subjected to axial compression. Composite Structures 34, 371–379.

Rezaeepazhand, J., Wisnom, M.R., 2009. Scaled models for predicting buckling of delaminated orthotropic beam-plates. Composite Structures 90, 87–91.

Rezaeepazhand, J., Yazdi, A.A., 2011. Similitude requirements and scaling laws for flutter prediction of angle-ply composite plates. Composites Part B: Engineering 42, 51–56.

Sabour, M.H., Bhat, R.B., 2010. Thermal scale modeling by fem and test. Journal of Aerospace Engineering 23, 24–33.

Sadowski, T., Bęc, J., 2011. Effective properties for sandwich plates with aluminium foil honeycomb core and polymer foam filling - static and dynamic response. Computational Materials Science 50, 1269–1275.

Sapountzakis, E.J., Dourakopoulos, J.A., 2008. Shear deformation effect in flexural-torsional vibrations of beams by bem. Acta Mechanica 203, 197–221.

Schleyer, G.K., Hsu, S.S., White, M.D., 2004. Scaling of pulse loaded mild steel plates with different edge restraint. International Journal of Mechanical Sciences 46, 1267–1287.

Schroeder, L.C., Adams, R.R., Bailey, M.C., Belvin, W.K., Butler, D.H., Campbell, T.G., 1989. Near-field testing of the 15-meter hoop-column antenna. Report NASA TM-4073. National Aeronautics and Space Administration.

Schwingshackl, C.W., Aglietti, G.S., Cunningham, P.R., 2006. Determination of honeycomb material properties existing alternatives and an alternative dynamic approach. Journal of Aerospace Engineering 19, 177–183.

Shannon, R.L., 1972. A thermal scale modeling study for Apollo and Apollo applications - Volume 2. Report NASA CR-115753. National Aeronautics and Space Administration.

Sharf, I., 1996. Geometrically non-linear beam element for dynamics simulation of multibody systems. International Journal for Numerical Methods in Engineering 39, 763–786.

Shih, C.F., Chen, J.C., Garba, J.A., 1987. Verification of large beam-type space structures. Report N87-22712. National Aeronautics and Space Administration.

Shokrieh, M.M., Askari, A., 2013. Similitude study of impacted composite laminates under buckling loading. Journal of Engineering Mechanics 139, 1334–1340.

Shubert, M., Pandheeradi, M., Arnold, F., Habura, C., . An abaqus extension for welding simulations, in: 2010 SIMULIA Customer Conference.

Signes, E.G., 1972. A simplified method for calculating cooling rates in mild and low alloy steel weld metals. (Welding Research Supplement to the) Welding Journal 51, 473–484.

Simitses, G.J., 2001. Structural similitude for flat laminated surfaces. Composite Structures 51, 191–194.

Simitses, G.J., Rezaeepazhand, J., 1992. Structural similitude and scaling laws for laminated beam plates. Report NASA CR-190585. National Aeronautics and Space Administration.

Simitses, G.J., Rezaeepazhand, J., 1993a. Structural similitude and scaling laws for cross-ply laminated plates, in: American Society for Composites, Technomic Publishing Company, Inc. pp. 265–274.

Simitses, G.J., Rezaeepazhand, J., 1993b. Structural similitude for laminated structures. Composites Engineering 3, 751–765.

Simitses, G.J., Rezaeepazhand, J., Sierakowski, R.L., 1997. Scaled models for laminated cylindrical shells subjected to external pressure. Mechanics of Advanced Materials and Structures 4, 267–280.

Simitses, G.J., Starnes, J. H., J., Rezaeepazhand, J., 2000. Structural similitude and scaling laws for plates and shells: a review.

Sinatra, R., Deville, P., Szell, M., Wang, D., Barabási, A.L., 2015. A century of physics. Nature Physics 11, 791–796.

Singer, J., Arbocz, I., Weller, T., 1997. Buckling experiments: Experimental methods in buckling of thin-walled structures. volume 1: Basic Concepts, Columns, Beams and Plates. John Wiley and Sons, Chickester, England.

Singhatanadgid, P., Na Songkhla, A., 2008. An experimental investigation into the use of scaling laws for predicting vibration responses of rectangular thin plates. Journal of Sound and Vibration 311, 314–327.

Singhatanadgid, P., Ungbhakorn, V., 2002a. Buckling similitude invariants of symmetrically laminated plates subjected to biaxial loading, in: SEM Annual Conference and Exposition, Milwaukee, WI, USA.

Singhatanadgid, P., Ungbhakorn, V., 2002b. Scaling laws for vibration response of anti-symmetrically laminated plates. Structural Engineering and Mechanics 14, 345–364.

Singhatanadgid, P., Ungbhakorn, V., 2005. Scaling laws for buckling of polar orthotropic annular plates subjected to compressive and torsional loading. Thin-Walled Structures 43, 1115–1129.

Snyman, I.M., 2010. Impulsive loading events and similarity scaling. Engineering Structures 32, 886–896.

Soedel, W., 1971. Similitude approximations for vibrating thin shells. Journal of the Acoustical Society of America 49, 1535–1541.

Sonin, A.A., 2001. The physical basis of dimensional analysis. Department of Mechanical Engineering,MIT, Cambridge, MA.

Springer, A.M., 1998. Application of rapid prototyping methods to high speed wind tunnel testing. Report NASA TP-1998-208396. National Aeronautics and Space Administration.

Steeves, E.C., Catherine, J.J., 1968. Lateral vibration characteristics of a 1/40-scale dynamic model of Apollo-Saturn V launch vehicle. Report NASA TN-D-4872. National Aeronautics and Space Administration.

Steinchen, W., Kramer, B., Kupfer, G., 1995. Photoelastic investigation using new stl-resins.

Stoykov, S., Ribeiro, P., 2010. Nonlinear forced vibrations and static deformations of 3d beams with rectangular cross section: The influence of warping, shear deformation and longitudinal displacements. International Journal of Mechanical Sciences 52, 1505–1521.

Stubbs, S.M., 1971. Investigation of technique for conducting landing-impact tests at simulated planetary gravity. Report NASA TN-D-6459. National Aeronautics and Space Administration.

Sutherland, L.S., Guedes Soares, C., 2007. Scaling of impact on low fibre-volume glass-polyester laminates. Composites Part A: Applied Science and Manufacturing 38, 307–317.

Szilard, R., 2004. Theories and Applications of Plate Analysis: Classical Numerical and Engineering Methods. Wiley.

Szirtes, T., 2007. Applied dimensional analysis and modeling. 2 ed., Elsevier Butterworth-Heinemann.

Szucs, E., 1980. Similitude and modeling. Elsevier, New York.

Tabri, K., Määttänen, J., Ranta, J., 2008. Model-scale experiments of symmetric ship collisions. Journal of Marine Science and Technology 13, 71–84.

Tan, Q.M., 2011. Dimensional analysis with case studies in mechanics. Springer-Verlag, Berlin.

Tarfaoui, M., Gning, P.B., Davies, P., Collombet, F., 2007. Scale and size effects on dynamic response and damage of glass/epoxy tubular structures. Journal of Composite Materials 41, 547–558.

Thomas, B.G., Samarasekera, I.V., Brimacombe, J.K., 1987. Mathematical model of the thermal processing of steel ingots: Part i. heat flow model. Metallurgical Transactions B 18, 119–130.

Thompson, William M., J., 1967. An investigation of the response of a scaled model of a liquid-propellant multistage launch vehicle to longitudinal excitation. Report NASA TN-D-3975. National Aeronautics and Space Administration.

Thornton, E.A., 1971. Vibration analysis of a 1/15-scale dynamic model of a space shuttle configuration. Report NASA CR-111984. National Aeronautics and Space Administration.

Torkamani, S., Jafari, A.A., Navazi, H.M., 2008. Scaled down models for free vibration analysis of orthogonally stiffened cylindrical shells using similitude theory.

Torkamani, S., Navazi, H.M., Jafari, A.A., Bagheri, M., 2009. Structural similitude in free vibration of orthogonally stiffened cylindrical shells. Thin-Walled Structures 47, 1316–1330.

Tsai, S.W., Hahn, H.T., 1980. Introduction to composite materials. Technomic Publishing Company, Inc, United States of America.

Tuttle, M., Singhatanadgid, P., Hinds, G., 1999. Buckling of composite panels subjected to biaxial loading. Experimental Mechanics 39, 191–201.

Ungbhakorn, V., 2001. A new approach for establishing structural similitude for buckling of symmetric cross-ply laminated plates subjected to combined loading. Thammasat International Journal of Science and Technology 6.

Ungbhakorn, V., Singhatanadgid, P., 2003a. Scaling law and physical similitude for buckling and vibration of antisymmetric angle-ply laminated cylindrical shells. International Journal of Structural Stability and Dynamics 3, 567–583.

Ungbhakorn, V., Singhatanadgid, P., 2003b. Similitude and physical modeling for buckling and vibration of symmetric cross-ply laminated circular cylindrical shells. Journal of Composite Materials 37, 1697–1712.

Ungbhakorn, V., Singhatanadgid, P., 2003c. Similitude invariants and scaling laws for buckling experiments on anti-symmetrically laminated plates subjected to biaxial loading. Composite Structures 59, 455–465.

Ungbhakorn, V., Singhatanadgid, P., 2009. A scaling law for vibration response of laminated doubly curved shallow shells by energy approach. Mechanics of Advanced Materials and Structures 16, 333–344.

Ungbhakorn, V., Wattanasakulpong, N., 2007. Structural similitude and scaling laws of anti-symmetric cross-ply laminated cylindrical shells for buckling and vibration experiments. International Journal of Structural Stability and Dynamics 7, 609–627.

Usami, T., Kumar, S., 1996. Damage evaluation in steel box columns by pseudodynamic tests. Journal of Structural Engineering 122, 635–642.

Vassalos, D., 1999. Physical modeling and similitude of marine structures. Ocean Engineering 26, 111–123.

Viot, P., Ballère, L., Guillaumat, L., Lataillade, J.L., 2008. Scale effects on the response of composite structures under impact loading. Engineering Fracture Mechanics 75, 2725–2736.

Wahab, M.A., Painter, M.J., 1997. Numerical models of gas metal arc welds using experimentally determined weld pool shapes as the representation of the welding heat source. International Journal of Pressure Vessels and Piping 73, 153–159.

Watkins, J.R., 1966. Sets of similarity ratios for thermal modeling. Report NASA TN-D-3452. National Aeronautics and Space Administration.

Wen, H.M., Jones, N., 1993. Experimental investigation of the scaling laws for metal plates struck by large masses. International Journal of Impact Engineering 13, 485–505.

Williams, M., Blakeborough, A., 2001. Laboratory testing of structures under dynamic loads: an introductory review. Philosophical Transactions of the Royal Society of London A: Mathematical, Physical and Engineering Sciences 359, 1651–1669.

Wissmann, J.W., 1968. Dynamic stability of space vehicles structural dynamics model testing. Report NASA CR-1195. National Aeronautics and Space Administration.

Wolowicz, C.H., Bowman, James S., J., Gilbert, W.P., 1979. Similitude requirements and scaling relationships as applied to model testing. Report NASA TP-1435. National Aeronautics and Space Administration.

Wu, J.J., 2003. The complete-similitude scale models for predicting the vibration characteristics of the elastically restrained flat plates subjected to dynamic loads. Journal of Sound and Vibration 268, 1041–1053.

Wu, J.J., 2005. Dynamic analysis of a rectangular plate under a moving line load using scale beams and scaling laws. Computers & Structures 83, 1646–1658.

Wu, J.J., 2006. Prediction of the dynamic characteristics of an elastically supported full-size flat plate from those of its complete-similitude scale model. Computers & Structures 84, 102–114.

Wu, J.J., 2007. Prediction of lateral vibration characteristics of a full-size rotor-bearing system by using those of its scale models. Finite Elements in Analysis and Design 43, 803–816.

Wu, J.J., Cartmell, M.P., Whittaker, A.R., 2002. Prediction of the vibration characteristics of a full-size structure from those of a scale model. Computers & Structures 80, 1461–1472.

Xu, S., Beynon, J.H., Ruan, D., Lu, G., 2012. Experimental study of the out-of-plane dynamic compression of hexagonal honeycombs. Composite Structures 94, 2326–2336.

Yazdi, A.A., Rezaeepazhand, J., 2011a. Accuracy of scale models for flutter prediction of cross-ply laminated plates. Journal of Reinforced Plastics and Composites 30, 45–52.

Yazdi, A.A., Rezaeepazhand, J., 2011b. Structural similitude for flutter of delaminated composite beam-plates. Composite Structures 93, 1918–1922.

Yazdi, A.A., Rezaeepazhand, J., 2012. Applicability of small-scale models in prediction flutter pressure of delaminated composite beam-plates. International Journal of Damage Mechanics 22, 590–601.

Yigit, A.S., Christoforou, A.P., 2007. Limits of asymptotic solutions in low-velocity impact of composite plates. Composite Structures 81, 568–574.

Yim, W.T., . Akashi bridge, in: Bridge Engineering Conference.

Young, D.F., 1971. Basic principles and concepts of model analysis. Experimental Mechanics 11, 325–336.

Yu, W., Li, Z.L., 2016. Structural similitude for prestressed vibration and buckling of eccentrically stiffened circular cylindrical panels and shells by energy approach. International Journal of Structural Stability and Dynamics 16.

Yulong, L., Yongkang, Z., Pu, X., 2008. Study of similarity law for bird impact on structure. Chinese Journal of Aeronautics 21, 512–517.

Zalesak, J., 1975. Modal coupling procedures adapted to NASTRAN analysis of the 1/8-scale shuttle structural dynamics model - Volume I: Technical report. Report NASA CR-132666. National Aeronautics and Space Administration.

Zang, C., Grafe, H., Imregun, M., 2001. Frequency–domain criteria for correlating and updating dynamic finite element models. Mechanical Systems and Signal Processing 15, 139–155.

Zhang, Z., Chen, H., Ye, L., 2011. A stiffened plate element model for advanced grid stiffened composite plates/shells. Journal of Composite Materials 45, 187–202.

Zhao, Y.P., 1998. Suggestion of a new dimensionless number for dynamic plastic response of beams and plates. Archive of Applied Mechanics 68, 524–538.

Zhu, W., Li, D., Zhang, Z., Ren, K., Zhao, X., Yang, D., Zhang, W., Sun, Y., Tang, Y., 2011. Design and fabrication of stereolithography-based aeroelastic wing models. Rapid Prototyping Journal 17, 298–307.

Ziemian, C., Ziemian, R., Barker, E., 2010. Shake-table simulation study of small scale layered models. Rapid Prototyping Journal 16, 4–11.

Appendices

A.

A.1. Demonstration of similitude theory applied to a differential equation

Application of the similitude theory to equation (4.1a) is here briefly presented. Following the procedure described by Simitses and Rezaeepazhand (1992) (and available in section 2.5.3.1 of this manuscript), firstly the following scaling factors are defined for each variable in equation (4.1a):

$$\lambda_x = \frac{x_m}{x_p},\ \lambda_y = \frac{y_m}{y_p},\ \lambda_{\ddot{u}_0} = \frac{(\ddot{u}_0)_m}{(\ddot{u}_0)_p},\ \lambda_\rho = \frac{\rho_m}{\rho_p},\ \lambda_{N_x} = \frac{(N_x)_m}{(N_x)_p},\ \lambda_{N_{xy}} = \frac{(N_{xy})_m}{(N_{xy})_p} \tag{A.1}$$

Additionally, according to the general definition (A.12), derived in appendix A.2, the scaling factors for the partial derivatives are the following:

$$\lambda\left(\frac{\partial N_x}{\partial x}\right) = \frac{\lambda_{N_x}}{\lambda_x}, \qquad \lambda\left(\frac{\partial N_{xy}}{\partial y}\right) = \frac{\lambda_{N_{xy}}}{\lambda_y} \tag{A.2}$$

The governing equation (4.1a) which for the prototype structure is written as follows:

$$\frac{\partial (N_x)_p}{\partial x_p} + \frac{\partial (N_{xy})_p}{\partial y_p} = \rho_p\,(\ddot{u}_0)_p \tag{A.3}$$

can also be written for the scaled model structure as follows:

$$\frac{\partial (N_x)_m}{\partial x_m} + \frac{\partial (N_{xy})_m}{\partial y_m} = \rho_m\,(\ddot{u}_0)_m \tag{A.4}$$

Then, the parameters and variables in prototype equation (A.3) are replaced by the equivalent predicted value obtained applying the scaling factors (A.1) and (A.2) to the parameters and variables of the scaled model (for example replacing $(\ddot{u}_0)_p$ by its prediction $(\ddot{u}_0)_m/\lambda_{\ddot{u}_0}$):

$$\frac{\dfrac{\partial (N_x)_m}{\partial x_m}}{\dfrac{\lambda_{N_x}}{\lambda_x}} + \frac{\dfrac{\partial (N_{xy})_m}{\partial y_m}}{\dfrac{\lambda_{N_{xy}}}{\lambda_y}} = \frac{\rho_m}{\lambda_\rho}\,\frac{(\ddot{u}_0)_m}{\lambda_{\ddot{u}_0}} \tag{A.5}$$

In the third step, the equality of equations (A.3) and (A.5) is imposed, given that both are the differential equation of the prototype. This is achieved equating the coefficients obtained by grouping the scaling factors in each term of equation (A.5), as follows:

$$\frac{\lambda_{N_x}}{\lambda_x} = \frac{\lambda_{N_{xy}}}{\lambda_y} = \lambda_\rho\,\lambda_{\ddot{u}_0} \tag{A.6}$$

The necessary conditions (A.6) are the same as similarity conditions (4.4a), presented in

section 4.2 with omission of previous demonstration.

A.2. Derivation of scaling factors for partial derivatives

In literature, the similitude theory is applied to governing equations which usually are in differential form. The ratio which defines the scaling factor for a given variable is straightforward and usually explained, such as in equation (2.22) of this manuscript; however no further explanation is usually presented regarding how the scaling factor is defined for the partial derivatives.

From the literature analysis, those without previous experience in the field of similitude theory may conclude that the first derivative of $f(x_1, x_2, ..., x_i, ..., x_n)$ in order to the variable x_i, this is, the scaling factor for $\frac{\partial f}{\partial x_i}$ is given by $\frac{\lambda_f}{\lambda_{x_i}}$. A possible derivation of this scaling factor is presented in this section.

In this demonstration, for the sake of simplicity, the selected function $f(x_1, y_1)$ has only two variables. Its partial derivative in order to x_1 can be defined as follows:

$$\frac{\partial f}{\partial x_1} = lim_{\Delta x_1 \to 0} \frac{f(x_1 + \Delta x_1,\ x_2) - f(x_1,\ x_2)}{\Delta x_1} \tag{A.7}$$

Following the procedure described by Simitses and Rezaeepazhand (1992) (and available in section 2.5.3.1 of this manuscript), firstly the following scaling factors are defined for each variable in equation (A.7):

$$\lambda_{x_1} = \frac{x_{1m}}{x_{1p}},\ \lambda_{x_2} = \frac{x_{2m}}{x_{2p}},\ \lambda_f = \frac{f_m}{f_p} \tag{A.8}$$

Then, partial derivative (A.7) is written for the prototype and for the scaled model structure as follows:

$$\frac{\partial f_p}{\partial x_{1p}} = lim_{\Delta x_{1p} \to 0} \frac{f_p(x_{1p} + \Delta x_{1p},\ x_{2p}) - f_p(x_{1p},\ x_{2p})}{\Delta x_{1p}} \tag{A.9}$$

$$\frac{\partial f_m}{\partial x_{1m}} = lim_{\Delta x_{1m} \to 0} \frac{f_m(x_{1m} + \Delta x_{1m},\ x_{2m}) - f_p(x_{1m},\ x_{2m})}{\Delta x_{1m}} \tag{A.10}$$

In the third step, the parameters and variables in prototype equation (A.9) are replaced by the equivalent scaled/predicted value obtained applying the scaling factors (A.8) to the parameters and variables of the scaled model (for example replacing Δx_{1p} by the scaled valued $\Delta x_{1m}/\lambda_{x_1}$):

$$\frac{\partial f_p}{\partial x_{1p}} = lim_{\Delta x_{1m} \to 0} \frac{\frac{f_m(x_{1m} + \Delta x_{1m},\ x_{2m})}{\lambda_f} - \frac{f_m(x_{1m},\ x_{2m})}{\lambda_f}}{\frac{\Delta x_{1m}}{\lambda_{x_1}}} \tag{A.11}$$

$$= \frac{\lambda_{x_1}}{\lambda_f} \times lim_{\Delta x_{1m} \to 0} \frac{f_m(x_{1m} + \Delta x_{1m},\ x_{2m}) - f_m(x_{1m},\ x_{2m})}{\Delta x_{1m}}$$

Lastly, dividing equation (A.10) by equation (A.11) yields the scaling factor for the partial

derivative:

$$\lambda_{\left(\frac{\partial f}{\partial x_1}\right)} = \frac{\frac{\partial f_m}{\partial x_{1m}}}{\frac{\partial f_p}{\partial x_{1p}}} = \frac{\lambda_f}{\lambda_{x_1}}$$

which can be generalized as follows:

$$\lambda_{\left(\frac{\partial f}{\partial x_i}\right)} = \frac{\lambda_f}{\lambda_{x_i}} \tag{A.12}$$

B.

B.1. Deduction of the material and stacking sequence (MSS) module

B.1.1. Material properties

From the relations between the stiffnesses and the engineering constants (Reddy, 2004):

$$\begin{aligned} Q_{11} &= \frac{E_1}{\Delta} \\ Q_{22} &= \frac{E_2}{\Delta} \\ Q_{12} &= \frac{\nu_{12} E_2}{\Delta} \end{aligned}$$

$$\Delta = 1 - \nu_{12}\nu_{21} = 1 - \frac{E_2}{E_1}\nu_{12}^2 \implies E_1.\Delta = E_1 - E_2\nu_{12}^2$$

$$\begin{aligned} Q_{44} &= G_{23} \\ Q_{55} &= G_{13} \\ Q_{66} &= G_{12} \end{aligned}$$

the following scaling factors can be derived:

$$\lambda_\Delta = 1 \tag{B.1a}$$
$$\lambda_{E_1} = \lambda_{E_2}\lambda_{\nu_{12}}^2 \tag{B.1b}$$
$$\lambda_{Q_{11}} = \lambda_{E_1} \tag{B.1c}$$
$$\lambda_{Q_{22}} = \lambda_{E_2} \tag{B.1d}$$
$$\lambda_{Q_{12}} = \lambda_{\nu_{12}}\lambda_{E_2} \tag{B.1e}$$
$$\lambda_{Q_{44}} = \lambda_{G_{23}} \tag{B.1f}$$
$$\lambda_{Q_{55}} = \lambda_{G_{13}} \tag{B.1g}$$
$$\lambda_{Q_{66}} = \lambda_{G_{12}} \tag{B.1h}$$

For **isotropic materials**, considering the relations between the engineering constants:

$$\begin{aligned} \lambda_{E_1} = \lambda_{E_2} &= \lambda_E \\ \lambda_{\nu_{12}} = \lambda_{\nu_{21}} &= \lambda_\nu \\ \lambda_{G_{12}} = \lambda_{G_{13}} = \lambda_{G_{23}} &= \lambda_G \end{aligned}$$

one obtains:

$$\begin{aligned} \lambda_\nu &= 1 \\ \lambda_{Q_{11}} = \lambda_{Q_{22}} = \lambda_{Q_{12}} &= \lambda_E \\ \lambda_{Q_{44}} = \lambda_{Q_{55}} = \lambda_{Q_{66}} &= \lambda_G \end{aligned}$$

B.1.2. Material (ply) orientation

The effect of orientation on orthotropic material properties can be studied taking into account the expressions for the reduced stiffnesses $\bar{Q}_{ij}$:

$$\begin{aligned} \bar{Q}_{11} &= m^4 Q_{11} + n^4 Q_{22} + 2m^2 n^2 (Q_{12} + 2Q_{66}) \\ \bar{Q}_{12} &= m^2 n^2 (Q_{11} + Q_{22} - 4Q_{66}) + (m^4 + n^4)\, Q_{12} \\ \bar{Q}_{16} &= m^3 n\, Q_{11} - mn^3\, Q_{22} - mn(m^2 - n^2)(Q_{12} + 2Q_{66}) \\ \bar{Q}_{22} &= n^4 Q_{11} + m^4 Q_{22} + 2m^2 n^2 (Q_{12} + 2Q_{66}) \\ \bar{Q}_{26} &= mn^3\, Q_{11} - m^3 n\, Q_{22} + mn(m^2 - n^2)(Q_{12} + 2Q_{66}) \\ \bar{Q}_{44} &= m^2\, Q_{44} + n^2\, Q_{55} \\ \bar{Q}_{45} &= mn(Q_{55} - Q_{44}) \\ \bar{Q}_{55} &= n^2\, Q_{44} + m^2\, Q_{55} \\ \bar{Q}_{66} &= m^2 n^2 (Q_{11} + Q_{22} - 2Q_{12}) + (m^2 - n^2)^2\, Q_{66} \end{aligned}$$

where the following trigonometric identities can be substituted (Tsai and Hahn, 1980):

$$\begin{aligned} m^4 &= \frac{1}{8}(3 + 4\cos(2\theta) + \cos(4\theta)) \\ m^3 n &= \frac{1}{8}(2\sin(2\theta) + \sin(4\theta)) \\ m^2 n^2 &= \frac{1}{8}(1 - \cos(4\theta)) \\ mn^3 &= \frac{1}{8}(2\sin(2\theta) - sin(4\theta)) \\ n^4 &= \frac{1}{8}(3 - 4\cos(2\theta) + \cos(4\theta)) \end{aligned}$$

Applying the similitude theory, the scaling factors for complete similitude can be derived:

- If the principal axes of material are not coincident with the xyz coordinate system:

$$\theta \neq \frac{k\pi}{2}, \qquad k = 0, 1, 2, ...$$

then:

$$\lambda_{m^4} = \lambda_{m^3n} = \lambda_{m^2n^2} = \lambda_{mn^3} = \lambda_{n^4} = 1$$
$$\lambda_\theta = 1$$

$$\lambda_{Q_{11}} = \lambda_{Q_{12}} = \lambda_{Q_{22}} = \lambda_{Q_{66}} = \lambda_{Q^b}$$
$$\lambda_{\bar{Q}_{11}} = \lambda_{\bar{Q}_{12}} = \lambda_{\bar{Q}_{16}} = \lambda_{\bar{Q}_{22}} = \lambda_{\bar{Q}_{26}} = \lambda_{\bar{Q}_{66}} = \lambda_{Q^b}$$

$$\lambda_{Q_{44}} = \lambda_{Q_{55}} = \lambda_{Q^s}$$
$$\lambda_{\bar{Q}_{44}} = \lambda_{\bar{Q}_{45}} = \lambda_{\bar{Q}_{55}} = \lambda_{Q^s}$$

but, from equations (B.1), these relations yield:

$$\lambda_\theta = 1$$
$$\lambda_{E_1} = \lambda_{E_2} = \lambda_{\nu_{12}} = \lambda_{G_{12}} = \lambda_{Q^b} = 1$$
$$\lambda_{G_{13}} = \lambda_{G_{23}} = \lambda_{Q^s}$$

- If the orientation of the material axes is such that:

$$\theta = \frac{k\pi}{2}, \qquad k = 1, 3, 5, ...$$

then:

$$\lambda_\theta = 1$$
$$\lambda_{\bar{Q}_{11}} = \lambda_{Q_{22}}$$
$$\lambda_{\bar{Q}_{22}} = \lambda_{Q_{11}}$$
$$\lambda_{\bar{Q}_{ij}} = \lambda_{Q_{ij}} \qquad ij \in \{12, 44, 55, 66\}$$

- On the other hand, if the principal axes of material and the xyz coordinate system are coincident:

$$\theta = \frac{k\pi}{2}, \qquad k = 0, 2, 4...$$

then the effect of the material orientation vanishes and the scaling factors for the stiffnesses Q_{ij} and for the reduced stiffnesses $\bar{Q}_{ij}$ are the same:

$$\lambda_\theta = 1$$
$$\lambda_{\bar{Q}_{ij}} = \lambda_{Q_{ij}} \qquad ij \in \{11, 12, 22, 44, 55, 66\}$$

Note that the **isotropic materials** can be included in this case, being governed by more restrictive conditions for the reduced stiffnesses:

$$\lambda_\theta = 1 \tag{B.2a}$$
$$\lambda_\nu = 1 \tag{B.2b}$$
$$\lambda_{\bar{Q}_{ij}} = \lambda_{Q_{ij}} = \lambda_E \qquad ij \in \{11, 12, 22\} \tag{B.2c}$$
$$\lambda_{\bar{Q}_{ij}} = \lambda_{Q_{ij}} = \lambda_G \qquad ij \in \{44, 55, 66\} \tag{B.2d}$$

B.1.3. Stacking sequence (on laminates)

For any equivalent single-layer theory the reduced stiffness matrix of the laminate $[\bar{Q}]$ is obtained by adding the matrix $[\bar{Q}]^{(k)}$ of each ply :

$$[\bar{Q}] = \sum_{k=1}^{N} [\bar{Q}]^{(k)}$$

Therefore, for **complete similitude** the same number of plies (N) has to be kept, and the scaling factors for (each of) the reduced stiffnesses of each ply $\bar{Q}_{ij}^{(k)}$ have to be the same, and equal to the scaling factor for the reduced stiffness $\bar{Q}_{ij}$ of the laminate:

$$\lambda_{\bar{Q}_{ij}} = \lambda_{\bar{Q}_{ij}^{(k)}} \qquad k = 1, 2, ..., N \tag{B.3}$$

Laminated cross-ply configuration: For laminated structures with a stacking sequence similar to $[0_n/90_n]_m$, the following conditions exist for the 0^o and 90^o plies :

$$\begin{aligned} \lambda_{E_1^{(0)}} &= \lambda_{E_2^{(90)}} \\ \lambda_{E_2^{(0)}} &= \lambda_{E_1^{(90)}} \\ \lambda_{\nu_{12}^{(0)}} \lambda_{E_2^{(0)}} = \lambda_{\nu_{12}^{(90)}} \lambda_{E_2^{(90)}} \implies \lambda_{\nu_{12}^{(0)}} &= \lambda_{\nu_{21}^{(90)}} \end{aligned}$$

Usually the plies of a laminated structure are all of the same material. Theoretically for a cross-ply laminate, different materials for the model and prototype could be used. However it should be noted how difficult it is to find two materials respecting the three previous conditions, mainly the first two.

General laminated configuration: For laminated configurations, with arbitrary stacking sequence (including therefore the angle-ply configurations), the material of each lamina will have to be the same in the model and in the prototype.

Sandwich configurations: For sandwich structures made of isotropic layers, and from equations (B.2) and (B.3), theoretically it can again be concluded that for a cross-ply laminate, different materials could be used for the model and prototype.

As an example, consider a sandwich with three layers, being the bottom and upper layer of the same material and different from the material of the core; two materials different from those of the model would have to be found, respecting the referred equations and with some kind of advantage to justify that change. Once again it should be noted that respect all these conditions is very unlikely.

B.2. The non-linear equations of motion for general plates

Ashton and Whitney (1970) define the following nonlinear equations of motion :

$$\frac{\partial}{\partial x}\left(\sigma_x(1+\frac{\partial u}{\partial x})+\sigma_{xy}\frac{\partial u}{\partial y}+\boxed{\boxed{\sigma_{xz}\frac{\partial u}{\partial z}}}\right)+$$
$$+\frac{\partial}{\partial y}\left(\sigma_{yx}(1+\frac{\partial u}{\partial x})+\sigma_y\frac{\partial u}{\partial y}+\boxed{\boxed{\sigma_{yz}\frac{\partial u}{\partial z}}}\right)+$$
$$+\frac{\partial}{\partial z}\left(\sigma_{zx}(1+\frac{\partial u}{\partial x})+\sigma_{zy}\frac{\partial u}{\partial y}+\boxed{\boxed{\sigma_z\frac{\partial u}{\partial z}}}\right)+f_x=\rho_0\frac{\partial^2 u}{\partial t^2} \quad \text{(B.4a)}$$

$$\frac{\partial}{\partial x}\left(\sigma_x\frac{\partial v}{\partial x}+\sigma_{xy}(1+\frac{\partial v}{\partial y})+\boxed{\boxed{\sigma_{xz}\frac{\partial v}{\partial z}}}\right)+$$
$$+\frac{\partial}{\partial y}\left(\sigma_{yx}\frac{\partial v}{\partial x}+\sigma_y(1+\frac{\partial v}{\partial y})+\boxed{\boxed{\sigma_{yz}\frac{\partial v}{\partial z}}}\right)+$$
$$+\frac{\partial}{\partial z}\left(\sigma_{zx}\frac{\partial v}{\partial x}+\sigma_{zy}(1+\frac{\partial v}{\partial y})+\boxed{\boxed{\sigma_z\frac{\partial v}{\partial z}}}\right)+f_y=\rho_0\frac{\partial^2 v}{\partial t^2} \quad \text{(B.4b)}$$

$$\frac{\partial}{\partial x}\left(\boxed{\sigma_x\frac{\partial w}{\partial x}}+\boxed{\sigma_{xy}\frac{\partial w}{\partial y}}+\sigma_{xz}(1+\frac{\partial w}{\partial z})\right)+$$
$$+\frac{\partial}{\partial y}\left(\boxed{\sigma_{yx}\frac{\partial w}{\partial x}}+\boxed{\sigma_y\frac{\partial w}{\partial y}}+\sigma_{yz}(1+\frac{\partial w}{\partial z})\right)+$$
$$+\frac{\partial}{\partial z}\left(\boxed{\sigma_{zx}\frac{\partial w}{\partial x}}+\boxed{\sigma_{zy}\frac{\partial w}{\partial y}}+\sigma_z(1+\frac{\partial w}{\partial z})\right)+f_z=\rho_0\frac{\partial^2 w}{\partial t^2}$$

For linear small deformation theory all the nonlinear terms involving stresses would be neglected. In the following deduction, small strains but moderate rotations (geometric non-linearity) are considered, and therefore the terms marked with $\boxed{\times}$ are also considered. These terms involving products of stresses and plate slopes allow one to include the effect of the inplane forces and boundary shear loading on bending, appearing when the rotations become moderate.

For the sake of clarity, note that the terms marked with $\boxed{\boxed{\times}}$ could be included if one wanted to consider the effect of the transverse shear stresses and transverse loading on stretching.

The reader should realize from the Modular Approach being presented in this manuscript, that this kind of simplifications can be considered when establishing the scaling relationships, without introducing errors as in the numerical simulation techniques. Regarding the complete structural similarity among two systems, as soon as one considers some kind of non-linearity on the governing equations or on the strains, the similarity conditions will impose a reduced model including "automatically" all the non-linearities. This is, for complete similitude of scaled models one considers either a total linear model or a model including all the non-linearities; there are not any other option between these two extremes.

Integrating over the thickness, using the second fundamental theorem of calculus or/and considering the integration by parts when necessary, and assuming a linear variation of the inplane displacements:

$$\begin{Bmatrix} u(x,y,z,t) \\ v(x,y,z,t) \\ w(x,y,z,t) \end{Bmatrix} = \begin{Bmatrix} u_0(x,y,t) + z\theta_y(x,y,t) \\ v_0(x,y,t) - z\theta_x(x,y,t) \\ w_0(x,y,t) \end{Bmatrix}$$

one obtains:

$$\frac{\partial N_x}{\partial x} + \frac{\partial N_{xy}}{\partial y} + q_x = \int_{-\frac{h}{2}}^{\frac{h}{2}} (\rho_0 \frac{\partial^2 u}{\partial t^2}) dz \tag{B.5a}$$

$$\frac{\partial N_{xy}}{\partial x} + \frac{\partial N_y}{\partial y} + q_y = \int_{-\frac{h}{2}}^{\frac{h}{2}} (\rho_0 \frac{\partial^2 v}{\partial t^2}) dz \tag{B.5b}$$

$$N_x \frac{\partial^2 w}{\partial x^2} + 2N_{yx} \frac{\partial^2 w}{\partial x \partial y} + N_y \frac{\partial^2 w}{\partial y^2} + \frac{\partial Q_x}{\partial x} + \frac{\partial Q_y}{\partial y} + \\ + \frac{\partial w}{\partial y}(\frac{\partial N_y}{\partial y} + \frac{\partial N_{xy}}{\partial x}) + \frac{\partial w}{\partial x}(\frac{\partial N_x}{\partial x} + \frac{\partial N_{yx}}{\partial y}) + q_z = \int_{-\frac{h}{2}}^{\frac{h}{2}} (\rho_0 \frac{\partial^2 w}{\partial t^2}) dz \tag{B.5c}$$

with,

$$q_x = \left[\sigma_{zx} + \sigma_z \frac{\partial u}{\partial z} \right] \Big|_{-\frac{h}{2}}^{\frac{h}{2}} + \int_{-\frac{h}{2}}^{\frac{h}{2}} f_x dz$$

$$q_y = \left[\sigma_{zy} + \sigma_z \frac{\partial v}{\partial z} \right] \Big|_{-\frac{h}{2}}^{\frac{h}{2}} + \int_{-\frac{h}{2}}^{\frac{h}{2}} f_y dz$$

$$q_z = \left[\sigma_{zx} \frac{\partial w}{\partial x} + \sigma_{zy} \frac{\partial w}{\partial y} + \sigma_z \right] \Big|_{-\frac{h}{2}}^{\frac{h}{2}} + \int_{-\frac{h}{2}}^{\frac{h}{2}} f_z dz$$

Additionally, equations (B.4a) and (B.4b) with all except those marked with $\boxed{\times}$ nonlinear terms involving stresses, were multiplied by z. Then, integrating over the thickness and considering integration by parts when necessary, one obtains:

$$\frac{\partial M_x}{\partial x} + \frac{\partial M_{xy}}{\partial y} - Q_x + m_x = \int_{-\frac{h}{2}}^{\frac{h}{2}} (z\rho_0 \frac{\partial^2 u}{\partial t^2}) dz \tag{B.6a}$$

$$\frac{\partial M_{xy}}{\partial x} + \frac{\partial M_y}{\partial y} - Q_y + m_y = \int_{-\frac{h}{2}}^{\frac{h}{2}} (z\rho_0 \frac{\partial^2 v}{\partial t^2}) dz \tag{B.6b}$$

with,

$$m_x = [z\sigma_{zx}] \Big|_{-\frac{h}{2}}^{\frac{h}{2}} + \int_{-\frac{h}{2}}^{\frac{h}{2}} z f_x dz$$

$$m_y = [z\sigma_{zy}] \Big|_{-\frac{h}{2}}^{\frac{h}{2}} + \int_{-\frac{h}{2}}^{\frac{h}{2}} z f_y dz$$

Reddy (2004) derived the governing equations for thick and for thin plates in separate deductions, applying the Virtual Work Principle. Ashton and Whitney (1970) derived the

governing equations for Kirchhoff plates from the elasticity equations. The difference for the deduction presented here is that they did not considered neither body forces nor shear stresses on boundary faces, which is equivalent to:

$$f_x = f_y = f_z = q_x = q_y = m_x = m_y = 0$$

Ashton additional neglected the rotary inertia terms. Anyway, note that the equations derived here can be simplified to obtain the same results as these authors.

B.3. The non-linear equations of motion for general beams

As for plate analysis, the non-linear equations of motion (B.4) are considered. Excluding all the terms including null partial derivatives ($\frac{\partial v}{\partial y}, \frac{\partial w}{\partial z}$) and negligible stresses (ϵ_y, τ_{yz}), the equations simplify to:

$$\frac{\partial}{\partial x}\left(\sigma_x + \sigma_{xy}\frac{\partial u}{\partial y} + \sigma_{xz}\frac{\partial u}{\partial z}\right) + \frac{\partial}{\partial y}\left(\sigma_{yx}\right) + \frac{\partial}{\partial z}\left(\sigma_{zx} + \sigma_z\frac{\partial u}{\partial z}\right) + f_x = \rho_0\frac{\partial^2 u}{\partial t^2}$$

$$\frac{\partial}{\partial x}\left(\sigma_x\frac{\partial v}{\partial x} + \sigma_{xy} + \sigma_{xz}\frac{\partial v}{\partial z}\right) + \frac{\partial}{\partial y}\left(\sigma_{yx}\frac{\partial v}{\partial x} + \sigma_y\right) + \frac{\partial}{\partial z}\left(\sigma_{zx}\frac{\partial v}{\partial x} + \sigma_z\frac{\partial v}{\partial z}\right) + f_y = \rho_0\frac{\partial^2 v}{\partial t^2}$$

$$\frac{\partial}{\partial x}\left(\sigma_x\frac{\partial w}{\partial x} + \sigma_{xy}\frac{\partial w}{\partial y} + \sigma_{xz}\right) + \frac{\partial}{\partial y}\left(\sigma_{yx}\frac{\partial w}{\partial x} + \sigma_y\frac{\partial w}{\partial y}\right) + \frac{\partial}{\partial z}\left(\sigma_{zx}\frac{\partial w}{\partial x} + \sigma_z\right) + f_z = \rho_0\frac{\partial^2 w}{\partial t^2}$$

In the following deductions the second fundamental theorem of calculus will be used, and when necessary in the integration by parts will be assumed a linear variation of the in-plane displacements:

$$\begin{Bmatrix} u(x,y,z,t) \\ v(x,z,t) \\ w(x,y,t) \end{Bmatrix} = \begin{Bmatrix} u_0(x,t) + z\theta_y(x,t) - y\theta_z(x,t) \\ v_0(x,t) - z\theta_x(x,t) \\ w_0(x,t) + y\theta_x(x,t) \end{Bmatrix}$$

Integrating all the equations of motion in order to the cross section yield:

$$\frac{\partial}{\partial x}\left(N_x^{beam} + \boxed{Q_y^{beam}\frac{\partial u}{\partial y}} + \boxed{Q_z^{beam}\frac{\partial u}{\partial z}}\right) + \left[z\left[\sigma_{xy}\right]\Big|_{y=-\frac{b}{2}}^{y=\frac{b}{2}}\right]\Bigg|_{z=-\frac{h}{2}}^{z=\frac{h}{2}} + \\ + \left[y\left[\sigma_{xz} + \boxed{\sigma_z\frac{\partial u}{\partial z}}\right]\Big|_{z=-\frac{h}{2}}^{z=\frac{h}{2}}\right]\Bigg|_{y=-\frac{b}{2}}^{y=\frac{b}{2}} + \int_A f_x\, dA = \int_A\left(\rho_0\frac{\partial^2 u}{\partial t^2}\right)dA$$

$$\frac{\partial}{\partial x}\left(\frac{\partial v_0}{\partial x}N_x^{beam} - \boxed{\frac{\partial \theta_x}{\partial x}M_x^{beam}} + Q_y^{beam} + \boxed{Q_z^{beam}\frac{\partial v}{\partial z}}\right) + \\ + \left[z\left[\sigma_{yx}\left(\frac{\partial v_0}{\partial x} - \frac{z}{2}\frac{\partial \theta_x}{\partial x}\right) + \sigma_y\right]\Big|_{y=-\frac{b}{2}}^{y=\frac{b}{2}}\right]\Bigg|_{z=-\frac{h}{2}}^{z=\frac{h}{2}} + \\ + \left[y\left[\sigma_{xz}\frac{\partial v}{\partial x} + \sigma_z\frac{\partial v}{\partial z}\right]\Big|_{z=-\frac{h}{2}}^{z=\frac{h}{2}}\right]\Bigg|_{y=-\frac{b}{2}}^{y=\frac{b}{2}} + \int_A f_y\, dA = \int_A\left(\rho_0\frac{\partial^2 v}{\partial t^2}\right)dA$$

$$\frac{\partial}{\partial x}\left(N_x^{beam}\frac{\partial w_0}{\partial x}+\boxed{\int_A\left(y\sigma_x\frac{\partial\theta_x}{\partial x}\right)dA}+\boxed{Q_y^{beam}\frac{\partial w}{\partial y}}+Q_z^{beam}\right)+$$
$$+\left[z\left[\sigma_{xy}\frac{\partial w}{\partial x}+\sigma_y\frac{\partial w}{\partial y}\right]\Big|_{y=-\frac{b}{2}}^{y=\frac{b}{2}}\right]\Big|_{z=-\frac{h}{2}}^{z=\frac{h}{2}}+$$
$$+\left[y\left[\sigma_{xz}\left(\frac{\partial w_0}{\partial x}-\frac{y}{2}\frac{\partial\theta_x}{\partial x}\right)+\sigma_z\right]\Big|_{z=-\frac{h}{2}}^{z=\frac{h}{2}}\right]\Big|_{y=-\frac{b}{2}}^{y=\frac{b}{2}}+\int_A f_z\,dA=\int_A\left(\rho_0\frac{\partial^2 w}{\partial t^2}\right)dA$$

Additionally, pre-multiplying the 1^{st} and 2^{nd} equation of motion by z and integrating over the cross section, yields:

$$\frac{\partial}{\partial x}\left(M_y^{beam}+\boxed{M_x^{beam^{yz}}\frac{\partial u}{\partial y}}+\boxed{\int_A\left(z\sigma_{xz}\frac{\partial u}{\partial z}\right)dA}\right)+$$
$$+\left[\frac{z^2}{2}\left[\sigma_{xy}\right]\Big|_{y=-\frac{b}{2}}^{y=\frac{b}{2}}\right]\Big|_{z=-\frac{h}{2}}^{z=\frac{h}{2}}+\left[y\left[z\left(\sigma_{xz}+\sigma_z\frac{\partial u}{\partial z}\right)\right]\Big|_{z=-\frac{h}{2}}^{z=\frac{h}{2}}\right]\Big|_{y=-\frac{b}{2}}^{y=\frac{b}{2}}-$$
$$-Q_z^{beam}-\boxed{\int_A\left(\sigma_z\frac{\partial u}{\partial z}\right)dA}+\int_A z\,f_x\,dA=\int_A\left(z\,\rho_0\frac{\partial^2 u}{\partial t^2}\right)dA$$

$$\frac{\partial}{\partial x}\left(\boxed{\frac{\partial v_0}{\partial x}M_y^{beam}-\int_A\left(z^2\sigma_x\frac{\partial\theta_x}{\partial x}\right)dA}+M_x^{beam^{yz}}+\boxed{\int_A\left(z\sigma_{xz}\frac{\partial v}{\partial z}\right)dA}\right)+$$
$$+\left[z^2\left[\sigma_{xy}\left(\frac{1}{2}\frac{\partial v_0}{\partial x}-\frac{z}{3}\frac{\partial\theta_x}{\partial x}\right)+\sigma_y\right]\Big|_{y=-\frac{b}{2}}^{y=\frac{b}{2}}\right]\Big|_{z=-\frac{h}{2}}^{z=\frac{h}{2}}+\left[y\left[z\left(\sigma_{xz}\frac{\partial v}{\partial x}+\sigma_z\frac{\partial v}{\partial z}\right)\right]\Big|_{z=-\frac{h}{2}}^{z=\frac{h}{2}}\right]\Big|_{y=-\frac{b}{2}}^{y=\frac{b}{2}}-$$
$$-Q_z^{beam}\frac{\partial v_0}{\partial x}-\boxed{\int_A\left(-z\,\sigma_{xz}\frac{\partial\theta_x}{\partial x}+\sigma_z\frac{\partial v}{\partial z}\right)dA}+\int_A z f_y\,dA=\int_A\left(z\rho_0\frac{\partial^2 v}{\partial t^2}\right)dA$$

On the other hand, pre-multiplying the 1^{st} and 3^{rd} equation of motion by y and integrating over the cross section, yields:

$$\frac{\partial}{\partial x}\left(M_z^{beam}+\boxed{\int_A\left(y\sigma_{xy}\frac{\partial u}{\partial y}\right)dA}+\boxed{M_x^{beam^{xz}}\frac{\partial u}{\partial z}}\right)+\left[z\left[y\sigma_{yx}\right]\Big|_{y=-\frac{b}{2}}^{y=\frac{b}{2}}\right]\Big|_{z=-\frac{h}{2}}^{z=\frac{h}{2}}-$$
$$-Q_y^{beam}+\left[\frac{y^2}{2}\left[\sigma_{xz}+\sigma_z\frac{\partial u}{\partial z}\right]\Big|_{z=-\frac{h}{2}}^{z=\frac{h}{2}}\right]\Big|_{y=-\frac{b}{2}}^{y=\frac{b}{2}}+\int_A y\,f_x\,dA=\int_A\left(y\,\rho_0\frac{\partial^2 u}{\partial t^2}\right)dA$$

$$\frac{\partial}{\partial x}\left(\boxed{M_z^{beam}\frac{\partial w_0}{\partial x}+\int_A\left(y^2\sigma_x\frac{\partial\theta_x}{\partial x}\right)dA}+\boxed{\int_A(y\sigma_{xy})\,dA}+M_x^{beam^{xz}}\right)+$$

$$+\left[z\left[y\left(\sigma_{xy}\frac{\partial w}{\partial x}+\sigma_y\frac{\partial w}{\partial y}\right)\right]\Big|_{y=-\frac{b}{2}}^{y=\frac{b}{2}}\right]\Big|_{z=-\frac{h}{2}}^{z=\frac{h}{2}}-Q_y^{beam}\frac{\partial w_0}{\partial x}-\boxed{\int_A\left(y\sigma_{xy}\frac{\partial\theta_x}{\partial x}+\sigma_y\frac{\partial w}{\partial y}\right)dA}+$$

$$+\left[y^2\left[\sigma_{xz}\left(\frac{1}{2}\frac{\partial w_0}{\partial x}+\frac{y}{3}\frac{\partial\theta_x}{\partial x}\right)+\frac{\sigma_z}{2}\right]\Big|_{z=-\frac{h}{2}}^{z=\frac{h}{2}}\right]\Big|_{y=-\frac{b}{2}}^{y=\frac{b}{2}}+\int_A yf_z\,dA=\int_A\left(y\rho_0\frac{\partial^2 w}{\partial t^2}\right)dA$$

Neglecting the boxed nonlinear terms in the previous equations, one obtains:

$$\frac{\partial N_x}{\partial x}^{beam}+q_x^{beam}=\int_A\left(\rho_0\frac{\partial^2 u}{\partial t^2}\right)dA \tag{B.7a}$$

$$\frac{\partial^2 v_0}{\partial x^2}N_x^{beam}+\frac{\partial v_0}{\partial x}\frac{\partial N_x}{\partial x}^{beam}+\frac{\partial Q_y}{\partial x}^{beam}+q_y^{beam}=\int_A\left(\rho_0\frac{\partial^2 v}{\partial t^2}\right)dA \tag{B.7b}$$

$$\frac{\partial^2 w_0}{\partial x^2}N_x^{beam}+\frac{\partial w_0}{\partial x}\frac{\partial N_x}{\partial x}^{beam}+\frac{\partial Q_z}{\partial x}^{beam}+q_z^{beam}=\int_A\left(\rho_0\frac{\partial^2 w}{\partial t^2}\right)dA \tag{B.7c}$$

$$\frac{\partial M_y}{\partial x}^{beam}-Q_z^{beam}+m_y^{beam}=\int_A\left(z\;\rho_0\frac{\partial^2 u}{\partial t^2}\right)dA \tag{B.7d}$$

$$\frac{\partial M_z}{\partial x}^{beam}-Q_y^{beam}+m_z^{beam}=\int_A\left(y\;\rho_0\frac{\partial^2 u}{\partial t^2}\right)dA \tag{B.7e}$$

and given that:

$$M_x^{beam}=M_x^{beam^{xz}}+M_x^{beam^{yz}}$$
$$m_x^{beam}=m_x^{beam^{xz}}+m_x^{beam^{yz}}$$

additionally, the equilibrium of moments for the beam torsion:

$$\frac{\partial M_x}{\partial x}^{beam}-Q_y^{beam}\frac{\partial w_0}{\partial x}-Q_z^{beam}\frac{\partial v_0}{\partial x}+m_x^{beam}=\int_A\rho_0\left(y\frac{\partial^2 w}{\partial t^2}+z\frac{\partial^2 v}{\partial t^2}\right)dA \tag{B.8}$$

where

$$q_x=\int_A f_x\,dA+\left[z\left[\sigma_{xy}\right]\Big|_{y=-\frac{b}{2}}^{y=\frac{b}{2}}\right]\Big|_{z=-\frac{h}{2}}^{z=\frac{h}{2}}+\left[y\left[\sigma_{xz}+\sigma_z\frac{\partial u}{\partial z}\right]\Big|_{z=-\frac{h}{2}}^{z=\frac{h}{2}}\right]\Big|_{y=-\frac{b}{2}}^{y=\frac{b}{2}}$$

$$q_y=\int_A f_y\,dA+\left[z\left[\sigma_{yx}\left(\frac{\partial v_0}{\partial x}-\frac{z}{2}\frac{\partial\theta_x}{\partial x}\right)+\sigma_y\right]\Big|_{y=-\frac{b}{2}}^{y=\frac{b}{2}}\right]\Big|_{z=-\frac{h}{2}}^{z=\frac{h}{2}}+$$
$$+\left[y\left[\sigma_{xz}\frac{\partial v}{\partial x}+\sigma_z\frac{\partial v}{\partial z}\right]\Big|_{z=-\frac{h}{2}}^{z=\frac{h}{2}}\right]\Big|_{y=-\frac{b}{2}}^{y=\frac{b}{2}}$$

$$q_z = \int_A f_z \, dA + \left[z \left[\sigma_{xy} \frac{\partial w}{\partial x} + \sigma_y \frac{\partial w}{\partial y} \right] \Big|_{y=-\frac{b}{2}}^{y=\frac{b}{2}} \right] \Big|_{z=-\frac{h}{2}}^{z=\frac{h}{2}} + \\ + \left[y \left[\sigma_{xz} \left(\frac{\partial w_0}{\partial x} - \frac{y}{2} \frac{\partial \theta_x}{\partial x} \right) + \sigma_z \right] \Big|_{z=-\frac{h}{2}}^{z=\frac{h}{2}} \right] \Big|_{y=-\frac{b}{2}}^{y=\frac{b}{2}}$$

$$m_y = \int_A z \ f_x \ dA + \left[\frac{z^2}{2} \left[\sigma_{xy} \right] \Big|_{y=-\frac{b}{2}}^{y=\frac{b}{2}} \right] \Big|_{z=-\frac{h}{2}}^{z=\frac{h}{2}} + \left[y \left[z \left(\sigma_{xz} + \sigma_z \frac{\partial u}{\partial z} \right) \right] \Big|_{z=-\frac{h}{2}}^{z=\frac{h}{2}} \right] \Big|_{y=-\frac{b}{2}}^{y=\frac{b}{2}}$$

$$m_z = \int_A y \ f_x \ dA + \left[z \left[y \sigma_{yx} \right] \Big|_{y=-\frac{b}{2}}^{y=\frac{b}{2}} \right] \Big|_{z=-\frac{h}{2}}^{z=\frac{h}{2}} + \left[\frac{y^2}{2} \left[\sigma_{xz} + \sigma_z \frac{\partial u}{\partial z} \right] \Big|_{z=-\frac{h}{2}}^{z=\frac{h}{2}} \right] \Big|_{y=-\frac{b}{2}}^{y=\frac{b}{2}}$$

$$m_x = \int_A y f_z \, dA + \int_A z f_y \, dA + \left[z \left[y \left(\sigma_{xy} \frac{\partial w}{\partial x} + \sigma_y \frac{\partial w}{\partial y} \right) \right] \Big|_{y=-\frac{b}{2}}^{y=\frac{b}{2}} \right] \Big|_{z=-\frac{h}{2}}^{z=\frac{h}{2}} + \\ + \left[y^2 \left[\sigma_{xz} \left(\frac{1}{2} \frac{\partial w_0}{\partial x} + \frac{y}{3} \frac{\partial \theta_x}{\partial x} \right) + \frac{\sigma_z}{2} \right] \Big|_{z=-\frac{h}{2}}^{z=\frac{h}{2}} \right] \Big|_{y=-\frac{b}{2}}^{y=\frac{b}{2}} + \\ + \left[z^2 \left[\sigma_{xy} \left(\frac{1}{2} \frac{\partial v_0}{\partial x} - \frac{z}{3} \frac{\partial \theta_x}{\partial x} \right) + \sigma_y \right] \Big|_{y=-\frac{b}{2}}^{y=\frac{b}{2}} \right] \Big|_{z=-\frac{h}{2}}^{z=\frac{h}{2}} + \\ + \left[y \left[z \left(\sigma_{xz} \frac{\partial v}{\partial x} + \sigma_z \frac{\partial v}{\partial z} \right) \right] \Big|_{z=-\frac{h}{2}}^{z=\frac{h}{2}} \right] \Big|_{y=-\frac{b}{2}}^{y=\frac{b}{2}}$$

For thin-beam theory, replacing the transverse force resultants:

$$Q_z^{beam} = \frac{\partial M_y}{\partial x}^{beam} + m_y^{beam} - \int_A \left(z \ \rho_0 \frac{\partial^2 u}{\partial t^2} \right) dA$$

$$Q_y^{beam} = \frac{\partial M_z}{\partial x}^{beam} + m_z^{beam} - \int_A \left(y \ \rho_0 \frac{\partial^2 u}{\partial t^2} \right) dA$$

the equilibrium equations can be reduced to the following four:

$$\frac{\partial N_x}{\partial x}^{beam} + q_x^{beam} = \int_A \left(\rho_0 \frac{\partial^2 u}{\partial t^2} \right) dA \tag{B.9a}$$

$$\frac{\partial^2 v_0}{\partial x^2} N_x^{beam} + \frac{\partial v_0}{\partial x} \frac{\partial N_x}{\partial x}^{beam} + \\ + \frac{\partial^2 M_z}{\partial x^2}^{beam} + \frac{\partial m_z}{\partial x}^{beam} + q_y^{beam} = \int_A \left(\rho_0 \frac{\partial^2 v}{\partial t^2} + \frac{\partial}{\partial x} \left(y \ \rho_0 \frac{\partial^2 u}{\partial t^2} \right) \right) dA \tag{B.9b}$$

$$\frac{\partial^2 w_0}{\partial x^2} N_x^{beam} + \frac{\partial w_0}{\partial x} \frac{\partial N_x}{\partial x}^{beam} + \\ + \frac{\partial^2 M_y}{\partial x^2}^{beam} + \frac{\partial m_y}{\partial x}^{beam} + q_z^{beam} = \int_A \left(\rho_0 \frac{\partial^2 w}{\partial t^2} + \frac{\partial}{\partial x} \left(z\, \rho_0 \frac{\partial^2 u}{\partial t^2} \right) \right) dA \quad \text{(B.9c)}$$

$$\frac{\partial M_x}{\partial x}^{beam} + m_x^{beam} - \left(\frac{\partial M_z}{\partial x}^{beam} + m_z^{beam} \right) \frac{\partial w_0}{\partial x} - \\ - \left(\frac{\partial M_y}{\partial x}^{beam} + m_y^{beam} \right) \frac{\partial v_0}{\partial x} = \int_A \rho_0 \left(y \frac{\partial^2 w}{\partial t^2} + z \frac{\partial^2 v}{\partial t^2} \right) dA \quad \text{(B.9d)}$$

The static version of equations (B.9) were also derived, by the Newton's second law, for the analysis of the elastic bending and torsion of twisted non-uniform rotor blades (Hodges and Dowell, 1974). Considering two vectorial equations for the equilibrium of an differential element, the authors initially written three force equilibrium equations and another three moment equilibrium equations:

$$\begin{aligned} \frac{\partial N_x}{\partial x} + p_x &= 0 \\ \frac{\partial Q_y}{\partial x} + p_y &= 0 \\ \frac{\partial Q_z}{\partial x} + p_z &= 0 \\ \frac{\partial M_x}{\partial x} + Q_z \frac{\partial v}{\partial x} - Q_y \frac{\partial w}{\partial x} + m_x &= 0 \\ \frac{\partial M_y}{\partial x} - Q_z + N_x \frac{\partial w}{\partial x} + m_y &= 0 \\ \frac{\partial M_z}{\partial x} + Q_y - N_x \frac{\partial v}{\partial x} + m_z &= 0 \end{aligned}$$

This equations are the same as equations (B.7) and (B.8) in the linear static terms, but not in the nonlinear terms. In the presented deduction the non-linear terms including N_x are included in the equilibrium of the transverse resultant forces, as a consequence of the curvature of the beam. On the other hand, in the cited report those nonlinear terms are included in the moment equilibrium equations. Lastly, note that both approaches yield the same governing equations for thin beams.

C.

C.1. Specifying limits for welding heat input

C.1.1. Introduction

Some recommendations regarding the maximum and minimum heat input are provided by welding codes such as the following European and American standards:

- EN 1011-2:2001 - Welding - Recommendations for welding of metallic materials
- AWS D1.1:2000 - Structural Welding Code - Steel

Some of the most frequently applied structural steel grades (S235JR, S275JR and S355JR) were selected to present a more detailed analysis. The European code provides two methods for avoidance of hydrogen induced cracking: Method A and Method B. With a manganese content ranging from 1.4 to 1.6% (see table C.1), those steel grades are covered by the Method A. On the other hand, for the same purpose, from the American standard the HAZ Hardness Control method is available. All these methods allow to directly or indirectly specify the minimum heat input.

Table C.1.: Normative chemical ladle composition according to EN 10025-2 (2004), for the steels: S235JR, S275JR and S355JR.

	Ladle analysis (EN 10025-2, 2004)							
	%C	%Si	%Mn	%P	%S	%N	%Cu	%"Other"
S235JR	0.20	-	1.40	0.035	0.035	0.012	0.55	-
S275JR	0.22	-	1.50	0.035	0.035	0.012	0.55	-
S355JR	0.24	0.55	1.60	0.035	0.035	0.012	0.55	-

C.1.1.1. Carbon equivalent

Both the Carbon Equivalent (CE) defined by the AWS as follows:

$$CE = C + \frac{Mn + Si}{6} + \frac{Cr + Mo + V}{5} + \frac{Ni + Cu}{15} \tag{C.1}$$

and the Carbon Equivalent Value (CEV) defined by the European code as:

$$CEV = C + \frac{Mn}{6} + \frac{Cr + Mo + V}{5} + \frac{Ni + Cu}{15} \tag{C.2}$$

were estimated with basis on the maximum concentration of each element available from table C.1.

Additionally, table C.2 includes the normative values for the maximum Carbon Equivalent Value (CEV^{max}) according to EN 10025-2 (2004). It is notorious that the normative CEV^{max} values are clearly lower than the CEV prediction.

The calculation of the CE is the same as that for the CEV, except that, adding $\frac{\%Si}{6}$, it accounts for silicon's effect on the hardenability. Based on this, a more realistic estimation of the maximum Carbon Equivalent (CE^{max}) was obtained summing $\frac{\%Si}{6}$ to the normative CEV^{max}.

Table C.2.: Comparison of the CE and CEV values for different structural steel grades.

	CEV	CEV^{max}	CE	CE^{max}
	eq. (C.2)	(EN 10025-2, 2004)	eq. (C.1)	$CEV^{max} + \frac{\%Si}{6}$
S235JR	0.47	0.38	0.47	0.38
S275JR	0.51	0.42	0.51	0.42
S355JR	0.54	0.47	0.64	0.56

Note that the similarity between the equations (C.1) and (C.2) is explained as follows. Based on the analysis of steels with very low silicon contents, the CE value was originally developed as an hardenability formula, but has come to be used as a hydrogen cracking formula. Although the effect of silicon is negligible in terms of cracking behavior, subsequent researches had shown that silicon had an effect on hardenability similar to that of manganese, as expressed by equation (C.1) (Bailey, 1994).

C.1.1.2. HAZ hardness control method (AWS D1.1, 2006)

The HAZ hardness control method assumes that cold cracking will not occur if the hardness of the HAZ is kept below some critical value. Its main value is in determining the minimum heat input (and hence minimum weld size) that prevents excessive hardening, subjected the following limitations:

- The guideline based on this method is restricted to fillet welds;
- It is assumed that cracking will not occur if the hardness of the HAZ is kept below some critical values;
- The method may be conservative for plain carbon and plain carbon-manganese steels and optimistic for some low-alloy steels, particularly those containing columbium (niobium) due to their additional hardenability;
- The hydrogen level and restraint are not explicitly considered;
- The method is not applicable to quenched and tempered steels.

Laboratory tests show that HAZ cracking is generally prevented if the HAZ Vickers hardness is less than 350Vh. With low-hydrogen electrodes, although harness of 400HV could be tolerated without cracking, it may not be tolerable in service (AWS D1.1, 2006).

For the sake of simplicity, about 60 points were digitalized from (AWS D1.1, 2006, Annex I, figure I-2), and through data fitting the following relations between the critical cooling rate R^c_{540} and the carbon equivalent CE were obtained (with $R^2 = 1$):

$$400HV: \qquad CE = 0.0966 \times (\log R^c_{540})^2 - 0.5075 \times \log R^c_{540} + 1.0069 \tag{C.3a}$$

$$350HV: \qquad CE = 0.0956 \times (\log R^c_{540})^2 - 0.4974 \times \log R^c_{540} + 0.9572 \tag{C.3b}$$

Alternatively, fitting the data in function of CE (with $R^2 = 1$):

$$400HV: \qquad R^c_{540} = 10^{220.26\times CE^4 - 492.21\times CE^3 + 412.61\times CE^2 - 157.32\times CE + 24.61} \tag{C.4a}$$

$$350HV: \qquad R^c_{540} = 10^{176.56\times CE^4 - 384.83\times CE^3 + 314.38\times CE^2 - 117.52\times CE + 18.43} \tag{C.4b}$$

C.1.1.3. Method A for the avoidance of hydrogen cracking (EN 1011-2, 2001)

The Method A is based on extensive experimental data mainly from carbon-manganese steels. Non-alloyed, fine grained and low alloy steels are covered for the range of chemical composition presented in table C.3 and for a carbon equivalent value (CEV) ranging from 0.30 to 0.70%. Note that the CEV formula (C.2) may not be suitable for boron-containing steels.

The welding conditions are given in graphical form, relating the minimum pre-heat temperature with the combined thickness, heat input, hydrogen scale and maximum carbon equivalent. The concept of combined thickness allows to virtually cover all types of joints.

Table C.3.: Range of application of the CEV expression

	CEV - equation (C.2)
Carbon	0.05 to 0.25
Silicon	0.8 max.
Manganese	1.7 max.
Chromium	0.9 max.
Copper	1.0 max.
Nickel	2.5 max.
Molybdenum	0.75 max.
Vanadium	0.20 max.

C.1.2. Minimum heat input

C.1.2.1. Using the hardness control method

Given the critical cooling rate R^c_{540} values in table C.4, predicted through equations (C.4), the minimum heat input can be obtained, from AWS D1.1 (2006, Figures I-3), for discrete plate thicknesses.

Table C.4.: Critical cooling rate R^c_{540} estimated according to the AWS, based on the assumed CE^{max} values from table C.2.

	R^c_{540} [$°C/s$] for maximum hardness:	
	$\leq$ 400 HV	$\leq$ 350 HV
	eq. (C.4a)	eq. (C.4b)
S235JR	99	55
S275JR	51	33
S355JR	29	20

In order to allow for mathematical manipulation, and for the sake of simplicity, alternatively equations (8.17) can be used. As seen in figure C.1, the digitalized data points

from AWS D1.1 (2006, Figure I-3a) are reasonably well predicted replacing $C_{2D}^{H} = 0.74$ and $C_{3D}^{H} = 1.47$ (from table 8.1) and the following material properties for carbon steels (at room temperature ($T_0 = 20$)): $\rho = 7850\ kg/m^3$, $k = 53\ W/m/°C$, $c = 440\ J/kg/°C$, available from Acevedo (2011).

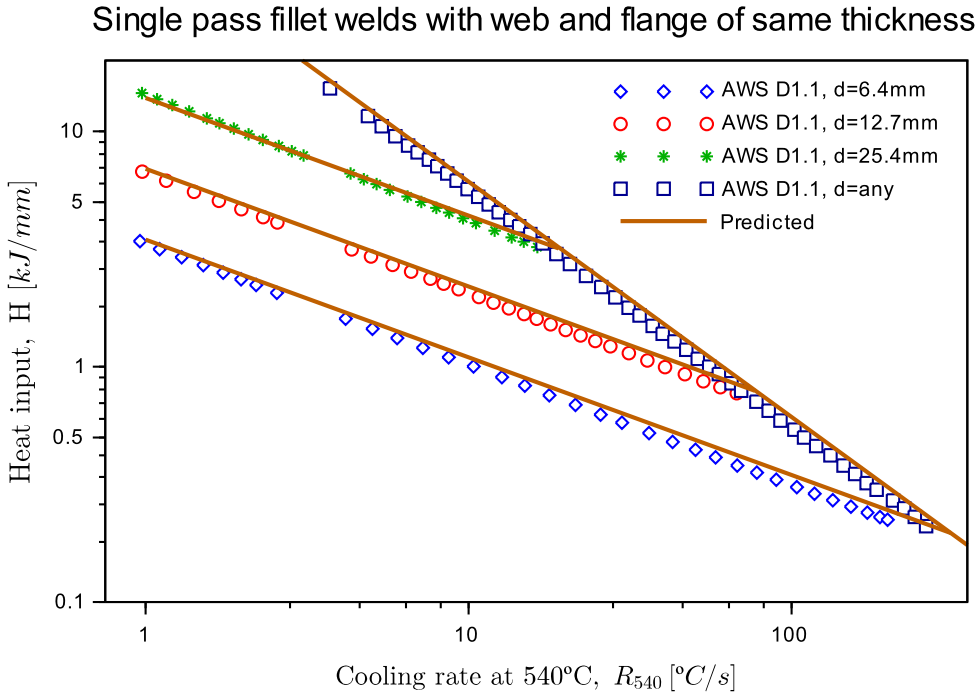

Figure C.1.: Single pass fillet welds with web and flange of same thickness: comparison of the prediction from equations (8.17) with digitalized data points from AWS D1.1 (2006, Figure I-3a).

C.1.2.2. Comparison between hardness control method and method A

Having equations (8.17) correctly adjusted to the data in AWS D1.1 (2006, Figures I-3), the minimum heat input required to keep the maximum HAZ hardness below 400HV can be plotted against the average thickness of a T-joint, as in figure C.2, for different CE values.

On the other hand the equivalent data given by (EN 1011-2, 2001, method A, figure C.2) was digitalized. The pre-heat temperature is $20°C$, the average plate thickness is 1/3 of the combined thickness, an hydrogen scale D is selected assuming solid wires for gas-shielded arc welding are used, and the CEV^{max} normative values are considered.

For an easier comparison, the ratio between the minimum heat inputs defined by the HAZ hardness control method and method A is available in figure C.3. No comparison is made for the S235JR steel grade because no additional specific data is available in EN 1011-2 (2001) for $CEV \leq 0.44$ and hydrogen scale D.

It is notorious that even allowing for maximum HAZ hardness up to 400HV, the HAZ hardness control establishes a clearly higher minimum heat input than the method A for hydrogen control. In part these results are explained considering that the AWS D1.1 (2006) allows for a generic low-hydrogen type of filler metal, including those used in SMAW, GMAW, fluxed cored arc and submerged arc. Such materials correspond in the Method A from EN 1011-2:2001 to the scales B, C and D.

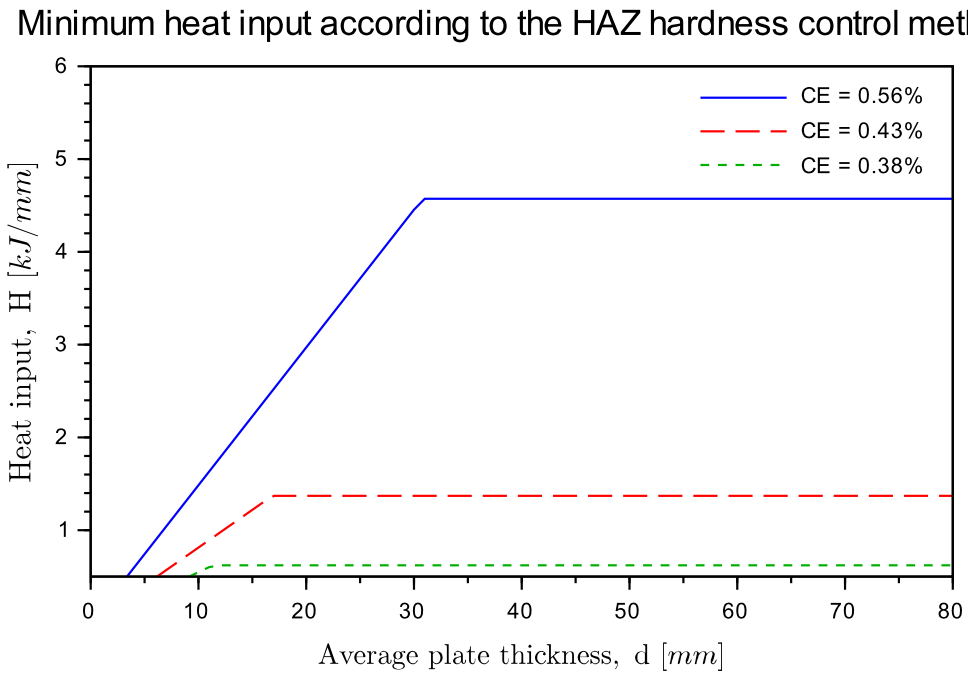

Figure C.2.: Minimum heat input specified by the HAZ hardness control method for 400HV and different CE values.

Repeating the previous comparison, but now considering the data from scale B (see figure C.4), the minimum heat input determined by the HAZ hardness control method may be surpassed, depending on the thickness, due to the increased hydrogen content.

C.1.3. Maximum heat input

Both AWS D1.1 (2006) and EN 1011-2 (2001) do not provide any limitations on the maximum heat input. AWS D1.1 (2006) addresses the need to keep the cooling rate high in quenched and tempered steels in order to preserve the strength and toughness of the HAZ material, but in the end suggests the strict adoption of the parameters proposed by the steel producers, given the wide range of possible maximum heat input.

C.2. Properties of S235JR structural steel

In this section, thermo-physical properties are defined for the structural steels in general, and, whenever necessary, in particular for steel S235JR.

Given the lack of data, the Eurocode physical properties diagrams may be used, although suffering from some important limitations Akhlaghi (2014):

- The values for the thermal properties are only available below the melting temperature, given that for fire-resistant design of structures they are of no interest;
- The range of heating rates in Eurocode is assumed between 2 and $50°C/min$, while in welding this value is of the order of $10^{2}°C/min$.

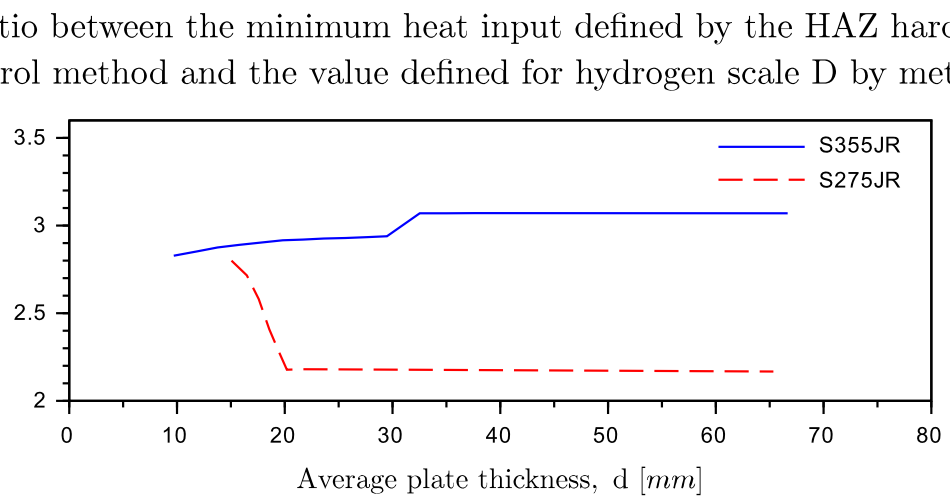

Figure C.3.: Ratio between the minimum heat inputs defined by the HAZ hardness control method for 400HV and method A for hydrogen scale D.

C.2.1. Thermo-physical properties

Acevedo (2011) used the characteristic values given by EN 1993-1-2 (2005): the thermal conductivity and specific heat of carbon steels are presented in table C.5, while the average value $7850 kg/m^3$ was fixed for the density. The authors pointed out that the high peak of specific heat at $735°C$ is mainly due to phase transformation of ferrite-pearlite to austenite; considering that the peak for that temperature is theoretically an indefinite pole (for pure metals), it would be more appropriate to use the experimentally obtained value: 1100 $J/kg/°C$.

Acevedo (2011) obtained the same residual stress predictions trough numerical simulations, using either $c_{(T=735°C)}$ equal to 5000 or 1100 $J/kg/°C$. Following a more extreme approach, FEM simulations were compared with experimental results in a study on welding temperate distribution based on the properties of table C.5, almost neglecting the previously referred high peak (Attarha and Sattari-Far, 2011).

Inspired by other researches, such as that presented by Goldak et al. (1984), in order to account for convective stirring at high velocities ($\approx 1 m/s$) found in the weld pool, Acevedo (2011) and Akhlaghi (2014) increased the conductivity value to about three times its value at the solidus temperature, when the melting temperature is exceeded. In table C.5, the thermal values included in brackets were predicted for S235JR according to this approach.

The solidus ($1480°C$) and liquidus ($1511°C$) temperatures were estimated following the empirical relations based on the composition data:

$$T_{liq} = 1537 - 88(\%C) - 25(\%S) - 5(\%Cu) - 8(\%Si) - 5(\%Mn) - \\ - 2(\%Mo) - 4(\%Ni) - 1.5(\%Cr) - 18(\%Ti) - 2(\%V) - 30(\%P) \qquad \text{(C.5)}$$

$$T_{sol} = 1535 - 200(\%C) - 12.3(\%Si) - 6.8(\%Mn) - 124.5(\%P) - \\ - 183.9(\%S) - 4.3(\%Ni) - 1.4(\%Cr) - 4.1(\%Al) \qquad \text{(C.6)}$$

adopted by Thomas et al. (1987) and the same recently applied by Akhlaghi (2014).

The latent heat of solidus-liquidus transformation influences the temperature field: the

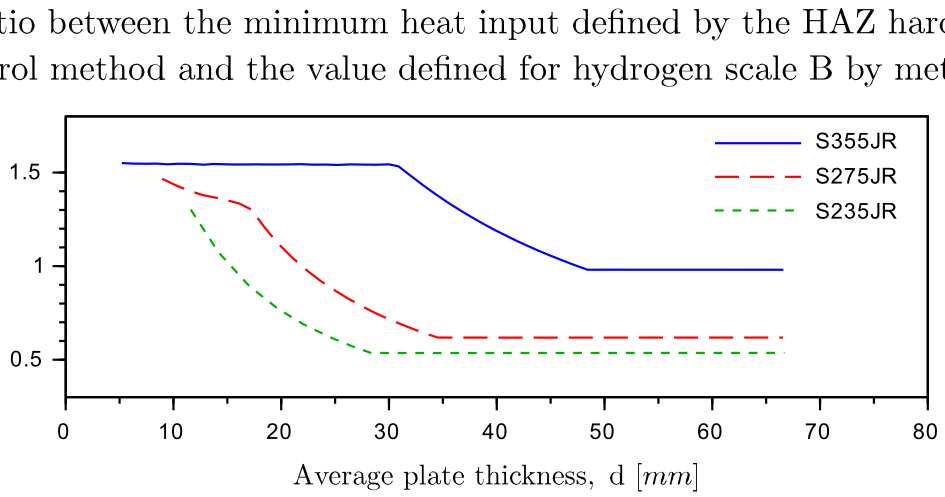

Figure C.4.: Ratio between the minimum heat inputs defined by the HAZ hardness control method for HV<400HV and method A for hydrogen scale B.

melting front gets closer to the heat source and the solidification is delayed. This is, the molten pool shape becomes more stretched in the direction of welding, when the latent heat is considered (Akhlaghi, 2014). Very often this parameter is omitted in the publications concerning welding simulations. Acevedo (2011) considered a value of 247 kJ/kg, available from other publication dating back to 1965; on the other hand Thomas et al. (1987) assumed a value of 272 kJ/kg, which is more in accordance with updated material databases where the latent heat for carbon steels is estimated to range between 270 and 275 kJ/kg (Granta Design Limited, 2013).

Table C.5.: Thermo-physical properties for carbon steels, in particular for steel S235JR when marked with †

	based on (Attarha and Sattari-Far, 2011)			based on (Acevedo, 2011)	
Temp. $[°C]$	Density $[kg/m^3]$	Conductivity† $[J/m/°C]$	Specific heat† $[J/kg/°C]$	Conductivity $[J/m/°C]$	Specific heat $[J/kg/°C]$
0	7900	45.9	444	-	-
20	-	-	-	53.3	440
100	7880	44.8	472	50.7	488
200	7830	43.4	503	47.3	530
300	7790	41.4	537	44	565
400	7750	38.9	579	40.7	606
500	-	-	-	37.4	667
600	7660	33.6	692	34	760
650	-	-	-	-	814
700	-	-	-	30.7	1008
735	-	-	-	-	5000
750	-	-	-	-	1483
800	7560	28.7	837	27.3	803
900	-	-	-	27.3	650
1200	7370	28.6	860	27.3	650
1300	7320	29.5	863	-	-
T_{sol}	7320	(29.5)	-	(27.3)	-
T_{liq}	7320	(103.3)	-	(81.9)	-
2000	-	(103.3)	-	(81.9)	-